GALAXY EVOLUTION: THE DRAGONS SURVEY AND LUMINOSITY FUNCTIONS WITH PHOTOMETRIC REDSHIFTS

by

Samuel J. Schmidt

B.Sc. in Physics, Carnegie Mellon University, 2000

M.Sc. in Physics, University of Pittsburgh, 2002

Submitted to the Graduate Faculty of
the Department of Physics and Astronomy in partial fulfillment
of the requirements for the degree of

Doctor of Philosophy

University of Pittsburgh

2007

UNIVERSITY OF PITTSBURGH

DEPARTMENT OF PHYSICS AND ASTRONOMY

This dissertation was presented

by

Samuel J. Schmidt

It was defended on

November 30th 2007

and approved by

Prof. Andrew Connolly, University of Pittsburgh

Prof. Ravi Sheth, University of Pennsylvania

Prof. David Turnshek, University of Pittsburgh

Prof. Vladimir Savinov, University of Pittsburgh

Prof. Rupert Croft, Carnegie Mellon University

Dissertation Director: Prof. Andrew Connolly, University of Pittsburgh

Copyright © by Samuel J. Schmidt
2007

GALAXY EVOLUTION: THE DRAGONS SURVEY AND LUMINOSITY FUNCTIONS WITH PHOTOMETRIC REDSHIFTS

Samuel J. Schmidt, PhD

University of Pittsburgh, 2007

This thesis examines two complementary approaches to the study of galaxy evolution using multiwavelength large area galaxy surveys. The first part of the thesis focuses on a statistical study of the overall galaxy population, namely the evolution of galaxy luminosity functions, while the second part of the thesis aims to study an interesting population of rare galaxies selected based on their radio and optical properties, namely high redshift radio galaxies selected from SDSS and FIRST.

We compute the luminosity function (LF) for the general galaxy population and as a function of type using photometric redshifts derived from the SDSS Southern Survey. We present a new maximum likelihood estimator and show that it accounts for the uncertainties associated with photometric redshifts. In addition to three existing parameterizations, we introduce the use of cubic BSplines to fit the luminosity function. We show evidence for the evolution of the luminosity function, but defer much of the analysis until a better photometric redshift dataset is available.

The second part of the thesis describes the Distant Radio Galaxies Optically Non-detected in SDSS (DRaGONS) survey. Our new selection criteria appear to be very efficient at identifying high redshift radio galaxies, including a substantial population of shallow spectrum radio sources missed by competing selection techniques. These sources, when confirmed, will have a dramatic effect on the empirical z-alpha relation. I describe the environment of early galaxy formation through the study of nearby Extremely Red Objects (EROs) and faint K-band galaxy counts. We find an excess number of faint EROs and galaxies around a subset of DRaGONS candidates, indicating that massive galaxies form in overdense environments. 10% of DRaGONS galaxies are redder than expected, which indicates moderate obscuration and the possible presence of ongoing star formation. These objects, which we dub Red DRaGONS, could represent a significant radio-loud population missing from optically selected AGN surveys.

TABLE OF CONTENTS

LIST OF TABLES

LIST OF FIGURES

PREFACE

This thesis is dedicated to my parents and my grandparents, without whose help and encouragement I wouldn't have made it this far, and to my little buddy Oliver, who it's been an absolute joy to watch grow up. Thanks to all of my friends, particularly Jeremy and Bambi for letting me hang around so much, and Rich and Ryan for all of the card playing and such. Thanks also to my brother and sisters, Derek, Rachel, and Abby, as they would kill me if I didn't mention them (and the same goes for Michele). As for the actual thesis work: Special thanks to Ravi Sheth for realizing that the original estimator that we were using to estimate the luminosity function was incorrect, and more thanks for coming up with the correct estimator. Thanks to Jeremy Brewer for supplying lots of useful code, including the catalog calibration used in the latter half of DRaGONS, as well as the matched aperture deep stripe 82 catalogs used in the luminosity function analysis. Thanks to Mihir Arjunwadkhar and Chris Genovese for supplying the BSplines code in C++ used in the spline fits of the luminosity function, as well as for the discussion that went along with its implementation. Thanks to all of the graduate students and others who helped along the way, or at least provided people to talk to in the office: Michele, Ummi, Ramin, Cameron, Niraj, Ching-Wa, Suman, Dan, Anna, Arne, and anyone who I'm forgetting at the moment from the more than seven years that I've been here. Thanks to Alberto Conti and Andrew Hopkins for detailed help with luminosity functions and radio galaxies, respectively, as well as Jeff, Ryan, Simon, Joerg and Dan Vanden Berk for additional suggestions along the way. Thanks to everyone who helped out by coming along observing for DRaGONS, suffering along through rain, snow, ice, dust, fire, wind, fog, and everything else that we lost time for: Andy, Andrew, Ryan, Niraj, Jeremy, Julia Bryant, and Bhuvanesh Jain.

Parts of this work are based on observations collected at Kitt Peak National Observatory,

National Optical Astronomy Observatory, which is operated by the Association of Universities for Research in Astronomy, Inc. (AURA) under cooperative agreement with the National Science Foundation.

FLAMINGOS was designed and constructed by the IR instrumentation group (PI: R. Elston) at the University of Florida, Department of Astronomy, with support from NSF grant AST97-31180 and Kitt Peak National Observatory.

The SDSS is managed by the Astrophysical Research Consortium for the Participating Institutions. The Participating Institutions are the American Museum of Natural History, Astrophysical Institute Potsdam, University of Basel, University of Cambridge, Case Western Reserve University, University of Chicago, Drexel University, Fermilab, the Institute for Advanced Study, the Japan Participation Group, Johns Hopkins University, the Joint Institute for Nuclear Astrophysics, the Kavli Institute for Particle Astrophysics and Cosmology, the Korean Scientist Group, the Chinese Academy of Sciences (LAMOST), Los Alamos National Laboratory, the Max-Planck-Institute for Astronomy (MPIA), the Max-Planck-Institute for Astrophysics (MPA), New Mexico State University, Ohio State University, University of Pittsburgh, University of Portsmouth, Princeton University, the United States Naval Observatory, and the University of Washington.

This thesis makes use of data products from the Two Micron All Sky Survey, which is a joint project of the University of Massachusetts and the Infrared Processing and Analysis Center/California Institute of Technology, funded by the National Aeronautics and Space Administration and the National Science Foundation.

This research has made use of data obtained from or software provided by the US National Virtual Observatory, which is sponsored by the National Science Foundation.

This work was partially supported by NSF ITR grant ACI0121671, NSF CAREER grant AST 99-84924, and NASA grant AISR NAG5-11996, and the Zacceus Daniel Fellowship.

1.0 INTRODUCTION

“Shimmering, travelling by
Magical waves just under the sky
It knows no time, it knows no bounds
Coming clear beneath the clouds
Destination here and now
I behold travellin’ light”

-“(I Believe in) Travellin’ Light” Belle & Sebastian

In this thesis, I will discuss galaxy evolution, and examining how galaxies first formed in the distant past. Galaxies evolve over very long ”astronomical” timescales, from tens of millions of years to billions of years. Thankfully, the finite speed of light provides just such a tool: because light from distant galaxies takes millions to billions of years to reach us, we are essentially seeing what far away galaxies looked like in the distant past, and the farther away the galaxy is, the further back in time we look. Thus, as long as there is no positional dependence to how galaxies form and evolve (i. e. the Universe is homogeneous and isotropic, which it appears to be), we can use distance as a substitute for time, which enables us to study how, statistically, the galaxy population changes as we look to greater distances. We can also identify the earliest galaxies to form simply by finding those that are farthest away.

The past decade has seen major developments in astrophysics: the emergence of the ”Concordance model” of cosmology, where the energy density of the Universe is dominated by Dark Energy and Dark Matter (Spergel et al., 2003, e.g.), and the success of the halo model/hierarchical clustering proving to be excellent fits to new observations. A detailed understanding of how galaxies form and evolve, however, has proven elusive. While the large scale clustering of dark matter halos is relatively simple, and depends only on gravity, galaxy formation depends on complicated nonlinear processes involving gas, dust, feedback, often collectively called “gastrophysics”. No complete picture of galaxy evolution exists, and it is only in the past few years that the data has become available to study how galaxies evolve in an observational sense.

The advent of large surveys covering a range of wavelengths (FIRST in the radio, 2MASS in the near-infrared, 2df and SDSS (York et al., 2000) in the optical, and soon PanSTARRS, DES, and LSST) has opened up the realm of statistical analysis in the field of galaxy evolution, with orders of magnitude more data than the previous generation of surveys. We can use this flood of data in many ways, two that are important here: employ the massive amount of data to study the statistical average evolution of the overall galaxy population with time, and exploit the combined information from large areas of the sky and multiple wavelengths to efficiently isolate and study rare galaxy populations.

The most fundamental observable of galaxies is their apparent brightness, and therefore, one of the most basic measures of galaxies is their distribution of luminosities. Studying how this distribution, which we will refer to as the Luminosity Function, or LF, changes over time can tell us about how galaxies evolve, as well as differentiate between different theoretical galaxy formation scenarios. Determination of the Universal luminosity function for all galaxies is very important; however, we also know that galaxies come in a number of populations, or more accurately, from an almost continuous distribution of galaxy ”types”. The common ”Hubble tuning fork” (Hubble, 1926) diagram of galaxy types, which groups galaxies into ellipticals, spirals , and irregulars, was an early example of classifying galaxies based on their visible morphology. Galaxy type is also commonly determined using galaxy colors or spectral properties (e. g. Yip (2005) and references therein). Determining the type dependent galaxy luminosity function will shed light on how these different populations evolve, when they form, and hopefully give us insight into the mechanisms of their formation and evolution. Any viable galaxy formation theory will have to reproduce this complex picture of how galaxies evolve.

One method to both increase sample size and depth for galaxy surveys is to use photometric rather than spectroscopic redshifts (see Section 2.1.5 and Appendix B for details); however, there is a tradeoff in accuracy in exchange for the larger sample size. Understanding the effect of these uncertainties is very important, particularly since large future surveys will be purely photometric (e. g. LSST). In this thesis I will discuss a new maximum likelihood estimator that compensates for such uncertainties when computing the galaxy luminosity function.

Another approach to discovering how galaxies evolve is to simply search for the very farthest galaxies detectable in order to see how galaxies looked in the distant past. But, studies of galaxy evolution at higher redshift are challenging. As you increase redshift, the bulk of the light from stars begins to shift out of the UV and optical and into the near infrared and beyond, making detection in the optical more difficult. The greater distances mean cosmological dimming, so the objects are also simply much fainter, and require deep imaging. Several techniques have been developed to detect high redshift galaxies. The most simple being Lyman Break galaxy techniques, where the Lyman break (which is formed by neutral Hydrogen absorbing all photons shortward of 912 $\mathring{A}$) passing through certain filters is used to identify "dropout" galaxies not detected in the bluest filters (e.g. Steidel et al., 1996). Lyman alpha emitters are found by taking deep imaging to select objects where very bright Ly α emission in the very narrow redshift range falls within the narrow filter bandpass. Extremely Red Objects (EROs) are a loosely defined class of objects, most of which are at fairly high redshifts. The BzK criteria (Daddi et al., 2004) is designed to select both passive and star forming galaxies at $1.4 \leq z \leq 2.5$ from a specific region of color-color space. Each of these techniques are sensitive to a specific set of high redshift galaxies (star forming, red, etc...), none of which span a representative sample of galaxies, so care must be taken when making assumptions from such samples. The alternative approach to finding high redshift objects is to take very long integration exposures of a small area in order to directly observe objects free of any selection effects. Such surveys with small area but great depth are referred to as "pencil beam" surveys. The drawbacks of pencil beam surveys are the expense of lengthy telescope time necessary, and that the small area makes them susceptible to sample variance. Therefore, optimally, we seek a combination of deep imaging and areal coverage that will allow us to uniformly select a sample of high redshift galaxies. We aim to take advantage of existing large datasets in order to accomplish this goal. Our new selection criteria is, essentially, a "dropout" (in this case, non-detection in and SDSS band) technique in order to select a sample of massive high redshift radio galaxies.

In the hierarchical galaxy formation scenario indicated by the concordance cosmological model, the very first stars should form in the first objects to collapse, which will be in the most dense regions of the Universe. Since they begin collapsing first, and with the old hilltops on top of hilltops argument, these sites of initial overdensity will eventually evolve into massive galaxy clusters, which host giant radio galaxies. Hence, finding high redshift radio galaxies should lead us to some of the sites of the earliest star formation. We have developed a novel technique to efficiently identify high redshift radio galaxies over a very wide area of the sky.

There are two main goals of this thesis: First, to understand the luminosity distribution of galaxies and how it evolves, both in general and as a function of galaxy type. This will be done with galaxies with photometric redshifts derived from the SDSS Southern Survey using a new maximum likelihood technique that is accounts for the uncertainties inherent in photometric redshifts. Quantifying the statistical evolution of the galaxy population will enable us to differentiate between galaxy formation scenarios and provide the raw data to study the detailed astrophysical processes that drive this evolution. The second goal is to undertake a complete census of high redshift radio galaxies in order to study how the very first galaxies formed, as well as the interplay between star formation and AGN activity in the very early Universe.

1.1 OUTLINE OF THESIS

The structure of this thesis is as follows: In Chapter 2 I will discuss galaxy luminosity functions. I will describe several methods to compute the LF, and show the effect of photometric redshift uncertainties on measurements of the LF using these techniques. I then present a new maximum likelihood estimator constructed to account for such errors. Finally, I will show results from applying this estimator to photometric redshift data from SDSS Stripe 82. In Chapter 3 I will discuss a search for massive high redshift galaxies: the DRaGONS survey. Chapter 3 presents target selection, observations, reduction, analysis and results for nearly two hundred high redshift radio galaxy candidates. I then present studies of the radio galaxy environment, aimed at understanding how massive galaxies form. Much of this Chapter 3 is taken from or expands on Schmidt et al. (2006). Chapter 4 will contain conclusions and discussion of further work with these two projects. Also included are appendices describing B(asic) Splines and photometric redshifts in more detail. Throughout this thesis, I assume $\Omega_M = 0.3$, $\Omega_\Lambda = 0.7$. For the Luminosity Function measurements, I assume a Hubble Constant $h = 0.7$.

2.0 GALAXY LUMINOSITY FUNCTIONS

Note: The material in this chapter is part of a collaborative effort, to which many people contributed. The correct form of the maximum likelihood estimator discussed in Section 2.1.5 was formulated by Ravi Sheth. The BSplines code used throughout this Chapter was written by Mihir Arjunwadkhar and Chris Genovese and modified to work with astronomical data. The photometric redshift code used throughout the thesis was written by Tamas Budavari and used with his permission. Andy Connolly and Alberto Conti provided essential feedback during the initial phases of this work that allowed the project to get off the ground.

The galaxy luminosity function, or LF, denoted $\phi(M)$, is one of the basic measurements that can be applied to the overall galaxy population. It is simply the (comoving) number density of galaxies as a function of luminosity (number of galaxies per absolute magnitude per Mpc^3) as measured through a specific filter. The simplicity of this statistic makes it very useful for discriminating between different galaxy and cosmological models: i.e. one of the first tests that a galaxy formation model must pass is whether or not it can successfully reproduce the galaxy luminosity function. Almost as soon as galaxies were recognized as separate "island universes" outside of the Milky Way, work began on determining their luminosity function. By estimating their luminosity based on the brightest stars in each galaxy Hubble (1936a) observed that the LF for local galaxies appeared to be a Gaussian. In fact, in the follow up paper, Edwin Hubble saw some of the first evidence that the luminosity function was not universal, as he noted that the LF for local irregular galaxies showed that they were about half as bright as the others (Hubble, 1936b). An in depth review of the history of LF determinations is given by Binggeli et al. (1988), though we will discuss only some of those relevant to methods used in this work. As they note, however, the Gaussian form of the LF found by Hubble was shown to be biased by neglected selection effects, namely the exclusion of fainter dwarf galaxies. This is always a concern when using apparent magnitude limited samples, as we shall use in this thesis, to examine cosmological quantities. This is due to a Malmquist bias: given a flux limited sample, the average luminosity of galaxies will increase with redshift, as less luminous objects at a given redshift will begin to fall below the fixed flux cutoff. Viewed another way, objects with fainter absolute magnitudes can be seen over a smaller volume of space than the more luminous ones. Schmidt (1968) described a new way to compensate for this effect, though his original sample consisted of quasars rather than galaxies, by calculating the maximum volume that each quasar would be visible over, given its absolute magnitude, binning the objects in absolute magnitude, and weighting each one by the inverse of the maximum volume to calculate a density estimate; hence its name: the 1/Vmax estimator of the luminosity function (see Section 2.1.1 for slightly more detail). This estimator requires binning of the data, and assumes no spatial correlation in the underlying galaxy distribution and is, thus, biased by the presence of large scale structure of the galaxies. Sandage et al. (1979) (STY) developed a new maximum likelihood based LF estimator which avoids any density dependence, though assuming a parametric form for the LF is necessary (see Section 2.1.2 for details). Efstathiou et al. (1988) (EEP) used this maximum likelihood method to develop a "nonparametric" luminosity function estimator, referred to as the stepwise maximum likelihood, or SWML, method (see Section 2.1.4 for details). While there are many other estimators, the ones most common in the literature are the STY and SWML estimators, and variants thereof. In Section 2.1.5 I will discuss an extension to the STY LF estimator that accounts for the large uncertainties associated with photometric redshifts. Examination of the environmental dependence of the luminosity function will not be discussed in this thesis, i.e. the data will not differentiate between group, cluster and "field" (non cluster) galaxies, which adds the complication of group/cluster finding to the LF determination (e.g. Croton et al. (2005)).

From the original Gaussian distribution postulated by Hubble, additional data showed that, while the number of luminous galaxies did decrease dramatically as a function of absolute magnitude, the luminosity function was in fact dominated by faint galaxies not initially seen by Hubble. As still more data became available it was noted that the global luminosity function is well fit by a Schechter function (Schechter, 1976), with the form:

$$\phi(L) = \phi_\star \left(\frac{L}{L_\star}\right)^\alpha \exp^{-\left(\frac{\mathrm{L}}{\mathrm{L}_\star}\right)} \tag{2.1}$$

where L is Luminosity, $\phi_\star$ is the density normalization (in $\mathrm{h}^3\,\mathrm{Mpc}^{-3}$, $L_\star$ is the so called characteristic luminosity at the "knee" of the Schechter function, and α is the power law slope of the Schechter function tail at the faint end. In terms of absolute magnitude, the luminosity function becomes:

$$\phi(M) = (0.4\ln 10)\,\phi_\star\,\left[10^{-0.4(\mathrm{M}-\mathrm{M}_\star)}\right]^{1+\alpha} \exp\left[10^{-0.4(\mathrm{M}-\mathrm{M}_\star)}\right] \tag{2.2}$$

The Schechter function has proven a popular parameterization for the LF, and it is widely used in the literature. The flexibility of this functional form is illustrated in Figure 2.1, which shows Schechter functions with various values of $M*$, α and $\phi*$. However, caution must be used when interpreting these simple three parameter fits, as $M*$ and α are correlated. This correlation is most likely due to the fact that the two Schechter parameters ($M*$ and α, $\phi*$ is determined separately) must reflect the mean luminosity and variance of the dataset. This is very similar to the correlation of the velocity function parameters described in Sheth et al. (2003). Also, the Schechter function fit is very sensitive to the range of the input data. Figure 2.2 shows an example of a dataset that contains only very bright galaxies, which leaves α poorly constrained. Conversely, seemingly disparate values of $M*$ and α can fit identical data very well over a limited range of absolute magnitudes. The best way to determine if differing Schechter functions agree is to examine the values over the relevant data range.

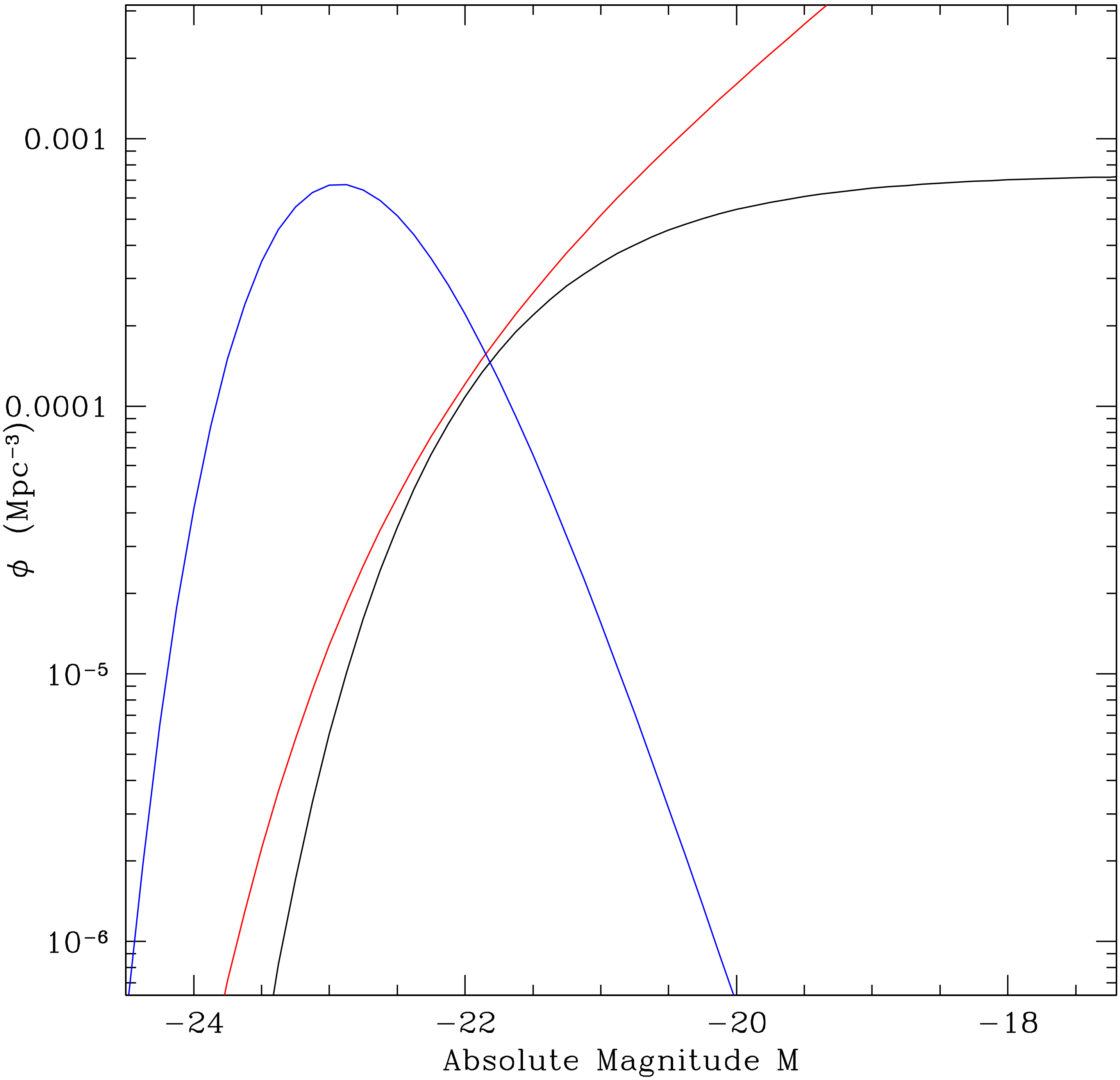

Figure 2.1 Example of Schechter functions with a range of M_* and α values to show their flexibility. $M_* = -22.5$, $\alpha = -1.0$, $\phi_* = 0.002$ (black), $M_* = -21.3$, $\alpha = -2.0$, $\phi_* = 0.008$ (red),$M_* = -21.3$, $\alpha = 3.0$, $\phi_* = 0.001$ (blue).

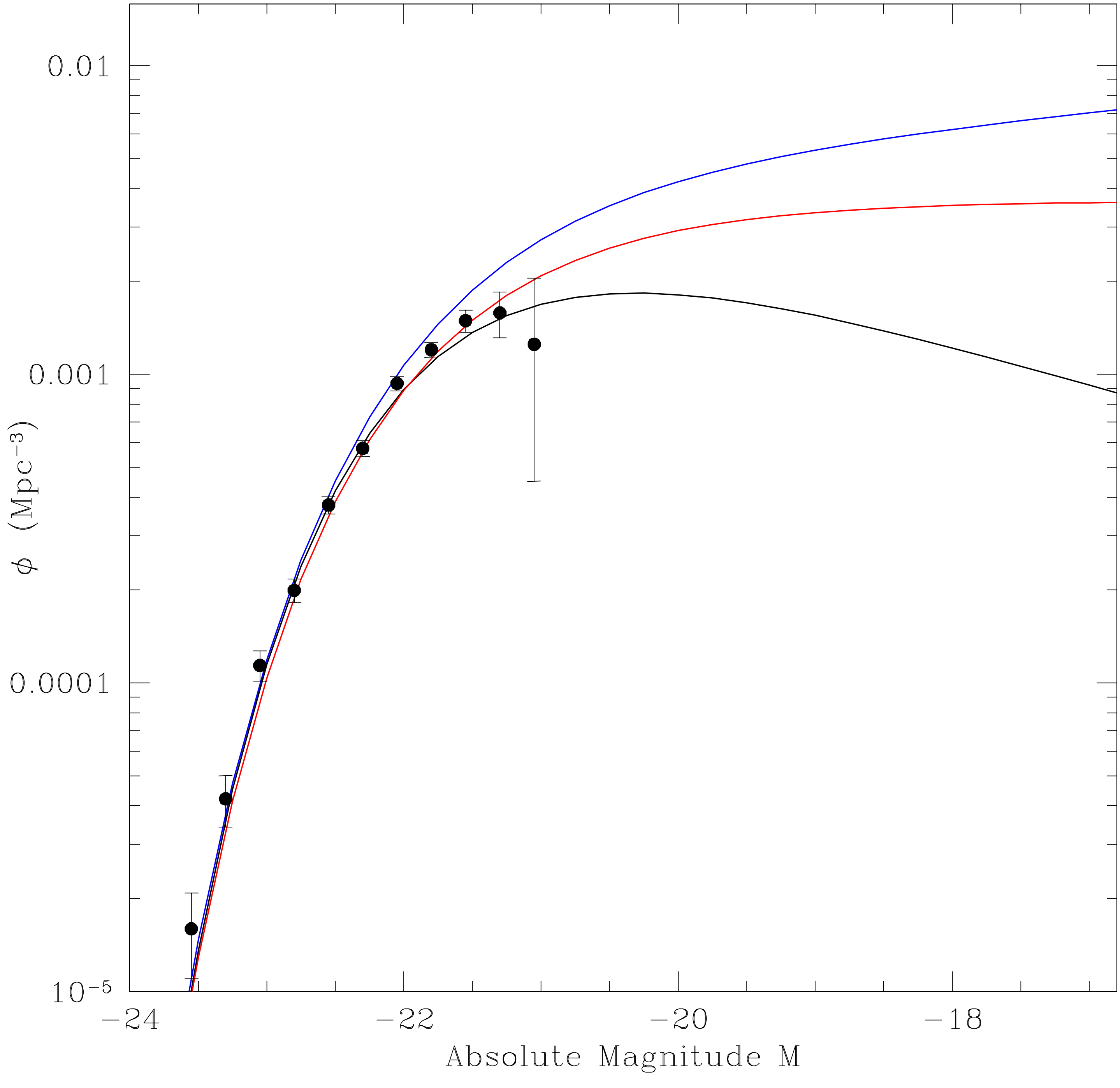

Figure 2.2 Maximum likelihood Schechter function fits to a dataset where α is poorly constrained.

As mentioned above, even in the earliest examinations of the LF it was noted that the galaxy luminosity function is *not* universal as a function of galaxy type. Only with the undertaking of large area sky surveys has the number of galaxies with firm redshifts been large enough to subdivide the sample by type (e.g Folkes et al. (1999); Blanton et al. (2001)). A wide variety of methods have been used to define galaxy "type", from human inspection of morphological type (Dressler, 1980; Shimasaku et al., 2001), spectroscopic type (Folkes et al., 1999), restframe color and galaxy concentration (Blanton et al., 2001; Goto et al., 2003), Spectral Energy Distribution fitting (Lin et al., 1999), all of which are different methods that distinguish early/red galaxies from late/blue ones. As a function of type, red (massive) galaxies make up the majority of the bright galaxies, while blue galaxies dominate at fainter absolute magnitudes. While galaxies occupy a continuous range of types, that is there are often no well defined breaks between different galaxy classes, but rather a smooth transition, nearly all examinations divide the dataset into large type bins. For our photometric redshift sample, we will use a continuous type parameter corresponding to the best fit template returned by the photoz code, though we will divide this sample into four broad type bins (see Section 2.4 for details).

By providing large samples over a wide redshift range, modern surveys have also enabled the study of how the galaxy luminosity function evolves with redshift, though so far such results are limited to the brightest galaxies at higher redshifts, or a deeper small area survey with smaller catalogs. The lack of features in the exponential and power law forms of the bright and faint end of the luminosity function make it very difficult to differentiate between luminosity evolution (an increase in the average luminosity with lookback time, indicated by a horizontal shift in the LF) and density evolution (a change in the number density of galaxies as a function of redshift) without a sample that covers a large magnitude range over a broad swath of redshift. The break, or "knee" of the Schechter function does show the scale, and a range of magnitudes that cover this break is necessary. In apparent magnitude limited samples, only the brightest galaxies occupying the bright end of the LF will meet the faint magnitude cut (due to Malmquist bias), leaving the faint end of the LF poorly constrained. Deep pencil beam surveys to find faint galaxies cover small areas of the sky, and consequently will have small numbers of the rare luminous galaxies, in which case the exponential tail is highly uncertain.

One method of characterizing the evolution is to parameterize both luminosity and density evolution as a function of redshift, e.g. the Q and P parameters of Lin et al. (1999) and Blanton et al. (2003), where the Schechter parameters $M*$, α and $\phi*$ are replaced by $M*(z) = M*(0) - Q(z)$, α and $\phi*(z) = \phi*(0)\,10^{0.4\,P\,z}$. The more straightforward approach is to simply bin the data in redshift and compute the LF in discrete redshift intervals (e.g. Loveday (2004)). We will perform the latter, simply binning the data. While this approach is not optimal, since we know that galaxies do in fact evolve, estimates of the LF computed in this way make for simple comparisons to observations in the literature, and does not force a specific parametric form for the evolution.

Several additional details of galaxy selection can impact the luminosity function. Star-galaxy separation is done by measuring the concentration of each object. The star-galaxy cut will determine the number of stars that are mistaken as galaxies and contaminate our sample, as well as the number of high concentration galaxies misclassified as stars missing from our sample. Details of star-galaxy separation and its effects are discussed in Section 2.2.3. Galaxy surface brightness is also a concern. All of the methods for computing the LF discussed in the following section assume that we completely sample all galaxies within the apparent magnitude limits specified. However, galaxies with low concentration and surface brightness near the sky background may not be detected by the SDSS pipeline. There is an observed relation between surface brightness and luminosity (de Jong and Lacey, 2000). This means that nearly all galaxies not detected in SDSS will be at the faint end of the LF. Cosmological surface brightness dimming exacerbates this problem at higher redshifts, though this problem should be offset by observations that galaxies appear to be more compact at higher lookback times. While our luminosity functions could be missing a fraction of galaxies at the faint end due to this low surface brightness selection, we will make no attempt to correct for any missing galaxies until the surface brightness limits of the Stripe 82 data are studied further; however, because we limit our photometric redshift sample to high signal to noise galaxies several magnitudes brighter than the completeness limit of the sample, surface brightness effects should be minimal (see Section 2.2.3 for more on Stripe 82).

Several prior methods of computing the luminosity function using photometric redshifts exist in the literature. Subbarao et al. (1996) developed a modified version of the Lynden-Bell C-method (Lynden-Bell, 1971) that accounts for photometric redshift errors replacing the delta function of the C-method with a Gaussian representing the spread in probable redshifts for each galaxy. Wolf et al. (2003) calculate the luminosity function for the COMBO-17 survey, which consists of medium band photometric redshifts for galaxies in a 0.78 square degree patch of the sky. They make no attempt to account for the errors introduced by the uncertain redshifts, and compute best fit Schechter function parameters using the STY method (see Section 2.1.2) and the stepwise maximum likelihood method (SWML, see Section 2.1.4). Chen et al. (2003) calculate the LF for the Las Campanas Infrared Survey (LCIRS), and develop a new likelihood estimator that is very similar to our estimator, presented in Section 2.1.5. However, Sheth (2007) has shown that this method may not be correct. Budavári et al. (2005) compute the luminosity function for galaxies found in both SDSS and an early data release of GALEX using empirical photozs and the 1/Vmax method (see Section 2.1.1). Again, no explicit attempt is made to account for the photoz uncertainties for this SDSS/GALEX data in the estimator, though the authors do estimate errors based on monte-carlo realizations of the data. As will be seen in Section 2.2.2 even modest uncertainties in photometric redshifts can have dramatic effects on the measured shape of the luminosity function. Accounting for such errors is extremely important, especially in light of new surveys that will derive all of their redshift information photometrically (e. g. LSST).

2.1 METHODS

I will discuss several techniques for estimating the luminosity function. In all of the methods, we must convert the observed apparent magnitude to a luminosity or absolute magnitude. This is done by:

$$M = m - 5\log D_L(z) - 25 - K(z,t) \tag{2.3}$$

where m is the apparent magnitude of the galaxy, M is the absolute magnitude, D_L is the Luminosity distance in Mpc (as written in Hogg (2000)) as a function of redshift z, given by:

$$D_L(z) = (1+z)\frac{c}{H_0}\int_0^z \frac{dz'}{(\Omega_M(1+z)^3 + \Omega_\Lambda)^{1/2}} \tag{2.4}$$

for a flat (Ω_k=0) Universe. $K(z,t)$ is the K-correction, which depends on redshift and type, and accounts for the difference in flux passing through the fixed wavelength filter due to the redshifting of the spectrum. For spectroscopically determined redshifts $D_L(z)$ and $K(z)$ can be determined very precisely (provided that the wavelength coverage of the spectrum is wide enough to compute the K-correction). However, the use of photometric redshifts introduces a sizeable uncertainty to the redshift (and type) that has a large impact on determining the absolute magnitude. The effects of these uncertainties will be discussed in Section 2.2.2 Examples of the lf determinations will be given for the datasets in Sections 2.2.1 and 2.2.2.

2.1.1 1/Vmax

The 1/Vmax method was developed by Schmidt (1968) to estimate the radio and optical luminosity function of quasars for an apparent magnitude limited sample, and is sometimes referred to as the "classical" method. The technique is simple: for every object in your sample, find the maximum redshift at which the object can be seen, given the apparent magnitude limits of the dataset (if the dataset has a bright magnitude cutoff, a minimum redshift is also needed). Calculate the maximum comoving volume, Vmax, from the redshift. Since the luminosity function is simply a comoving space density as a function of brightness, the LF can be estimated by binning the objects in magnitude and summing the values of 1/Vmax in each bin. This formulation assumes a homogeneous distribution of objects in space, and any spatial clustering in the sample will distort the shape of the luminosity function, therefore caution is advised when applying this technique on datasets with small areal coverage. Sheth (2007) has formulated the 1/Vmax estimator in the presence of large redshift uncertainties, though we do not implement the method here.

2.1.2 STY Maximum Likelihood

The most common method for calculating the galaxy LF is the maximum likelihood estimator of Sandage, Tammann, and Yahil (Sandage et al., 1979, hereafter STY). The main advantage of the STY method is that it is not biased by clustering and large scale structure,if we assume that the LF is not correlated with their location in space, or local density. This is a simplification, as we do know that the galaxy distribution is different for cluster and field galaxies; however, for large samples this will have a minimal effect. As this is a likelihood method, it requires the assumption of a parametric form followed by the determination the best fit parameters with the maximum likelihood. Unlike the 1/Vmax method, the STY formulation does not require the assumption of spatial homogeneity of the galaxy distribution. Instead, it simply requires the assumption that galaxy magnitudes are not correlated with position, or in other words, that the galaxy density and luminosity functions are completely independent.

The essence of the STY method is computing the probability of observing a galaxy with absolute magnitude M_i at a redshift z_i in the volume surveyed. This is just the number of galaxies between M and $M + dM$ divided by the total number of galaxies, which can be written:

$$p_i(M_i, z_i)\, dM = \frac{N(M_i, x, z_i)\, dV}{\int_{M_{min}(z_i)}^{M_{max}(z_i)} N(M_i, x, z_i)\, dM\, dV} dM \tag{2.5}$$

where $N(M, x, z)$ is the number of galaxies in volume dV between M and $M + dM$, and $M_{min}(z_i)$ and $M_{max}(z_i)$ are the minimum and maximum absolute magnitudes over which galaxy i is visible given the apparent magnitude limits of the dataset. $N(M, x, z)$ can be replaced by $\phi(M)D(x)$:

$$p_i(M_i, z_i) dM = \frac{\phi(M_i)\, D(x)\, dV}{\int_{M_{min}(z_i)}^{M_{max}(z_i)} \phi(M)\, D(x)\, dM\, dV} dM \tag{2.6}$$

Where $\phi(M)$ is the luminosity function, $D(x)$ represents the galaxy density function. Because we have assumed that the density function is completely independent of $\phi(M)$ it can be taken outside the integral in the denominator, and thus cancels out of the probability equation, as does the dV. This leaves:

$$p_i(M_i, z_i) = \frac{\phi(M_i)}{\int_{M_{min}(z_i)}^{M_{max}(z_i)} \phi(M)dM} \tag{2.7}$$

and the likelihood is just the product of the probabilities for the N total galaxies, given by:

$$\mathcal{L} = \prod_{i=1}^{N} p_i(M_i, z_i) \tag{2.8}$$

2.1.3 Normalization

One consequence of the density dependence canceling out in the STY method is that the absolute normalization of the luminosity function, $\phi*$, must be computed separately. A commonly used technique for determining $\phi*$ is given by Davis and Huchra (1982) and presented more clearly in Lin et al. (1996).

The mean density of our sample of N galaxies is given by:

$$\overline{\rho} = \frac{\sum_{i=1}^{N} w(z_i)}{\int_{z_1}^{z_2} S(z)w(z)\frac{dV}{dz}dz} \tag{2.9}$$

where z_1 and z_2 are the redshift limits of the sample, $S(z)$ is the Selection function:

$$S(z) = \int_{M_{min(z)}}^{M_{max(z)}} \phi(M)dM \tag{2.10}$$

and $w(z)$ is the "weight function":

$$w(z) = \frac{1}{1 + \overline{\rho}S(z)J_3} \tag{2.11}$$

where J_3 is the second moment of the two-point correlation function:

$$J_3 = 4\pi \int_0^{\infty} r^2 \xi(r)dr \tag{2.12}$$

Notice that $\overline{\rho}$ appears in the denominator of Equation 2.11, on which $\overline{\rho}$ depends. It must, therefore, be determined iteratively, though in practice it rapidly converges.

$\phi*$ is then related to the mean density by:

$$\phi* = \frac{\overline{\rho}}{\int_{M_1}^{M_2} \phi(M) dM} \tag{2.13}$$

where $\phi*$ in the Equation 2.13 and denominator of Equation 2.10 are set to 1.

In contrast Chen et al. (2003) use a very simple method to estimate $\phi*$:

$$\phi* = \sum_{i=1}^{N} \frac{V^{-1}}{\int_{Mmin(z_i)}^{Mmax(z_i)} \phi(M) dM} \tag{2.14}$$

where V is the comoving volume of the survey, and $\phi*$ is, once again, set to 1 in the denominator.

We estimate the error in $\phi*$ by varying $M*$ and α within their 1σ error ellipse.

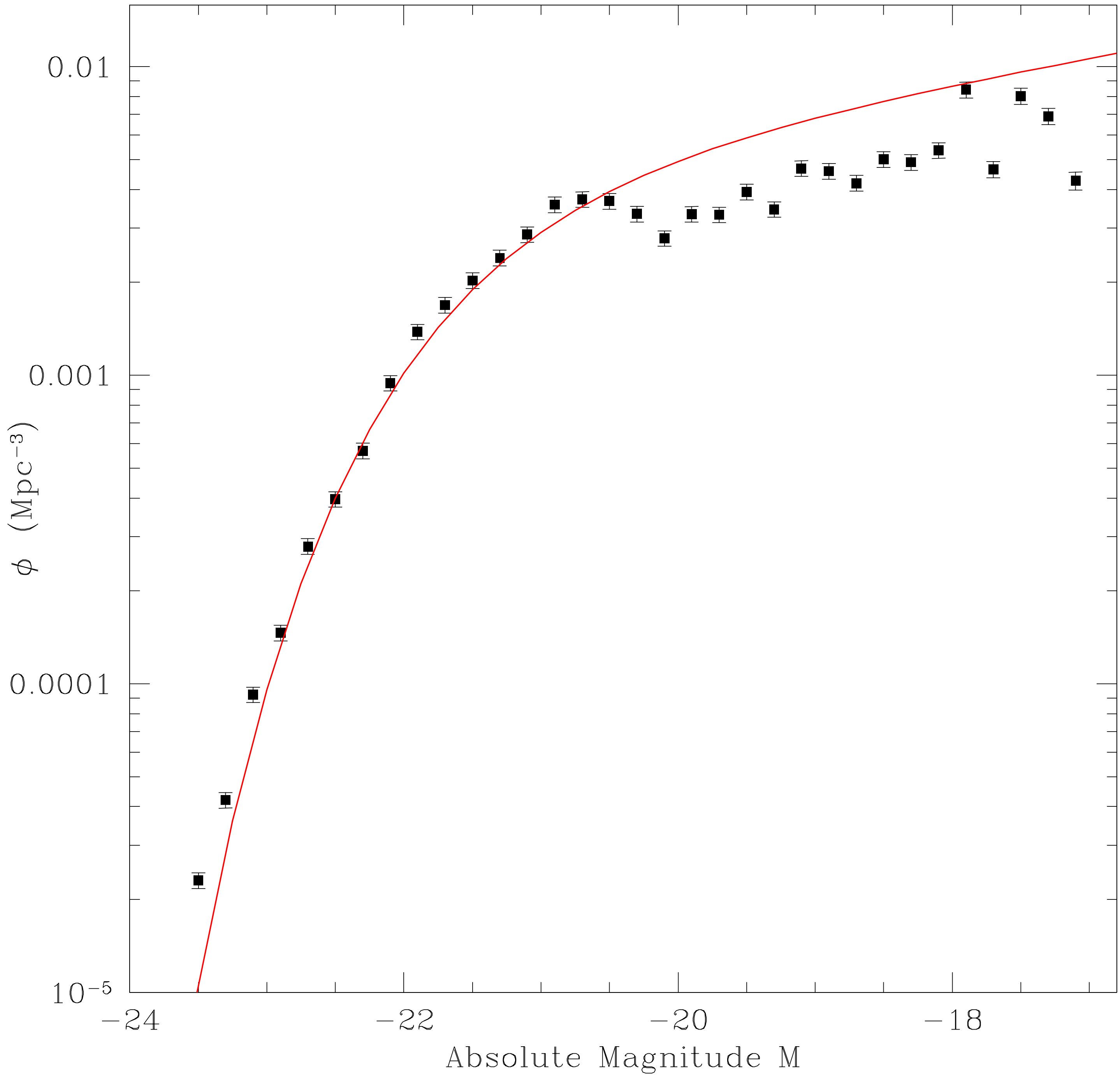

Figure 2.3 The 1/Vmax method applied to the spectroscopic dataset described in Section 2.2.1. The bin size is 0.25 magnitudes. Shown in red for comparison is the Schechter function fit of Blanton et al. (2001).

2.1.4 The Stepwise Maximum Likelihood (SWML) Method

The Stepwise Maximum Likelihood method (SWML) of Efstathiou et al. (1988) (hereafter EEP) is simply a "nonparametric" (actually overparametric) version of the STY estimator (see Lin et al. (1996) for the formulation of the SWML method), where the luminosity function is parameterized as a series of step functions in bins of width $\Delta\ M$:

$$\phi(M) = \phi_k \,\mathrm{for\, M - \Delta\, M/2\, \leq\, M\, <\, M + \Delta\, M/2} \tag{2.15}$$

i.e. a series of step functions, where we must determine the best fit weights, ϕ_k. Interestingly, this parameterization is equivalent to zeroth order (piecewise constant) splines, and are thus related to the BSplines formulation discussed in Sections 2.2 and Appendix A. This parameterization can be inserted into the STY likelihood Equation(2.22) in place of the Schechter function. The fact that every step function except one is nonzero for each galaxy allows us to pull the ln through the ϕ_k sum, which gives (using the notation of Lin et al. (1996):

$$\ln\mathcal{L} = \sum_{i=1}^{N}\sum_{k=1}^{Np} W(M_i - M_k)\phi_k - \sum_{i=1}^{N} \ln\left[\sum_{k=1}^{Np} \phi_k\, \Delta M\, H(M_k, M_{Min(zi)}, M_{Max(zi)})\right] \tag{2.16}$$

where W and H represent evaluating $\phi(M)$ and its integral, and are given by:

$$W(M_i - M_k) = \begin{cases} 1 \quad M_k - \Delta M/2 \leq M_i \leq M_k + \Delta M/2 \\ 0 \qquad\qquad otherwise \end{cases} \tag{2.17}$$

and

$$H(M_k, M_{Min}, M_{Max}) = \begin{cases} min[M_k + \Delta M/2,\ M_{Max}] - max[M_k - \Delta M/2, M_{Min}] \\ \text{if } M_k + \Delta M/2 \leq M_{Min} \& M_k - \Delta M/2 \leq M_{Max} \\ 0 \text{ otherwise} \end{cases} \tag{2.18}$$

By differentiating this likelihood expression with respect to ϕ_k and setting to zero, we can find a minimum value for the likelihood. This results in an iterative equation for the ϕ_ks that converges rapidly:

$$\phi_k = \frac{\sum_{i=1}^{N} W(M_i - M_k)}{\Delta M \sum_{i=1}^{N} H(M_k, M_{Min}, M_{Max}) / \sum_{j=1}^{Np} \phi_j \Delta M H(M_j, M_{Min}, M_{Max})} \tag{2.19}$$

where ϕ_k on the left is the $r+1$-th iteration and the ϕ_j's on the right hand side are fixed at the values determined in the r-th iteration. This procedure is repeated until some convergence criterion is met. This iterative solution is advantageous as, with the SWML method, the LF for large datasets is binned into a substantial number of steps, and searching the resulting high dimensional likelihood space is expensive computationally.

2.1.5 Modified Maximum Likelihood Estimator

In order to deal with the larger uncertainties associated with photometric redshifts, we have developed a new maximum likelihood estimator that is an extension of the STY method. The derivation of this method is discussed in detail in Sheth (2007).

Equation 2.7 assumes that the absolute magnitude of the galaxy, and therefore the redshift as well, is known very precisely. With photometric redshifts, we know that this is not the case, and that there is an uncertainty, σ_z, associated with each redshift measurement. There is also uncertainty in the galaxy type, but we will not address this issue here. I will briefly address this in Section 4.3. This redshift uncertainty propagates to an uncertainty in the absolute magnitude through Equations 2.4 and 2.3. As pointed out by Sheth (2007), this error is very different from errors associated with magnitude uncertainties. With magnitude/photometry errors, the redshift/distance is known, but an uncertainty in the apparent magnitude affects the absolute magnitude estimate. The case is just the opposite for photozs, where we know the magnitudes very precisely, but uncertainties in the redshift/distance propagate to an error in the absolute magnitude estimate. To account for magnitude errors Lin et al. (1996) simply convolve the LF with Gaussian of width σ_M to deconvolve the effect of the magnitude error. Because the redshift uncertainty affects the distance and volume estimates, as well as the magnitude, the case of photoz errors is not so straightforward.

We begin with Equation 2.5, although now, rather than a precise redshift z_i we have an probability distribution $p(z_{pi,z'})$. Equation 2.5 now becomes:

$$p_i(M_i, z_{pi})\, dM = \frac{\int_{z'} N(M, x, z')\, \frac{dV}{dz'} p(z_{pi}, z') dz'}{\int_{z'} \int_{M_{min}(z_i)}^{M_{max}(z_{pi})} N(M, x, z')\, dM\, \frac{dV}{dz'} p(z_{pi}, z') dz'} dM \tag{2.20}$$

As before, we can replace $N(M, x, z')$ with $\phi(M)D(x)$, and once again, $D(x)$ the spatial dependence of the LF, cancels out of the equation. However, as the absolute magnitude and volume are functions of redshift, we cannot remove them from the equation, and our final probability is:

$$p_i(M_i, z_{pi}) = \frac{\int_{z'} \phi(M_i(z')) \frac{dV}{dz'} p(z_{pi}, z') dz'}{\int_{z'} \int_{M_{min}(z')}^{M_{max}(z')} \phi(M) dM \frac{dV}{dz'} p(z_{pi}, z') dz'} \tag{2.21}$$

and, once again, we simply maximize the log likelihood:

$$\ln \mathcal{L} = \sum_{i=1}^{N} \ln(p_i(M_i, z_i)) \tag{2.22}$$

One consequence of this new form is that, unlike Equation 2.16, the probability in the redshift integral prevents us from simply stating that only one ϕ_k will be nonzero, so we cannot take the log inside the sum. Thus, no iterative solution for the SWML is possible. As with the STY estimator, this new estimator works with any parametric form. We will employ the Schechter function parameterization, as well as a new parameterization in terms of cubic BSplines (see Appendix A for details).

2.1.6 Error Estimates

A variety of methods are employed for estimating the errors on the luminosity function parameters, depending on the method employed. For the 1/Vmax estimator, we follow Schmidt (1968) and Condon (1989) and estimate the error on the LF in each magnitude bin as the square root of the sum of the inverse maximum volumes squared:

$$\sigma_i = \left[\sum_{i=1}^{N} \frac{1}{Vmax_i^2} \right]^{1/2} \tag{2.23}$$

For the Schechter function parameterization, we estimate the $1\,\sigma$ errors on $M*$ and α by jointly varying these two parameters around the maximum likelihood value in order to find the points where the likelihood increases by the β-point of the χ^2 distribution (see, e.g. Efstathiou et al. (1988)):

$$\ln, \mathcal{L} = \ln \mathcal{L}_{max} - \frac{1}{2}\chi^2_\beta \tag{2.24}$$

and the β point for $1\,\sigma$ for 2 degrees of freedom is 2.24.

For the SWML and BSplines LFs, similar to Efstathiou et al. (1988), we compute the Fisher Information matrix (Eadie et al., 1971) at the maximum likelihood parameter values, where the components of the information matrix are given by the negative second derivatives of the log likelihood:

$$I_{jk} = -\frac{\partial^2 \ln \mathcal{L}}{\partial X_j \, \partial X_k} \tag{2.25}$$

where the X_j's are either the ϕ_j's of the SWML method, or the a_j BSpline parameters. The full covariance matrix is then simply the inverse of the information matrix:

$$cov(X_{jk}) = (I^{-1}) \tag{2.26}$$

For $\phi*$, error estimates are computed by varying the parameters within the $1\,\sigma$ error contours. This is done numerically by sampling points within the $1\,\sigma$ contours and recomputing the density. No attempt is made to account for additional error due to cosmic variance.

2.2 DATA

We have created several datasets in order to illustrate the different luminosity function estimators, and specifically to show the effect of photometric redshift errors on the LF, including a small spectroscopically confirmed sample, several mock samples with well behaved error properties, and the final SDSS photometric redshift dataset on which the real analysis is performed. The selection/creation of these datasets is described here. All luminosity functions are done in the SDSS r band, using SDSS model magnitudes. Model magnitudes in SDSS are estimated by fitting two profiles, exponential and deVaucoleurs, to each galaxy and reports the better of the two fits.

2.2.1 An Example Spectroscopic Redshift Dataset

For direct comparison with existing results we constructed a dataset similar to, but not exactly the same, as that used in Blanton et al. (2001), where the luminosity function was computed for the SDSS Early Data Release (EDR). We select all galaxies with spectroscopic redshifts in the Right Ascension and Declination range $145.3 \leq RA \leq 236.0$, and $-1.25 \leq DEC \leq 1.25$. Due to several small gaps between plate boundaries the actual areal coverage is 210.5 square degrees. We then trim the data to include only galaxies with redshift range $0.0167 \leq z \leq 0.20$ ($5000\,\mathrm{km/s} \leq cz \leq 60000\,\mathrm{km/s}$ and apparent magnitude range $14.5 \leq r \leq 17.6$. The bright magnitude is motivated by saturation effects of very bright galaxies, and the faint by the spectroscopic completeness limit of SDSS. We note that we select based on SDSS model magnitudes, where Blanton et al. (2001) use Petrosian magnitudes. The result is a set of 9871 galaxies with spectroscopically confirmed redshifts in the approximate area of the SDSS Early Data Release.

Figure 2.4 shows the results of the 1/Vmax and STY LF estimators for this dataset. Shown for comparison is the best fit Schechter function found by Blanton et al. (2001), shifted to match the $h = 0.7$ Hubble constant used here. The best fit values for the Schechter function parameters are: $M_* = -21.6467 \pm 0.017$, $\alpha = -1.112 \pm 0.012$, and $\phi_* = 0.00480 \pm 0.00065$, while the best fit arrived at in Blanton et al. (2001) are: $M_* = -21.604 \pm 0.030$,

$\alpha = -1.20 \pm 0.030$, $\phi_* = 0.00501 \pm 0.00041$. The two curves agree very well at the bright end, though there is some disagreement at the faint end. This is most likely due to our not including an incompleteness correction for fiber collisions, where galaxies within $55''$ of another galaxy may not have spectroscopic redshifts due to the physical size of the fiber hole on the spectroscopic plates. Figure 2.5 shows the results of the SWML method and the 1/Vmax method for comparison. The SDSS EDR includes an abundance of large scale structure (the Sloan Great Wall is within this area of the sky). Because the 1/Vmax method is biased by the presence of such structure, we expect the results of the 1/Vmax estimator to differ from those of the SWML method, which Figure 2.5 clearly shows. Figure 2.6 shows the best fit spline fit using 18 knot points to define the BSpline basis, and Figure 2.7 shows the same, but also includes the error bounds of the spline fit. The spline fit follows the shape of the SWML fit, but for a smooth, continuous function rather than in steps. However, note that the Schechter function fit falls within the 1σ spline error contours for the entire absolute magnitude range; thus the spline fit does not deviate significantly from the Schechter functional form.

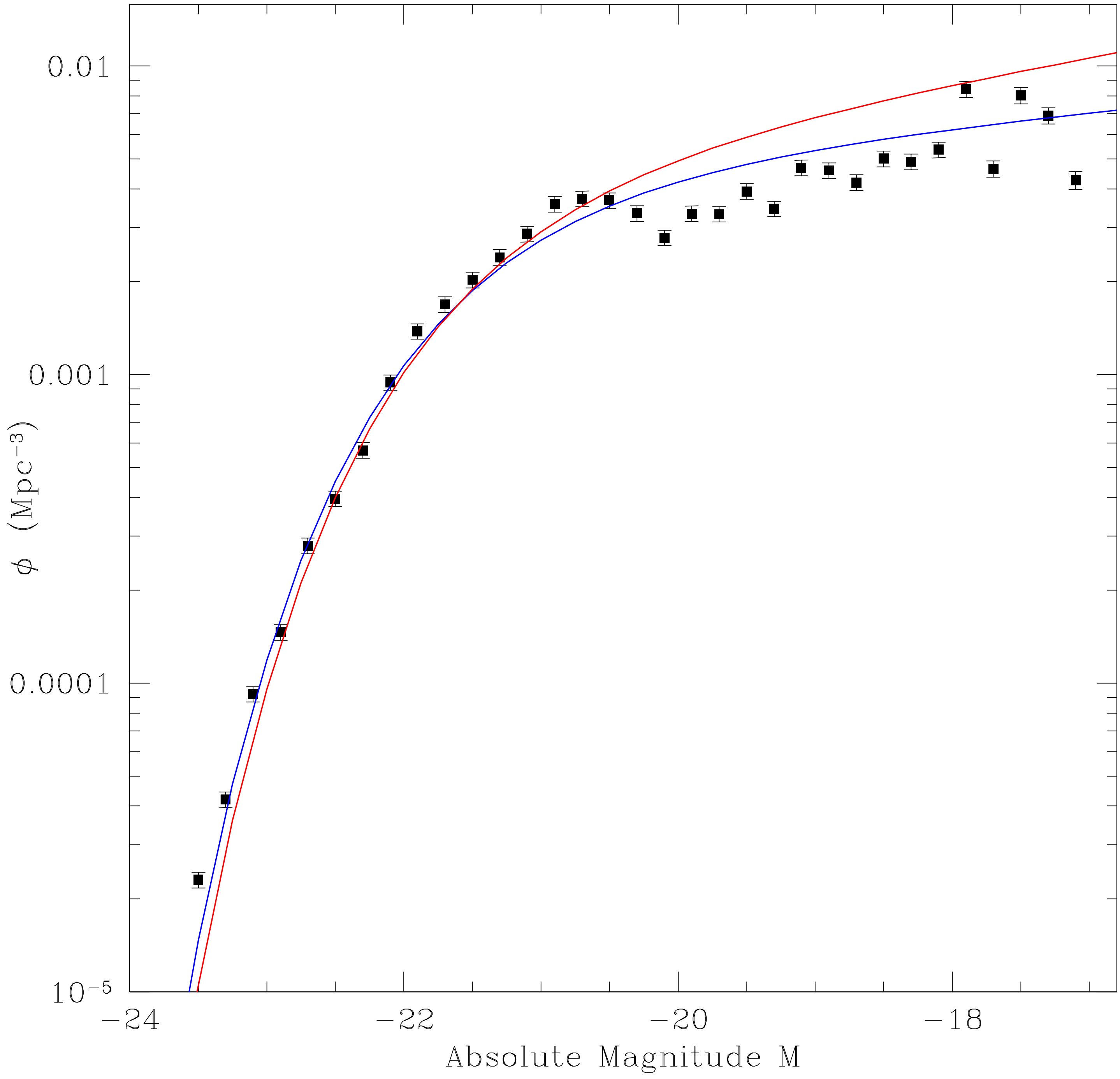

Figure 2.4 The STY maximum likelihood method best fit Schechter function (blue) to the small spectroscopic dataset. Shown for comparison are the 1/Vmax fit (black) and the Schechter function fit of Blanton et al. (2001)(red).

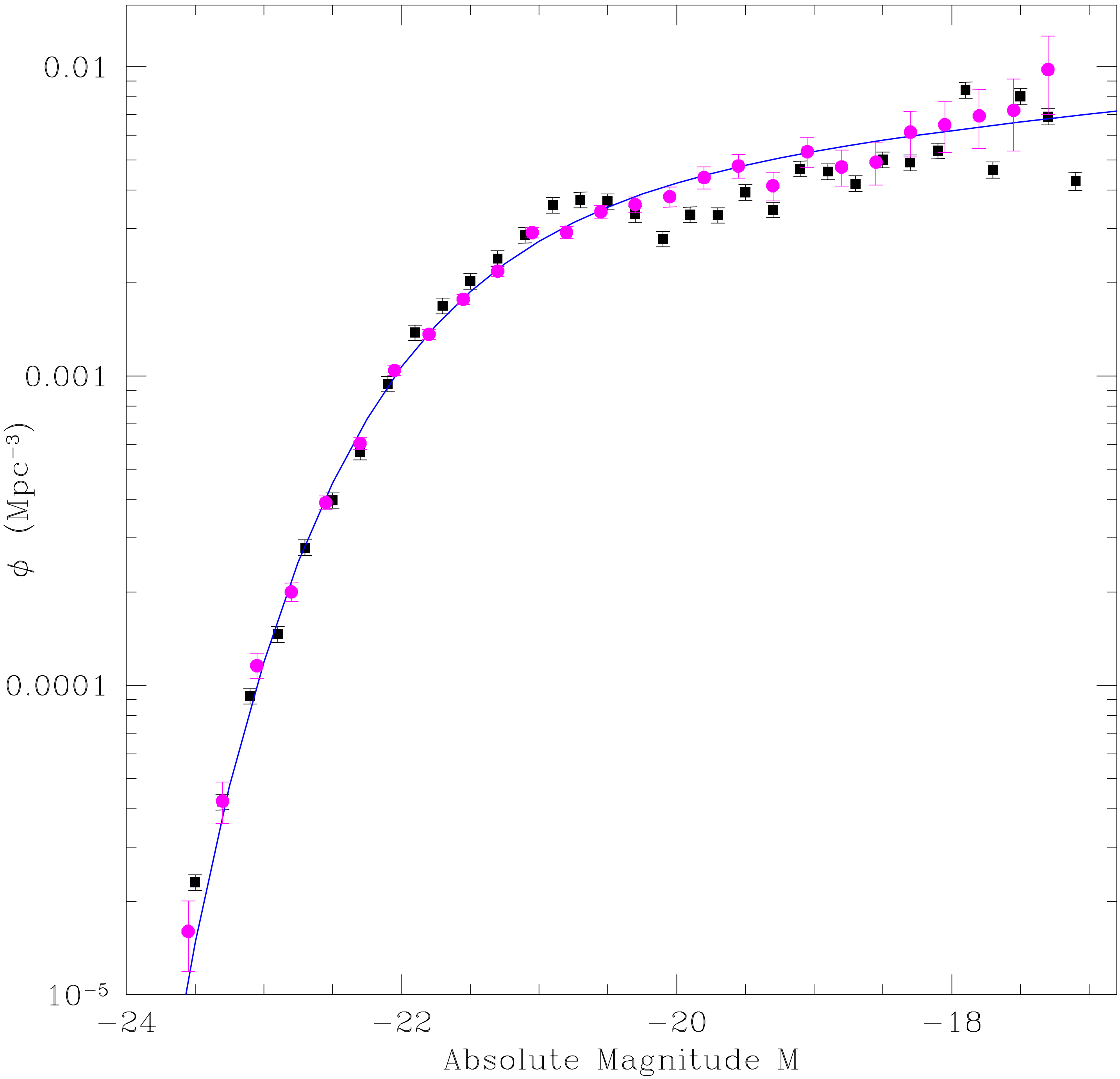

Figure 2.5 1/Vmax (black), Schechter (blue), and SWML (magenta) fits to the small spectroscopic dataset. The difference between the 1/Vmax and SWML values is due to the presence of large scale structure.

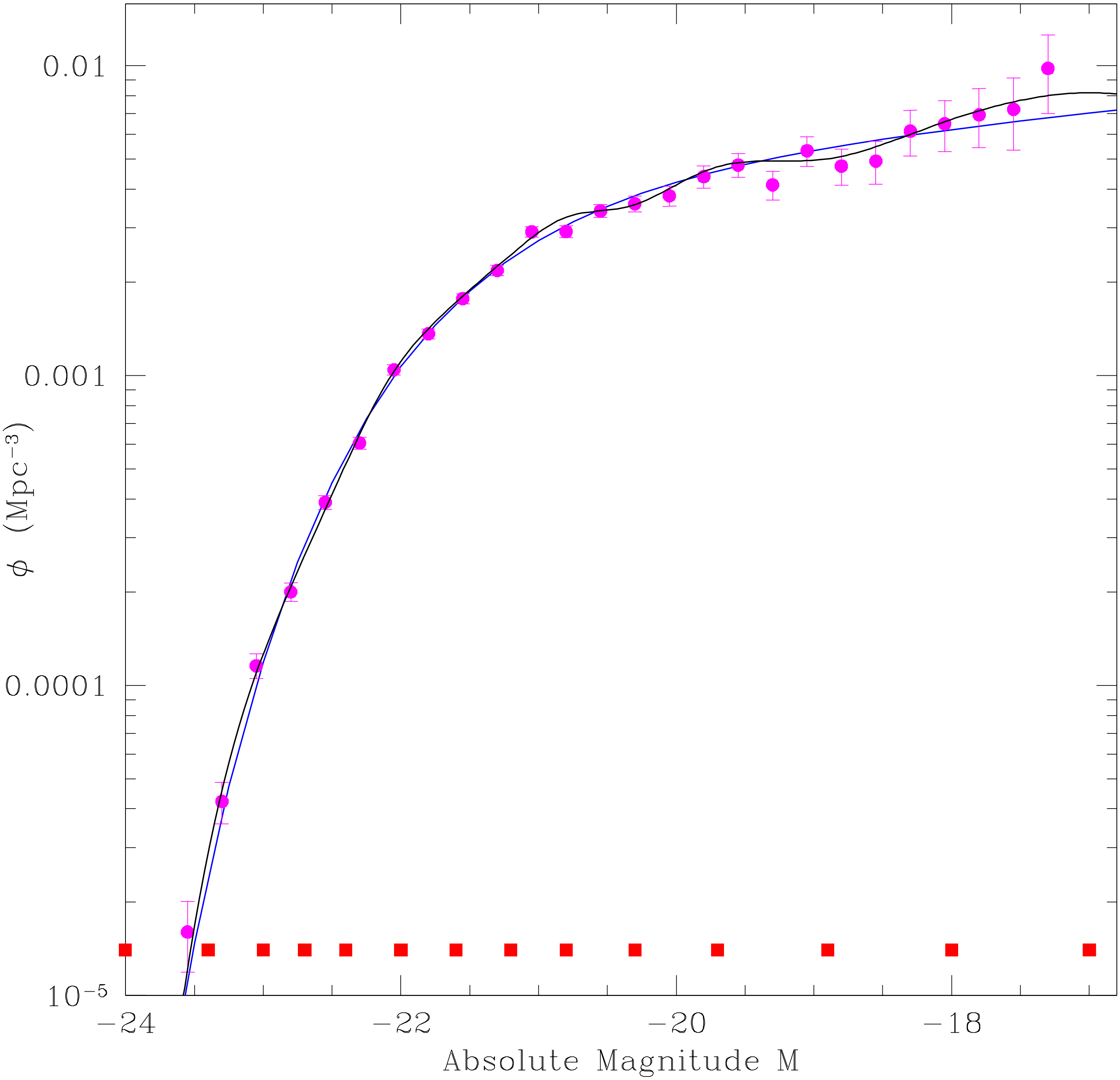

Figure 2.6 BSplines fit (black) to the small spectroscopic sample using 18 knot points. Shown for comparison are the best fit Schechter function from the STY method (blue) and the SWML method (magenta). The knot points are indicated by red squares along the bottom of the plot.

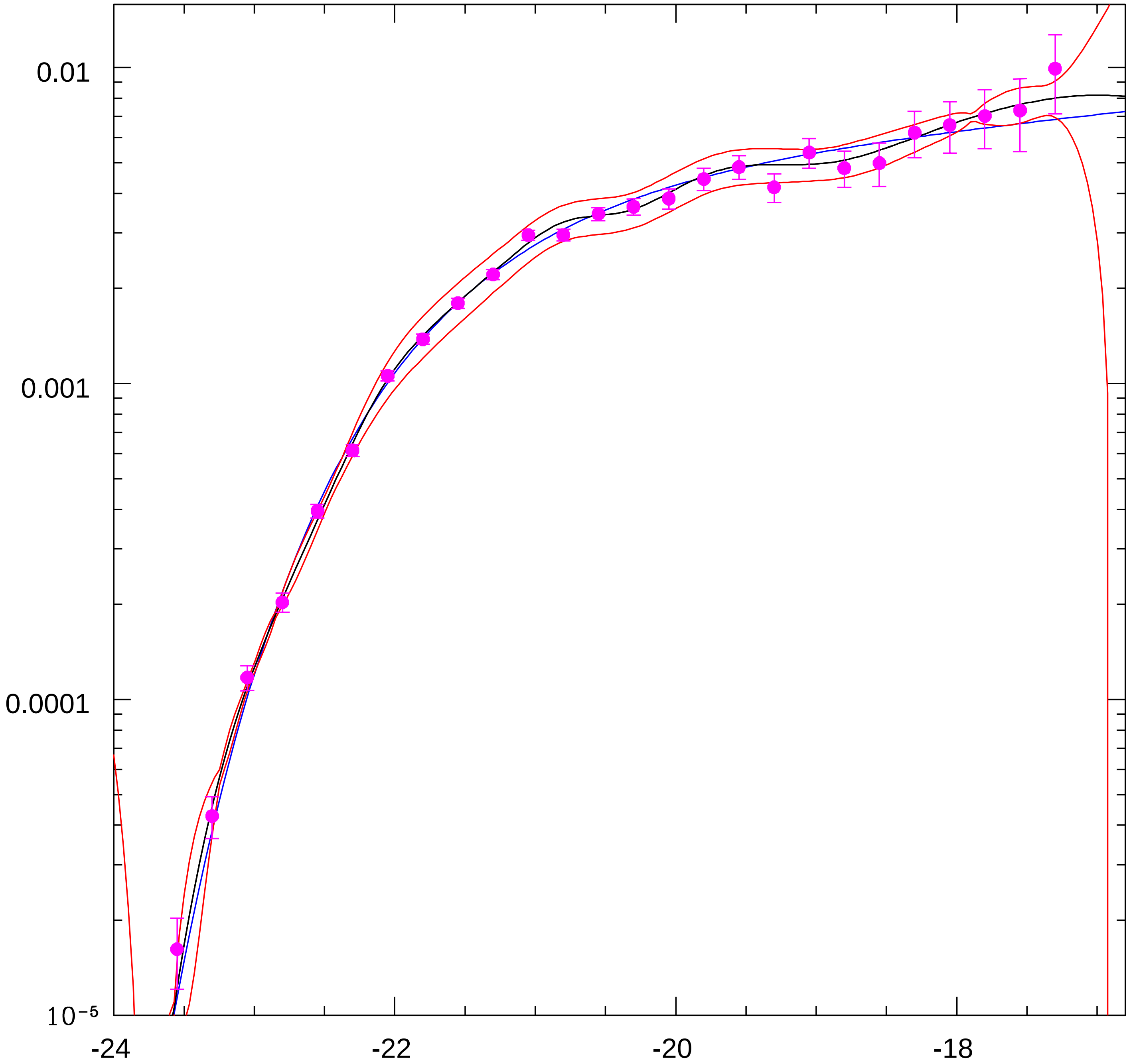

Figure 2.7 Errors (red) on the spline fit (black) to the LF. Errors are calculated by inverting the Information matrix. Shown for comparison are the best fit Schechter function from the STY method (blue) and the SWML method with errors (magenta).

2.2.2 Mock Photometric Redshift Datasets

In order to test the effects of redshift uncertainties, we have created several mock datasets where we can control the exact nature and magnitude of the redshift errors. With these datasets, we will know the "true" luminosity function in advance, and can accurately judge the performance of our maximum likelihood estimator. We generate a mock catalog where there are no uncertainties in the redshift, which we will call a mock "spectroscopic" catalog, and a corresponding one where the redshifts have a known distribution of errors, which we will refer to as a mock "photometric" catalog. No evolution of the LF is assumed, i.e. the shape of the luminosity function remains constant at every redshift.

For the mock spectroscopic catalog, we begin by creating a list of absolute magnitudes that are well represented by a Schecter function with $M*$=-21.25 and α=-1.15, parameters similar to those we expect for the SDSS r-band luminosity function at low redshift. We then generate an r-band magnitude, redshift, k-correction, and type for each galaxy. For simplicity one of only three galaxy types are assigned, and no error in type is assumed. Details of the datasets and LF fits are listed in Table 2.2.2.

For the mock photometric catalog, the same absolute magnitude distribution describe above is used, and we once again assign each galaxy a redshift (such that comoving volume density is constant), apparent magnitude, and galaxy type. We then calculate a redshift uncertainty, σ_z for each galaxy, where the redshift uncertainty increases with apparent magnitude, an example of which is shown in Figure 2.12, which shows the redshift uncertainty vs. apparent magnitude, as well as a histogram of the σ_z values. We will create several such error distributions to show the effects of large uncertainties on the LF determination. The redshift of each galaxy is then shifted by a value drawn from a Gaussian distribution of width σ_z, simulating the uncertainty in photometric redshifts. Note that the error reported in σ_z is *always* reflective of the actual uncertainty, i.e. we do not include the equivalent of "catastrophic outliers". Details of the datasets are listed in Table 2.2.2 and are described here:

The Low-z Specz sample consists of galaxies from the mock catalog that have apparent magnitudes of $15.0 \leq r < 21.0$ and redshifts $0.1 \leq z \leq 2.0$. The derived Schechter parameters of $M*=-21.293\pm0.0080$ and $\alpha=-1.149\pm0.0083$ are very close to the expected values of the input mock Schechter function, which had $M*=-21.25$ and $\alpha=-1.15$. Figure 2.8 shows the 1/Vmax results for the mock dataset, and Figure 2.9 shows both the 1/Vmax and SWML estimators. Note that they are almost identical for this data, which is to be expected, as the mock data was generated to have uniform comoving density, in which case the 1/Vmax method should be nearly identical to the SWML estimator. Figure 2.10 shows the BSpline fit to the data, which agrees very well with the SWML estimator. Figure 2.11 shows all four methods, and shows that they are consistent with each other, as well as with the parameters used to generate the dataset.

Figure 2.12 shows the distribution of redshift uncertainties generated for the first mock photometric dataset. Redshift errors are drawn from a Normal distribution of width $\sigma_z=0.05$ and, in order to approximate the distribution seen in real data, assigned such that errors increase exponentially with fainter apparent magnitude. For this dataset (labeled as ”Low-z Photoz Min Error” in Table 2.2.2), errors fall within the envelope defined by $\sigma_z\leq 0.05\exp(0.3(r-15.0))$, if the error generated is greater than this, an error of $\sigma_z=0.04\exp(0.1(r-15.0))$ is assigned to increase the number of lower error points. This error increase is slightly shallower than that observed with real data. For the ”Low-z Photoz Min Error” dataset, *all* of the galaxies are given a minimum error of at least $\sigma_z=0.03$ is assigned to the redshifts. This is done in order to test how the estimator performs when none of the galaxies have precisely determined redshifts. Figure 2.13 shows the Schechter and SWML fits for this dataset, as well as the fits for the Low-z Specz dataset for comparison. As expected, more galaxies are scattered from the center of the distribution to the tails, leading to a steeper faint end slope, a brighter value for the exponential dropoff, and a lower density near the ”knee” of the LF. The fits for the 1/Vmax and spline methods are shown in Figure 2.14, and the errors on the spline LF are shown in Figure 2.15. Now we apply our new estimator. Figure 2.16 shows the results for the Schechter and BSpline parameterizations, showing that we successfully recover the input LF. Figure 2.17 shows the $1\,\sigma$ error bounds for the spline curve, showing that the bright end of the LF is very uncertain, though the small number (~ 35000) of galaxies, and the fact that even the brightest galaxies have a minimum redshift uncertainty of $\sigma_z=0.03-0.05$ contribute to these large errors.

The datasets labeled "Hi-z Specz" and "Hi-z Photoz" have the same error distribution as the data above, though now are selected at $0.3 \leq z \leq 0.4$ and the apparent magnitude range is restricted to $17.5 \leq r < 21.0$. Figure 2.18 shows the 1/Vmax, SWML and Schechter fits to the Specz dataset, while Figure 2.19 adds the spline fit and its $1\,\sigma$ error contours. Figure 2.20 compares the dataset with redshift uncertainties to the unscattered data. Figure 2.21 shows the results of our new estimator, once again showing that we are able to recover the underlying LF and correct for the redshift uncertainties.

We now discuss a second dataset with a different redshift uncertainty distribution. This error distribution is chosen to roughly match that observed in SDSS photometric redshift samples, where errors are related to apparent magnitude up to $\sigma_z(r) \leq 0.01\exp(0.6(r-15.0))$, and the width of the σ_z distribution depends on the apparent magnitude of the data. We will use this $r-\sigma$ relation to create two more mock datasets: to show the effect of very large errors, we draw the redshift errors from a Gaussian of width $\sigma_z = 0.1$, much larger than that observed in the actual photometric data of Section 2.2.3, which has $\sigma_z = 0.037$. This dataset is labeled "Low-z Photoz 2" in Table 2.2.2. Another mock dataset with errors drawn from a Gaussian of width $\sigma_z = 0.05$, on the same order as that of the real SDSS data. This is labeled "Low-z Photoz 3" in Table 2.2.2.

Figure 2.22 shows the σ_z vs. apparent magnitude plot and σ_z histogram for the Low-z Photoz 2 dataset. Approximately 10% of the galaxies had very large initial uncertainties, which are instead set to $\sigma_z = 0.025$, resulting in the spike at that value of σ_z. The more realistic exponential data cut, combined with the large underlying redshift uncertainty input into this data results in a much higher percentage of galaxies with very large redshift errors, particularly for the faintest galaxies. Therefore, we expect the faint end of the LF to be particularly affected by these large errors. Figure 2.23 shows the 1/Vmax, SWML, and Schechter function fits to the Low-z Photoz 2 data. Figure 2.24 shows the resulting Schechter function fit from our new maximum likelihood estimator. This estimate is clearly wrong, with $M*$ overcorrected and too faint, and α much shallower at the faint end. As σ_z/z becomes slightly larger than unity, there is simply not enough information contained in the photometric redshift. This is a *very* important point: our maximum likelihood estimator breaks down for large values of σ_z/z. One cannot blindly apply the estimator to any dataset, careful attention must be paid to the magnitude of the photometric redshift errors. This dataset is an extreme example, with the uncertainties drawn from a Gaussian of width $\sigma = 0.1$. Testing with several more mock datasets shows that the maximum likelihood estimator breaks down when more than $10-20\%$ of galaxies have $\sigma_z/z \geq 1$, or if any sizeable (more than a few percent) have $\sigma_z/z \geq 2$. Because redshift uncertainty is correlated with apparent magnitude (i. e. signal to noise) this means that we must limit the sample to a bright enough sample such that the redshift uncertainties do not rise to the above levels.

We now create a mock dataset with a more realistic underlying error distribution with $\sigma = 0.05$, slightly larger than that observed in our real photometric redshift data, and which follows a similar $r - \sigma_z$ to the real SDSS data. Figure 2.25 shows the $r - \sigma_z$ distribution for the mock dataset, where once again, about 15% of the galaxies with initial large redshift errors had errors of $\sigma_z = 0.025$ assigned. This dataset contains far fewer galaxies with $\sigma_z > 0.1$ and no galaxies with $\sigma_z > 0.2$. Figure 2.26 shows the 1/Vmax, SWML, and Schechter function fits to this data. It is obvious that the smaller redshift errors lead to a less pronounced distortion of the LF, though the brightening of $M*$, steeper α, and lower $\phi*$ are all still present. Figure 2.27 shows the maximum likelihood fits for the Schechter function and BSplines parameterizations using our new estimator. Both are very close to the LF expected before redshift uncertainties are added. Figure 2.28 shows the error on the spline measurement. These results with realistic errors show that our estimator is successful at recovering the true luminosity function, as long as the errors, characterized by σ_z/z are not very large. We will now move on to real data in the following section.

Table 2.1 Mock Dataset Characteristics

	Mock Dataset Properties										
Dataset	# Galaxies	r_{max}	r_{min}	z_1	z_2	$M{*}_{meas}$	α_{meas}	$\phi{*}_{meas}$	$M{*}_{cor}$	α_{cor}	$\phi{*}_{cor}$
Low-z Specz	43205	15.0	21.0	0.1	0.2	-21.293±0.0080	-1.149±0.0083	0.000776±0.000060	…	…	…
Low-z Photoz Min Error	35062	15.0	21.0	0.1	0.2	-22.141±0.0092	-1.452±0.0092	0.000230±0.000022	-21.422±0.046	-1.126±0.034	0.000635±0.000073
Hi-z Specz	18596	17.5	21.0	0.3	0.4	-21.234±0.0122	-1.132±0.0128	0.00065±0.000091	…	…	…
Hi-z Photoz	14890	17.5	21.0	0.3	0.4	-21.702±0.0145	-1.389±0.0118	0.00027±0.000029	-21.218±0.055	-1.166±0.039	0.00049±0.00010
Low-z Photoz 2	37848	15.0	21.0	0.1	0.2	-21.512±0.0086	-1.290±0.0088	0.000590±0.000061	-20.990±0.035	-0.804±0.026	0.00129±0.00018
Low-z Photoz 3	40405	15.0	21.0	0.1	0.2	-21.499±0.0084	-1.239±0.0079	0.000580±0.000064	-21.312±0.061	-1.112±0.054	0.000790±0.00013

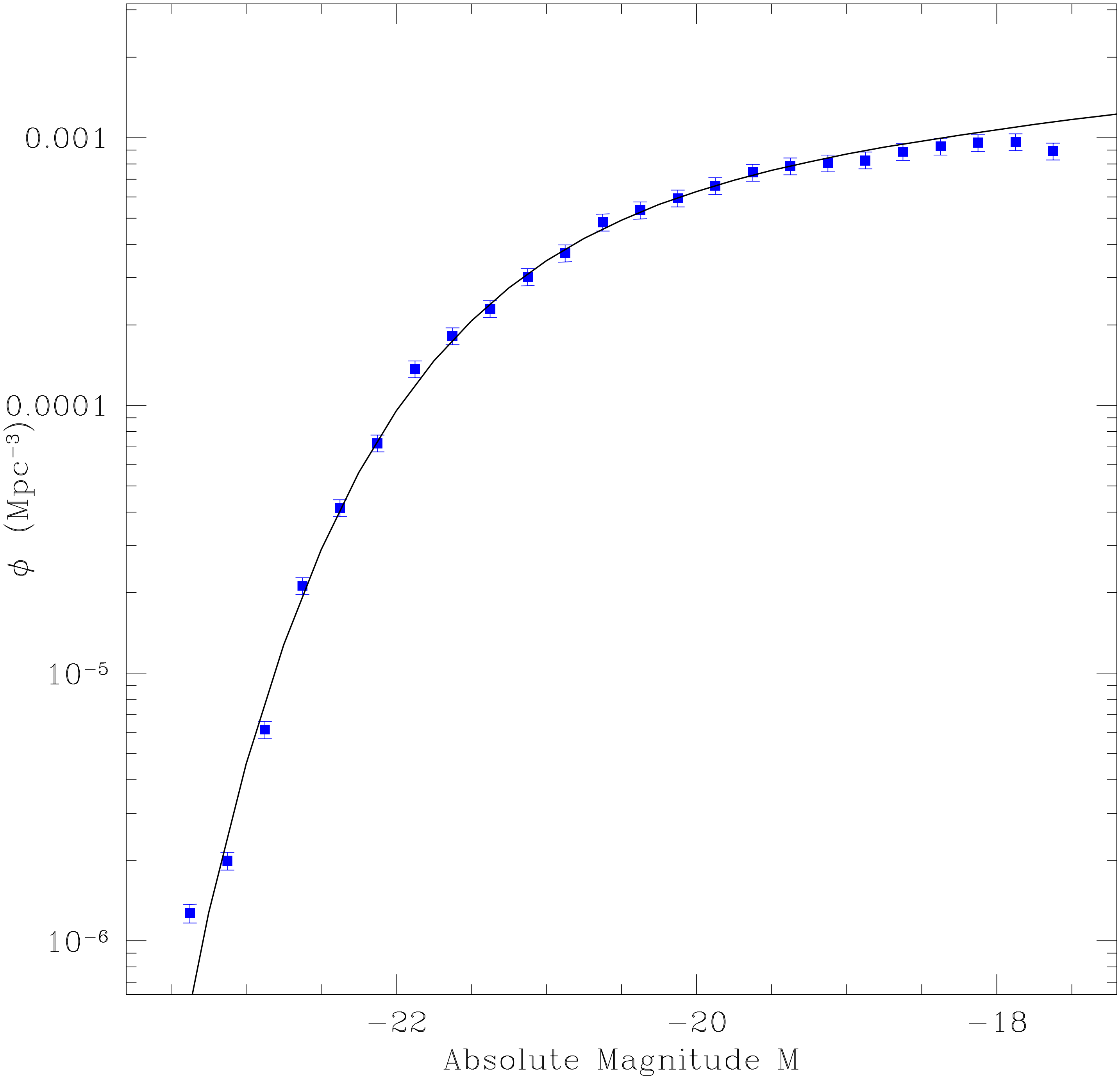

Figure 2.8 Luminosity function fits to the low redshift mock data with no errors in redshift. The black curve shows the best fit Schechter function given by the STY method, the blue points are from the 1/Vmax method.

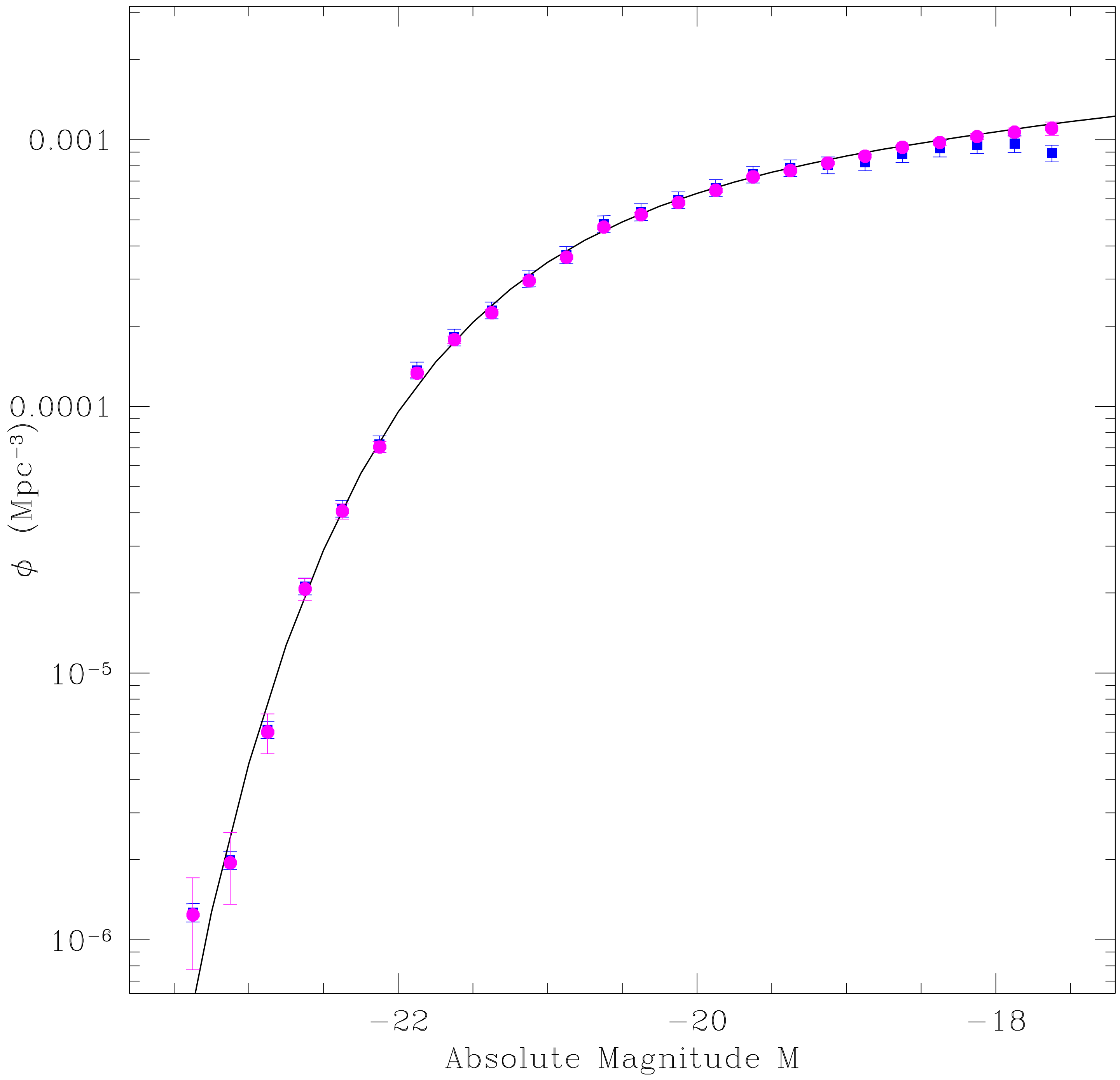

Figure 2.9 Luminosity function fits to the low redshift mock data with no errors in redshift comparing the 1/Vmax and SWML estimators. The black curve shows the best fit Schechter function given by the STY method, the blue points are from the 1/Vmax method, and the magenta points show the SWML estimator.

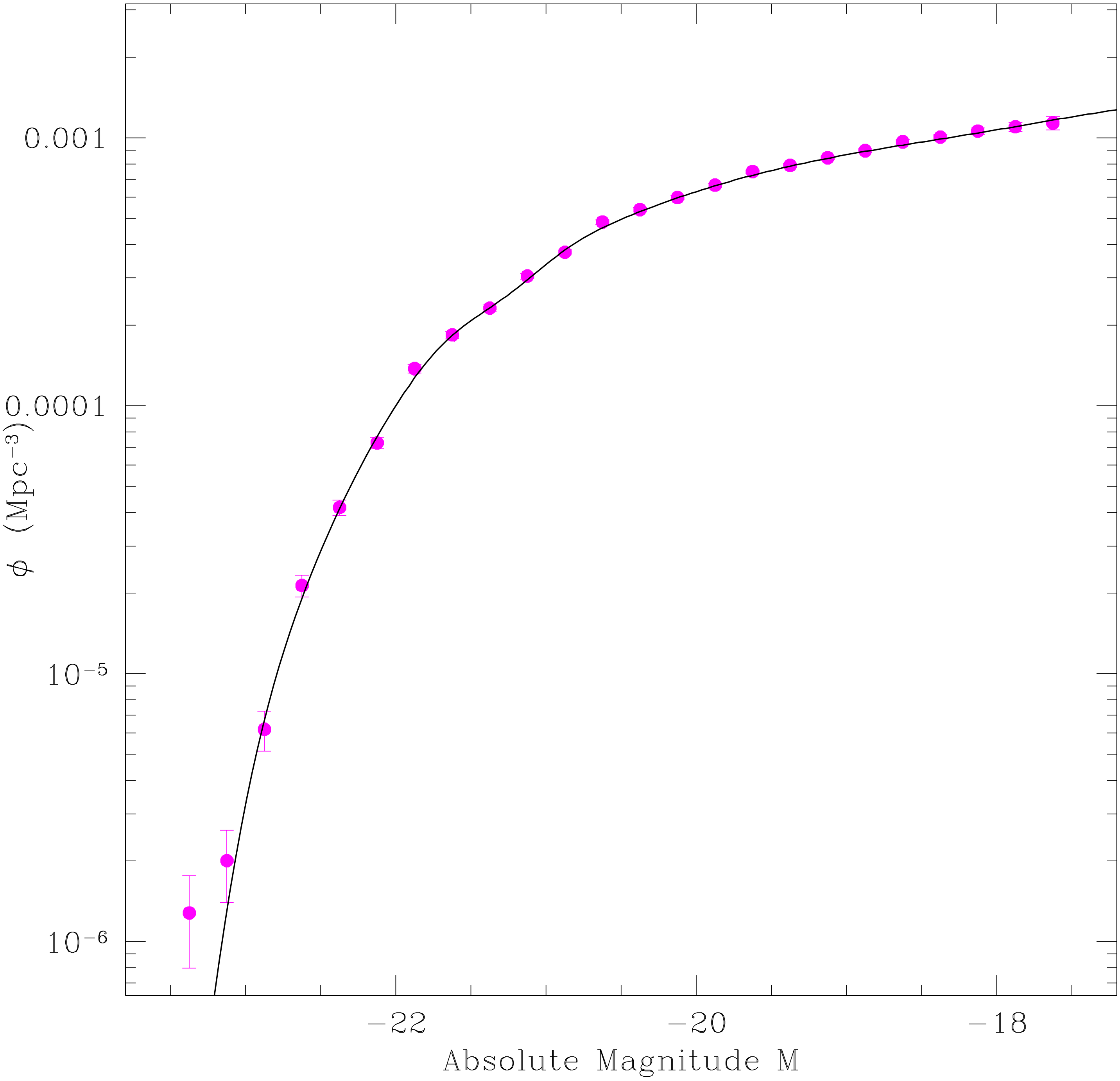

Figure 2.10 Luminosity function fits for the low redshift mock dataset with no errors. The magenta points show the SWML estimator, and the black curve represents the spline fit. As expected, both agree very well with the Schechter function fit.

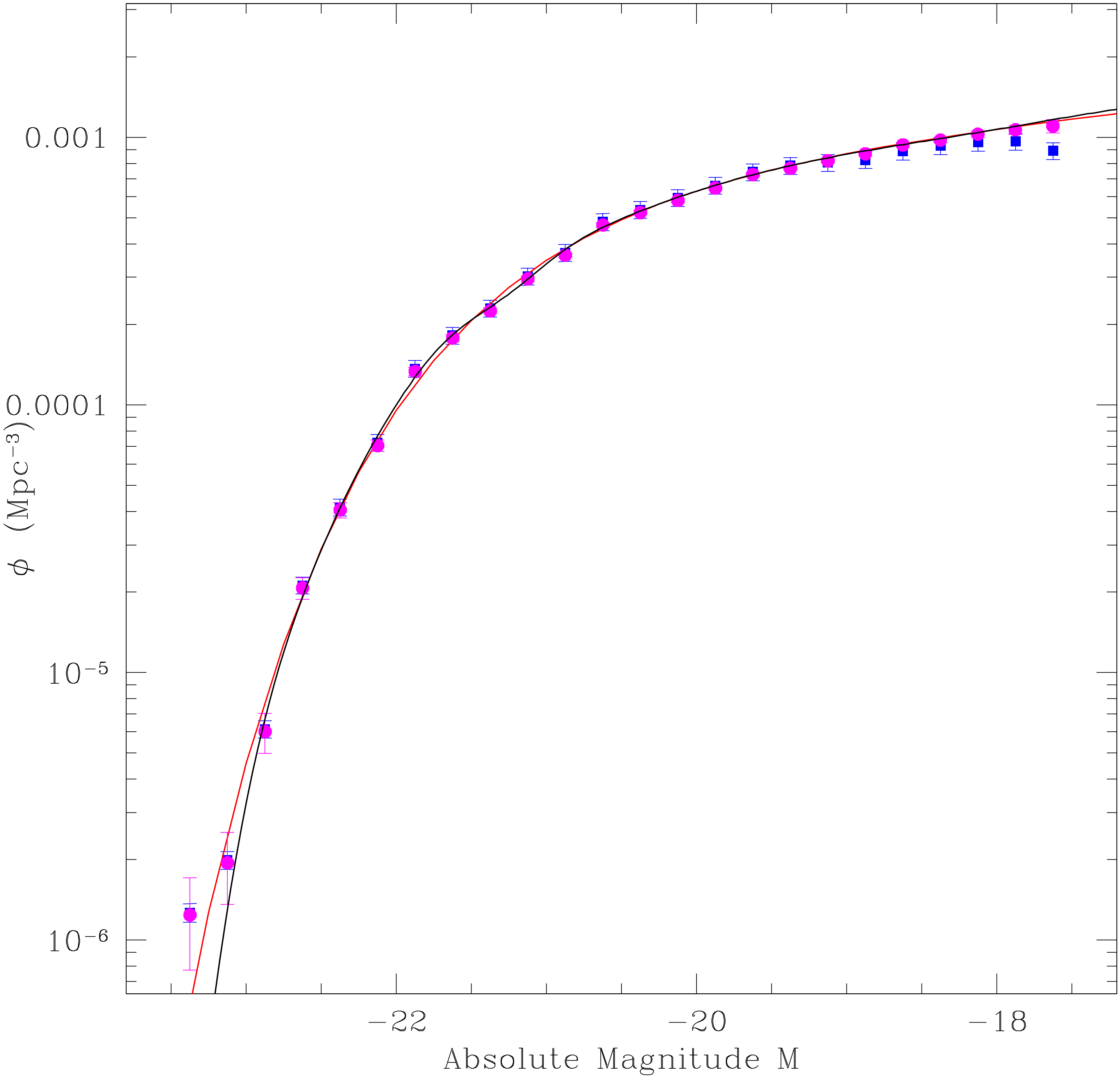

Figure 2.11 Luminosity function fits to the low redshift mock data with no errors in redshift. The red curve shows the best fit Schechter function given by the STY method, the blue points are from the 1/Vmax method, the magenta points are from the SWML method, and the black curve is the best fit spline.

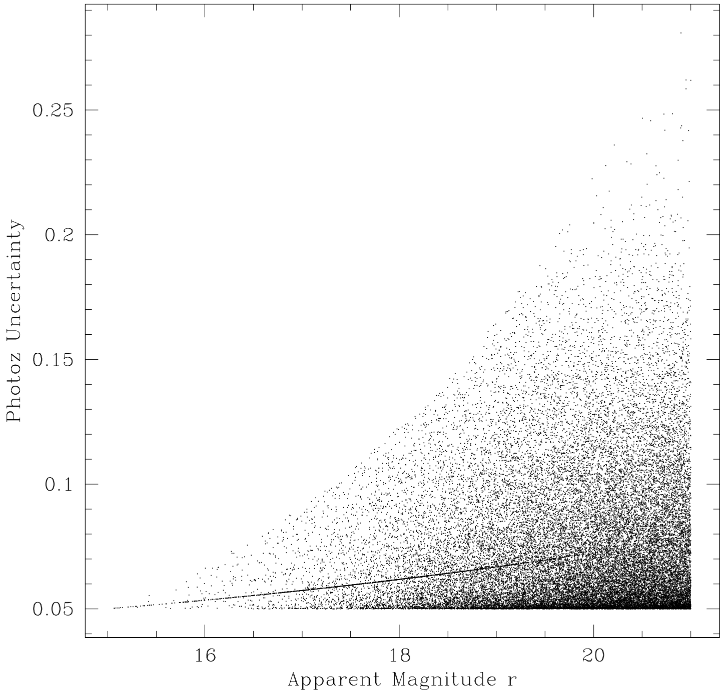

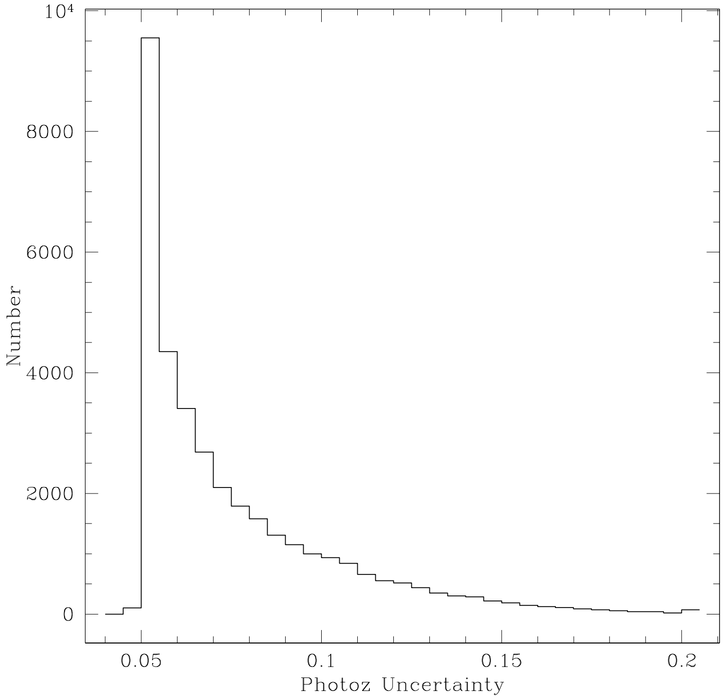

Figure 2.12 Top: Photometric redshift uncertainty as a function of apparent magnitude for the mock dataset. Bottom: Histogram of photometric redshift uncertainties.

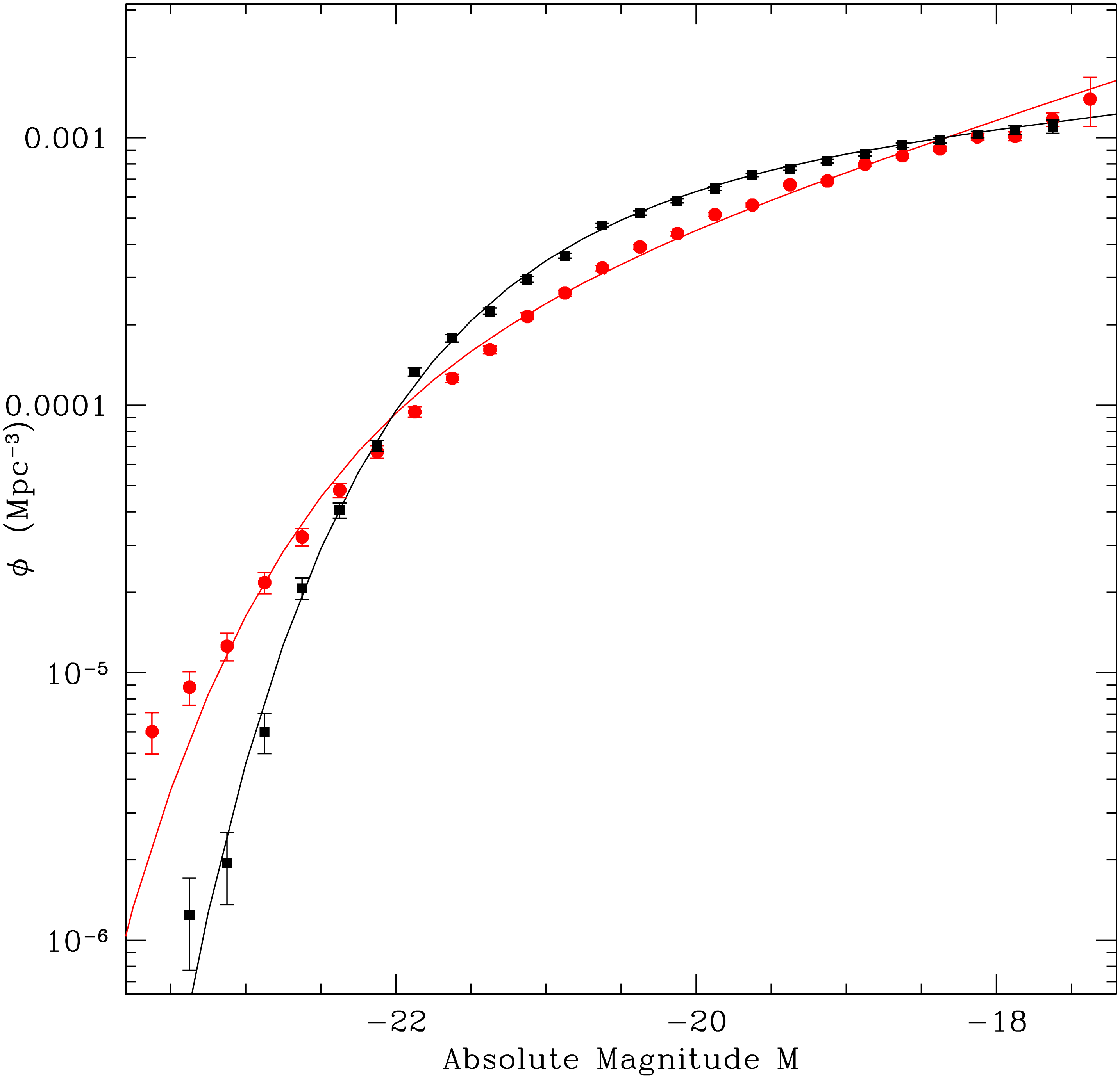

Figure 2.13 To illustrate the effect of photometric redshift uncertainties, the best fit Schecther and SWML results for the mock dataset with no errors are shown in black. In red, the same fits for the data with the uncertainties in redshift shown in Figure 2.12.

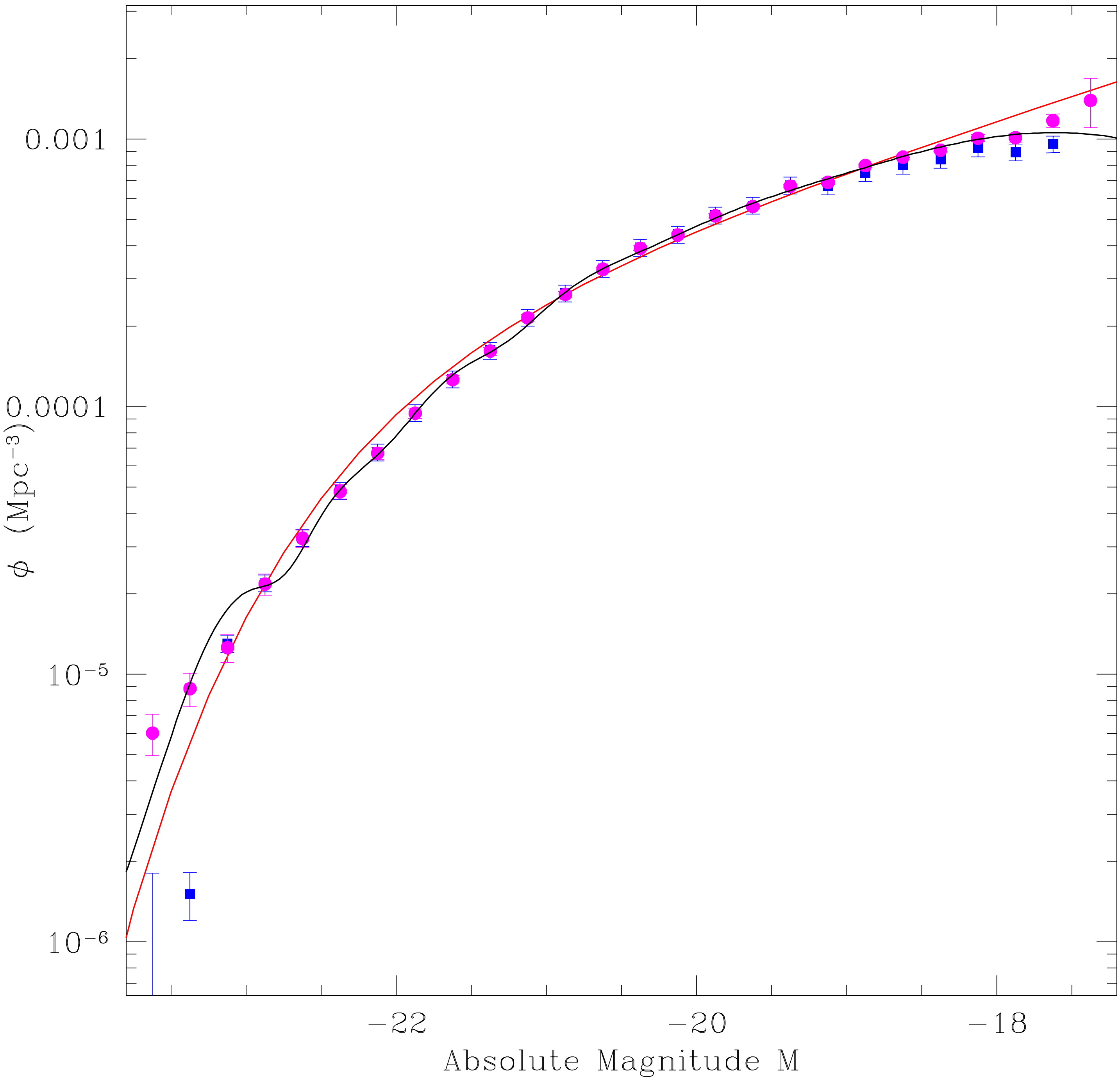

Figure 2.14 Luminosity function fits to the mock data with redshift uncertainties for the uncorrected estimators: 1/Vmax (blue), STY Schechter (red), SWML (magenta), and spline (black).

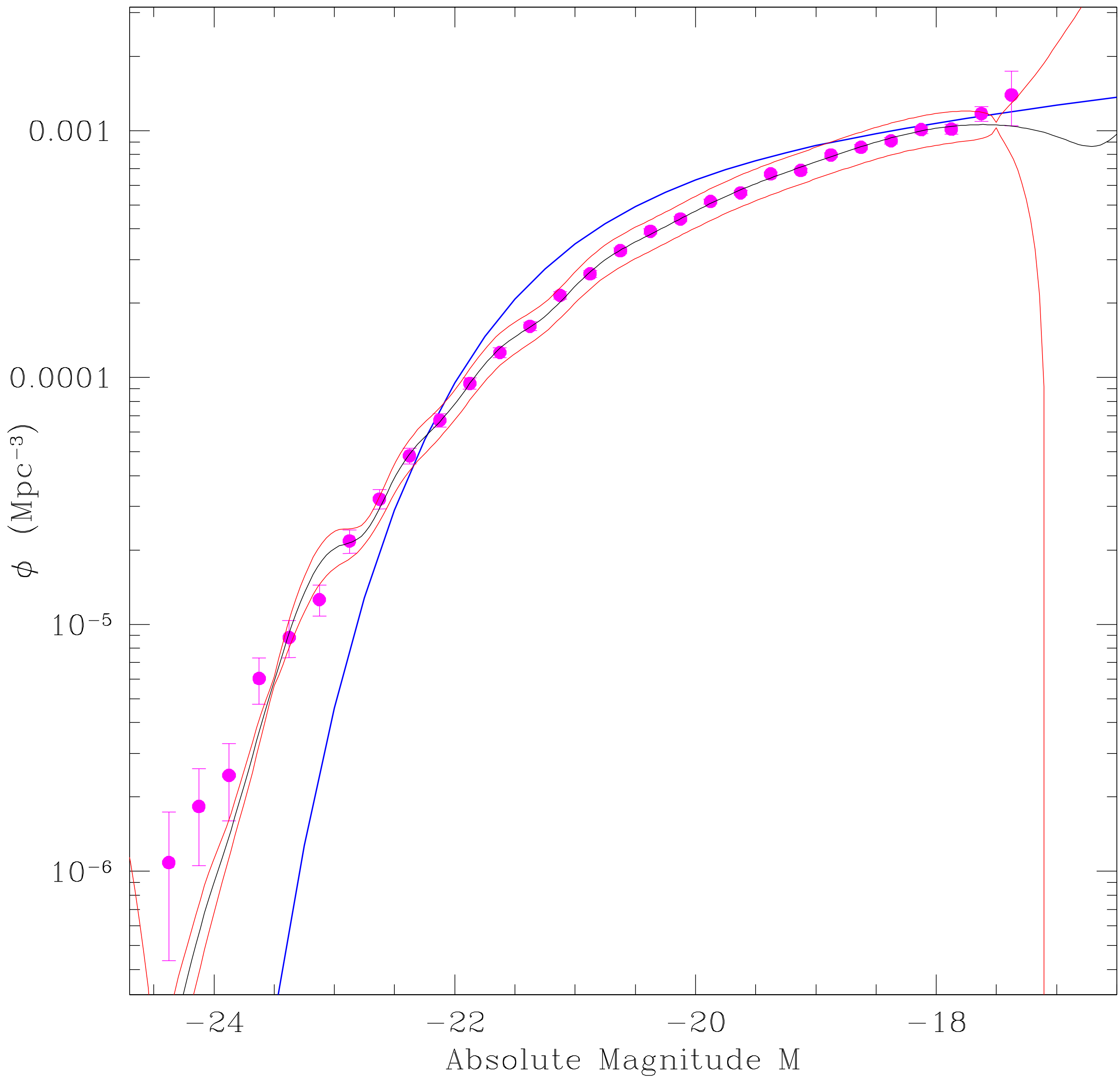

Figure 2.15 The BSpline Luminosity function fit to the mock data with redshift uncertainties (black) and 1σ error contours (red). Shown for comparison are the SWML fit (magenta), and the Schechter function distribution from which the absolute magnitudes were drawn before the photometric redshift uncertainty was added (blue).

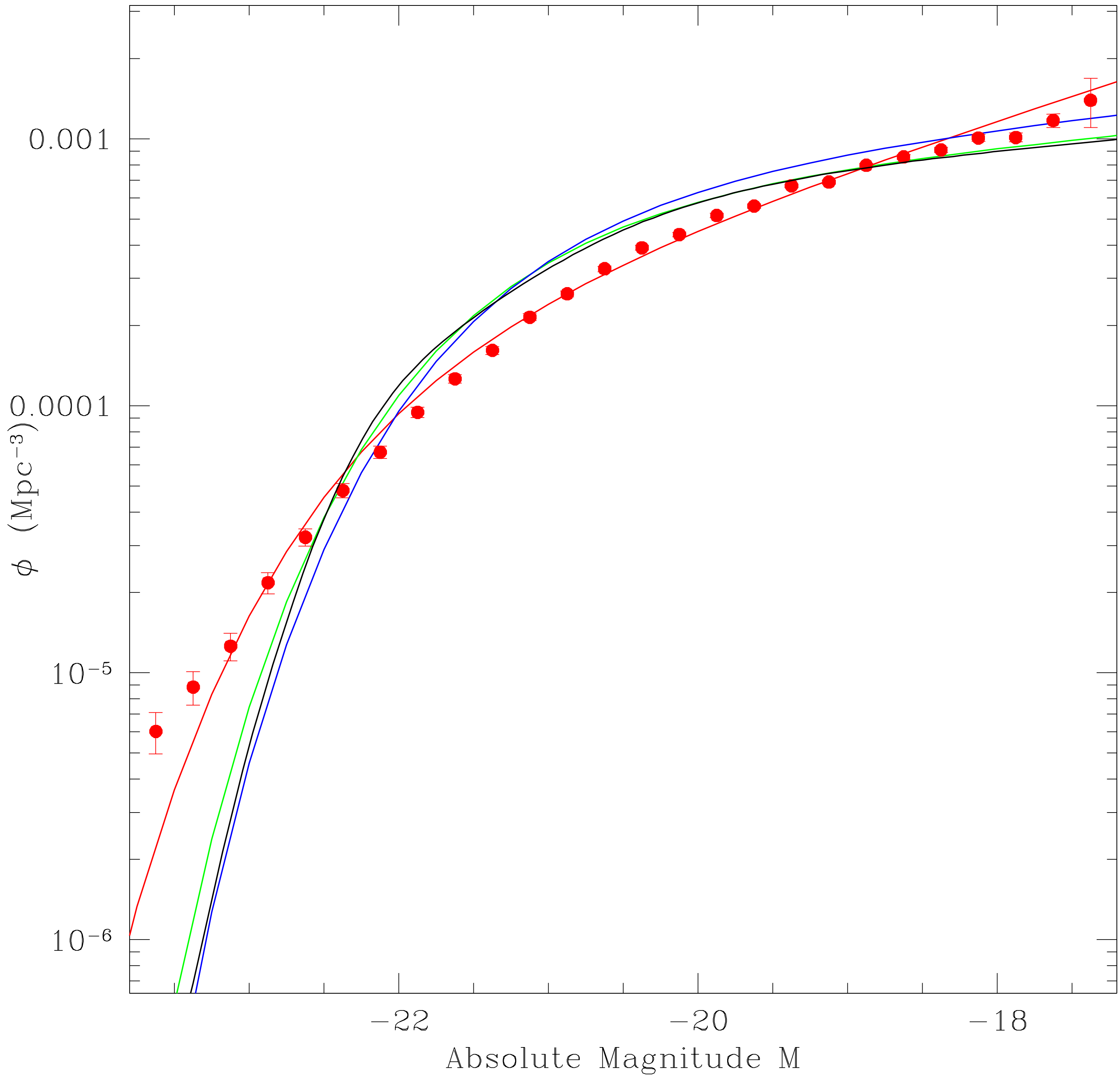

Figure 2.16 Results of running our new likelihood method on the mock dataset that includes photoz uncertainties for Schechter function (green), and spline (black). Shown for comparison are the Schechter and SWML fits with no accounting for errors(red), and the Schechter function fit to the data with no redshift uncertainties (blue).

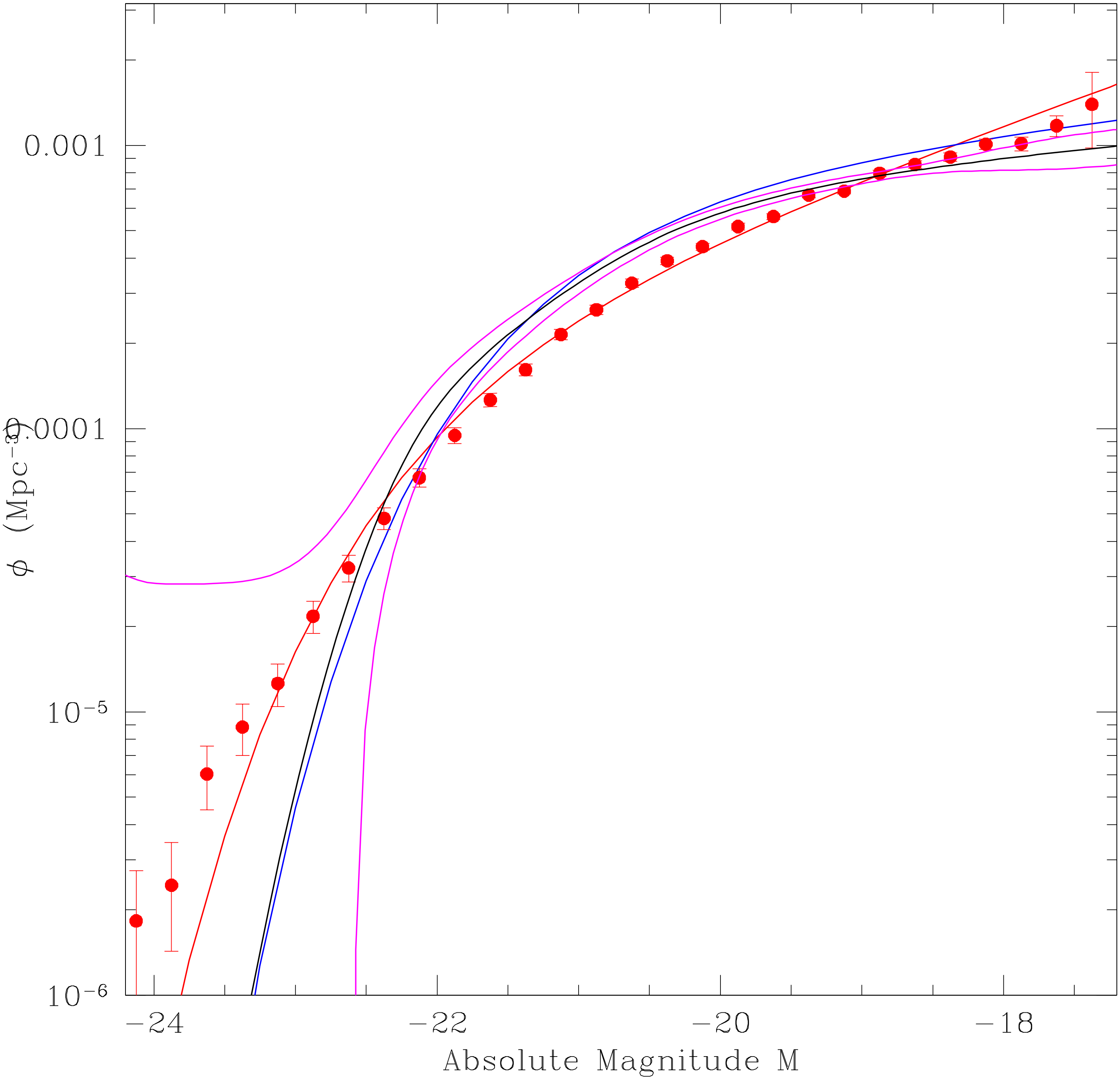

Figure 2.17 Same as Figure 2.16, but showing the 1 σ errors (magenta) on the spline fit (black). Shown for comparison are the Schechter and SWML fits with no accounting for errors(red), and the Schechter function fit to the data with no redshift uncertainties (blue).

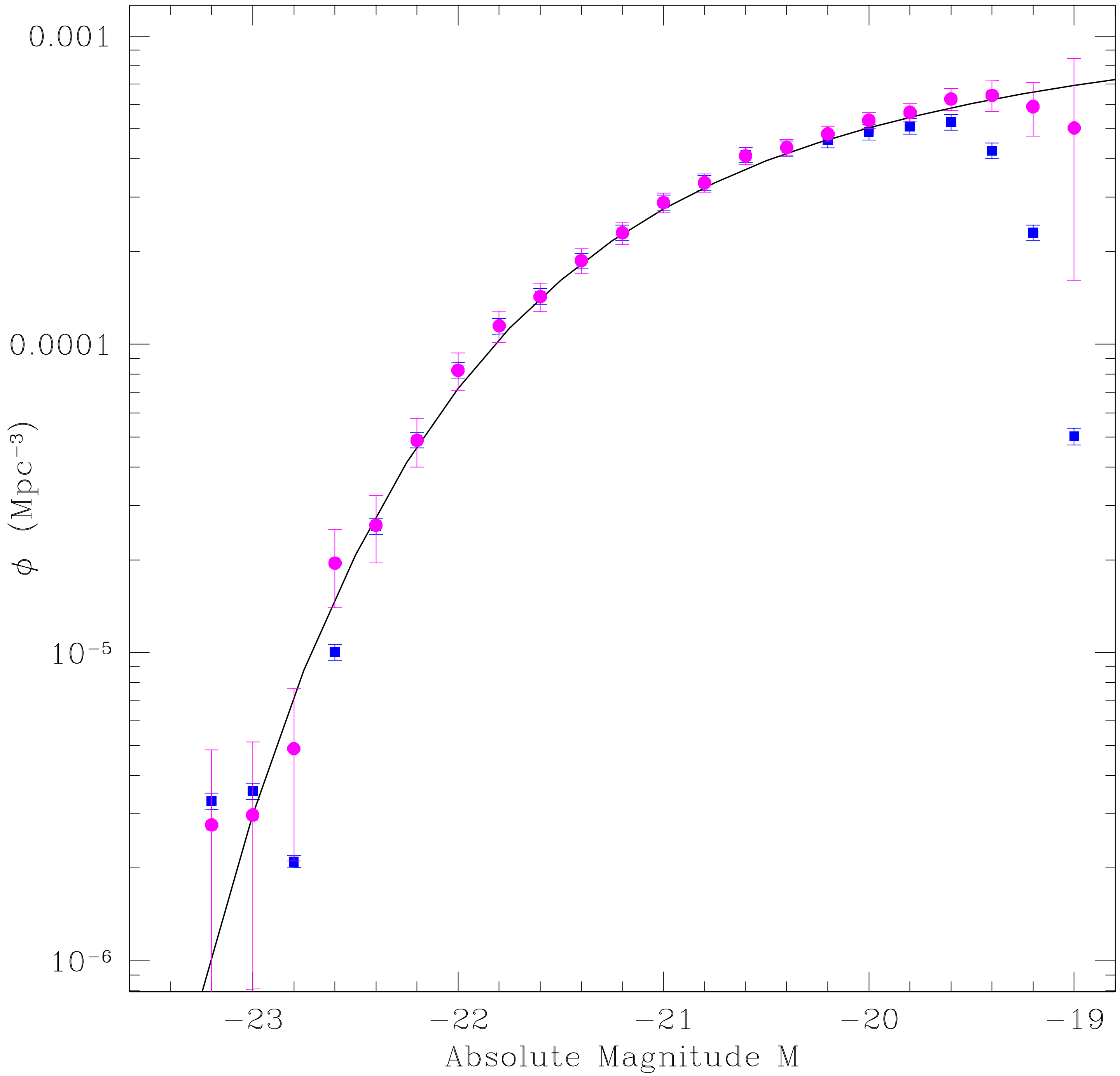

Figure 2.18 Luminosity function fits to the high redshift mock data with no redshift uncertainties for 1/Vmax (blue), STY Schechter (black), and SWML (magenta) methods.

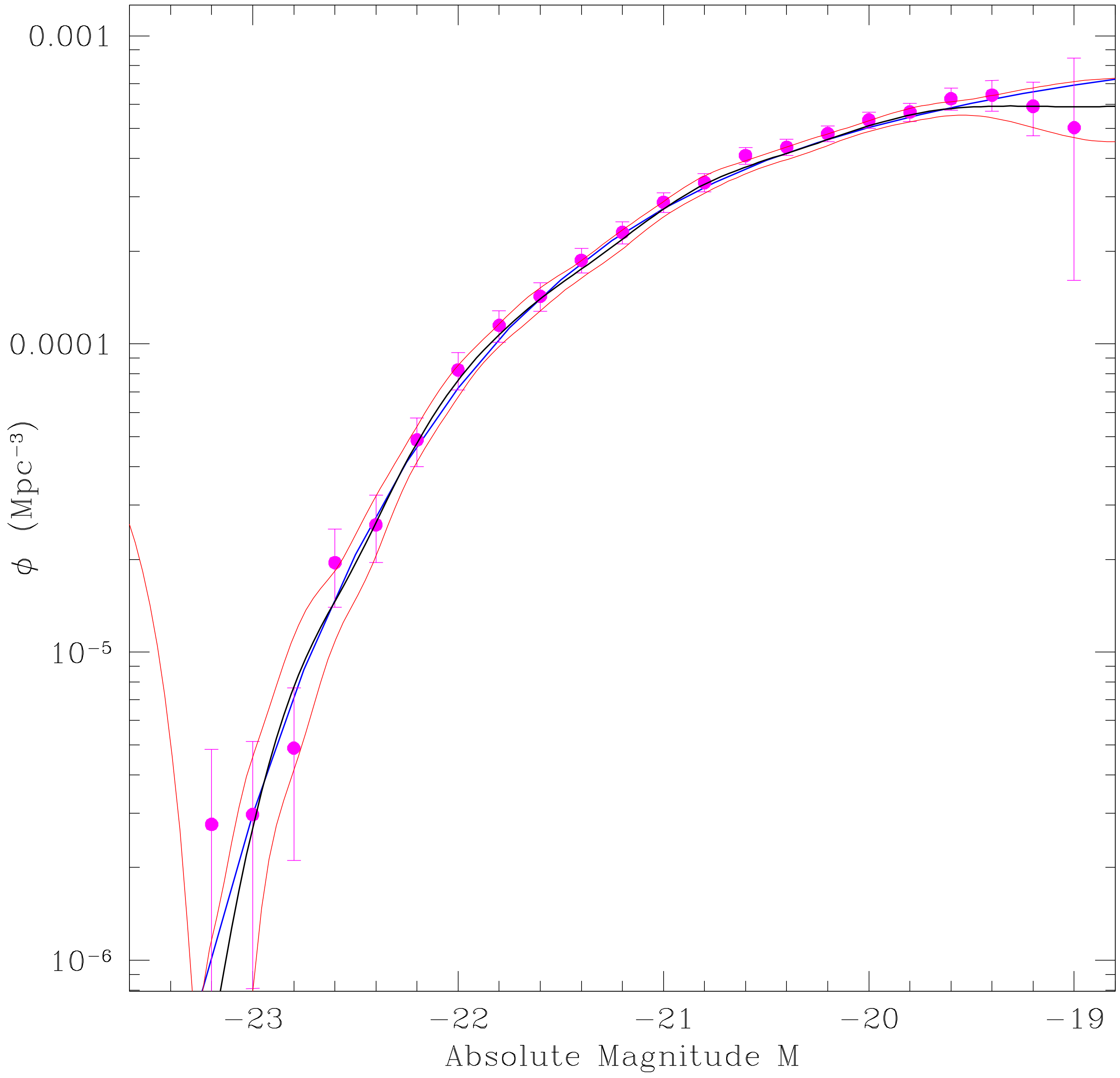

Figure 2.19 The BSpline Luminosity function fit to the mock data (black) and $1\,\sigma$ error contours (red). Shown for comparison are the SWML fit (magenta), and the Schechter function fit (blue).

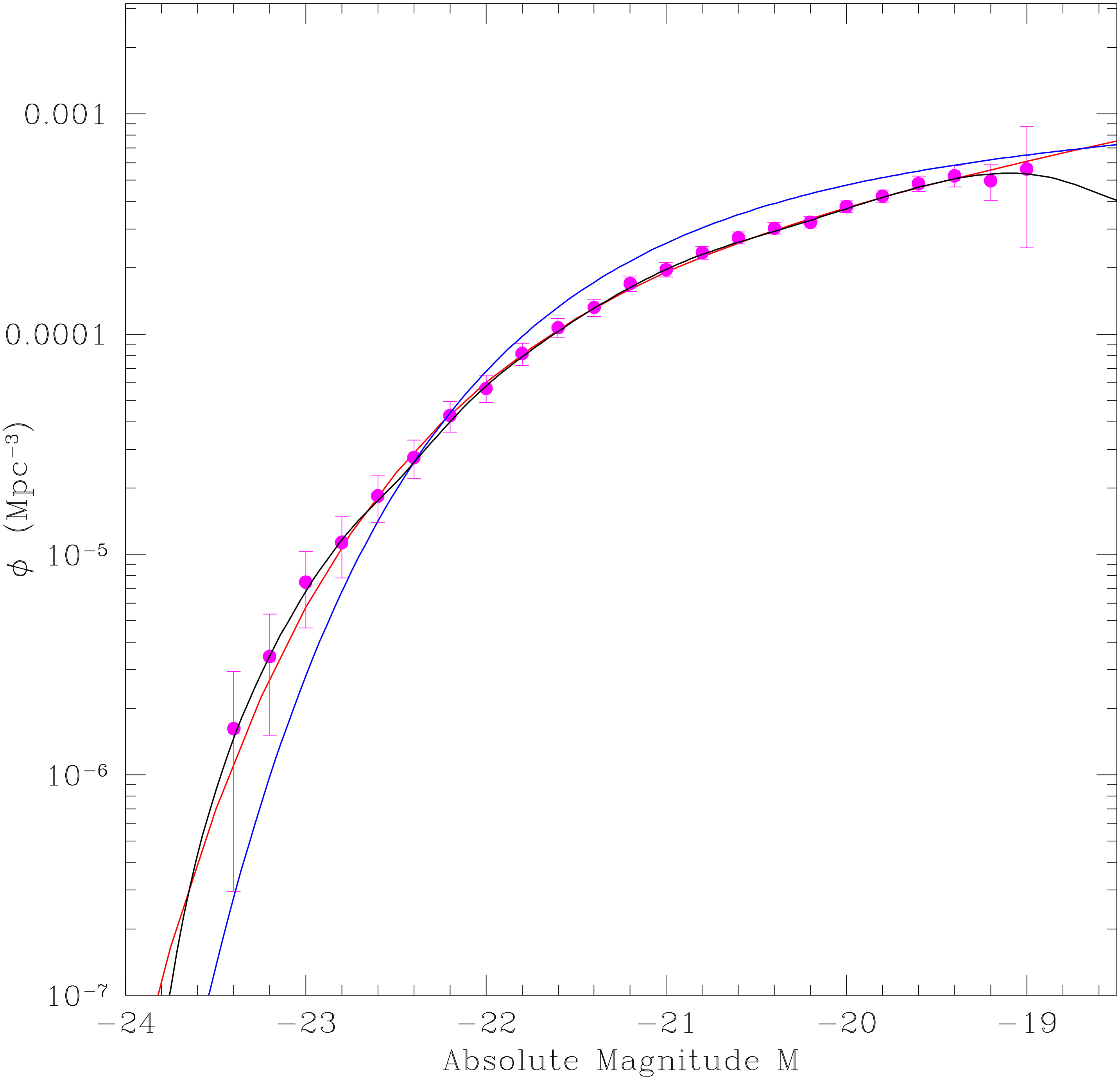

Figure 2.20 The BSpline fit (black) to the data including redshift errors. Shown for comparison are the SWML fit (magenta), and the Schechter function fit (red). The blue curve is the Schechter function fit to the data with no redshift errors.

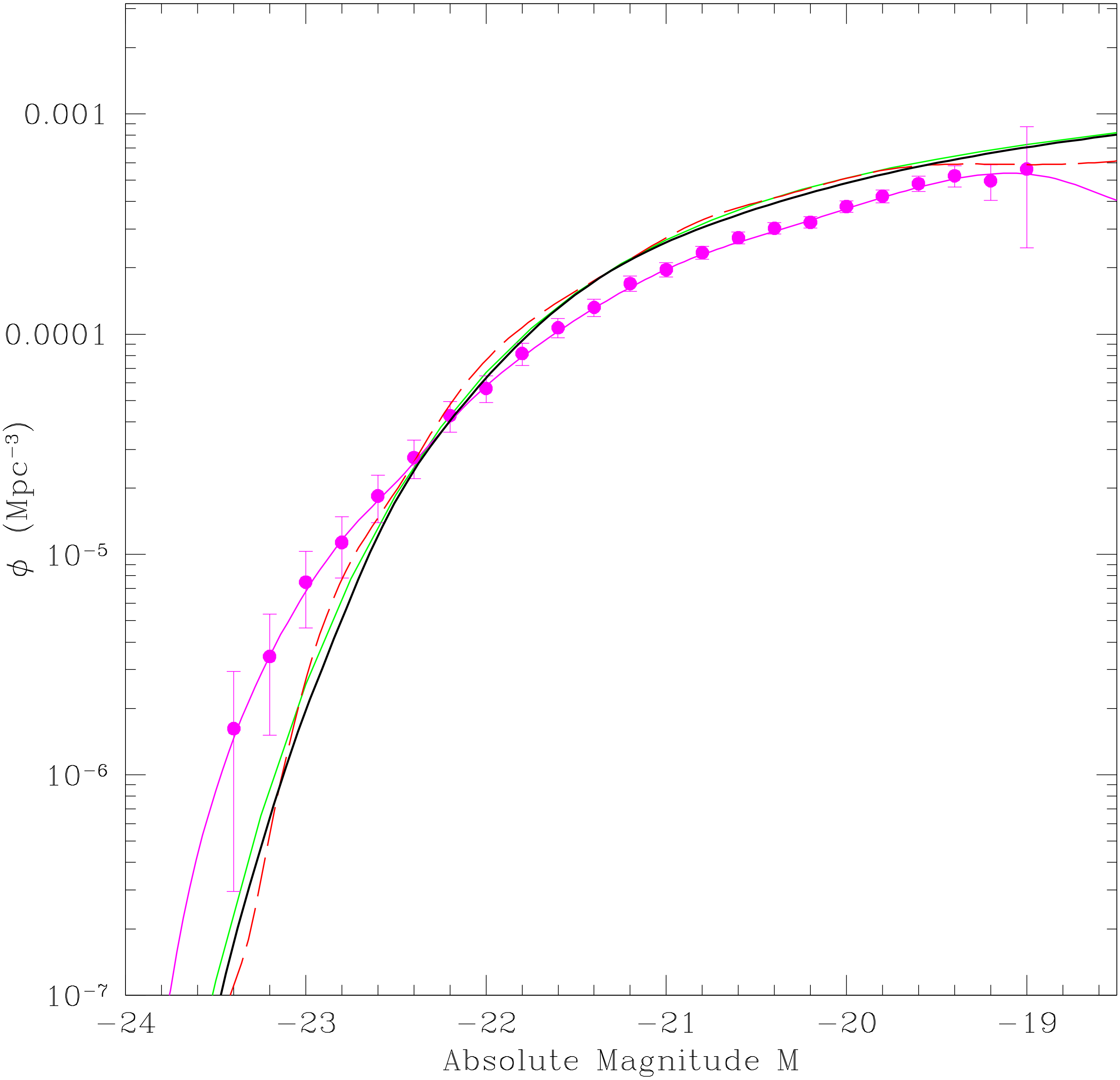

Figure 2.21 New estimator fits to the LF. The BSpline fit (black) and Schechter fit (green) for our modified estimator are shown. For comparison, also pictured are the original estimator SWML fit and spline fits (magenta), and the BSpline curve from the data with no redshift errors (red dashed).

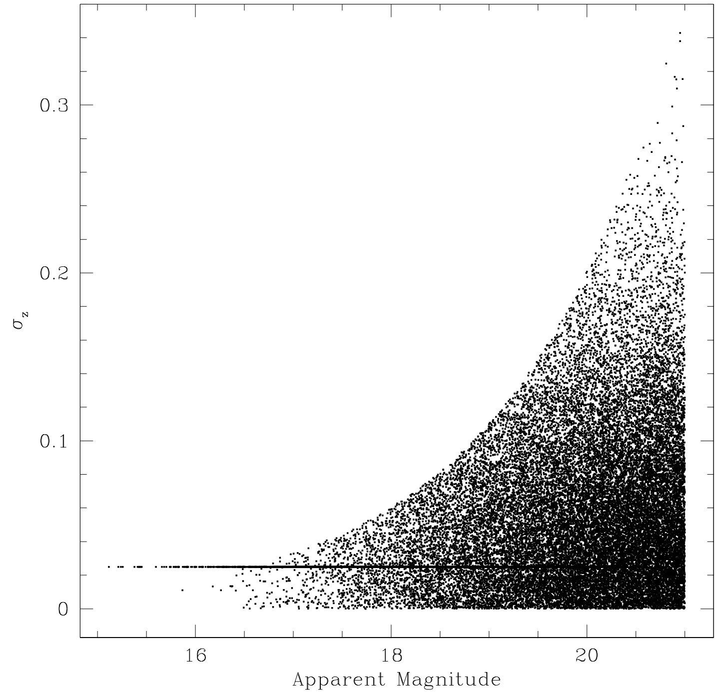

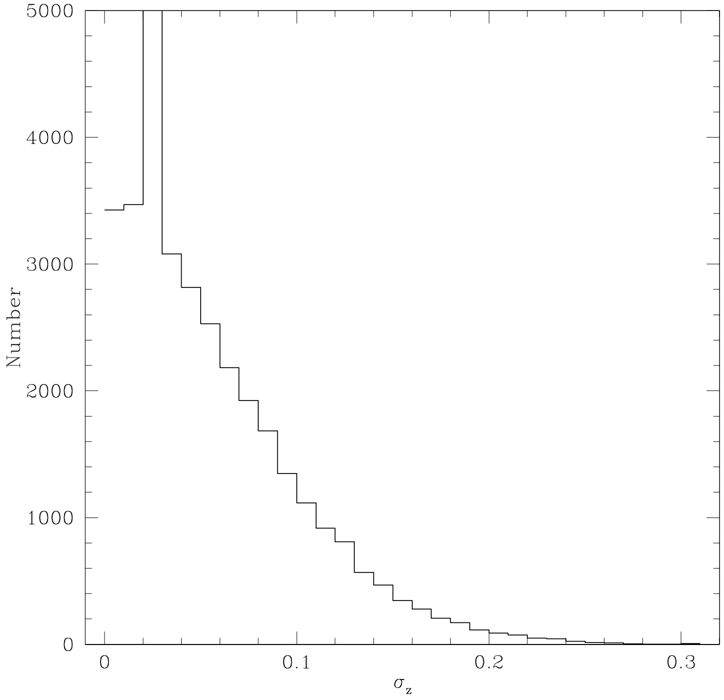

Figure 2.22 Top: Photometric redshift uncertainty as a function of apparent magnitude for the Low-z Photoz 2 mock dataset. Bottom: Histogram of photometric redshift uncertainties.

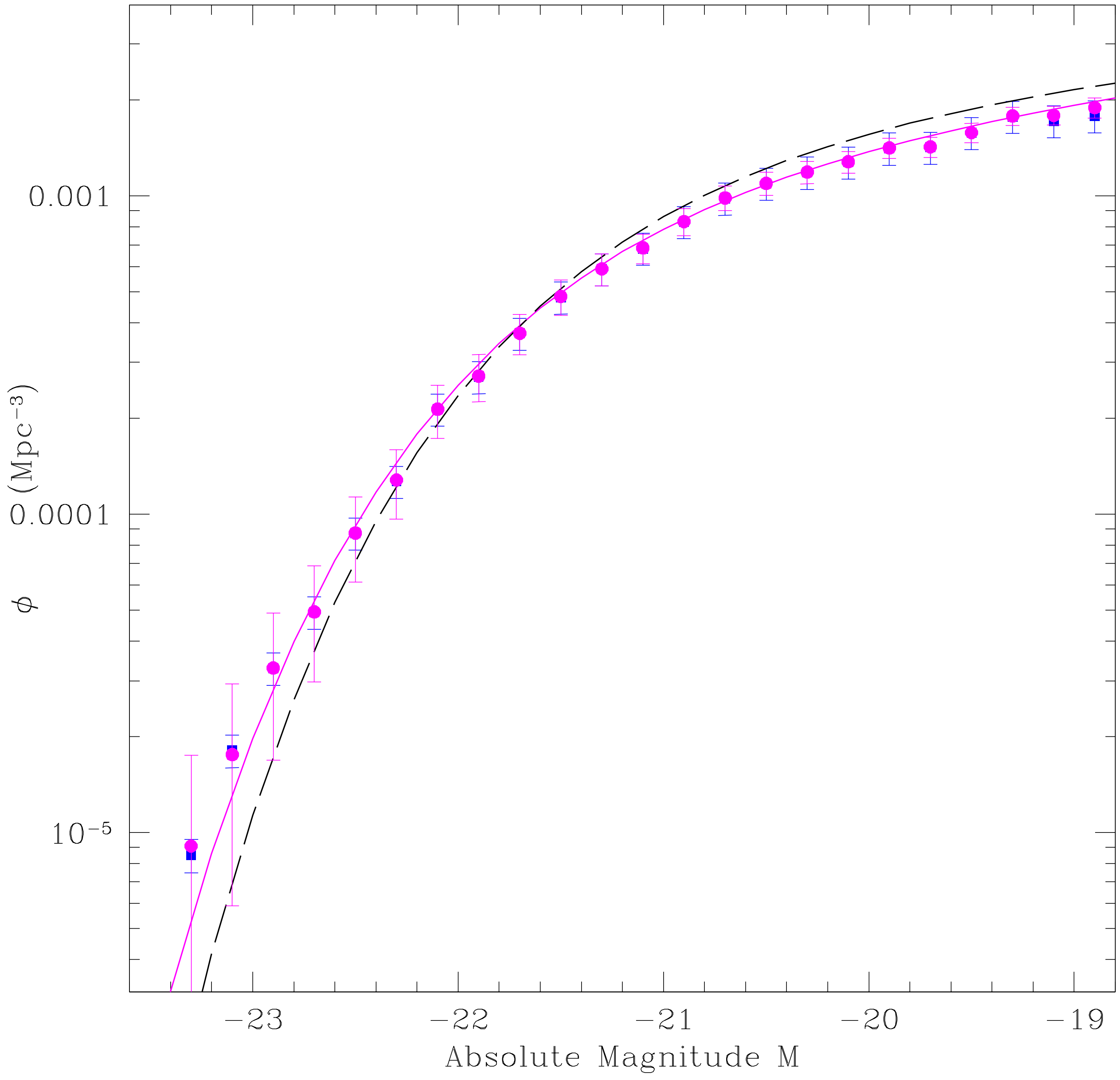

Figure 2.23 Luminosity function fits to the Low-z Photoz 2 mock data with redshift uncertainties of $\sigma_z = 0.1$ for 1/Vmax (blue), STY Schechter and SWML (magenta) methods. Shown for comparison is the Schechter function of the data with no redshift uncertainties (black dashed).

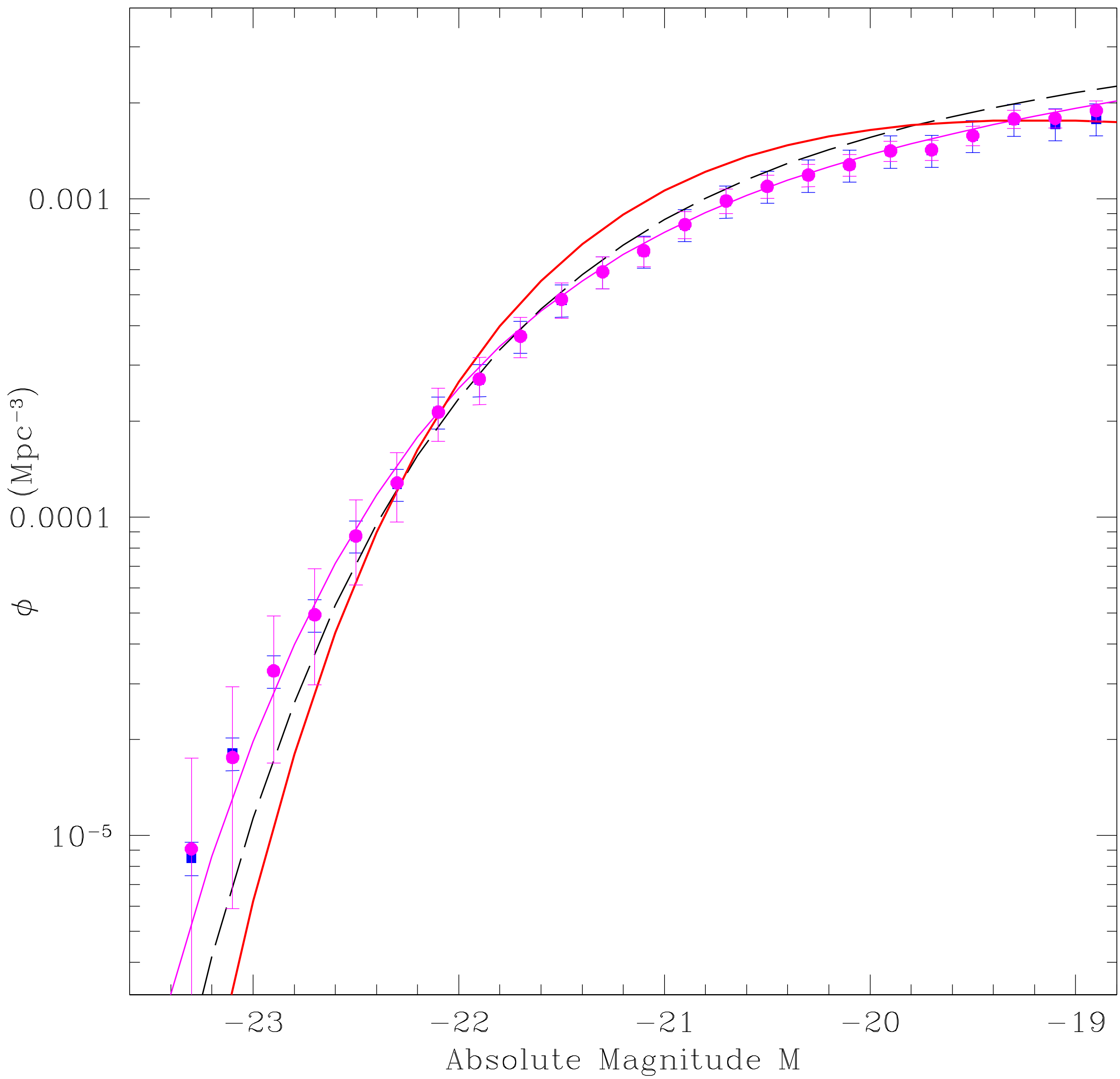

Figure 2.24 Luminosity function fits to the Low-z Photoz 2 mock data with redshift uncertainties of $\sigma_z = 0.1$ for 1/Vmax (blue), STY Schechter and SWML (magenta) methods. Shown for comparison is the Schechter function of the data with no redshift uncertainties (black dashed). The red curve shows the Schechter function fit for our new estimator.

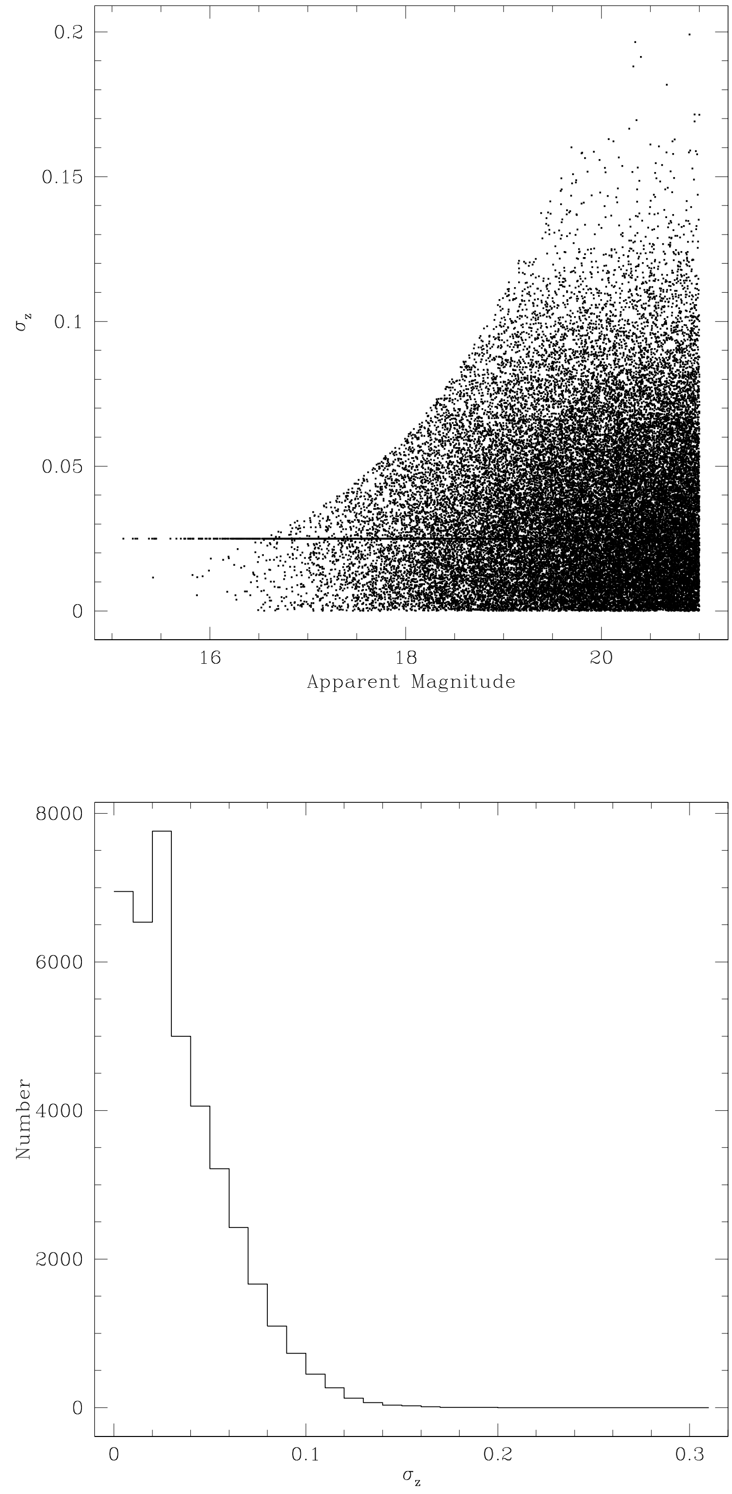

Figure 2.25 Top: Photometric redshift uncertainty as a function of apparent magnitude for the Low-z Photoz 3 mock dataset. Bottom: Histogram of photometric redshift uncertainties.

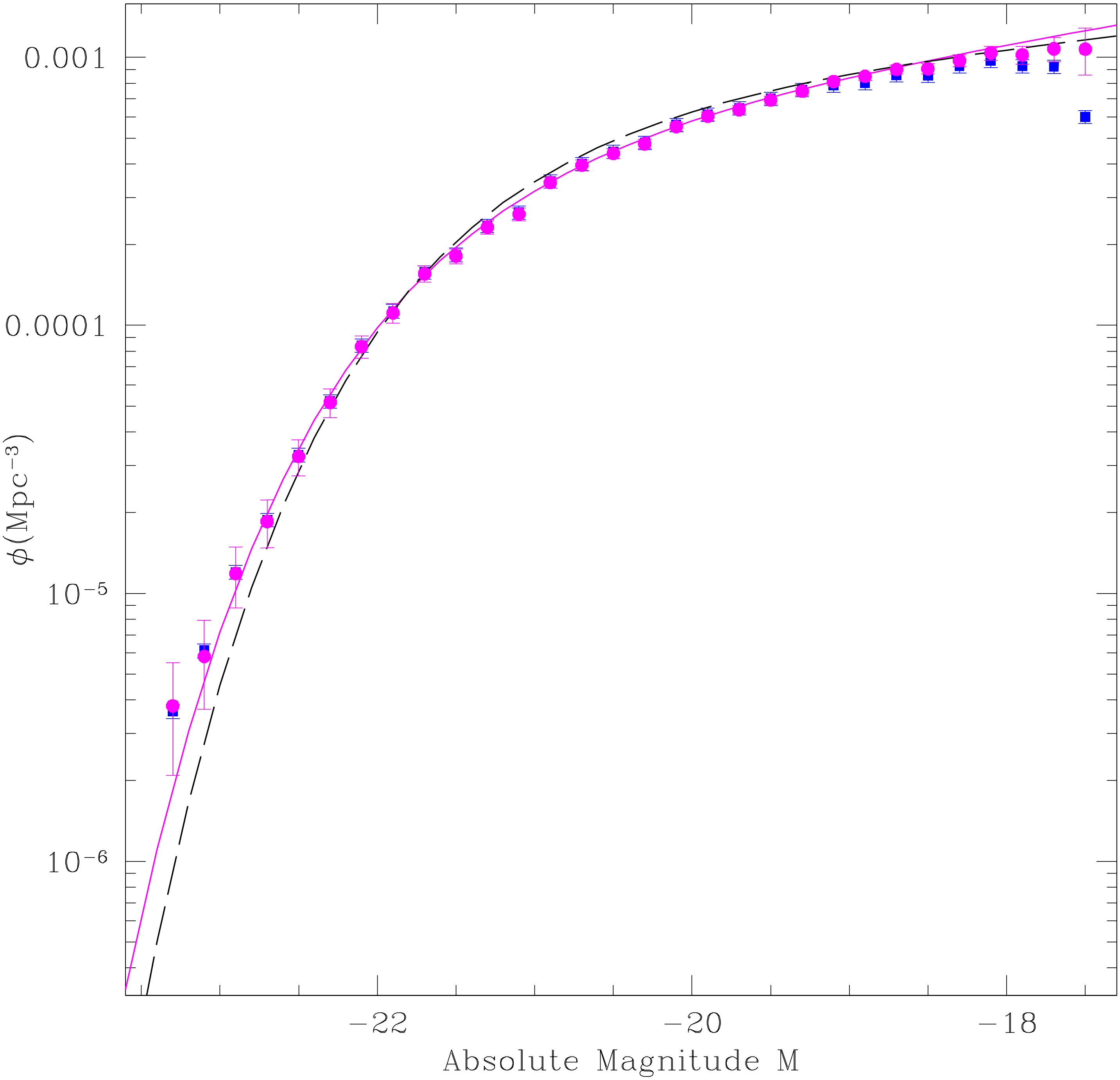

Figure 2.26 Luminosity function fits to the Low-z Photoz 3 mock data with redshift uncertainties of $\sigma_z = 0.05$ for 1/Vmax (blue), STY Schechter and SWML (magenta) methods. Shown for comparison is the Schechter function of the data with no redshift uncertainties (black dashed).

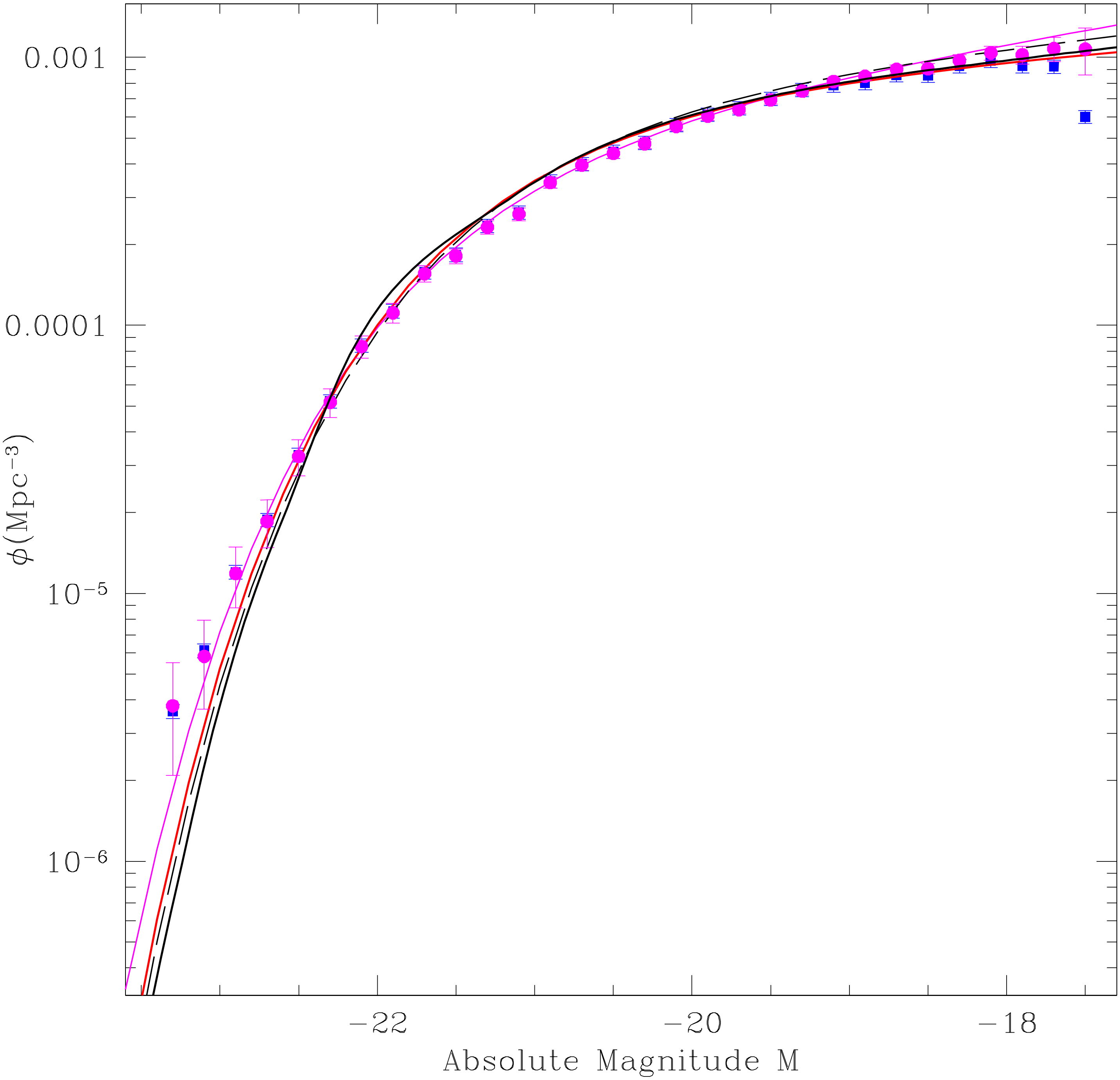

Figure 2.27 Luminosity function fits to the Low-z Photoz 3 mock data with redshift uncertainties of $\sigma_z =$ 0.0.05 for 1/Vmax (blue), STY Schechter and SWML (magenta) methods. Shown for comparison is the Schechter function of the data with no redshift uncertainties (black dashed). The red curve shows the Schechter function fit for our new estimator, and the thick black curve represents the new method BSpline fit.

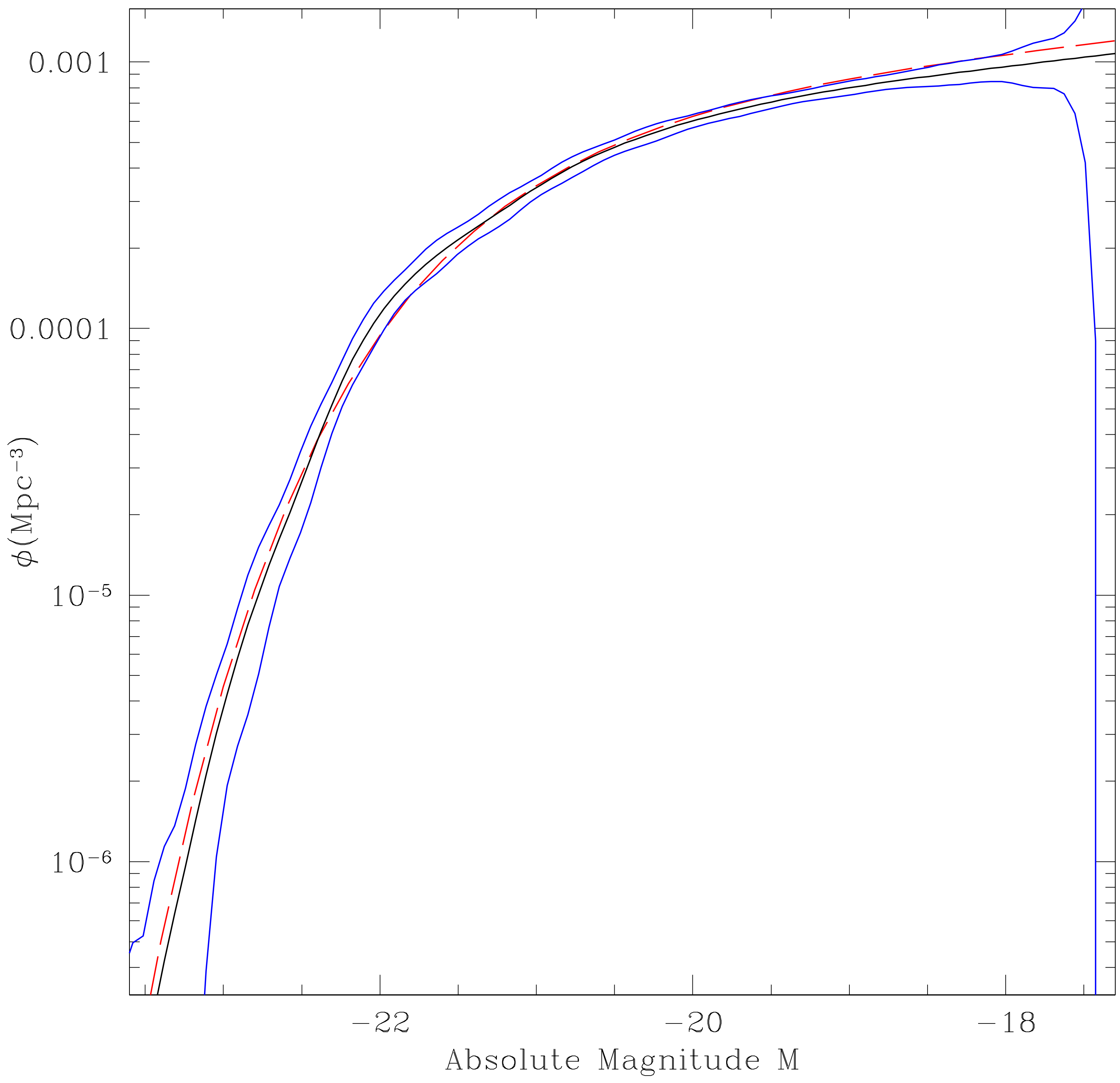

Figure 2.28 BSpline Luminosity function fit (black) and 1 σ error bound (blue) to the Low-z Photoz 3 mock data. The red curve shows the Schechter function fit for the input data with no redshift errors.

2.2.3 Photometric Redshift Dataset

The source of the data used to create our photometric redshift catalog is the SDSS Southern Survey, also known as "SDSS stripe 82", named for the initial SDSS data stripe in this region of the sky. Stripe 82, which is located on the celestial equator, is imaged multiple times during the course of SDSS operations. These images are then coadded to obtain deeper catalogs with higher signal to noise. This low noise data should reduce the magnitude errors in all five bands, increasing the accuracy of the photometric redshifts. The specific versions used to construct the photozs in this work are known as runs 100001 and 200001, and contain between 5 and 18 epochs of data, depending on position on the sky. The details of the construction and calibration of this catalog are the subject of a future paper (J. Brewer, in prep), and are briefly summarized here.

The coadded images are processed and calibrated using the GESTALT webservice tools (`http://nvogre.phyast.pitt.edu:8080/gestalt_home/`), specifically a webservice interface to SExtractor (Bertin and Arnouts, 1996) called WESIX. For optimal photometric redshifts, the flux in each passband should be from the same portion of the galaxy. Therefore, WESIX is run in dual image mode, resulting in matched aperture catalogs in the 5 SDSS bands, with r-band as the primary detection filter. Each of the five bands is calibrated to the SDSS magnitude scale by positionally cross-matching bright ($15 \leq r \leq 19$) stars in the images with their counterparts in single epoch SDSS data, fitting a linear relation between the stellar magnitudes in each dataset, and assuming that this relation continues to fainter magnitudes. The magnitudes are calibrated by matching SExtractor MAG_AUTO to SDSS model magnitudes. Model magnitudes in SDSS are the better of two fits to each galaxy: a deVaucouleurs or exponential profile, and are a good match to the total galaxy magnitude measured by SExtractor MAG_AUTO. Figure 2.29 shows the footprint of the stripe 82 data. Fields with fitted slopes more than 10% different from unity are rejected as bad. There are additional fields where no images are present in the SDSS Stripe 82 database. The bad slope and missing frames are clearly visible as empty regions in Figure 2.29, which shows the sky coverage footprint of the data used in constructing the photometric redshift catalog.

The resulting catalogs are then dereddened using the dust maps of Schlegel et al. (1998) to account for extinction due to dust absorption within our Galaxy. In the right ascension range $55 < RA < 60$ extinction from the Galaxy is significant. Figure 2.30 shows areas with $E(B-V) > 0.3$ (blue) and $E(B-V) > 0.2$ (red). Because excess reddenning can degrade the reliability of photometric redshifts, we trim the stripe 82 dataset to exclude the area $55 < RA < 60$, as well as the other frames where $E(B-V) > 0.2$. The final useable area, after accounting for this extinction cut and the missing and rejected frames, is 245.0 square degrees, with more than two million objects with $r \leq 21.0$. While small compared to the nearly ten thousand square degrees of the entire SDSS photometric catalog, this dataset is an order of magnitude larger than others used to explore the non-local luminosity function in the past, where typically smaller, deeper surveys have been used (e.g. Chen et al. (2003) and (Wolf et al., 2003)). With a slightly better understanding of the errors (see Section 4.1 for details) our new estimator can be applied to the entire SDSS photometric galaxy catalog in the future.

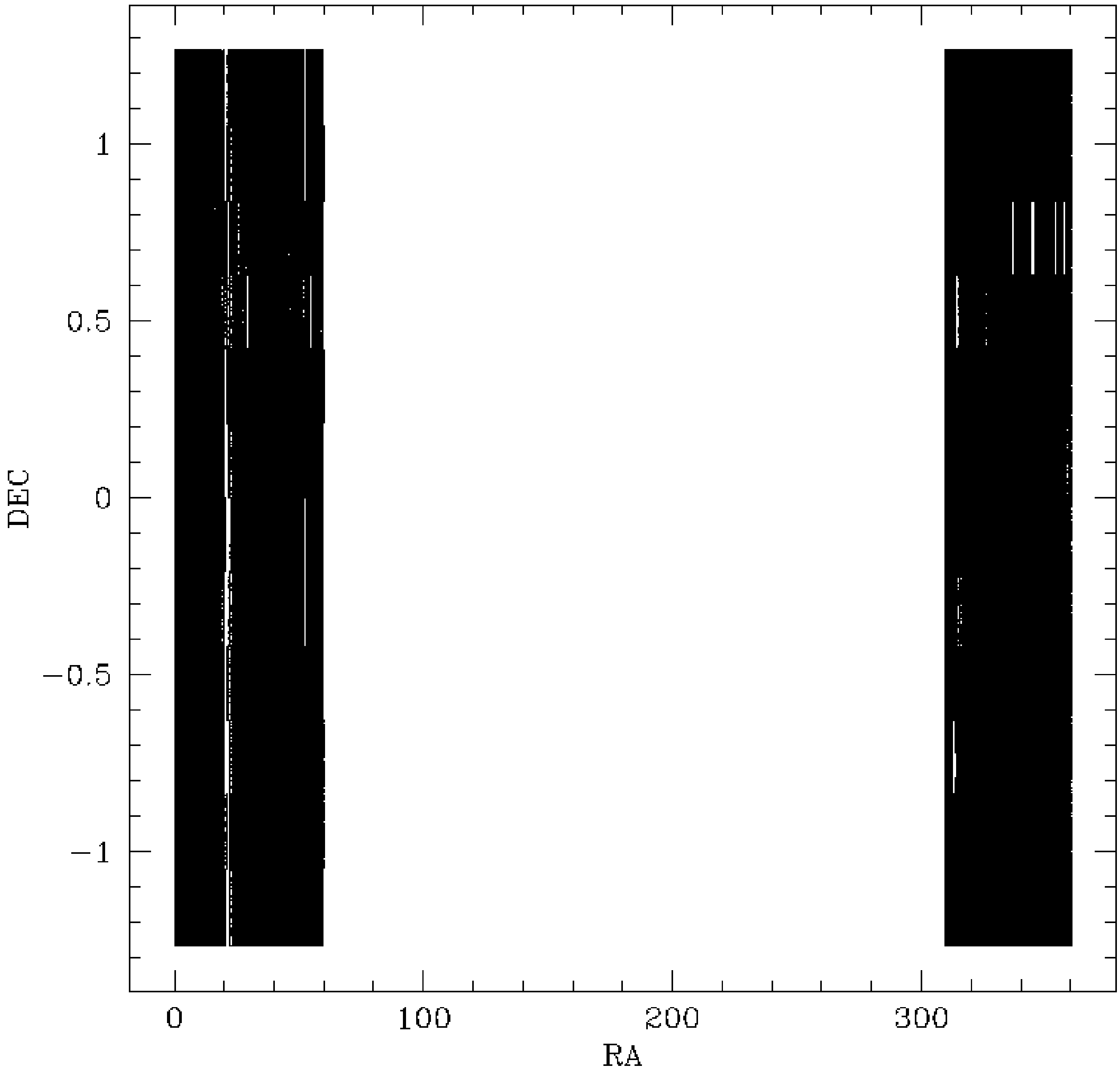

Figure 2.29 The SDSS Stripe 82 footprint

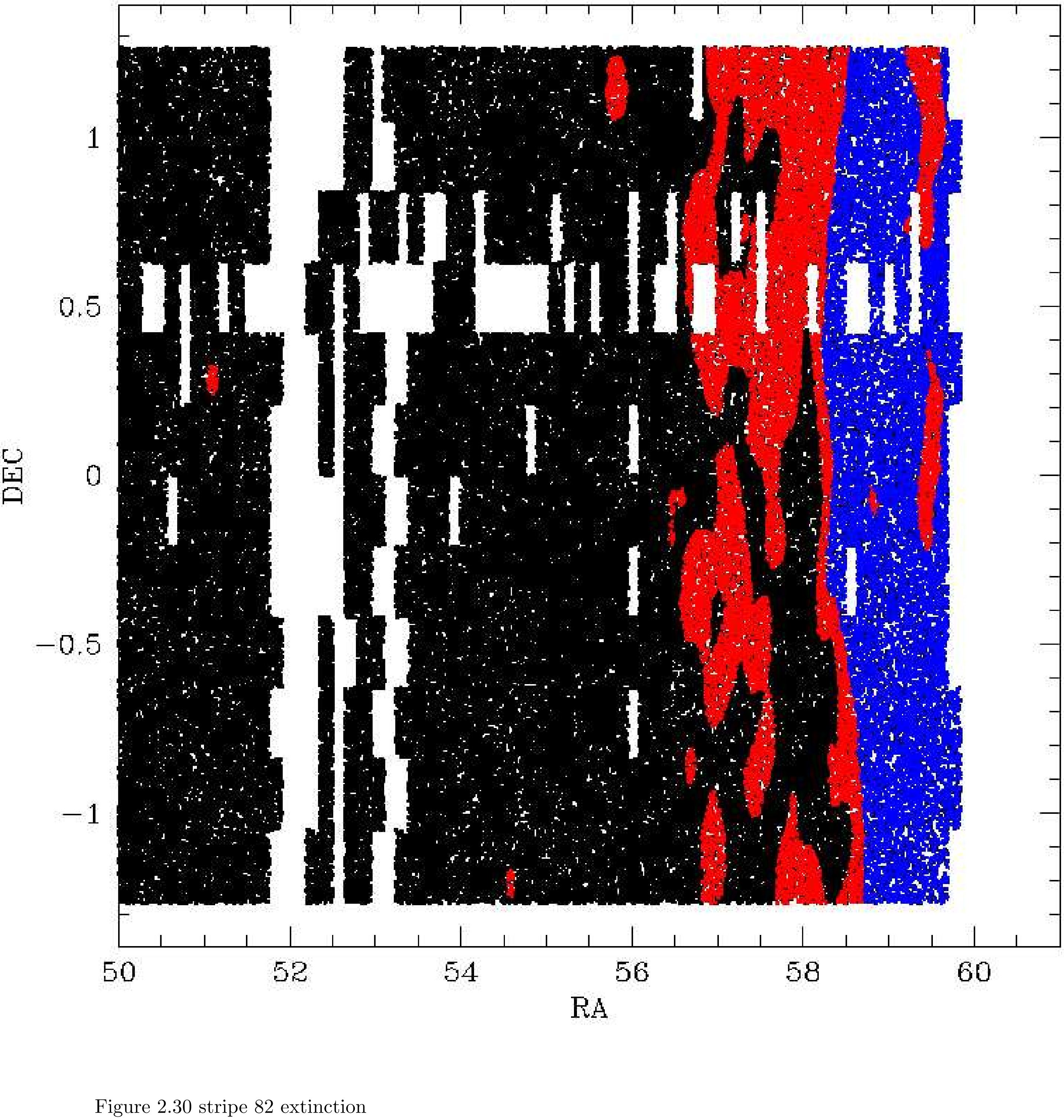

Figure 2.30 stripe 82 extinction

The first step in constructing the galaxy catalog is defining the galaxy sample. Star-galaxy separation is done based on each individual object's concentration, i.e. comparing total integrated flux of an object to the flux measured in a fixed aperture in order to distinguish extended objects from pointlike stars. This procedure will be detailed in a future paper (J. Brewer, in prep). Briefly, the concentrations of all objects in a particular apparent magnitude range are histogrammed. For bright galaxies, this histogram is bimodal, with two well defined peaks, one at very high concentration comprised of stars, and another broader peak consisting of galaxies. A hard concentration cut separates the sample into stars and galaxies. For bright objects ($r \leq 19.0$) there is little contamination, though as you move fainter, the peaks move closer together, and there is an increasing fraction of misclassified objects. Beyond $r \approx 21$ the peaks merge, and reliable star-galaxy separation is impossible. At these faint apparent magnitudes, stars are less numerous than galaxies, and we call all objects with $r > 21$ galaxies. The galaxies most likely to be misclassified are high concentration (starlike) galaxies, and high redshift galaxies, where cosmological dimming has rendered the extended parts of the galaxy undetectable, and only the compact center is visible. There is an observed correlation between surface brightness and luminosity: most very compact galaxies are very luminous, and therefore most likely bright enough in apparent magnitude to still pass our star-galaxy cut. Because we do not consider galaxies with $z > 0.3$, the cosmological dimming should only come into play for the fainter of our galaxies. In practice, the contamination of the sample should not have a large effect, as statistically a similar number of stars and galaxies are misclassified in each magnitude range. However, since photometric redshifts are computed only for objects classified as galaxies, this has the potential to identify stars as a zero redshift object (if it happens to have a spectrum similar to one of the photoz templates), and therefore more false galaxies are removed than false stars added. This could mean a small underestimate in the density of galaxies, though we will make no attempt to correct for it.

Photometric redshifts were computed using the code photoz++ (T. Budavari, private communication), a non-public photometric redshift code, a version of which is used to compute the photometric redshifts for SDSS. The theoretical underpinnings of the code are discussed in Csabai et al. (2003). Photoz++ is a template based photometric redshift code which compares the observed colors of each galaxy to the colors from a set of template spectra convolved with the SDSS filter functions at a variety of redshifts, and finding the closest match (i.e. a χ^2 minimization). Figure 2.31 shows the ten templates used as a basis for the photoz computation. The ”tweaked” templates discussed in Csabai et al. (2003) are not used. Photoz++ further interpolates additional templates between each of these ten basis templates for a final set of 71 templates, which comprise a ”continuous” type parameterization. No Bayesian priors are assumed (e.g. a dN/dz or Luminosity Function priors), as they are not implemented in the version of photoz++ used to create this dataset. For more detail on this code and photometric redshift techniques in general, see Appendix B.

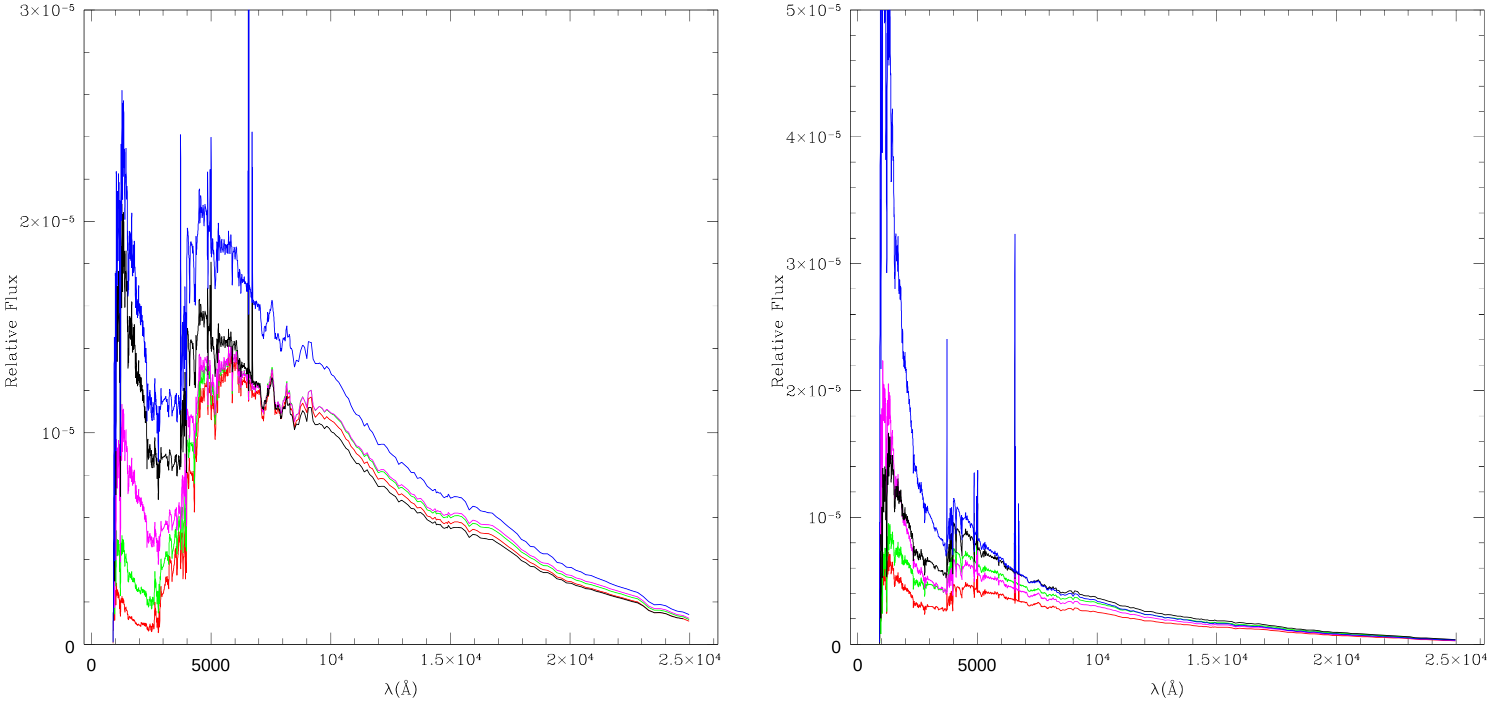

Figure 2.31 Ten template spectra used in the photometric redshift estimation.

The photoz++ code estimates the redshift uncertainty by assuming that the probability associated with the χ^2 residuals are approximately Gaussian, and estimates the width of the Gaussian by fitting a quadratic to the two points bracketing the highest likelihood point in marginalized (over type) χ^2 space. This simple method fails to reflect the true probability distribution for distributions that differ significantly from a Gaussian, often underpredicting the redshift uncertainty. The assumption of Gaussianity also leads to unreliable estimates for probability distributions with double peaked likelihoods, or significant non-Gaussian tails. This is a known problem, as the documentation on the SDSS Photoz website states: ”The quality, zerr [photoz uncertainty], and terr [type uncertainty] values are just estimates, they are not always reliable”(`http://cas.sdss.org/dr6/en/help/docs/algorithm.asp?key=photoz`). To improve this error estimate, we model the marginalized redshift probability distribution as the sum of two Gaussians over the *entire* redshift range, rather than only in the vicinity of the peak likelihood. Figure 2.32 shows examples of the photoz++ probability distribution as a function of redshift for four sample galaxies. The probability, marginalized over galaxy type, is shown in black, and the redshift uncertainty estimated by photoz++ is shown in red. The two green curves show the Gaussians fit by to the probability distribution, and their sum is shown in magenta. These examples clearly show the improvement of this new method in capturing the true probability distribution over the original method. If the uncertainties reported by the simple Gaussian fit are used, our estimator does not accurately recover the luminosity function for subsets of the photometric redshift data used for testing, the full probability distribution is necessary. Thus, this two Gaussian fit will be used to categorize the photoz uncertainties in all of the following work with the Stripe 82 data.

To eliminate galaxies where saturation becomes an issue, we limit the catalog to objects with $r \geq 15.0$. As photometric redshift errors increase with lower signal to noise data (i.e. fainter galaxies), we trim the input data to only include objects with $r \leq 21.0$ (after dereddening). We then run photoz++ on all remaining objects classified as galaxies.

Figure 2.33 shows a plot of the photometric redshift versus the spectroscopic redshift for the subset of approximately 23000 Stripe 82 galaxies for which spectra have been obtained. Table 2.2.3 lists the parameters describing the photoz versus specz data. An iterative $3\,\sigma$ sigma clip is employed to define “catastrophic outliers”, which are excluded in the determination of the parameters. Computed for the entire sample, as well as redshift sub-intervals are: the average redshift difference $< \Delta\, z > = pz - sz$, σ_z, the standard deviation of $< \Delta\, z >$, and the percentage of catastrophic outliers. For $0.1 \leq z \leq 0.3$ the scatter in $\Delta\, z$ is approximately Gaussian with a width $\sigma = 0.037$, though caution should be urged in interpreting this width, as nearly all of the galaxies with spectroscopic redshifts are from the SDSS main galaxy sample with $r \leq 17.7$. This subset of bright galaxies will have higher signal to noise, and therefore smaller photometric redshift uncertainties than the overall sample. There is obvious structure visible in Figure 2.33, including areas where a systematic shift from the specz = photoz line, and redshifts where there is a deficient number of galaxies, most notably near $z \approx 0.3 - 0.35$. This is most likely due to a small gap between the response curves of the SDSS g and r-band filters. Figure 2.34 shows the filter response curves of the five SDSS bands with an elliptical galaxy spectrum at two redshifts overlaid. At $z = 0$ the $4000\mathring{A}$ break, the major broad band discriminator for most SDSS photozs, falls within the g-band. However, the red spectrum shows the elliptical galaxy template shifted to $z = 0.33$, and the $4000\mathring{A}$ break now falls near $\lambda = 5300\mathring{A}$. The Figure shows that there is a gap in the filter bandpasses where neither g nor r-band has signficant response. This means that for redshifts near $z \approx 0.3$ photometric redshift predictions can be either "fuzzy", with much larger errors, or prone to catastrophic failure, due to the lack of specific information on the location of the $4000\mathring{A}$ break. Figure 2.35 shows the histogram of all photometric redshifts for galaxies with $r \leq 21.0$ in SDSS Stripe 82. The deficiency of galaxies at $z \sim 0.3$ is obvious, with the number of galaxies nearly half of what is expected given a reasonable dN/dz. An over-abundance of galaxies at $z \sim 0.45$ is also quite obvious. The red and magenta curves show the result of summing the probability distribution fits (two Gaussian in red and original one Gaussian quadratic in magenta) for the galaxies, equivalent to replacing the delta function photoz in the histogram with a Gaussian (or two). While the overall redshift distribution is much closer to expected, over and under abundances are still obvious. Use of Bayesian priors, specifically luminosity function and dN/dz priors would greatly improve the output redshift distribution. This will be discussed in the Future Work section. For this thesis, we will limit ourselves to $z \leq 0.3$ in order to avoid the problematic redshift range. However, there is also a noticeable deficit of galaxies near $z = 0.25$ that is worrisome.

As mentioned in Section 2.2.2, our maximum likeilihood estimator breaks down when any sizeable (i.e. more than a few percent) of the galaxies have photometric redshift uncertainties of more than $\sigma_z/z \sim 1$. Figure 2.36 shows histograms of the photoz++ (estimated Gaussian) $1\,\sigma$ widths of the photoz uncertainties for the $0.1 \leq z < 0.2$ dataset in bins of apparent magnitude; blue represents $18.5 \leq r < 19.5$, black shows $19.5 \leq r < 20.5$, and red $20.5 \leq r < 21.0$. The $r < 19.5$ galaxies can be fit by a Gaussian of width $\sigma = 0.037$, the

$19.5 \leq r < 20.5$ have a width $\sigma \sim 0.05$ with a tail to higher values, and $20.5 \leq r < 21.0$ has more than 10% of galaxies with $\sigma > 0.1$, with an obvious excess of galaxies with higher uncertainties, most likely due to the lower signal to noise of the fainter photometry. Therefore, we will trim the dataset to include $15 \leq r \leq 20.5$ for $0.1 \leq z < 0.2$ and $0.2 \leq z < 0.3$ datasets. Results for these datasets are presented in Section 2.3.

These datasets will then be further divided by galaxy type. While photoz++ supplies a ”continuous” type parameter, we will group the galaxies into four bins, with roughly equal number of galaxies per bin. This will make for easier comparison with past examinations of galaxy type in the literature. Results for the type dependent luminosity function are discussed in Section 2.4. Future use of the full type distribution will be discussed in Section 4.3.1.

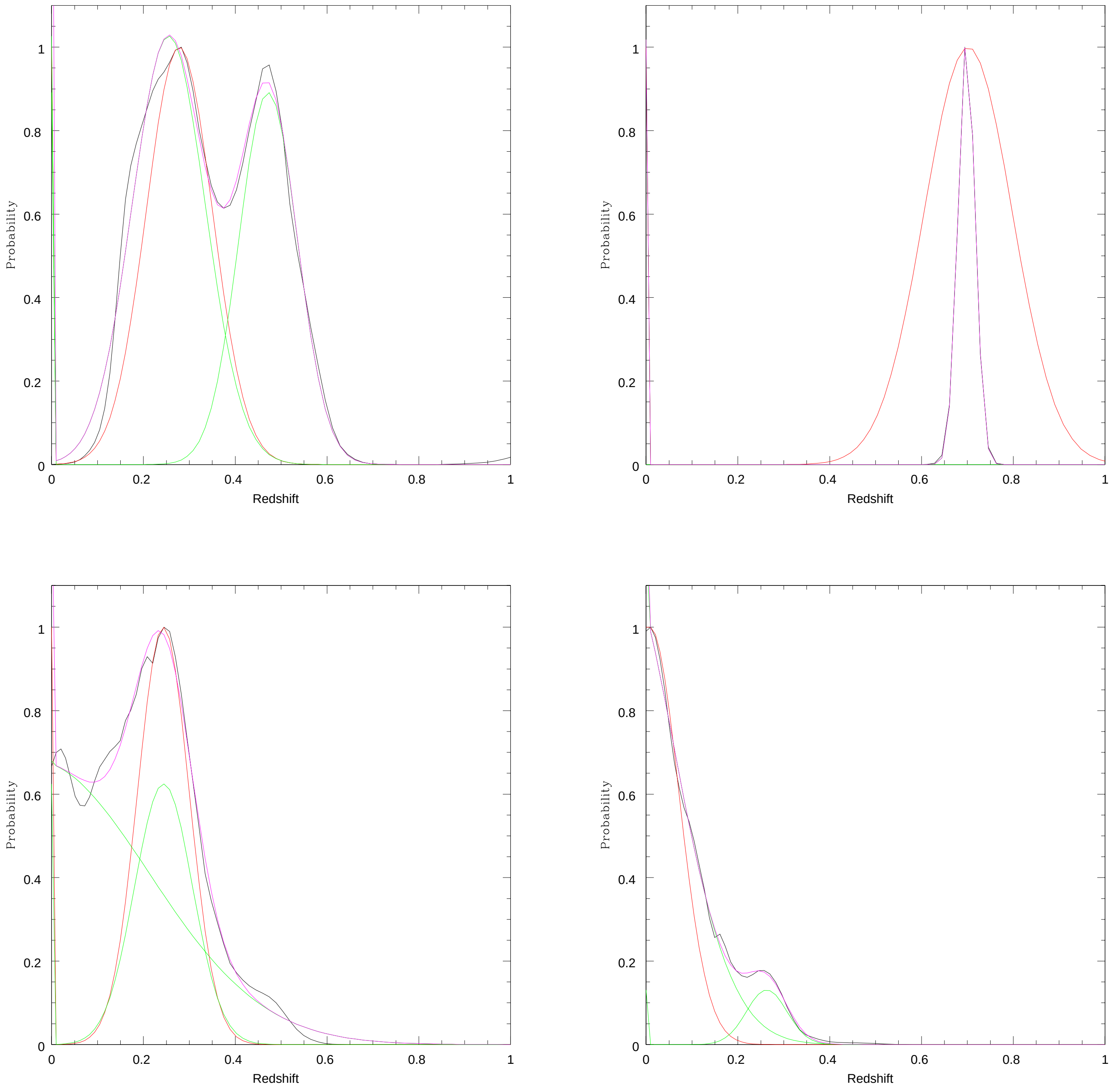

Figure 2.32 Marginalized (over type) probability (black curve) vs. redshift for four galaxies. The red curve represents the error estimate reported by the photoz code. The green curves represent the single Gaussian fits, and magenta the sum of the two Gaussians.

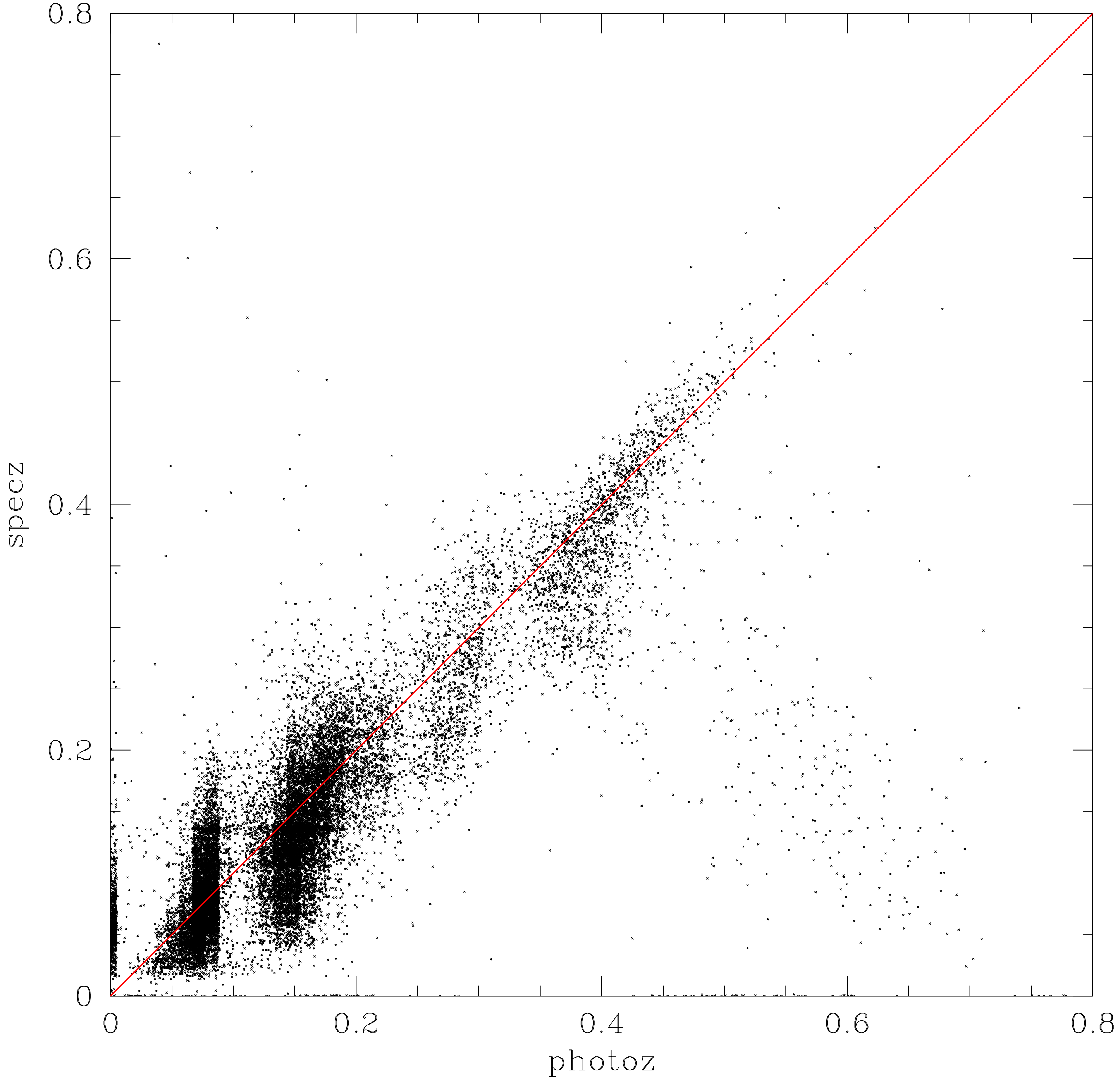

Figure 2.33 Spectroscopic redshifts vs. photometric redshifts for the ≈23000 objects in SDSS Stripe 82 with confirmed redshifts. The red line indicates Specz = Photoz.

Table 2.2 Characteristics of the specz versus photoz fits

Schechter LF Fits				
z range	# Galaxies	$< \Delta z >$	σ_z	% catastrophic
$0.0 \leq z \leq 1.0$	23433	+0.0085	0.0399	2.1
$0.0 \leq z \leq 0.2$	18988	+0.0103	0.0379	2.1
$0.2 \leq z \leq 0.4$	3785	+0.0013	0.0519	3.6
$0.4 \leq z \leq 0.6$	648	-0.0067	0.0197	8.2
$0.6 \leq z \leq 0.8$	11	-0.289	0.359	0.0

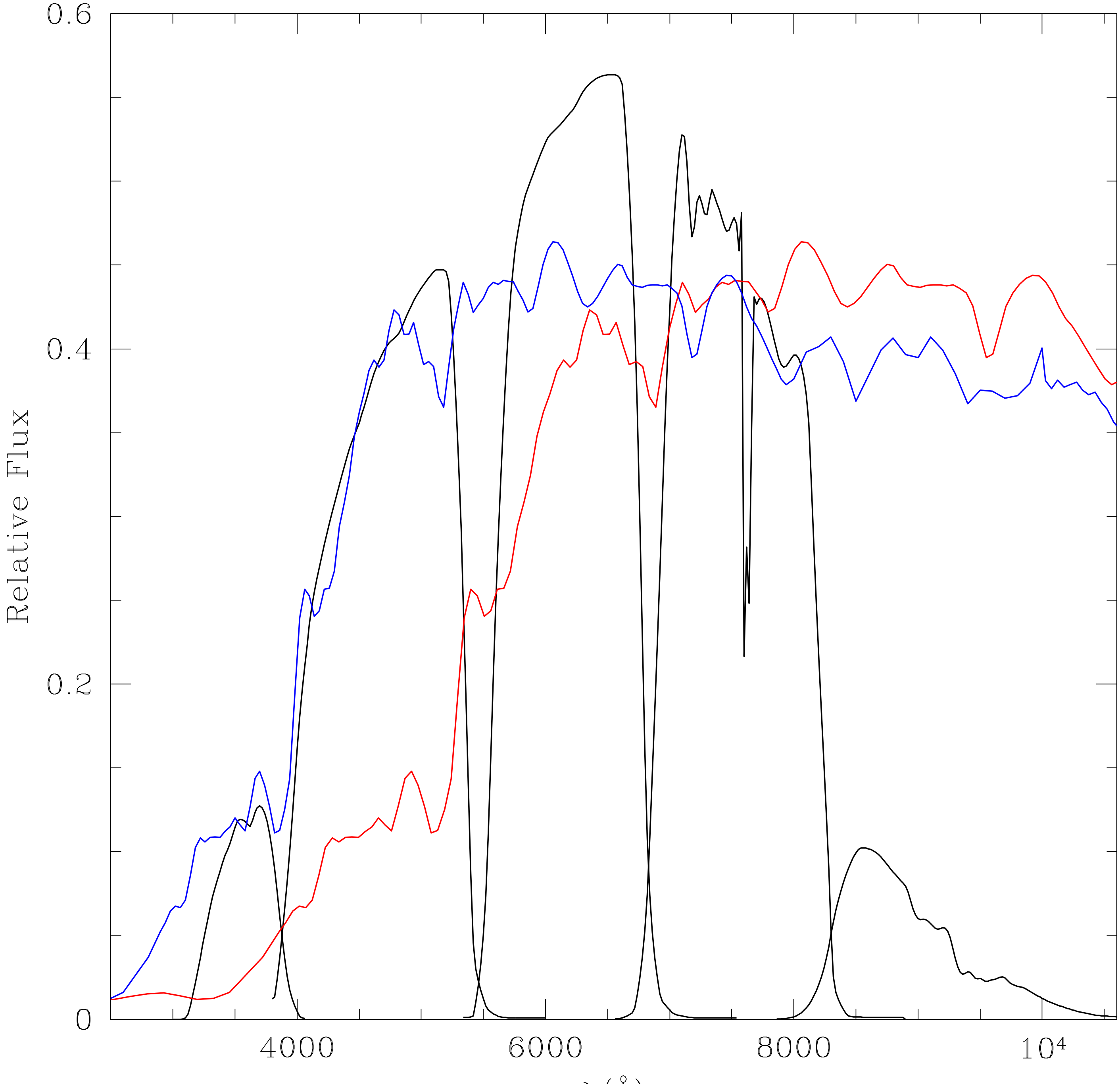

Figure 2.34 Plot of the five SDSS filter response curves (u, g, r, i, z left to right) as a function of wavelength. Overlaid is the elliptical galaxy spectrum of Coleman et al. (1980) at redshift $z = 0$ (blue) and $z = 0.33$ (red), showing that the $4000\mathring{A}$ break falls into the gap between g-band and r-band at $z \sim 0.3$.

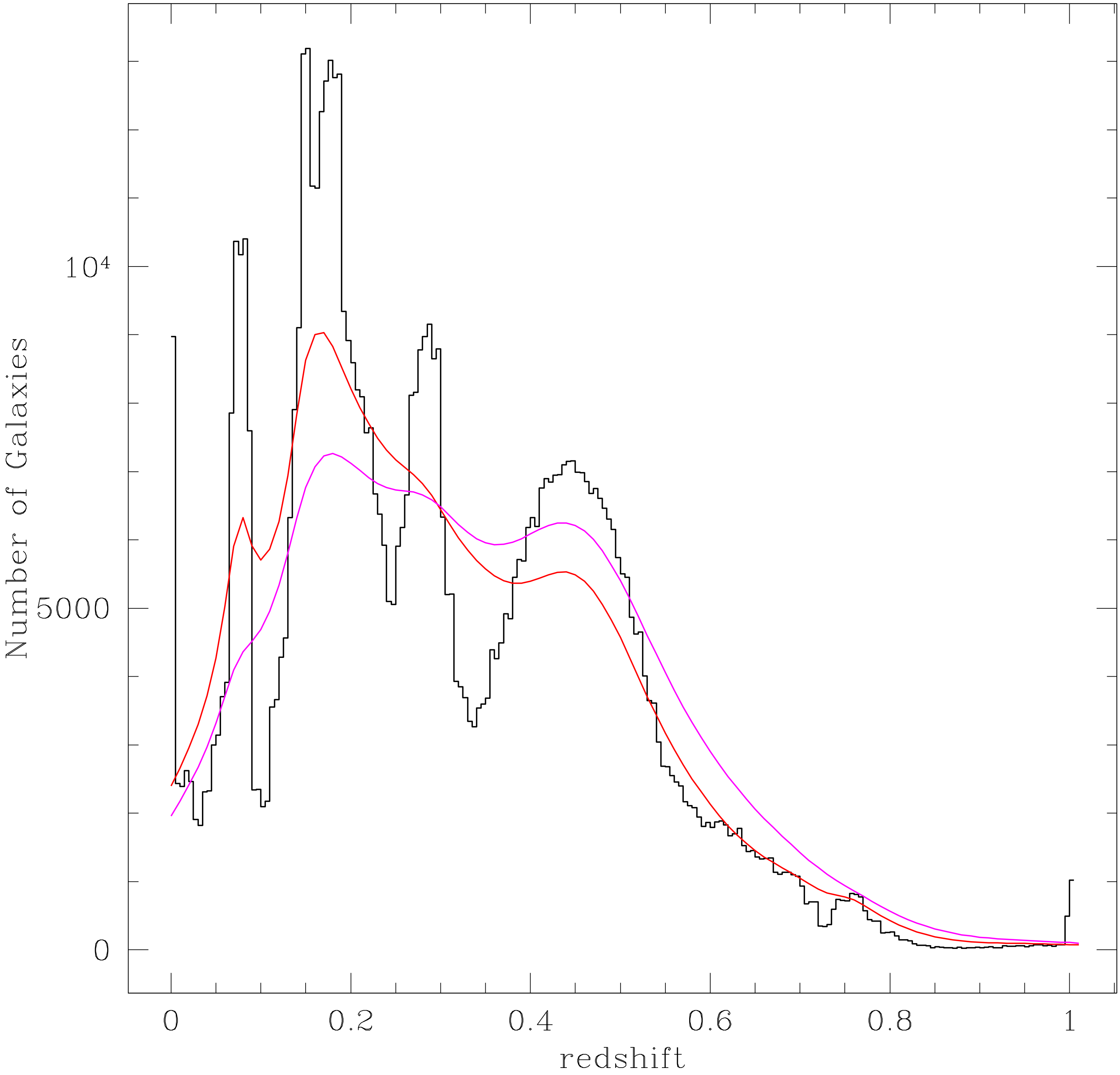

Figure 2.35 Histogram of all stripe 82 photometric redshifts for galaxies with $r \leq 21.0$. Shown in red is the sum of the two Gaussian probability distributions, in magenta the sum of the original single Gaussian probability distributions.

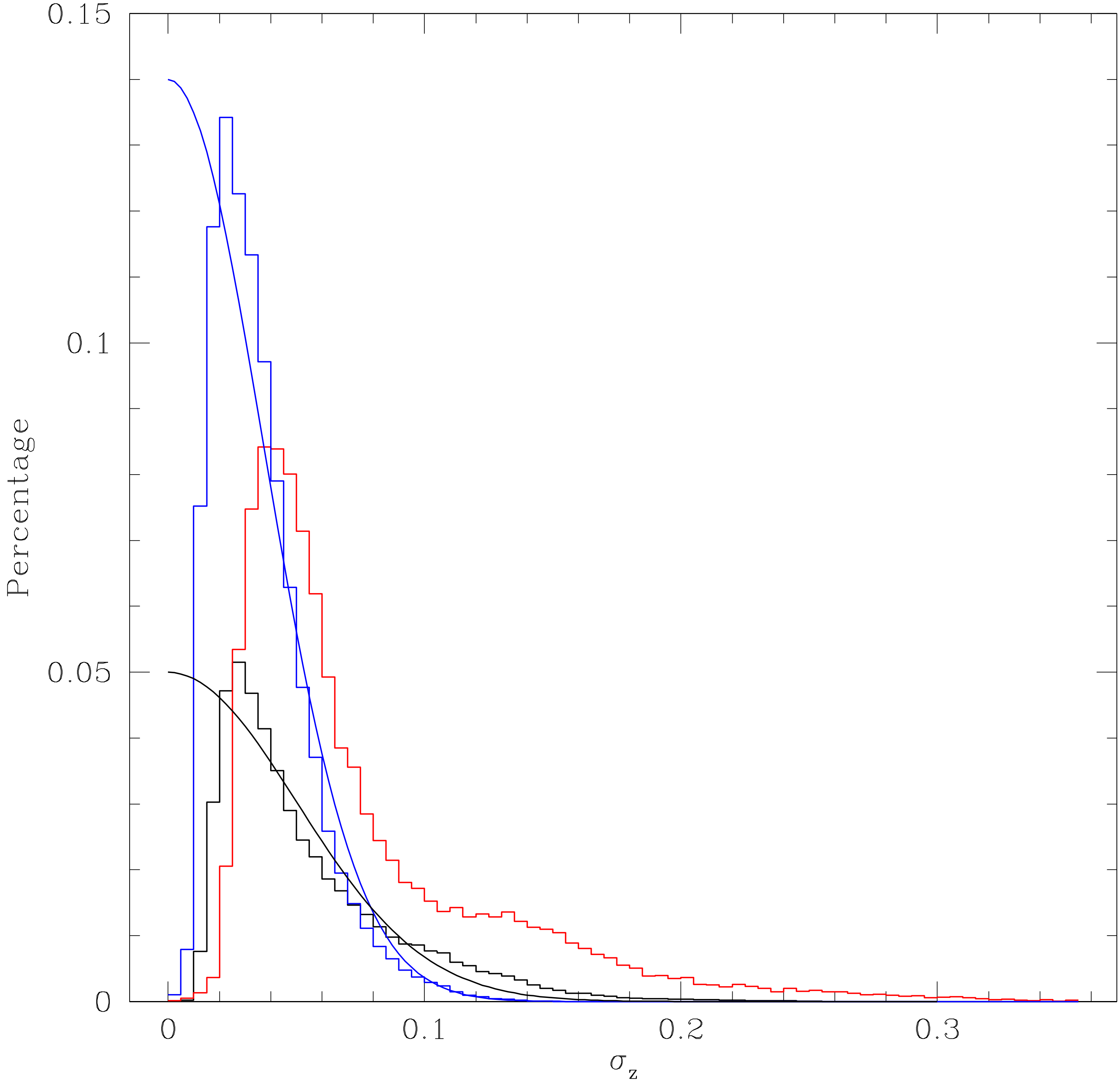

Figure 2.36 Histograms of (assumed Gaussian) photometric redshift uncertainties for the $0.1 \leq z < 0.2$ dataset. Blue represents $18.5 \leq r < 19.5$ galaxies, black $19.5 \leq r < 20.5$ and red $20.5 \leq r < 21.0$

Table 2.3 Schechter Function Fits to SDSS Stripe 82

Schechter LF Fits							
z range	# Galaxies	$M*_{STY}$	α_{STY}	$\phi*_{STY}$ (Mpc^{-3})	$M*_{cor}$	α_{cor}	$\phi*_{cor}(Mpc^{-3})$
$0.1 \le z \le 0.2$	138762	-22.218±0.0046	-1.423±0.00362	0.00272±0.000126	-21.753±0.0131	-1.097±0.0065	0.00575±0.00056
$0.2 \le z \le 0.3$	104398	-22.531±0.0055	-1.606±0.00342	0.00101±0.000162	-22.384±0.0177	-1.463±0.0121	0.00163±0.000293

2.3 THE GLOBAL GALAXY LUMINOSITY FUNCTION

The final dataset of all galaxies with $0.1 \le z \le 0.2$ and $15.0 \le r < 20.5$ contains 138762 galaxies, while the $0.2 \le z \le 0.3$ dataset with the same magnitude cuts contains 104398 galaxies. The results of the Schechter function fits for both the original STY estimator, as well as our modified estimator are presented in Table 2.3. All results use a value of the Hubble Constant of $h = 0.7$. To transform to $h = 1$ often used in the literature, simply subtract $5 \log h = -0.7745$ from $M*$ and divide $\phi*$ by $h^3 = 0.343$. All luminosity functions are for the SDSS r-band.

Figure 2.37 shows the STY Schechter function and SWML fits to the $0.1 \le z \le 0.2$ dataset. Shown for comparison is the spectroscopic SDSS r-band luminosity function discussed in Section 2.2.1. Once again the characteristic brighter $M*$, steeper α, and lower $\phi*$ are seen. There is also an excess of galaxies at the very faint end of the LF at $-18 \ge M_r \ge -19$. These are most likely galaxies with systematically misidentified redshifts that contaminate the sample. Further study of such systematics is needed, and will be discussed in Section 4.3. Figure 2.38 shows the maximum likelihood fit for our modified estimator, which is in excellent agreement with the spectroscopic luminosity function.

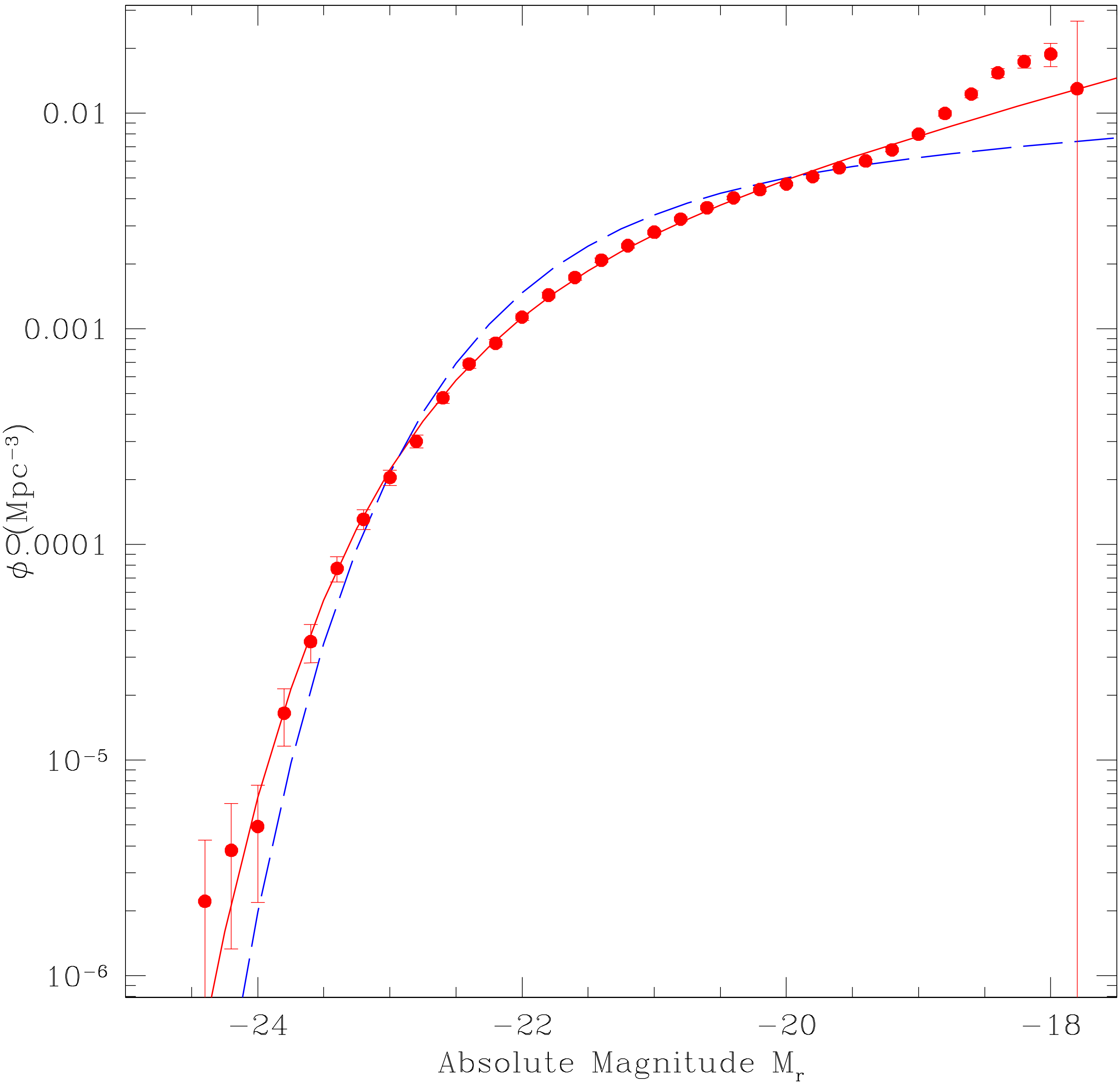

Figure 2.37 STY Schechter function and SWML fits to the $0.1 \leq z \leq 0.2$ data (red). Shown as a blue dashed curve for comparison is the spectroscopic luminosity function derived in Section 2.2.1.

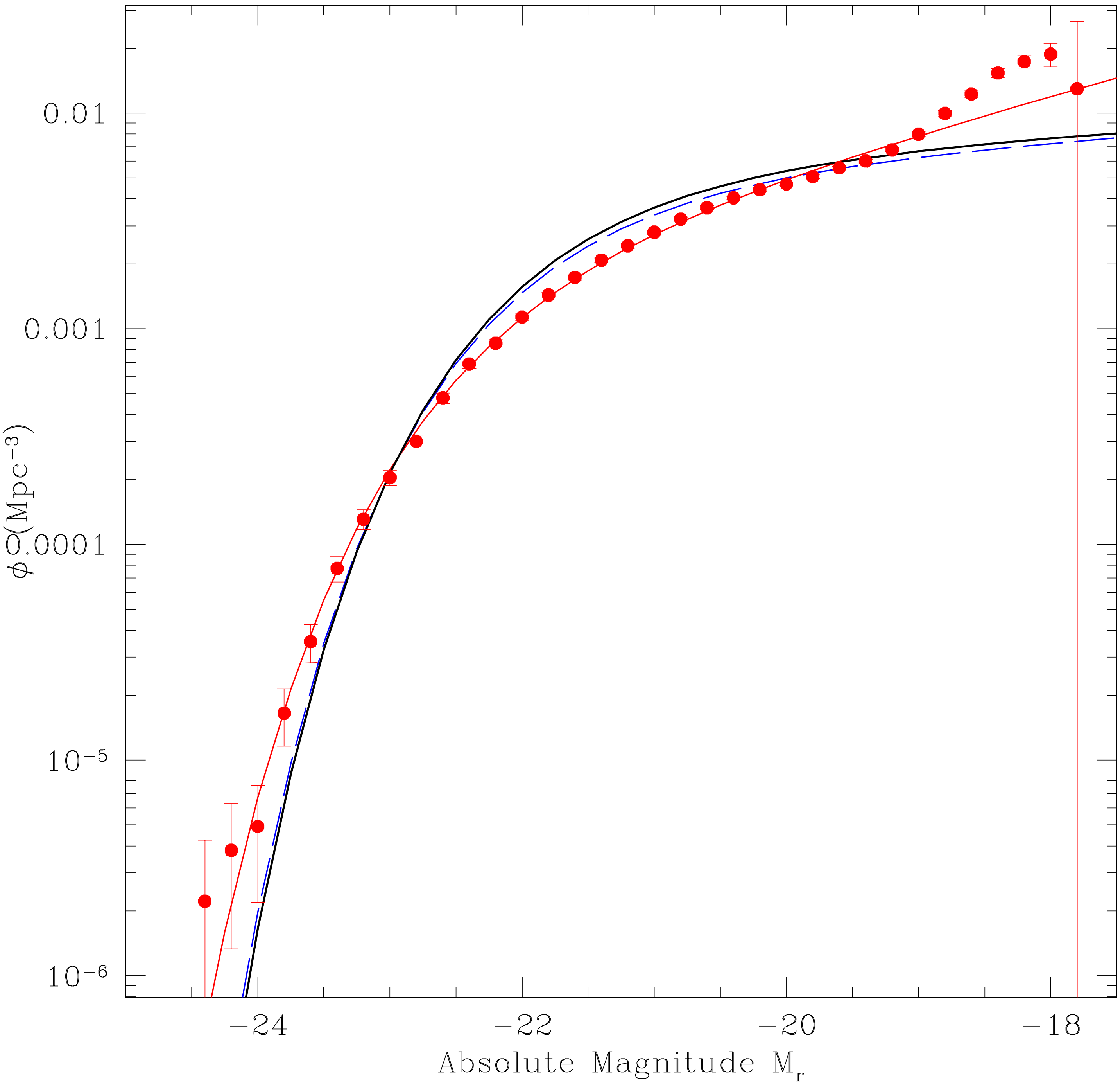

Figure 2.38 Same as Figure 2.37, but also showing the maximum likelihood Schechter function fit from our new estimator (black).

Figure 2.39 shows the 1/Vmax, STY Schechter, and SWML fits to the $0.2 \leq z \leq 0.3$ data, and the low redshift spectroscopic Schechter LF for comparison. Once again, there is an excess of galaxies over even the steep α at the very faintest absolute magnitudes. Figure 2.40 shows the Schechter fit for our modified estimator. There is very little change from the methods with no accounting for photoz errors and our modified estimator. In order to test this result at the bright end, we use the SDSS DR6 (`http://www.sdss.org/dr6/`) spectroscopic main galaxy sample to compute the SWML estimate of the luminosity function for $0.2 \leq z \leq 0.3$ for model magnitudes in the range $15.0 \leq r < 17.6$. Our estimate of the luminosity function is in excellent agreement with the DR6 result over the range of absolute magnitudes covered by the DR6 data. It should be noted that we use the SWML estimator because the lack of faint data leaves the value of α very uncertain in the Schechter parameterization. Figure 2.41 shows our fit compared to that reported for $0.2 \leq z \leq 0.4$ for the SDSS r-band by the COMBO-17 survey (Wolf et al., 2003). COMBO-17 is a medium band photometric redshift survey covering approximately one square degree. By adding a set of medium band filters to the typically used broad band filters, COMBO-17 in essence gets a crude spectrum based on 17 "pixels" rather than the five available with SDSS. They are able to construct a photometric redshift catalog with well controlled systematics and a relatively small photometric redshift uncertainty ($\sigma_z = 0.03$). Our much larger areal coverage allows us to better probe the bright end of the luminosity function compared to COMBO-17, where the very small area (0.78 square degrees) limits the number of rare very bright galaxies in the sample. As the figure shows, the COMBO-17 LF has a slightly brighter $M*$ and slightly lower density than seen in both our photometric redshift LF and the DR6 spectroscopic LF. The fact that COMBO-17 uses photometric redshifts with $\sigma_z \approx 0.03$ means that some portion of this difference may be due to the effect of photoz uncertainties already discussed, though the most obvious difference is in the redshift ranges covered by the two datasets. The luminosity function evolution towards brighter galaxies and lower densities in the past is very similar to the errors introduced by photoz uncertainties, and these two effects are hard to distinguish without a more careful comparison of the data. Qualitatively the LF is very close to that of COMBO-17, and whether the difference is due to the redshift binning or the lack of accounting for photoz errors in the COMBO-17 data, what is evident is a large change in the luminosity function from $0.1 \leq z \leq 0.2$ to $0.2 \leq z \leq 0.3$. $M*$ increases by more than half a magnitude, α becomes much steeper, and $\phi*$ decreases by nearly a factor of three. This rapid evolution is also noted in Loveday (2004). It is clear the the luminosity function has undergone substantial evolution since at least $z = 0.3$.

Figure 2.42 shows the maximum likelihood BSpline curve to the data. While the bright end of the LF is consistent with the Schechter function and the spectroscopic LF, there is an obvious problem with the very large dip at the faint end. This is most likely due to systematic problems with low signal to noise galaxies with the faintest apparent magnitudes, and is very similar to the effect of overcorrection of the faint end described in Section 2.2.2 when redshift errors become large. It could also result from the redshift error reported by photoz++ not reflecting the true error distribution for a certain number of the faint galaxies. Because the BSpline fit has many more free parameters, in this case 24 BSplines, as opposed to only two, $M*$ and α for the Schechter function fit, the BSplines are much more sensitive to such systematic effects. The poor fit of the spline function tells us that, even after the conservative cuts made above, there is still some residual problems with this dataset. Better photometric redshifts and errors are needed before the full power of our new estimator can be employed. This will be discussed in Section 4.3.1.

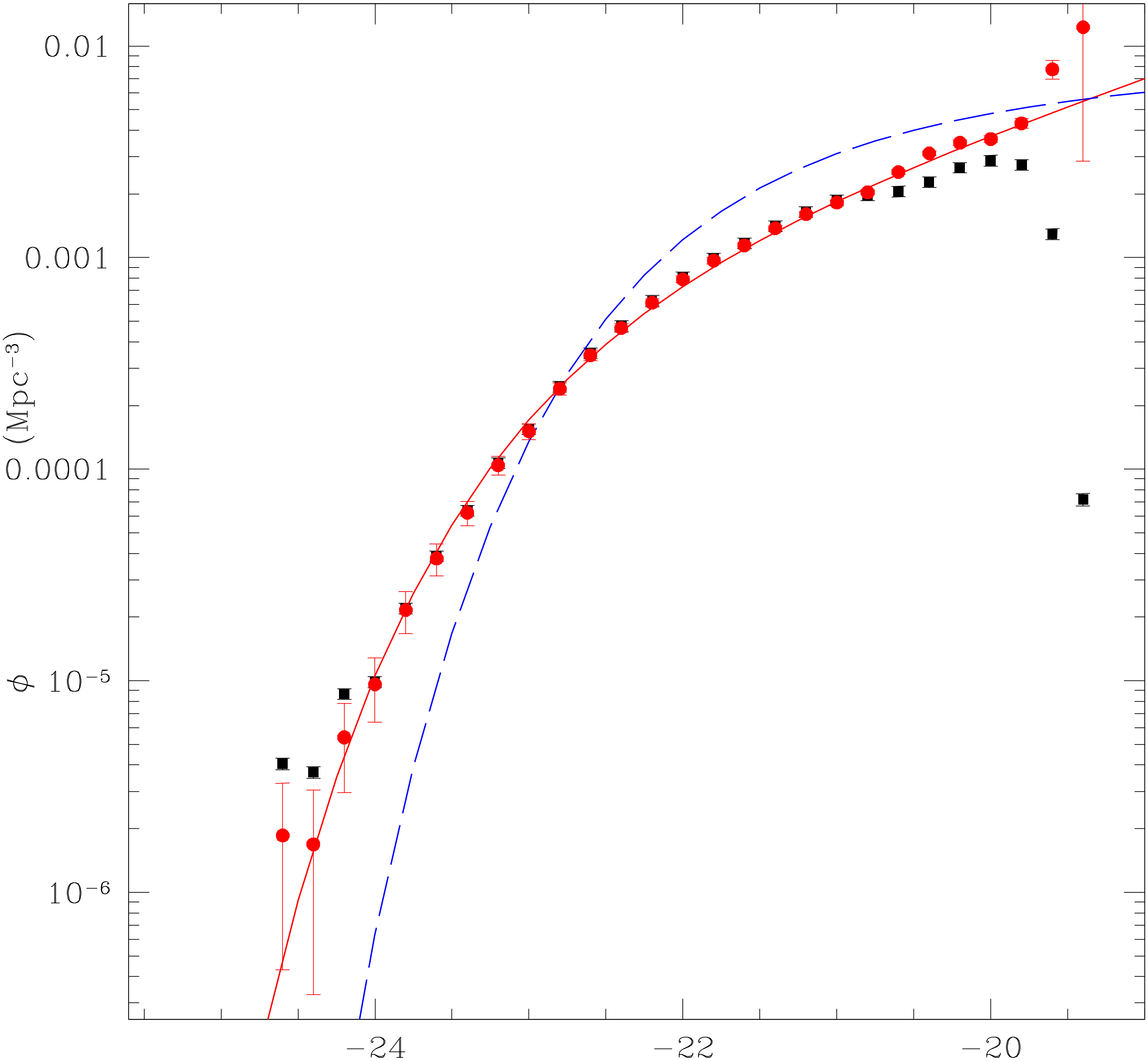

Figure 2.39 1/Vmax (black), STY Schechter function and SWML (red) fits to the $0.2 \leq z \leq 0.3$ data. The blue dashed curve for indicates the $0.1 \leq z \leq 0.2$ spectroscopic luminosity function derived in Section 2.2.1.

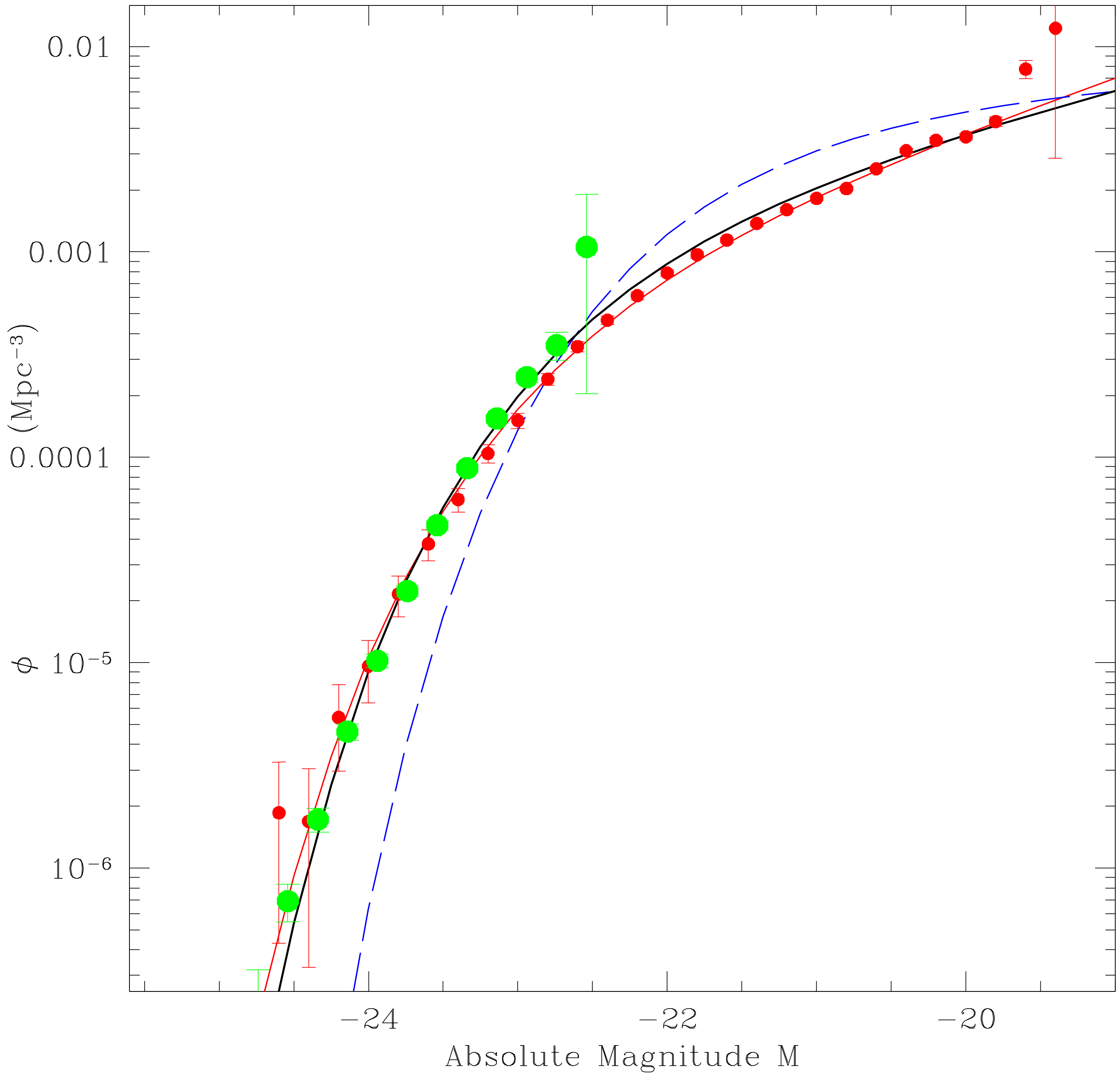

Figure 2.40 Schechter function fit for our modified estimator (thick black) for the 0.2 $\leq z \leq$ 0.3 dataset, as well as the STY Schechter function and SWML (red) fits to the data. The blue dashed curve for indicates the 0.1 $\leq z \leq$ 0.2 spectroscopic luminosity function derived in Section 2.2.1. The green circles represent the SWML LF determined from the SDSS DR6 spectroscopic sample.

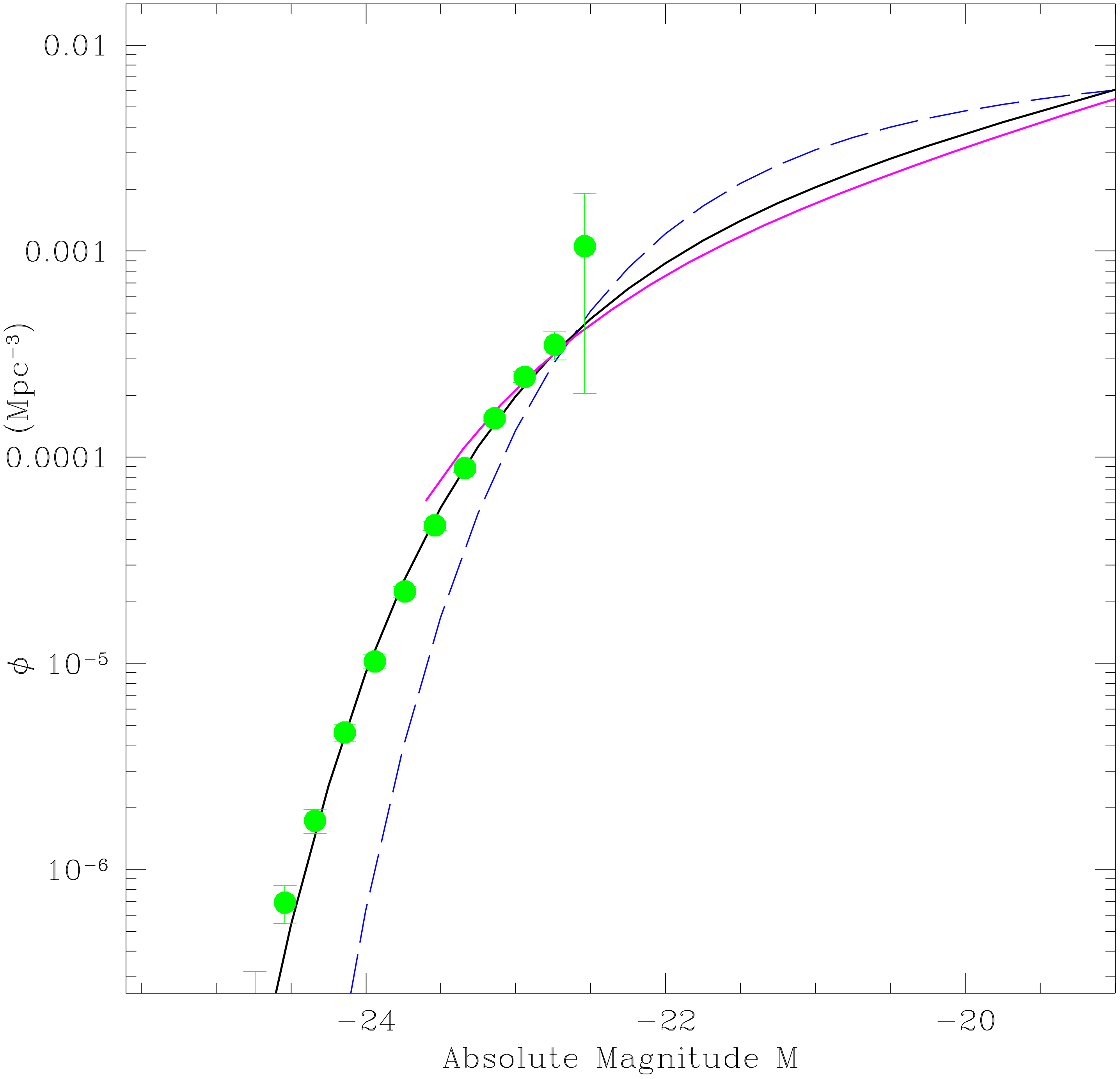

Figure 2.41 The COMBO-17 LF for $0.2 \leq z \leq 0.4$ (magenta) compared to the Schechter function fit for our modified estimator (thick black) for the $0.2 \leq z \leq 0.3$ dataset. The blue dashed curve for indicates the $0.1 \leq z \leq 0.2$ spectroscopic luminosity function derived in Section 2.2.1. The green circles represent the SWML LF determined from the SDSS DR6 spectroscopic sample.

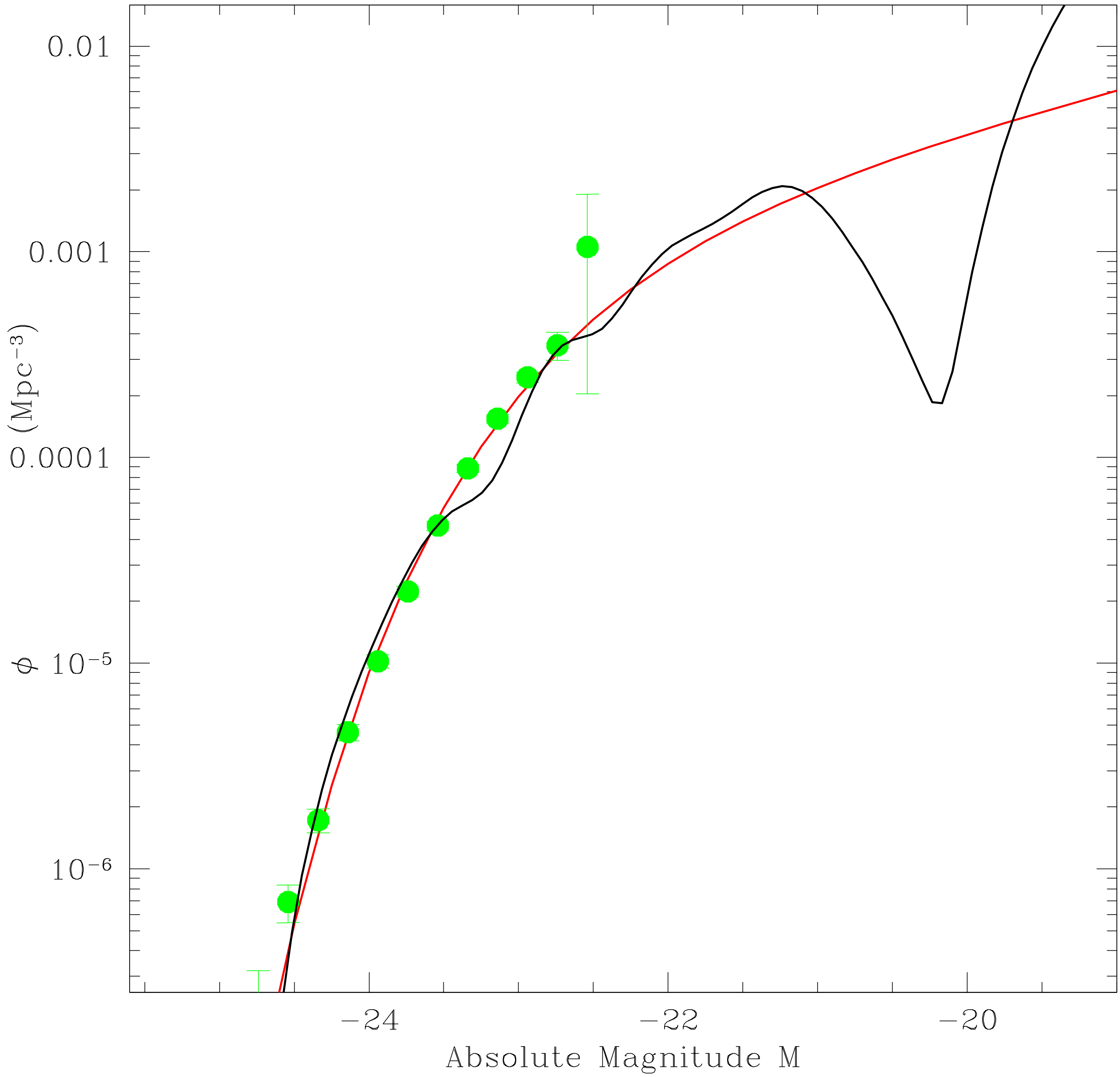

Figure 2.42 The BSpline LF for $0.2 \leq z \leq 0.3$ (black) compared to the Schechter function fit for our modified estimator (red). Green circles represent the SWML LF determined from the SDSS DR6 spectroscopic sample.

2.4 LUMINOSITY FUNCTIONS BY TYPE

As mentioned in the previous Section, template based photometric redshifts naturally give a prediction of each galaxy's type in the course of the χ^2 minimization procedure: the template with the best χ^2 value is also the most likely type for the galaxy. The galaxies are fit to the ten templates shown in Figure 2.31 and five spectra interpolated between each of those ten, as well as extrapolated redward from the reddest template, for a total of 71 templates. Photoz++ assigns a "continuous" type parameter between -0.1 and 1.0 based on these 71 templates, where 0 represents the reddest/earliest template, and 1.0 represents the bluest/latest, and the extrapolated redder spectra have a negative type. This procedure is similar to that followed for the SDSS template based photometric redshifts (Csabai et al., 2003), which uses a related version of the same photoz code used in this work. Figure 2.43 shows the histogram of galaxy types returned by photoz++ for galaxies with $0.1 \leq z \leq 0.2$. This distribution looks very different than the expected bimodal early/late distribution that we expect, for instance, the distribution shown in Budavári et al. (2003), which uses SDSS database photozs to study angular clustering. The distribution in Budavári et al. (2003) shows a narrow peak at type $t = 0.05$ and a broad peak at $t \sim 0.9$, and very few galaxies with $t \sim 0.3$ (see their Figure 3 for details). The major difference between our type distribution and the expected distribution is a major concern. Newer versions of the photoz++ code, which include a luminosity function prior, as well as a prescription for "tweaking" the input templates for improved photozs (see Csabai et al. (2003) for details) do not show problems with the type distribution, and future processing of the data will greatly benefit from the newer versions of the code. For the present analysis, we will simply break the data into quartiles, with roughly equal numbers of galaxies in each of the four bins. The divisions used to define the bins are shown as red lines in Figure 2.44. Table 2.4 lists the type ranges for the four bins, and the STY and corrected Schechter function values for each dataset. For $0.2 \leq z \leq 0.3$ we use the same type bins in order to check for evolution in similar galaxy types.

Broken into quartiles:

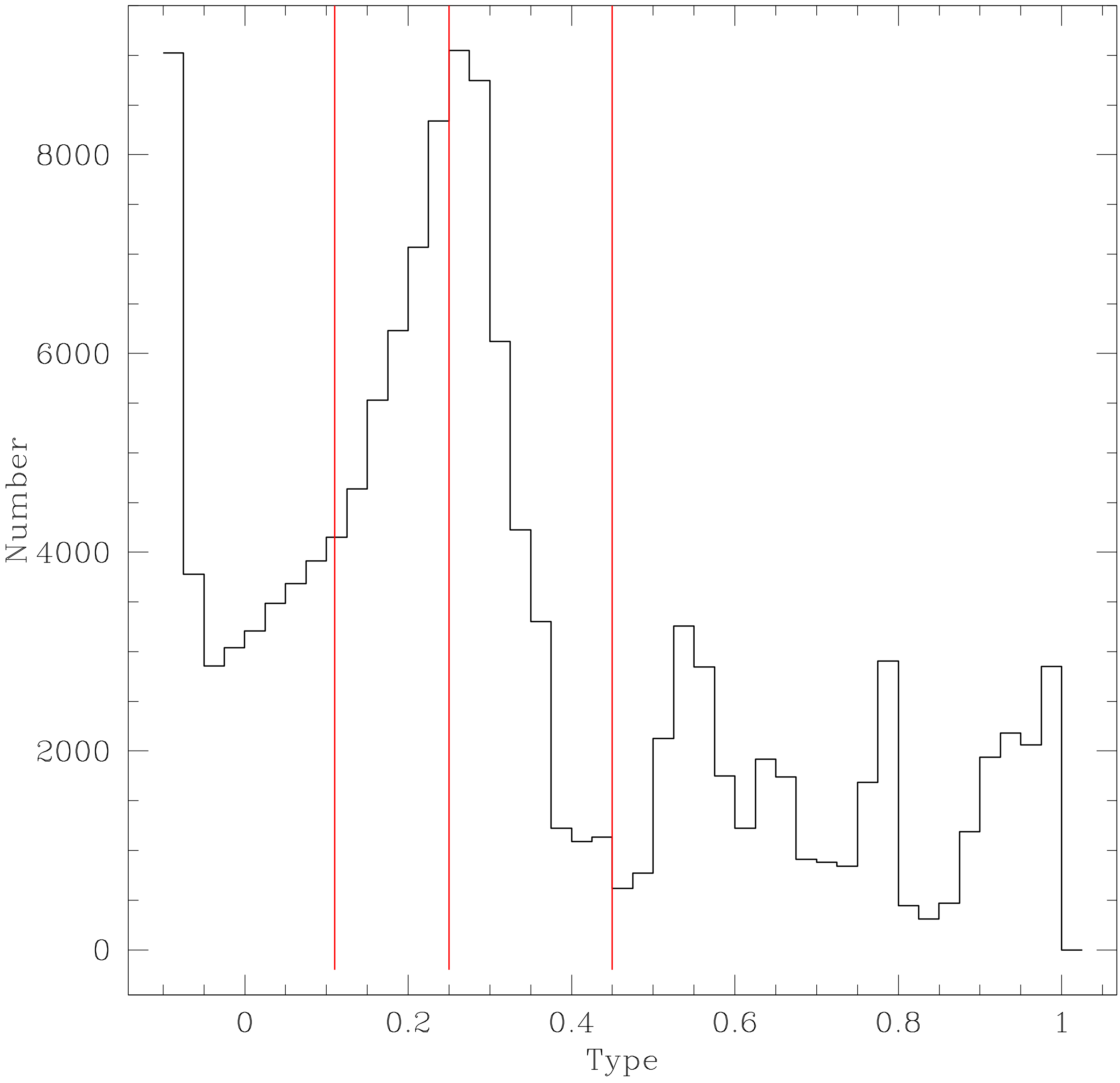

Figure 2.43 Histogram of galaxy types for $0.1 \leq z < 0.2$. The breaks used to define the four type bins are indicated by the red lines.

Table 2.4 Type Dependent Schechter Function Fits to SDSS Stripe 82

			Type Dependent Schechter LF Fits					
z Range	Type Range	# Galaxies	$M*_{STY}$	α_{STY}	$\phi*_{STY}$ (Mpc^{-3})	$M*_{cor}$	α_{cor}	$\phi*_{cor}(Mpc^{-3})$
$0.1 \leq z \leq 0.2$	$-0.1 \leq t < 0.11$	34660	-22.260±0.0090	-1.223±0.0087	0.000979±0.00010	-21.614	-0.665	0.00490
...	$0.11 \leq t < 0.25$	34279	-22.081±0.0089	-1.074±0.0099	0.001293±0.00011	-21.403	-0.451	0.00590
...	$0.25 \leq t < 0.45$	34894	-21.392±0.0091	-1.071±0.0097	0.00174±0.00014	-20.813	-0.419	0.00700
...	$0.45 \leq t < 1.0$	34929	-20.483±0.0095	-1.423±0.0072	0.00240±0.00021	-20.279	-1.132	0.00678
$0.2 \leq z \leq 0.3$	$-0.1 \leq t < 0.11$	29478	-22.231±0.0097	-1.029±0.011	0.000818±7.9e^{-5}	-21.344	+0.311	0.00311
...	$0.11 \leq t < 0.25$	32116	-21.882±0.0092	-0.788±0.012	0.00121±0.00016	-21.320	+0.1233	0.00349
...	$0.25 \leq t < 0.45$	10822	-21.442±0.016	-1.215±0.018	0.000408±6.3e^{-5}	-21.357	-1.000	0.000967
...	$0.45 \leq t < 1.0$	31839	-21.167±0.010	-1.910±0.012	0.00120±0.00014	-34.204[1]	-2.90	8.7e^{-14}

[1] The Schechter parameters for this type bin are very poorly constrained due to the extreme value of $\alpha \sim -3.0$

Figure 2.44 shows a comparison of the Schechter fits for the STY method and our modified estimator. The sum of the four individual Schechter fits is consistent with the single Schechter function fit to the entire dataset. We see that early/red galaxies dominate the bright end of the luminosity function, while late/blue galaxies dominate the faint end, in qualitative agreement with nearly all past results (Folkes et al., 1999; Lin et al., 1999; Blanton et al., 2001; Wolf et al., 2003; Croton et al., 2005, e.g.). Figure 2.45 shows the histogram of galaxy types for $0.2 \leq z \leq 0.3$ with the same bins for the lower redshift dataset. The distribution is very similar, but the peak at $t \approx 0.25$ has shifted to $t \approx 0.15 - 0.20$, and there are many fewer galaxies in the third quartile of the type distribution. Figure 2.46 shows the four Schechter function fits for the STY and modified estimators for the $0.2 \leq z \leq 0.3$ dataset. Several features stand out. First, the sum of the four Schechter functions is quite different from the single Schechter function fit, with both a lower value for the LF at the bright end, as well as a much steeper faint end of the LF. The combination of the four Schechter functions gives the LF twelve free parameters rather than the three of the single Schechter function, allowing for this further variation in shape. Whether this shape is real or an artifact of systematic effects in the data is not clear. The shape is similar to that of the BSpline fit in Figure 2.42, though the discrepant bright end values points toward a systematic problem, as does the redshift distribution seen in Figure 2.35, with a deficit of galaxies at $z \approx 0.25$. It is likely that the single Schechter function fit, which agrees with the spectroscopic data as well as COMBO-17, is hiding some of the systematic problems with the data, as this three parameter fit does not have enough freedom to show the effects seen in the four Schechter and BSpline fits. It is also possible that photometric redshift errors are overestimated for certain galaxy types in this redshift range, a conjecture that is certainly supported by the slight difference between the STY method and the spectroscopic dataset. Once again, better photometric redshifts are needed for conclusive results. Figure 2.47 shows a comparison of the four Schechter functions by type for both $0.1 \leq z \leq 0.2$ and $0.2 \leq z \leq 0.3$. Types 1 and 2 (red and magenta) show very little change at the bright end of the LF, but drop off considerably at the faint end over these two redshift intervals. There is a dramatic drop in the number of type 3 (green) galaxies, by more than a factor of two overall, and an increase and steepening to a pure power law form for type 4, with more type 4 galaxies at both the faint and bright end. While these results are called into question by the fact that the single Schechter function, sum of four type Schechter functions, and BSpline LF all disagree, this behavior is qualitatively similar to that expected, with red galaxies evolving much more slowly, while the number of blue galaxies evolves rapidly to higher and brighter values. We will not attempt any quantitative comparisons until a better photometric redshift dataset is obtained, which we will discuss in Sections 4.1 and 4.3.1.

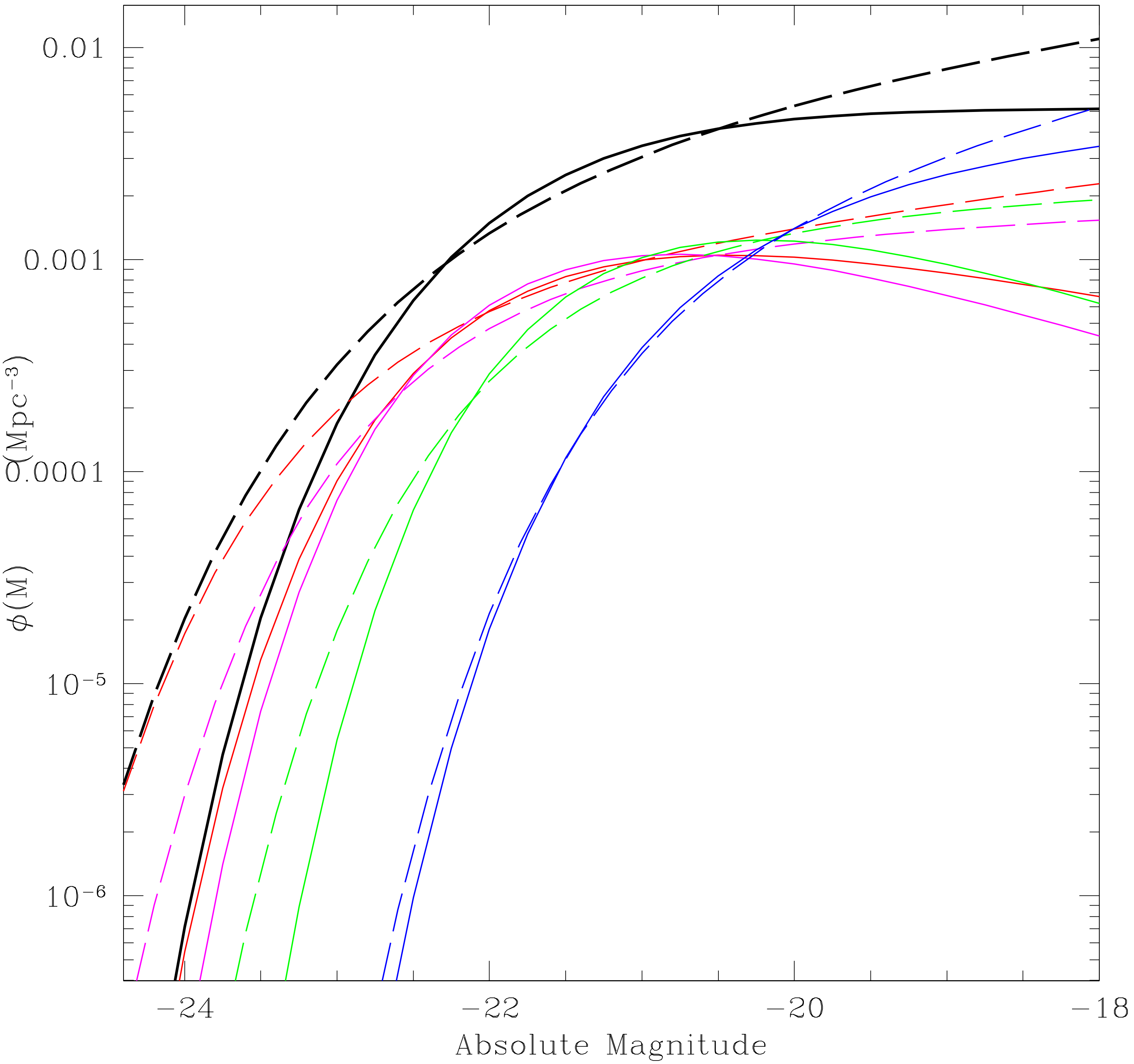

Figure 2.44 Schechter function luminosity functions for $0.1 \leq z < 0.2$ for four type bins for the STY estimator (dashed curves) and our modified maximum likelihood estimator (solid curves): Red is type 1 (early), magenta is type 2, green is type 3, and blue is type 4 (late). The black curves are the sum of the four Schechter functions. The short dashed line is the single Schechter function fit to the data for our modified estimator.

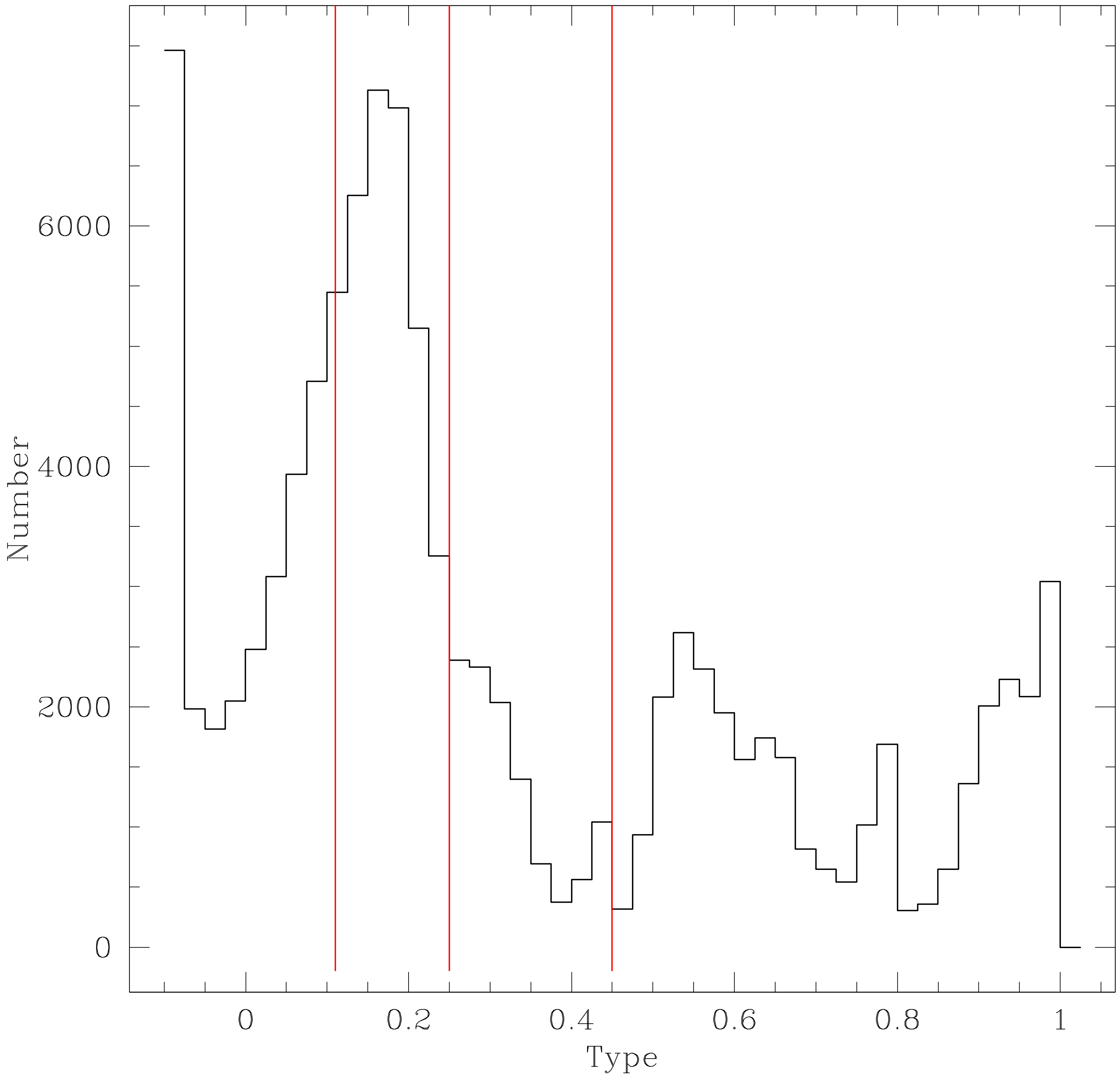

Figure 2.45 Histogram of galaxy types for $0.2 \leq z < 0.3$. The breaks used to define the four type bins are indicated by the red lines.

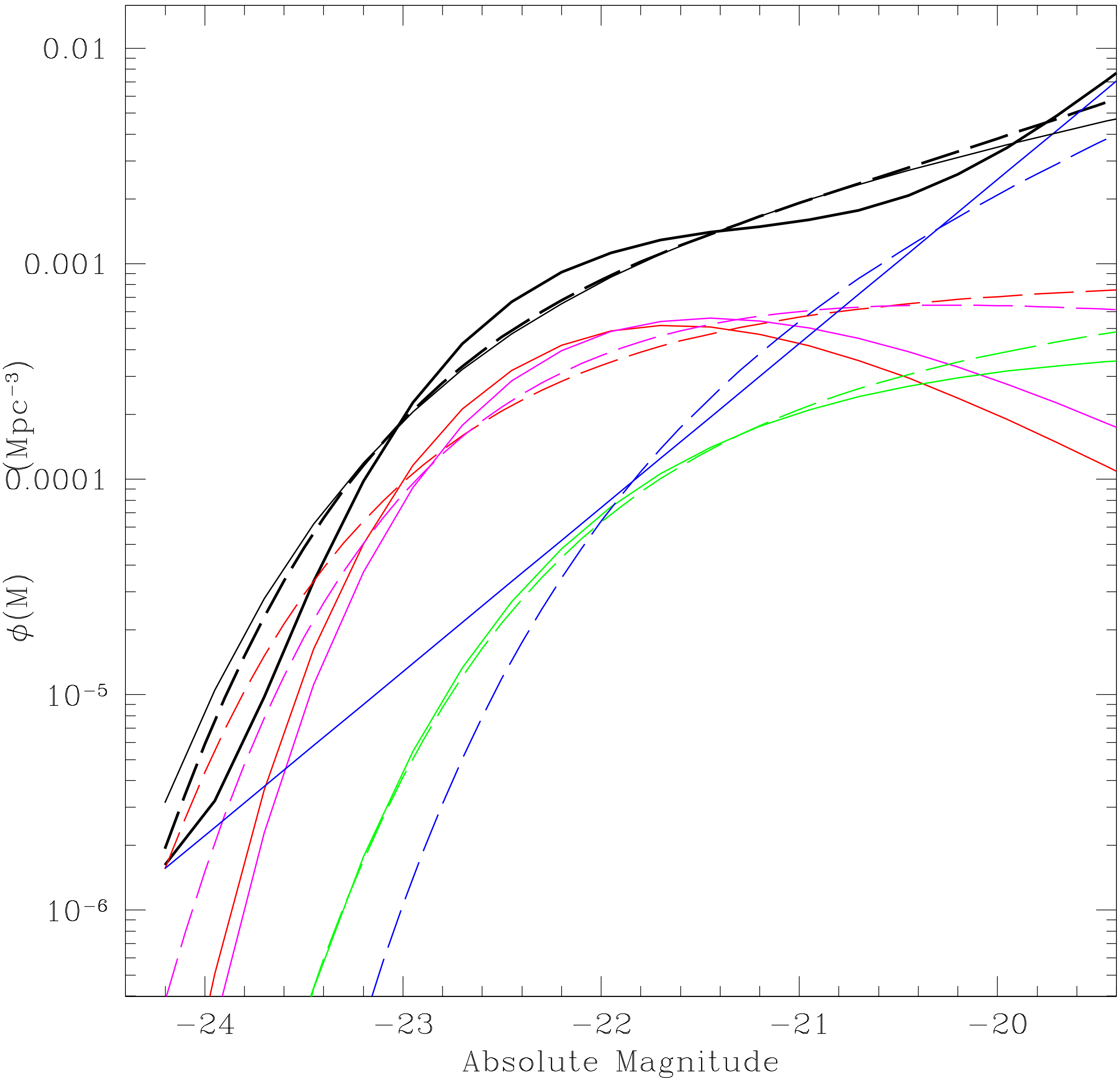

Figure 2.46 Schechter function luminosity functions for $0.2 \leq z < 0.3$ for four type bins for the STY estimator (dashed curves) and our modified maximum likelihood estimator (solid curves): Red is type 1 (early), magenta is type 2, green is type 3, and blue is type 4 (late). The black curves are the sum of the four Schechter functions. The thin black line is the single Schechter function fit to the data for our modified estimator.

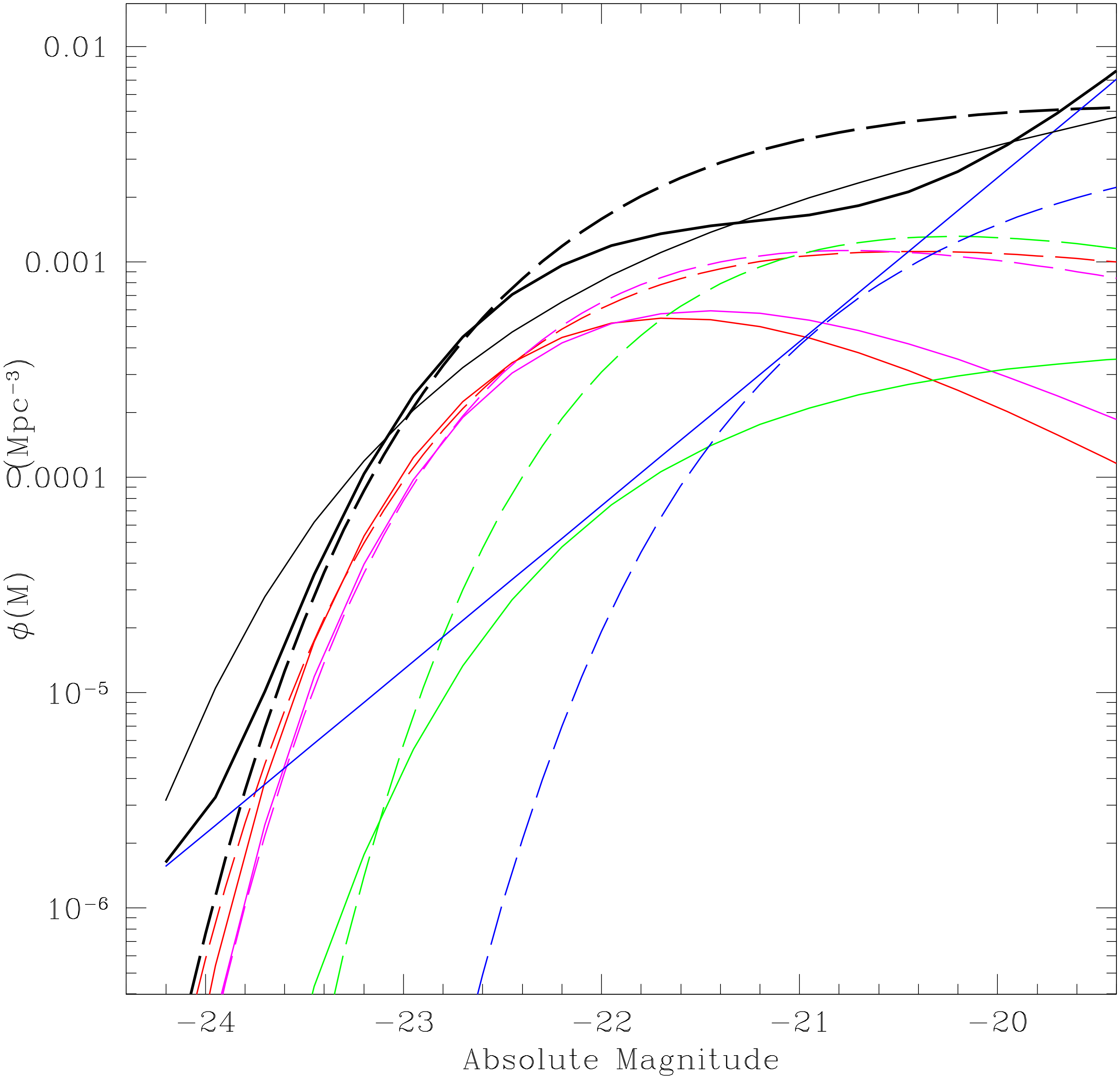

Figure 2.47 Schechter function fits for $0.1 \le z \le 0.2$ (dashed) and $0.2 \le z \le 0.3$ (solid) for type 1 (red) type 2 (magenta) type 3 (green) and type 4 (blue). Black lines represent the sum of the four Schechter functions.

3.0 THE DRAGONS SURVEY

"Beyond this point there be dragons."

-Phrase on the unexplored section of old maps

Note: Much of this chapter is taken from previously published work (Schmidt et al., 2006) detailing the DRaGONS Survey. Additional people contributed to this work, namely Andrew Hopkins ran the PEGASE models mentioned in Section 3.1 and many people helped with the actual observations at Kitt Peak and Apache Point Observatories: Andy Connolly, Andrew Hopkins, Ryan Scranton, Jeremy Brewer, Julia Bryant, Niraj Welikala, and Bhuvanesh Jain all spent some time at the telescopes.

Radio galaxies have long been used to probe the epoch of galaxy formation (Lilly and Longair, 1984; Graham and Dey, 1996; Blundell et al., 1998; Stern et al., 1999; Jarvis et al., 2001). Luminous radio galaxies are known to be highly biased relative to the underlying dark matter, residing in the most overdense regions of the Universe. Under the standard Cold Dark Matter hierarchy for galaxy formation these galaxies should be the first systems to collapse and, therefore, the site of some of the most evolved stellar populations. As the likely hosts of the earliest star formation, it may also be possible to probe the epoch of reionization (Barkana and Loeb, 2006). Isolating a sample of radio galaxies at high redshift would allow us to probe the physical processes that drive the formation and evolution of structure and the timescales that govern star formation in the early universe, as well as to distinguish between hierarchical and "down-sizing" (Cowie et al., 1996) formation scenarios (e.g., Rocca-Volmerange et al., 2004; De Lucia et al., 2006), and also the role of feedback on the local radio galaxy environment (Vardoulaki et al., 2006; De Lucia et al., 2006).

While radio surveys can address many fundamental questions in cosmology and galaxy formation the numbers of radio galaxies identified at high redshift remain small in comparison to low redshift surveys (Brand et al., 2005; Magliocchetti et al., 2004). Without large, statistically complete and homogeneously selected samples we cannot hope to constrain hierarchical galaxy formation models without the concern that sample variance might bias our analyses. For example, at redshifts $z > 3$ extensive optical and near-infrared (NIR) campaigns have yielded less than one hundred and fifty galaxies (van Breugel et al., 1998; De Breuck et al., 2001; Vardoulaki et al., 2006). The reason for the paucity of these samples comes from the necessity of surveying large volumes to identify the most massive systems. Given the broad redshift distribution of radio galaxies (e.g., Dunlop and Peacock, 1990), large numbers of radio targets must be observed in order to extract the high redshift component.

Below we describe a novel selection technique that utilizes existing optical and radio surveys to overcome these challenges in order to isolate high redshift candidates for follow up in the NIR. We show that this approach gives more than a factor of ten increase in efficiency over blind radio selected surveys. The resulting combination of NIR data with existing optical measurements from SDSS, and additional sources, allows us to study the environment of the high redshift radio galaxies.

Early in the development of infrared observations it was noted that EROs are often found in the vicinity of high redshift objects (McCarthy et al., 1992; Graham et al., 1994; Dey et al., 1995). More recently, targeted searches have been undertaken to search for clustering of galaxies (Hall et al., 2001) and extremely red objects (EROs) around high redshift quasars and radio galaxies (Cimatti et al., 2000; Wold et al., 2003; Zheng et al., 2006, and references therein). The focus of these investigations has been whether the increased surface density of EROs is physically associated with the radio galaxy or quasar, or whether it lies in the foreground, possibly as a cluster that may have gravitational lensing effects on the target. Our goal is to use detect Extremely Red Objects near the radio galaxy position in order to study their environment, and to check for the presence of foreground lensing clusters.

SDSS magnitudes have slight offsets from the AB system, and we will use 2MASS magnitudes for all K and K_S-band measurements for easy comparison with the high redshift radio galaxy literature. Data taken in 2003 and 2004 were taken through the K filter, while in 2005 and beyond the K_S filter was used. We add a correction to the K-band magnitudes in order to shift them to the K_S system (see Section 3.4 for details), and thus report all magnitudes in the 2MASS K_S system, though notation of K and K_S will be used interchangeably throughout this thesis. Note that while transformations from SDSS to AB are small in the optical, there is a large offset between AB and Vega magnitudes in the near infrared. A flat Lambda cosmology is assumed throughout, as indicated by numerous recent measurements, with $H_0 = 70\,\mathrm{km\,s^{-1}\,Mpc^{-1}}$, $\Omega_M = 0.3$, $\Omega_\Lambda = 0.7$ (e.g., Spergel et al., 2003).

3.1 TARGET SELECTION

The main obstacle to identifying high redshift radio galaxies is screening out the low redshift foreground. Figure 3.1 shows a theoretical dN/dz distribution for bright ($S_{1.4\mathrm{GHz}} > 100\,\mathrm{mJy}$) radio sources based on model radio luminosity functions and assuming pure luminosity evolution (Rowan-Robinson et al., 1993; Dunlop and Peacock, 1990). With a broad redshift peak at $z \sim 2$ extracting only the high-z galaxies through blind spectroscopic follow up of radio surveys is inefficient. Our goal is to eliminate the low redshift contamination through the inclusion of multi-wavelength information. We begin with the well known $K - z$ Hubble relation for radio galaxies (Lilly and Longair, 1984; van Breugel et al., 1998; Jarvis et al., 2001), which shows the strong correlation of K-band apparent magnitude and redshift. If we assume that this relation holds for all bright radio galaxies, then we can use model galaxy colors to predict the optical properties of these galaxies as they evolve.

Figure 3.2 shows the $r-K$, $g-K$, and $i-K$ color-redshift diagrams for two sets of galaxy models generated with the spectral synthesis code *PEGASE* (Fioc and Rocca-Volmerange, 1997). The upper curves are color tracks for an instantaneous burst model at solar metallicity and assuming no extinction for formation redshifts of $z_{\mathrm{form}} = 10$, 5, and 3, while the lower curves are for zero initial metallicity with an exponentially declining star-formation model with an e-folding time of $\tau = 0.5\,\mathrm{Gyr}$ and PEGASE "spheroid" type obscuration at these same formation redshifts. We choose solar metallicity for the instantaneous burst model to match the $r - K$ color of an elliptical galaxy at low redshift, as the PEGASE models do not update the metallicity in an instantaneous burst. Metallicity does evolve in the models of ongoing star formation, hence the assumption of zero initial metallicity for the $\tau = 0.5\,\mathrm{Gyr}$ e-folding star formation model. Although the spheroidal obscuration makes the ongoing star-formation model slightly redder than a typical elliptical galaxy at low redshift, we include it to approximate the effects of dust during the starburst (i.e. PEGASE does not allow for the destruction of dust). We would expect this model to be accurate at high redshift, but too red at low redshift. Since the low redshift models are excluded in both cases, this is not a concern. Shown for reference on each of the color redshift plots is the line representing the color of a point source at the $5\,\sigma$ limiting magnitude (AB) of the SDSS filter ($g_{\mathrm{lim}} = 23.3$, $r_{\mathrm{lim}} = 23.1$, $i_{\mathrm{lim}} = 22.3$) with the K-band magnitude assumed from a linear fit to the $K - z$ diagram, given by: $K = 4.62\log(z) + 17.2$, derived from a fit to the galaxies in van Breugel et al. (1998). Sources below the line on the diagram would be detected in each SDSS band, while sources above would not. Note that there will be some scatter in the cutoff due to the scatter in the $K - z$ Hubble diagram. The exact nature of the objects passing the magnitude cut will depend on the color dependence of the scatter in th $K - z$ relation. Combining the information in the $K - z$ diagram and Figure 3.2 we see that all of the optically bright galaxies are either at low redshift, or galaxies very near their initial formation redshift. We can now use the optical properties of the radio galaxies to eliminate the low redshift component of the distribution. Figure 3.3 shows a Monte-Carlo realization of the dN/dz distribution in Figure 3.1. The shaded histogram represents the galaxies that pass our selection criteria, assuming that all galaxies have the colors of the solar metallicity instantaneous burst with $z_{\mathrm{form}} = 5$. These histograms show that using optical properties is an effective way of screening out the low redshift component of the radio galaxy population. The PEGASE models predict that the radio galaxies get much bluer and brighter in the optical near their formation epoch due to the initial burst of star formation in the models. As the histogram in Figure 3.3 shows, some fraction of these galaxies will be excluded from optically selected samples near their formation epoch as they become bright and blue enough to be detected in most optical surveys. These model colors are especially sensitive to the assumptions made for the star formation (e.g. obscuration, e-folding time), and it is difficult to infer how accurate these color tracks will be near the initial starburst. We also note that there is evidence for moderate obscuration in some high redshift galaxies (e.g., Dey et al., 1995; Ouchi et al., 2004; Villar-Martín et al., 2006; Chary et al., 2005). Nevertheless, our models show that we may be somewhat biased against selecting unobscured galaxies with ongoing star formation near their formation epoch. Lowering the optical magnitude cutoff would allow these galaxies to enter our sample, although at the expense of the low redshift cutoff. Since we are primarily interested in galaxies with evolved stellar populations even at high redshift, as well as maintaining the efficiency of our search, we retain the optical selection to favor the low redshift cutoff at this minor expense of completeness.

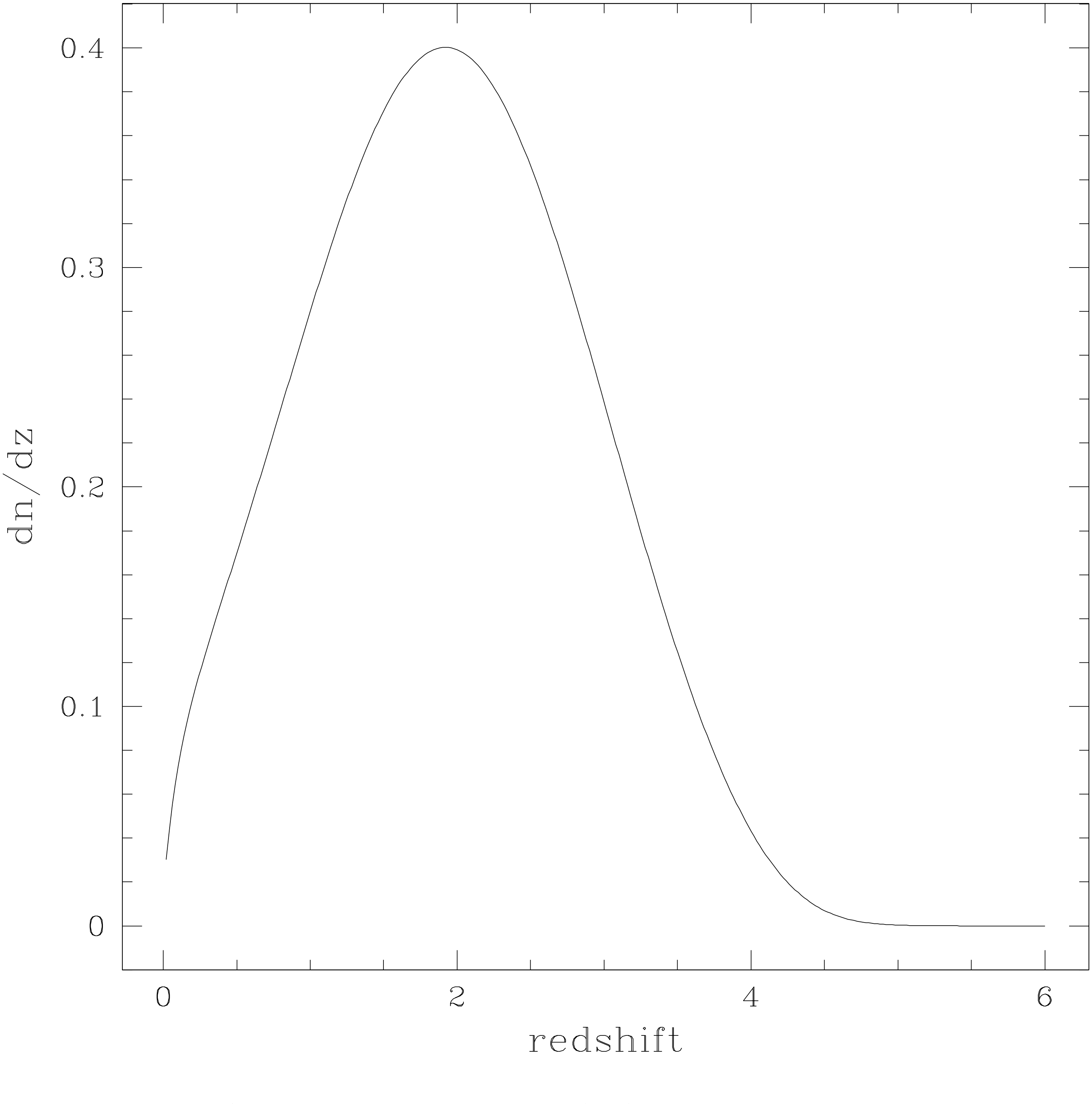

Figure 3.1 dN/dz based on the Dunlop and Peacock (1990) model for $S_{1.4\mathrm{GHz}} > 100\,\mathrm{mJy}$ radio sources. This shows the broad redshift distribution expected for bright radio sources. The y-axis scale is in arbitrary units.

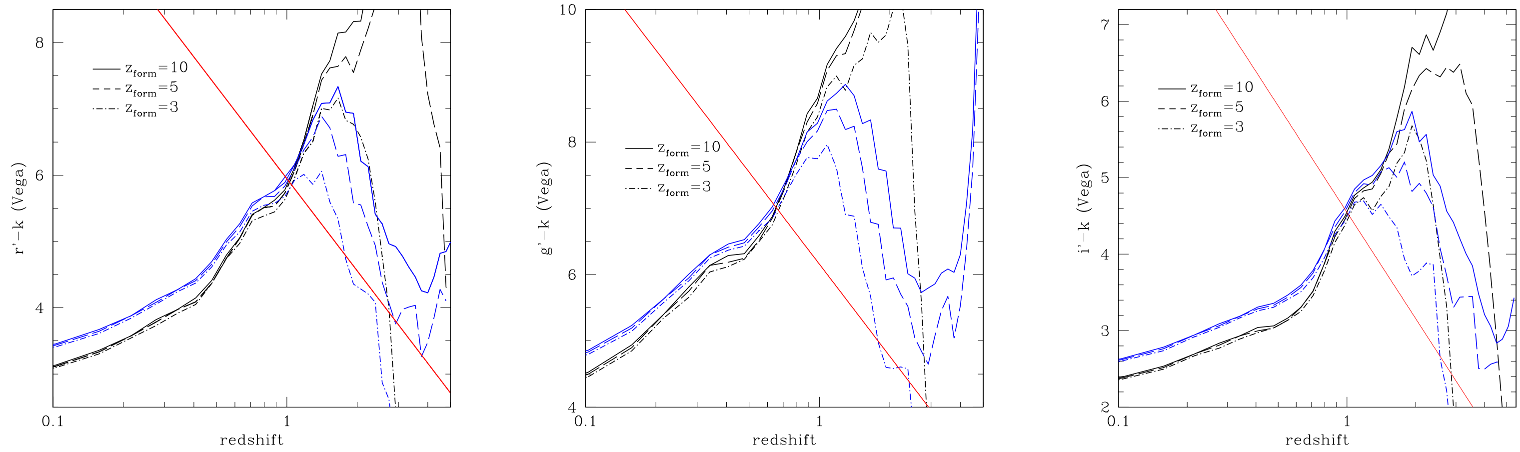

Figure 3.2 Color-redshift diagrams for two PEGASE models at three formation redshifts. The upper tracks represent a solar metallicity instantaneous burst model with no obscuration, while the lower tracks show a zero initial metallicity exponentially declining star formation with $\tau = 0.5\,\mathrm{Gyr}$ and "spheroid" extinction assumed. The diagonal lines represent $5\,\sigma$ limits in SDSS g, r, and i bands. Objects above the diagonal line will not be detected in the individual SDSS band.

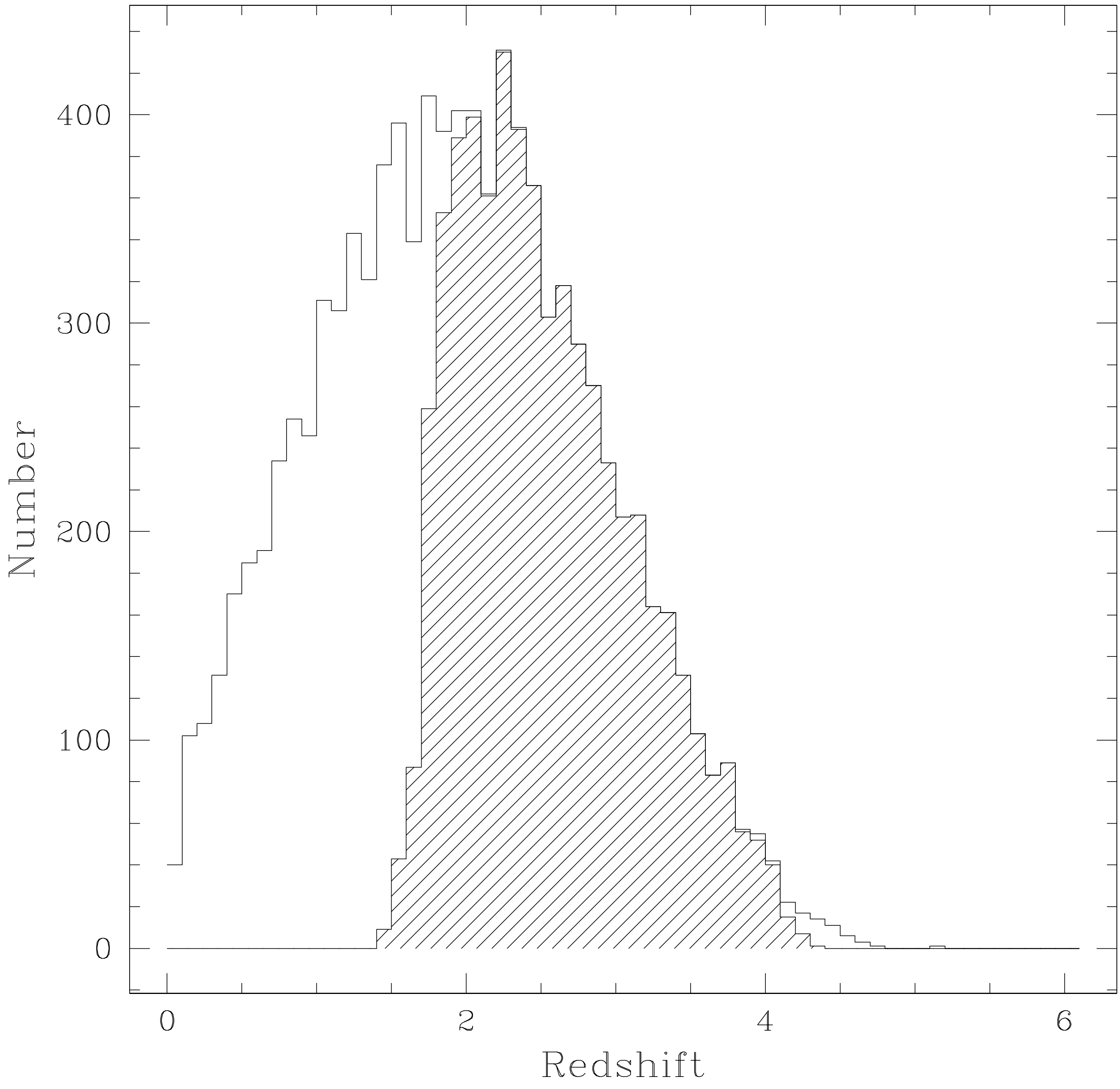

Figure 3.3 Monte-Carlo realization of the dN/dz distribution of Figure 3.1. The shaded histogram represents objects that pass our optical color cuts, assuming that all galaxies have a formation redshift $z_{\rm form} = 5.0$.

3.1.1 Selection Using *SDSS* and *FIRST*

We begin with the 2003 April 11 version of the FIRST catalog and select all sources with integrated flux $S_{1.4\mathrm{GHz}} > 100$ mJy. The primary motivation for this cut is to define a manageable sample size. Flux limits as low as ∼10 mJy are reasonable for selecting high-redshift radio galaxies. The $S_{1.4\mathrm{GHz}} > 100\,\mathrm{mJy}$ objects are positionally cross matched with photometric data from SDSS Data Release 4 (DR4), which covers more than 6600 square degrees in the Northern Sky. In addition to the > 100 mJy sources, all sources with $S_{1.4\mathrm{GHz}} > 50\,\mathrm{mJy}$ were cross matched for an area in the Southern Sky where deeper optical data is available from SDSS (known as "stripe 82", this 125 square degree area of the sky is repeatedly scanned by SDSS and the images coadded. Thirteen epochs of SDSS images were used for the coadded stripe 82 data in this thesis). Objects with candidate identifications in any of the u, g, r, i or z bands within a conservative radius of $5''$ are excluded. Radio sources with no cataloged SDSS counterpart are visually inspected to further exclude possible low signal-to-noise optical counterparts, as well as identifying and excluding extended or multiple-lobe radio sources with an obvious optical counterpart located some distance from the cataloged radio position (an optical source lying between independently cataloged radio lobes, for example). Note that we are not restricted to unresolved radio sources: Our selection criteria allow for extended and multicomponent radio sources to be included as well. To further eliminate likely low redshift sources, we optimally combine (Szalay et al., 1999) the g, r, and i SDSS images (the three most sensitive of the five SDSS filters) and eliminate any radio source with a candidate counterpart in the combined image.

The $5\,\sigma$ point source limiting AB magnitudes for SDSS are $u = 22.3$, $g = 23.3$, $r = 23.1$, $i = 22.3$, $z = 20.8$, (Ivezić et al., 2000). The coadded g, r, and i SDSS images allow us to extend the low redshift range being excluded by, in essence, improving our magnitude threshold by ≈ 1.0 magnitude. This can be thought of as providing an effective $2\,\sigma$ r-band magnitude limit of $r \approx 24.1$, although the specific limiting value is dependent on the details of individual target galaxy SEDs. Coadded images are processed with *SExtractor* version 2.3.2 (Bertin and Arnouts, 1996), and any objects with a detection greater than $2\,\sigma$ above the background are excluded from the sample. Remaining target candidates are again visually inspected to eliminate new (faint) optical identifications of extended or multi-lobe radio sources. This visual inspection introduces some subjectivity into the target selection criteria, but it is necessary in order to eliminate obvious SDSS counterparts to double lobed radio sources, and sources that are extended in the FIRST catalog. Candidate targets with nearby bright stars or other nearby bright confusing sources are also excluded from the final target list. These targets are then checked against the NASA Extragalactic Database (*NED*)[1] to screen out objects that had previously been observed. Five objects, 4C -00.62 ($z = 2.53$) (Roettgering et al., 1997), 3C 257 ($z = 2.474$) (Hewitt and Burbidge, 1991; van Breugel et al., 1998), 5C 7.271 ($z = 2.224$) (Willott et al., 2001), B20902+34/7C 0902+3420 ($z = 3.382$ targeted as a Lyman Break Galaxy) (Lilly, 1988; Steidel et al., 2003), and the unusually optically faint 4C +42.30 ($z = 1.29$) (Thompson et al., 1994) were previously identified with confirmed redshifts. The high redshift of four of these five radio galaxies support the effectiveness of our selection criteria. This process yields a total of 535 target objects. With 9142 $S_{1.4\mathrm{GHz}} > 100\,\mathrm{mJy}$ (and $> 50\,\mathrm{mJy}$ sources in stripe 82) radio sources in this area of DR4, less than one in ten meet our selection criteria, giving us an order of magnitude improvement in efficiency of finding high redshift radio galaxies over blind spectroscopic targeting of all radio galaxies.

Figure 3.4 shows a simulation of our multicolor optical selection in terms of $r - K$ color as a function of redshift for the same two sets of PEGASE spectral synthesis models used in Figure 3.2. The thick line shows the approximate effect of our optical selection criteria based on the gri coaddition. Using the model dN/dz of Dunlop and Peacock for radio sources brighter than 100 mJy with assumed pure luminosity evolution, we expect to exclude all sources with $z < 1.8$ and an average redshift for the sample of $z \sim 2.5$.

---

[1] The NASA/IPAC Extragalactic Database (NED) is operated by the Jet Propulsion Laboratory, California Institute of Technology, under contract with the National Aeronautics and Space Administration.

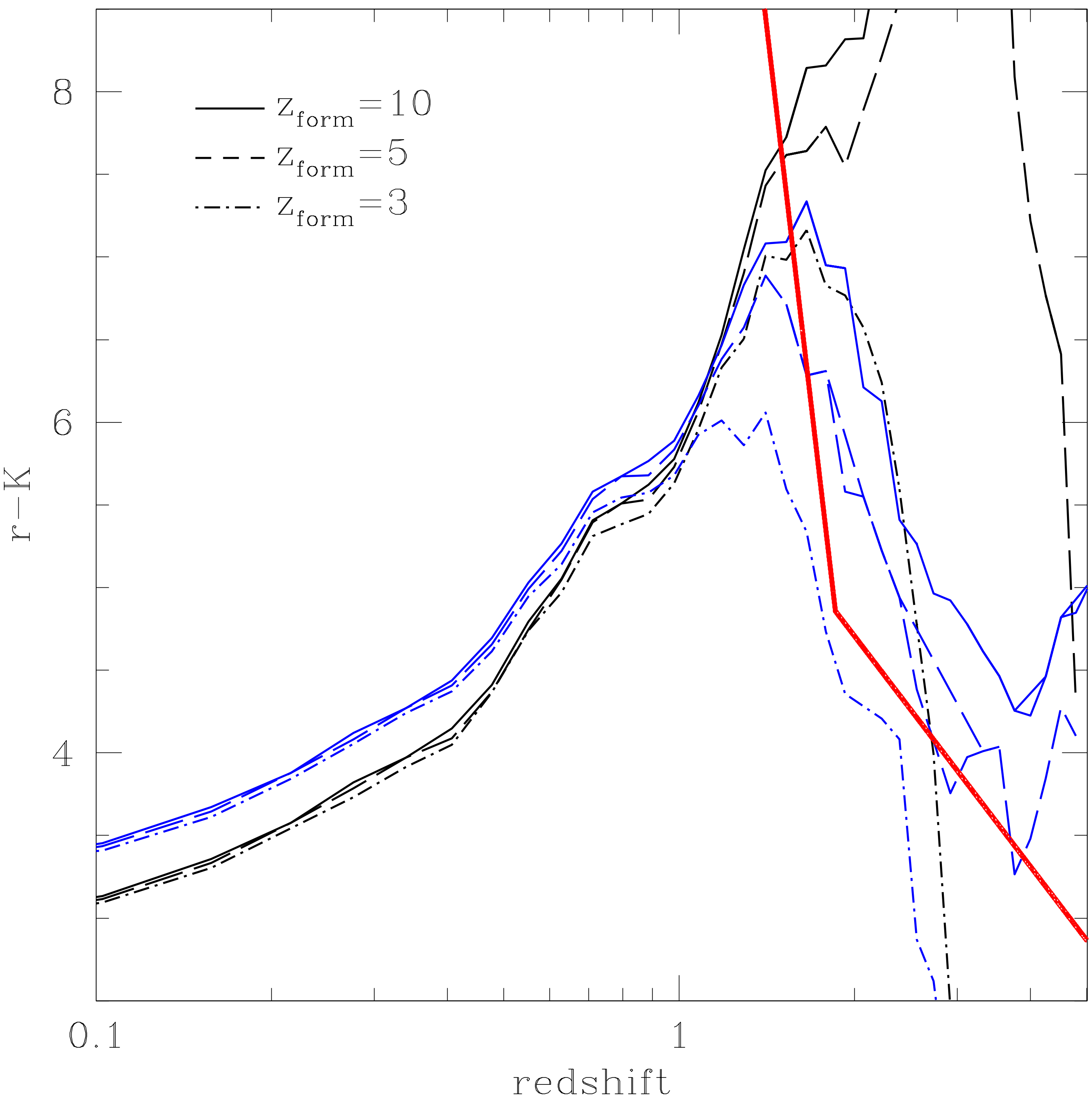

Figure 3.4 Optical color cuts compared to model $r - K$ color as a function of redshift. Objects above and to the right of the thick line pass the selection.

3.1.2 Selection Applied to Previous Surveys

As a test of our selection criteria, we apply our selection to subsets of the galaxies in a blind radio survey (Best et al., 1999) and the ultra-steep spectrum (USS) sample of De Breuck et al. (2001) designed to identify high redshift radio galaxies. Of the 178 radio sources with spectroscopic redshifts in Best et al. (1999), only 20 fall within SDSS Data Release 3 (DR3). These sources have redshifts ranging from $z = 0.004$ to $z = 2.474$, a mean redshift of $z = 0.78$, and a median of $z = 0.66$. Applying our selection criteria leaves only two targets at redshifts of $z = 1.339$ and $z = 2.474$, the only galaxy with $z > 1.5$ in the sample. Only 9 of the 62 USS sources of De Breuck et al. (2001) are within SDSS DR3, eight of which have firm redshifts. The mean and median redshift of this sample are 2.5 and 2.14 respectively. Applying our selection criteria eliminates the two $z < 1$ galaxies from the sample, as well as one unusually optically bright galaxy with $z = 2.48$, where Lyα falls within the g band, and De Breuck et al. (2001) note that it has relatively strong continuum emission. The five remaining galaxies have a mean and median of $z = 2.58$. As these two datasets show, our selection criteria is very effective at eliminating the low redshift foreground from both blind and USS samples. The exclusion of one $z > 2$ galaxy illustrates the fact that our selection may eliminate some galaxies with strong observed frame optical emission, though we choose to keep our selection criteria as they are for efficiency, at the price of some incompleteness.

3.2 THE OBSERVATIONS

The DRaGONS survey is naturally broken into two pieces: After being granted "survey" status by NOAO in 2005, we lengthened the target exposure time. With a few exceptions listed below, targets observed in 2003 and 2004 have exposure times of 15 to 20 minutes, while for objects observed in 2005 and beyond we aimed for a total integration time of 50 minutes. In addition, beginning in 2005 we switched from K-band to K_S-band in order to lengthen individual image frame exposure times and reduce telescope overhead, as well as better match with 2MASS calibration data (see below). This thesis will include analysis of data taken through 2006, though observations are ongoing. In addition to the K and K_S data, some further multiwavelength observations were made of select objects (see Section 3.9).

During 2003-2004, we acquired K-band images for 96 unique candidates over two sets of four nights: 2003 April 20-23 and 2004 May 31 to 2004 June 3. The official 40 night NOAO approved survey began in 2005. Observing was scheduled in six night groups during bright time: 2005 September 16-21, 2006 March 14-19, 2006 May 11-16, 2006 October 5-10, 2007 March 29 to 2007 April 3, and 2007 May 26 to 2007 June 1. All observations were done on the KPNO 4-meter Mayall telescope using the Florida Multi-object Imaging Near-IR grism Observational Spectrometer (*FLAMINGOS*) instrument. The detector is a 2048x2048 HgCdTe wide-field IR imager and multi-slit spectrometer with a pixel size of $0.3165''$, which gives a $10.8' \times 10.8'$ FOV on the 4 meter telescope. Conditions were highly variable during the April 2003 run, with a night and a half lost due a combination of high wind and moisture (first night seeing $1.0''$ to $1.5''$, subsequent nights $1.0''$ to $2.3''$ due to combination of cloud, wind, and moisture). The 2004 run was photometric on all four nights with seeing varying from $0.7''$ to $1.2''$. Exposures were 20 seconds each in the 2003 run and 15 seconds each in 2004 to account for brighter sky levels. We observed in a fixed five point dither pattern with a separation of 30 arcseconds. The September 2005 run lost approximately two nights to a combination of wind, rain, and thunder. Due to a failure of telescope dithering software, we observed in a custom sixteen point dither pattern. We lost two and a half nights in March 2006 to ice, wind, and snow, but otherwise had very good conditions. The cold air temperature allowed us to use longer single frame exposures of 40-55 seconds. The May 2006 run lost one and a half nights to clouds and wind, and varying seeing conditions ($1.0''$ to $1.5''$). Three nights were lost in October 2006 to clouds, rain, and lightning, with very good conditions on the remaining three nights. In total for 2005-2006, we lost six out of 24 nights to weather, or 25%. In addition, several objects were discarded throughout the runs when varying weather conditions affected portions of individual nights.

The $5\,\sigma$ limiting magnitude for the 20 minute exposures of 2003-2004 images is $K \sim 19.0$. For 2005-2006, with the longer ($\sim$ 48 minute total exposure times) the $5\,\sigma$ limit increases to $K \sim 20.0$. Three objects among those not detected after fifteen minutes exposures were observed a second time. Objects *J1411+0124*, *J1350+0352*, and *J2242-0808* have total integration times of 40, 61, and 29 minutes, respectively. *J1123+0530* is the well known $z = 2.474$ radio galaxy *3C 257* (Hewitt and Burbidge, 1991; van Breugel et al., 1998), one of the most luminous radio galaxies known. As it passed our selection criteria, it was observed in order to provide a consistency check with previous radio galaxy searches.

3.3 REDUCTION AND ASTROMETRY

We processed the data using standard *NOAO IRAF*[2] routines. A set of dark frames were taken and subtracted from each image. A set of 6-10 adjacent (in time) images were combined to create a sky flat for division (i.e. "running sky flats"). The images were approximately aligned based on the dither offsets, then the IRAF tasks *mscgetcat* and *msccmatch* were used to accurately register the images for coaddition. The IRAF task *msccmatch* uses a catalog of *USNO-A2* (Monet, 1998) stellar positions and magnitudes for image registration and transformation, which may include image shift, scale change, and axis rotation. The resulting astrometry displayed a systematic offset on most images of between $0.5''$ to $1.0''$, due to slight differences between the USNO-A2 and SDSS astrometry. We manually corrected for these systematic offsets when constructing catalogs of each field. Our final astrometry is accurate to subarcsecond precision, with the residual difference between the K-band and SDSS positions well fit by a Gaussian of width $0.25''$. Beginning with data taken in 2005, the *USNO-A2* catalog was replaced with a catalog of bright stars from the 2 Micron All Sky Survey (*2MASS*)[3]. This eliminated the systematic offsets evident with the USNO catalog, again giving subarcsecond precision to our final astrometry. Several small modifications were made to the pipeline in 2004, and the pipeline version was frozen at the beginning of 2005.

---

[2] IRAF is distributed by the National Optical Astronomy Observatories, which are operated by the Association of Universities for Research in Astronomy, Inc., under cooperative agreement with the National Science Foundation.

[3] This publication makes use of data products from the Two Micron All Sky Survey, which is a joint project of the University of Massachusetts and the Infrared Processing and Analysis Center/California Institute of Technology, funded by the National Aeronautics and Space Administration and the National Science Foundation.

3.4 PHOTOMETRY

Each FLAMINGOS field was processed with *SExtractor* version 2.3.2. Quoted K-band magnitudes are SExtractor MAG_AUTO unless otherwise noted. Due to the large field of view of the FLAMINGOS instrument, a large number (~50) of bright sources detected in 2MASS are present in each field. Using a custom webservice interface to the GESTALT webservice *WESIX* (`http://nvogre.phyast.pitt.edu:8080/gestalt_home/`) sources were cross matched with point sources from the 2MASS catalog having $K_s < 15.3$, the $5\,\sigma$ limiting magnitude for point sources. Saturated stars were excluded from the comparison. A linear least squares fit between the SExtractor and 2MASS objects was performed to determine the slope and zero point offset between the two datasets. This solution was assumed to continue linearly beyond the $K_s = 15.3$ limit. An example of this calibration is shown in Figure 3.5. The calibration code was updated in 2005 to include cuts on the calibration magnitudes perpendicular to the fit line (as indicated by the dashed lines in Figure 3.5). Previously, cuts were done based solely on the 2MASS magnitude, possibly biasing the slope due to outlier points near the cut boundaries.

Several adjustments were made in both observing and processing between 2004 and 2005. As mentioned in Section 3.2, observations in 2003-2004 were done in FLAMINGOS K-band, while those during 2005-2006 were observed in K_S-band. Figure 3.7 shows a comparison of these filters, along with the standard CTIO K filter and the 2MASS K_S filter. While the FLAMINGOS K_S filter is very close to the standard CTIO (and 2MASS) K_S filter, the FLAMINGOS K-band filter is a custom made filter. The FLAMINGOS online documentation states: “The K-band filter is a little short on the red side (2.35 vs. 2.42 micron), as compared to the CIT/CTIO system”. Carpenter (2001) list transforms between 2MASS and several common near infrared filtersets, with offsets between K and K_S between 0.00 and 0.045, but a color transform for the custom K filter of FLAMINGOS has yet to be computed. To identify differences introduced by the filter change we examine the galaxy number counts of the K and K_S data. Figure 3.6 shows the galaxy number counts for these two datasets. There is an offset of $\Delta\, K = 0.11$ magnitudes. This is larger than the expected difference from Carpenter (2001). It is possible that the bias introduced by cutting the calibration data based solely on 2MASS magnitudes in 2003 and 2004 may have affected the best fit slope between the FLAMINGOS and 2MASS data, but this would show up as a change in slope in the number counts, whereas the discrepancy in Figure 3.6 appears to show a constant offset, not a change in slope. We, therefore, note that the offset is most likely due to the different filters used in the two time periods, despite the lower offsets listed in Carpenter (2001). Because the transmission curve for the 2MASS K_S is very close to that of FLAMINGOS K_S, we will adopt K_S magnitudes and add a correction to the K-band magnitudes observed in 2003 and 2004:

$$K_{FLAM} = K_S + 0.11 \tag{3.1}$$

For radio galaxies not detected in K or K_S-band at the $2\,\sigma$ level, we report the $2\,\sigma$ magnitude of a point source as a lower limit. Throughout the thesis, we will adopt this K_S magnitude system, but will use K and K_S nomenclature interchangeably.

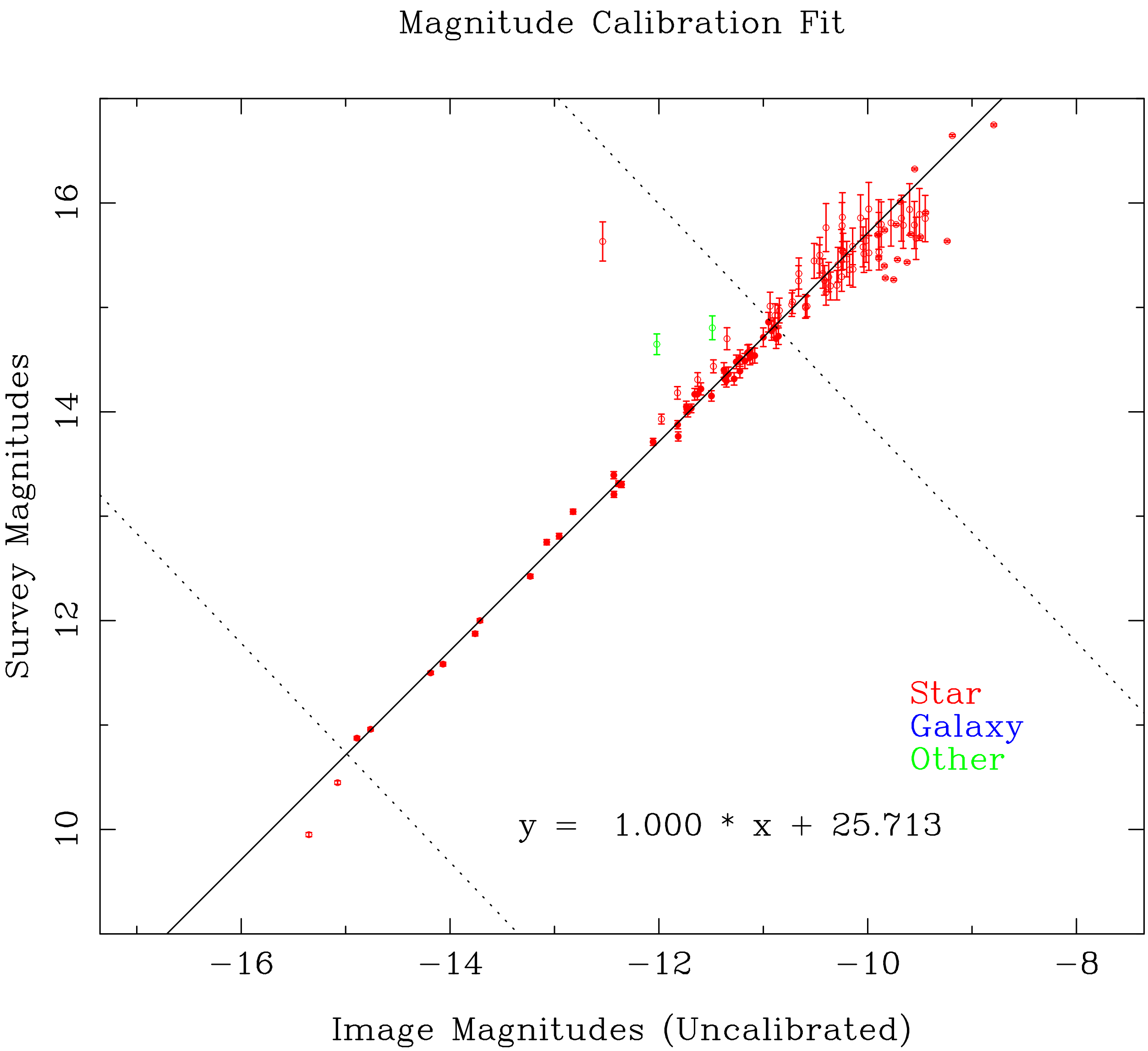

Figure 3.5 An example of the calibration of DRaGONS data using 2MASS. The y-axis is 2MASS K_S magnitude and the x-axis is the uncalibrated DRaGONS magnitude. Red points are marked as point sources in the 2MASS catalog, while green are extended. The dotted lines show the 2MASS magnitude limits used in the fit (perpendicular to the fitted slope to eliminate Malmquist bias). Fields with slopes more than 10% different from unity are rejected as bad. Error bars are magnitude errors reported by SExtractor.

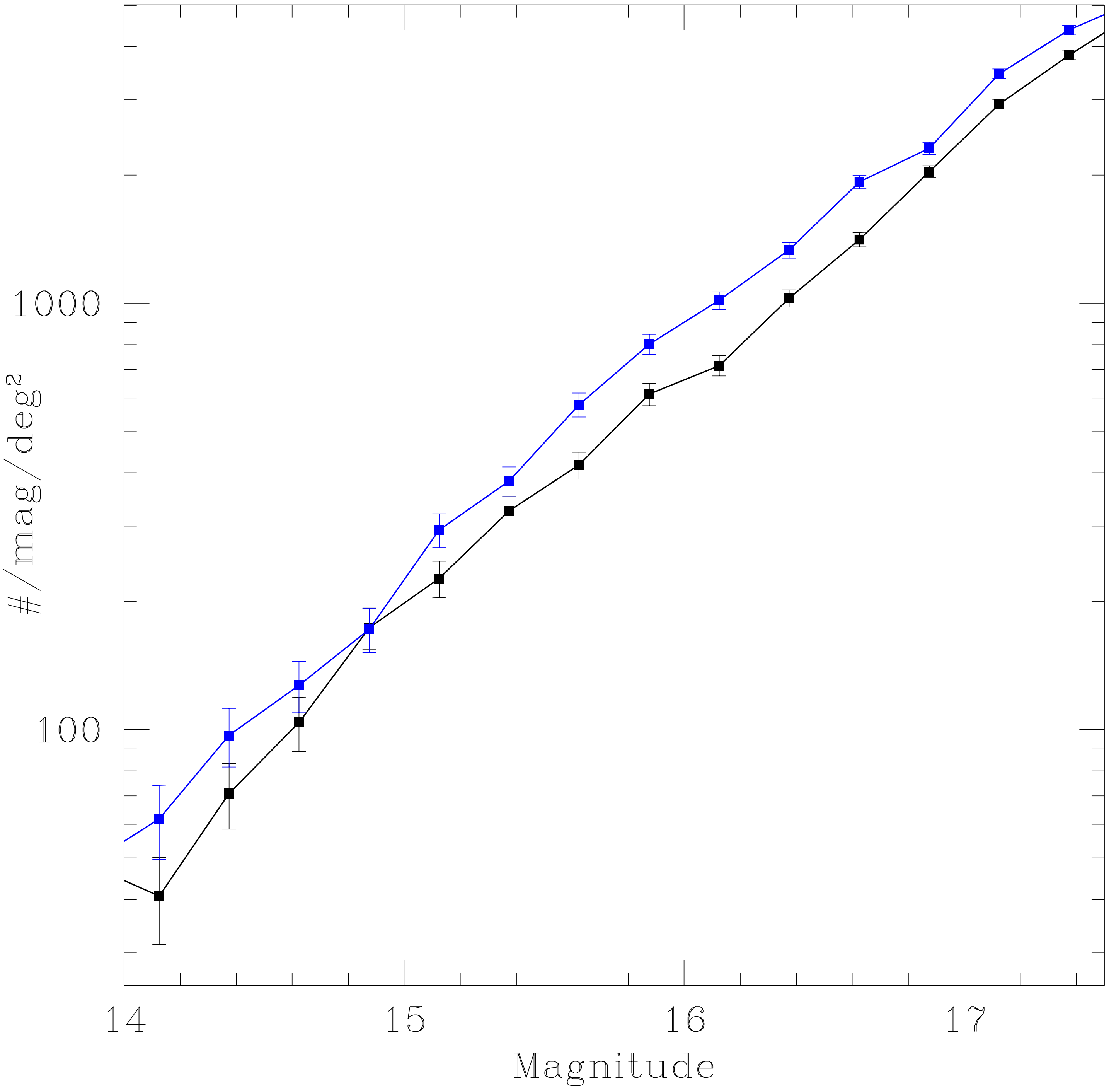

Figure 3.6 A comparison of the galaxy number counts for the 2003-2004 (blue) vs. 2005-2006 (black) data. The systematic offset of $\sim$ 0.11 mag is due to a combination of filter bandpass and adjustments to the processing and calibration pipeline.

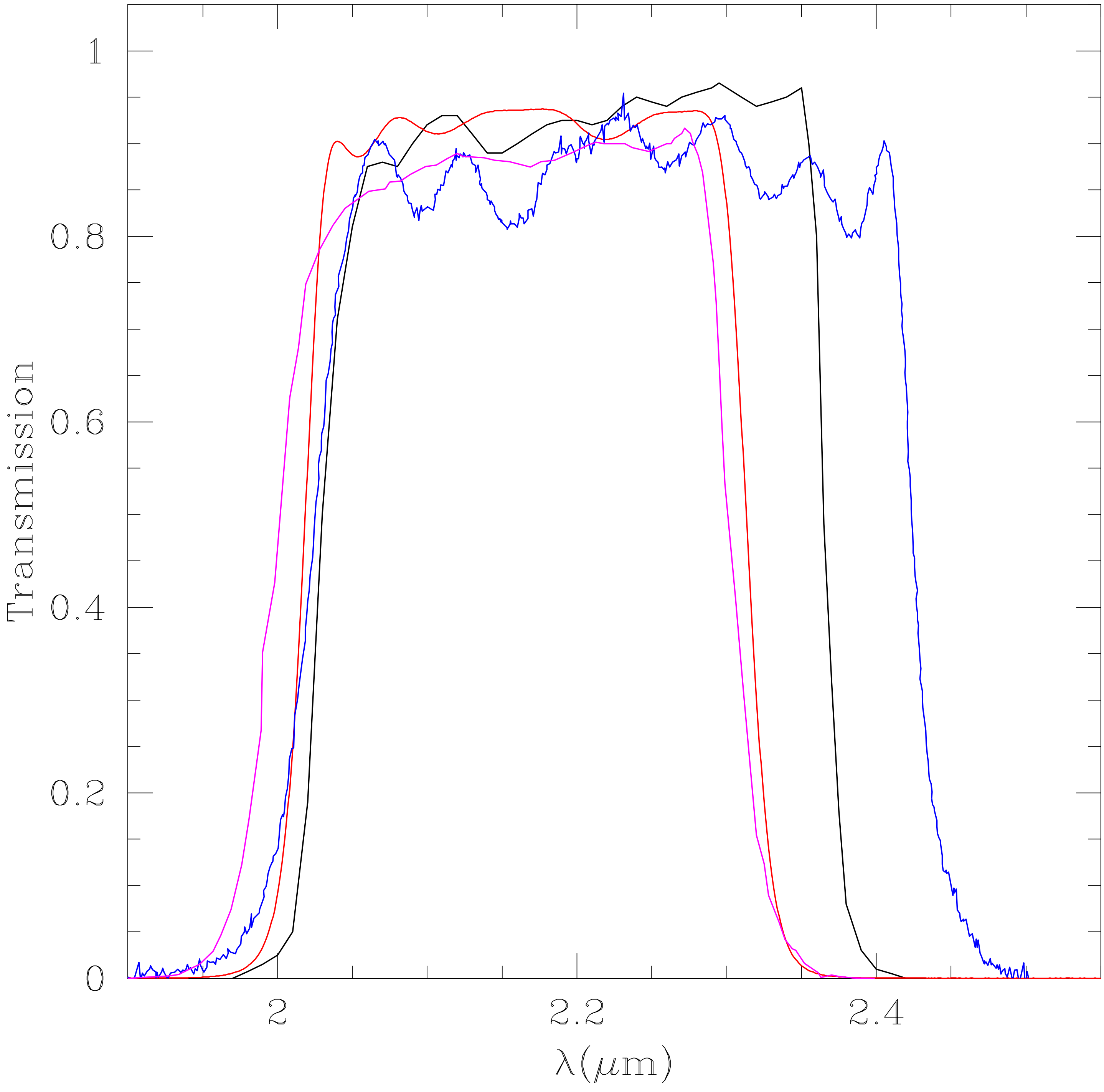

Figure 3.7 A comparison of the different K and K_S filter transmission curves. The black curve is the FLAMINGOS K-band, blue is the FLAMINGOS K_S-band, blue is the standard CTIO K-band, and magenta is the 2MASS K_S-band. Note that the FLAMINGOS K-band cuts off at $\lambda = 2.35\ \mu m$ rather than $\lambda = 2.42\ \mu m$ for the CTIO filter.

3.5 STAR-GALAXY SEPARATION AND ERO DEFINITION

The final K and K_S-band catalogs were positionally cross matched with the SDSS catalog using a webservice interface to OpenSkyQuery (`http://www.openskyquery.net`) in order to obtain $r - K$ colors. A simple nearest neighbor criterion was used, and objects with no SDSS counterpart within a three arcsecond radius were assigned a $5\,\sigma$ limiting magnitude of $r = 23.1$.

Star-Galaxy separation was done in two steps: For objects detected in SDSS with $r \leq 21.0$ we used the SDSS star-galaxy classification (*probPSF*, which is described in Scranton et al., 2002). For fainter r-band objects the separation was done by examining the difference between the K-band MAG_AUTO magnitude (from SExtractor) and a fixed $3.5''$ aperture magnitude returned by SExtractor as a function of MAG_AUTO to separate point-like objects from extended galaxies. Figure 3.8 shows the resulting star-galaxy separation. This separation was chosen to be in rough agreement with the star-galaxy classification from SDSS where reliable classification was available. The slope of the resultant number counts for both stars and galaxies are in good agreement with those of Daddi et al. (2000). Reliable separation was possible to $K = 17.0$, and all objects fainter than this are considered to be galaxies. This will lead to a slight contamination of our galaxy sample by faint stars, but because the slope of the stellar number counts is much smaller than galaxies, this will become less important at fainter magnitudes.

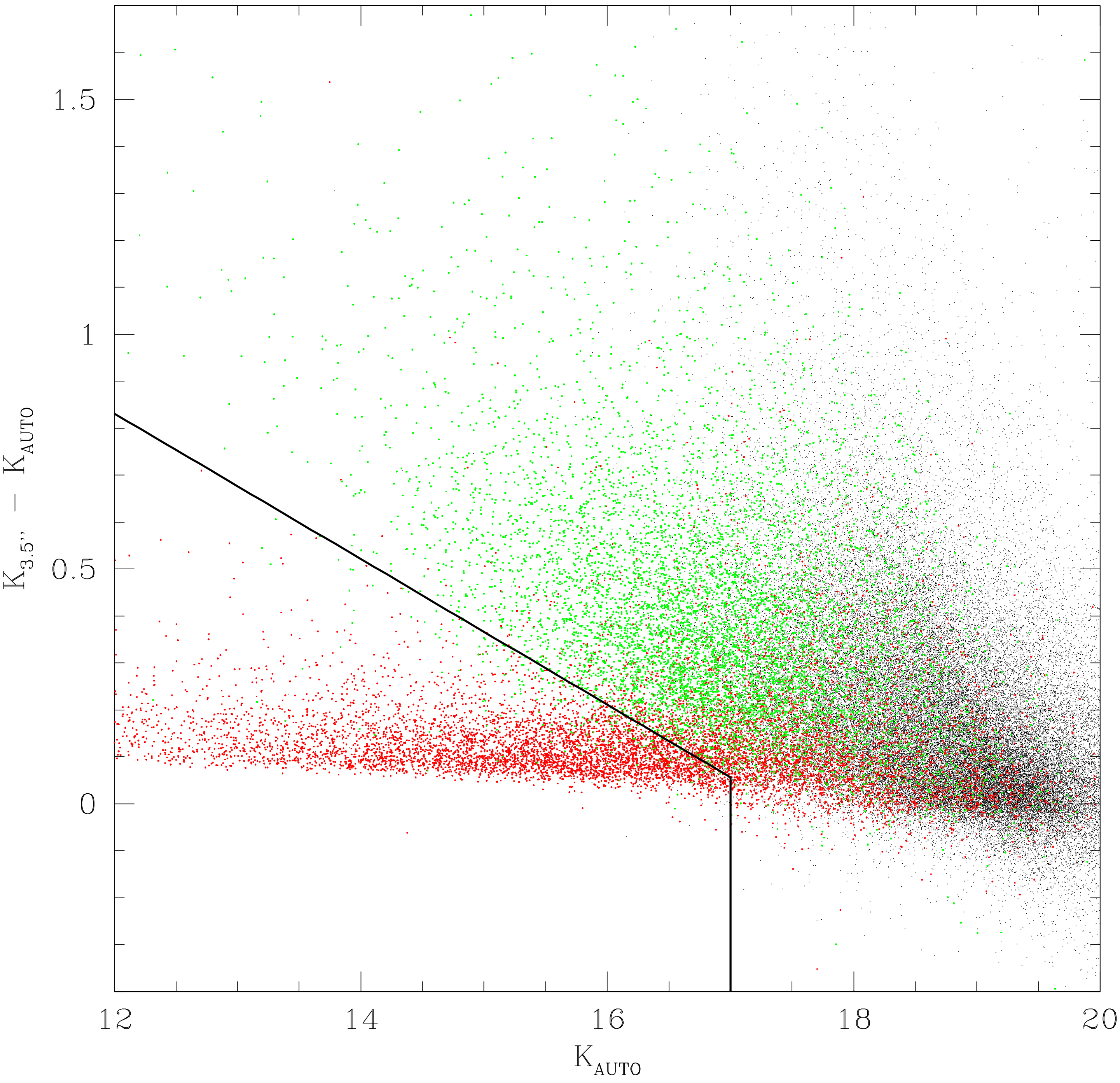

Figure 3.8 $K_{\mathrm{APER}(3.5'')} - K_{\mathrm{AUTO}}$ as a function of K_{AUTO}. Red and green points are $r < 21.0$ objects classified by SDSS as stars and galaxies respectively. Black points above and to the right of the black line are considered galaxies.

The exact definition of EROs in the literature is not standardized. Some authors use total magnitudes (Wold et al., 2003; Cimatti et al., 2002), some isophotal/aperture corrected (Daddi et al., 2000), some use matched aperture magnitudes in the R and K-bands(e.g. Elston et al., 2006), among others. There is the additional variation in the use of specific R and K (and K_S) filters used to select EROs, making comparison between ERO samples problematic. We chose our ERO definition by comparing to publicly available data in the Boötes field of the FLAMINGOS Extragalactic (*FLAMEX*) Survey (Elston et al., 2006), which lies in the NOAO Deep Wide Field Survey (*NDWFS*)[4] (Jannuzi and Dey, 1999), as well as SDSS. The Boötes field of the FLAMEX survey covers approximately 4.7 square degrees in both J- and K_s-bands. The FLAMEX survey was conducted with the FLAMINGOS instrument, and the its location within SDSS allows for a direct comparison with our data. The FLAMEX survey defines EROs based on 6″ matched aperture magnitudes in NDWFS R and FLAMEX K_s bands. Unfortunately, the SDSS catalog does not include aperture magnitudes, so we use SDSS model magnitudes in conjunction with 4″ aperture magnitudes in K-band to define our $r - K$ color, as this aperture appears to best mimic the FLAMEX results. Cross-matching the FLAMEX, SDSS, and NDWFS data in a subset of the Boötes field, we found that an ERO definition of $r - K_{\mathrm{APER}(4'')} \geq 5.50$ approximated the $R - K_S \geq 5.0$ definition of Elston et al. (2006).

3.6 THE RADIO GALAXIES

The results of our K and K_S-band observations are shown in Tables 3.1, 3.2, 3.3, and 3.4. Tables 3.1 and 3.3 list objects detected in 2003-2004 and 2005-2006 respectively, while Tables 3.2 and 3.4 list non-detections in the infrared. The column entries are:

1. Object Name: Name of source in IAU J2000 format. Objects with double lobe and multiple radio morphologies have the infrared object reported first and the individual radio components named a, b, c as necessary.

---

[4] The NOAO Deep Wide-Field Survey (Jannuzi and Dey 1999) is supported by the National Optical Astronomy Observatory (NOAO). NOAO is operated by AURA, Inc., under a cooperative agreement with the National Science Foundation.

2. Date: Date observed.
3. Radio RA and DEC: Position of radio detection from the FIRST catalog (J2000)
4. K-band (2003-2004) or K_S-band (2005-2006) RA and DEC: Position of the infrared detected object (J2000)
5. Extended: Y if object shows visible extension in the FIRST image or if the object is a double or multiple lobe radio source. N if object is unresolved in the radio image.
6. $f_{\rm peak}$: Peak 1.4 GHz flux density from FIRST catalog (mJy)
7. $f_{\rm int}$: Integrated 1.4 GHz flux density from FIRST catalog (mJy)
8. K or K_S: apparent magnitude and error for infrared object. Magnitudes are in the 2MASS system, which is slightly offset from the CIT system, given by: $K_s(\rm 2MASS) = \rm K(CIT) + 0.0000 \times (J - K)_{CIT} - 0.024 \pm 0.003$ (Carpenter, 2001). For nondetections (Tables 3.2 and 3.4) the $2\,\sigma$ detection limit is reported. Errors are those output by SExtractor.
9. Seeing: The full width half maximum seeing measured for the field, given in arcseconds.
10. z_{K-z}: estimated redshift based on a fit to the Hubble $K - z$ relation, given by $K = 4.62\log(z) + 17.2$. For nondetections the estimated redshift is given as a lower limit for the $2\,\sigma$ limiting magnitude.

Table 3.1: 2003-2004 Detections

Object Name[a]	date	radio RA	radio DEC	Extended?	K RA	K DEC	$f_{\rm peak}$(mJy)	$f_{\rm int}$(mJy)	K	seeing($''$)	z_{K-z}[b]
J0742+3256	23 April 2003	07:42:13.61	+32:56:51.16	N	07:42:13.60	+32:56:51.20	130.51	144.60	17.72±0.08	1.0	1.3
J0831+5210	23 April 2003	···	···	Y	08:31:44.83	+52:10:34.95	···	···	18.93±0.17	1.1	2.4
a	···	08:31:44.89	+52:10:41.28	···	···	···	97.07	113.73	···	···	···
b	···	08:31:44.74	+52:10:28.72	···	···	···	108.06	131.18	···	···	···
J0941+0127	23 April 2003	09:41:48.75	+01:27:36.45	N	09:41:48.77	+01:27:35.89	117.82	120.56	17.17±0.08	2.2	1.0
J0958+0324	20 April 2003	···	···	Y	09:58:24.95	+03:24:13.56	···	···	17.46±0.09	1.5	1.1
a	···	09:58:24.18	+03:24:20.84	···	···	···	72.53	190.15	···	···	···
b	···	09:58:23.57	+03:24:24.98	···	···	···	125.58	162.14	···	···	···
c	···	09:58:26.323	+03:24:01.51	···	···	···	166.91	286.56	···	···	···
J1102+0250[c]	21 April 2003	···	···	Y	11:02:06.59	+02:50:45.45	···	···	16.70±0.06	2.1	0.8
a	···	11:02:05.66	+02:50:58.19	···	···	···	29.48	127.69	···	···	···
b	···	11:02:06.05	+02:50:48.86	···	···	···	8.71	33.29	···	···	···
J1123+0530[d]	23 April 2003	···	···	Y	11:23:09.43	+05:30:18.60	···	···	17.51±0.11	1.7	1.2
a	···	11:23:09.06	+05:30:20.58	···	···	···	1514.62	1580.13	···	···	···
b	···	11:23:09.75	+05:30:13.83	···	···	···	150.31	163.07	···	···	···
J1135+0548	21 April 2003	11:35:17.81	+05:48:54.13	N	11:35:17.84	+05:48:54.06	190.84	212.63	18.77±0.15	2.1	2.2
J1155+0305	20 April 2003	···	···	Y	11:55:12.48	+03:05:18.93			17.36±0.06	1.1	1.1
a	···	11:55:11.94	+03:05:25.69	···	···	···	40.01	57.21	···	···	···
b	···	11:55:12.80	+03:05:14.61	···	···	···	77.26	105.60	···	···	···
J1208+0414	21 April 2003	···	···	Y	12:08:11.90	+04:14:59.37	···	···	18.15±0.14	1.7	1.6
a	···	12:08:11.69	+04:15:04.87	···	···	···	204.08	299.15	···	···	···
b	···	12:08:12.24	+04:14:55.55	···	···	···	264.65	341.17	···	···	···
J1208+4943	01 June 2004	···	···	Y	12:08:24.73	+49:43:29.72	···	···	17.03±0.04	0.8	0.9
a	···	12:08:24.04	+49:43:31.74	···	···	···	78.12	87.72	···	···	···
b	···	12:08:24.94	+49:43:28.61	···	···	···	88.83	111.26	···	···	···
J1236+0150	02 June 2004	12:36:00.15	+01:50:52.59	Y	12:35:59.60	+01:50:52.79	144.70	154.53	17.25±0.07	0.9	1.0
J1237+0135[e]	20 April 2003	···	···	Y	12:37:05.32	+01:35:53.27	···	···	17.96±0.07	0.9	1.5
a	···	12:37:7.681	+01:35:58.08	···	···	···	162.2	193.99	···	···	···
b	···	12:37:3.252	+01:35:53.98	···	···	···	180.7	232.25	···	···	···
J1250+6043	04 June 2004	12:50:24.47	+60:43:46.84	N	12:50:24.47	+60:43:46.59	288.67	304.05	17.81±0.09	1.1	1.4
J1259+0559	23 April 2003	···	···	Y	12:59:12.37	+05:59:03.10	···	···	18.36±0.14	1.9	1.8
a	···	12:59:11.93	+05:59:29.05	···	···	···	66.15	73.60	···	···	···
b	···	12:59:12.57	+05:58:52.43	···	···	···	53.98	105.19	···	···	···
J1308−0022	03 June 2004	···	···	Y	13:08:56.17	−00:22:36.65	···	···	19.05±0.15	1.1	2.5
a	···	13:08:56.36	−00:22:33.12	···	···	···	90.77	98.14	···	···	···
b	···	13:08:55.87	−00:22:42.98	···	···	···	134.01	143.03	···	···	···
J1312+0009	20 April 2003	13:12:32.83	+00:09:13.40	N	13:12:32.79	+00:09:13.17	109.42	112.61	19.03±0.17	1.1	2.5
J1313+6250	02 June 2004	13:13:15.63	+62:50:47.29	N	13:13:15.63	+62:50:47.36	128.32	132.18	18.43±0.10	1.1	1.8
J1315+0533	04 June 2004	13:15:17.92	+05:33:14.07	N	13:15:18.00	+05:33:09.93	140.25	146.96	18.72±0.13	1.0	2.1
J1332+0101	23 April 2003	···	···	Y	13:32:16.55	+01:01:48.26	···	···	17.05±0.08	2.0	0.9
a	···	13:32:16.78	+01:01:50.83	···	···	···	152.34	228.66	···	···	···
b	···	13:32:15.94	+01:01:40.81	···	···	···	118.60	184.03	···	···	···
J1336+0207	03 June 2004	13:36:34.43	+02:07:37.13	Y	13:36:34.33	+02:07:42.21	113.55	127.76	19.20±0.18	0.9	2.7
J1400+0053	21 April 2003	14:00:4.59	+00:53:19.0	N	14:00:04.64	+00:53:18.90	112.87	130.80	17.23±0.08	1.4	1.0
J1402+0342	23 April 2003	14:02:24.86	+03:42:27.10	N	14:02:24.89	+03:42:26.73	501.26	540.42	17.65±0.10	1.7	1.2
J1403+6048	04 June 2004	14:03:59.55	+60:48:07.85	N	14:03:59.62	+60:48:07.69	526.50	794.62	17.55±0.07	0.8	1.2
J1408+0116	02 June 2004	···	···	Y	14:08:33.38	+01:16:22.24	···	···	17.08±0.05	0.8	0.9
a	···	14:08:33.13	+01:16:23.99	···	···	···	290.25	320.12	···	···	···
b	···	14:08:33.58	+01:16:20.85	···	···	···	199.15	292.63	···	···	···
J1411+0124[f]	20-21 April 2003	···	···	Y	14:11:08.29	+01:24:40.56	···	···	19.93±0.18	1.3	3.9
a	···	14:11:08.32	+01:24:45.48	···	···	···	116.43	122.32	···	···	···
b	···	14:11:08.21	+01:24:33.78	···	···	···	60.89	64.17	···	···	···
J1423+0139	23 April 2003	14:23:03.45	+01:39:58.23	N	14:23:03.47	+01:39:58.46	202.21	211.64	17.37±0.09	2.0	1.1

Continued on Next Page…

Table 3.1 – Continued

Object Name[a]	date	radio RA	radio DEC	Extended?	K RA	K DEC	$f_{\rm peak}$(mJy)	$f_{\rm int}$(mJy)	K	seeing($''$)	z_{K-z}[b]
J1438+0150	20 April 2003	14:38:17.15	+01:50:31.05	N	14:38:17.20	+01:50:31.27	83.24	118.52	17.94±0.17	1.0	1.4
J1438+6149	03 June 2004	14:38:41.83	+61:49:33.79	N	14:38:41.87	+61:49:33.67	114.73	121.27	18.70±0.14	0.8	2.1
J1451+5404	01 June 2004	· · ·	· · ·	Y	14:51:43.43	+54:04:22.02	· · ·	· · ·	19.37±0.20	0.9	2.9
a	· · ·	14:51:43.66	+54:04:25.67	· · ·	· · ·	· · ·	265.89	274.33	· · ·	· · ·	· · ·
b	· · ·	14:51:43.23	+54:04:25.67	· · ·	· · ·	· · ·	271.59	280.30	· · ·	· · ·	· · ·
J1452+0032	21 April 2003	· · ·	· · ·	Y	14:52:00.78	+00:32:45.54	· · ·	· · ·	17.92±0.09	1.3	1.4
a	· · ·	14:52:01.46	+00:33:01.29	· · ·	· · ·	· · ·	112.59	143.03	· · ·	· · ·	· · ·
b	· · ·	14:51:59.91	+00:32:41.68	· · ·	· · ·	· · ·	471.04	496.02	· · ·	· · ·	· · ·
J1510+5244	03 June 2004	15:10:20.20	+52:44:30.20	N	15:10:20.16	+52:44:30.68	500.50	505.76	18.41±0.18	0.8	1.8
J1515+5744	20 April 2003	15:15:29.30	+57:44:57.32	Y	15:15:29.33	+57:44:56.25	78.56	144.16	19.14±0.18	1.0	2.6
J1523−0018	01 June 2004	15:23:16.19	−00:18:55.40	Y	15:23:16.23	−00:18:55.08	216.42	231.44	18.75±0.10	0.9	2.2
J1526+0408	23 April 2003	· · ·	· · ·	Y	15:26:37.15	+04:08:14.22	· · ·	· · ·	17.87±0.11	2.0	1.4
a	· · ·	15:26:38.90	+04:08:02.96	· · ·	· · ·	· · ·	18.14	53.66	· · ·	· · ·	· · ·
b	· · ·	15:26:36.59	+04:08:19.72	· · ·	· · ·	· · ·	43.55	102.76	· · ·	· · ·	· · ·
J1532+4432	04 June 2004	· · ·	· · ·	Y	15:32:50.13	+44:32:15.24	· · ·	· · ·	17.16±0.08	0.9	1.0
a	· · ·	15:32:50.85	+44:32:16.86	· · ·	· · ·	· · ·	92.53	117.98	· · ·	· · ·	· · ·
b	· · ·	15:32:49.66	+44:32:14.50	· · ·	· · ·	· · ·	86.96	131.67	· · ·	· · ·	· · ·
J1541+5259	23 April 2003	· · ·	· · ·	Y	15:41:18.87	+52:59:55.38	· · ·	· · ·	17.24±0.08	2.3	1.0
a	· · ·	15:41:18.75	+52:59:52.35	· · ·	· · ·	· · ·	100.27	115.12	· · ·	· · ·	· · ·
b	· · ·	15:41:18.81	+53:00:00.38	· · ·	· · ·	· · ·	67.11	77.90	· · ·	· · ·	· · ·
J1543+5711	03 June 2004	15:43:30.33	+57:11:32.40	Y	15:43:30.12	+57:11:32.37	55.88	103.39	18.24±0.08	0.9	1.7
J1547+4839	04 June 2004	15:47:42.06	+48:39:12.20	N	15:47:42.34	+48:39:09.33	186.86	214.75	19.49±0.18	0.9	3.1
J1548+0036	21 April 2003	15:48:16.21	+00:36:13.56	Y	15:48:16.22	+00:36:13.27	123.08	126.05	16.83± 0.04	1.7	0.8
J1548−0033	20 April 2003	· · ·	· · ·	Y	15:48:21.75	−00:34:00.80	· · ·	· · ·	19.06±0.14	0.9	2.5
a	· · ·	15:48:21.45	−00:33:59.28	· · ·	· · ·	· · ·	155.03	231.62	· · ·	· · ·	· · ·
b	· · ·	15:48:22.14	−00:34:00.64	· · ·	· · ·	· · ·	157.66	201.46	· · ·	· · ·	· · ·
J1549+4719	04 June 2004	15:49:53.47	+47:19:48.56	N	15:49:53.53	+47:19:48.25	104.66	106.33	18.20±0.11	0.9	1.6
J1554+4729	04 June 2004	15:54:25.63	+47:29:00.97	N	15:54:25.67	+47:29:00.56	137.54	149.73	18.70±0.09	0.9	2.1
J1559+5011	03 June 2004	15:59:47.89	+50:11:16.41	N	15:59:47.96	+50:11:16.44	127.0	130.28	18.38±0.11	0.8	1.8
J1604−0013	02 June 2004	16:04:12.71	−00:13:41.89	N	16:04:12.62	−00:13:41.28	117.91	128.28	17.13±0.05	0.9	1.0
J1604+4746	22 April 2003	16:04:27.85	+47:46:35.02	N	16:04:27.92	+47:46:34.48	351.96	366.10	18.70±0.13	1.3	2.1
J1606+4751[g]	04 June 2004	16:06:1.29	+47:51:52.17	Y	16:06:01.40	+47:51:46.30	3.07	12.31	17.47±0.07	0.9	1.1
a	· · ·	16:06:1.82	+47:52:01.68	· · ·	· · ·	· · ·	36.38	61.54	· · ·	· · ·	· · ·
b	· · ·	16:06:2.49	+47:51:21.20	· · ·	· · ·	· · ·	81.73	109.02	· · ·	· · ·	· · ·
J1609+3700	03 June 2004	16:09:28.11	+37:00:18.12	N	16:09:28.13	+37:00:18.0	96.52	102.52	17.80±0.08	0.8	1.3
J1617+4848	23 April 2003	16:17:25.42	+48:48:28.69	N	16:17:25.47	+48:48:28.38	236.95	244.32	18.00±0.11	1.9	1.5
J1629+4937	20 April 2003	16:29:21.38	+49:37:54.86	N	16:29:21.31	+49:37:54.27	183.38	197.05	19.50±0.19	1.0	3.1
J1632+4056	01 June 2004	16:32:16.27	+40:56:32.71	N	16:32:16.29	+40:56:32.63	200.82	203.15	18.89±0.13	0.8	2.3
J1634+4155	03 June 2004	16:34:43.60	+41:55:03.40	N	16:34:43.57	+41:55:03.09	216.39	263.47	18.30±0.11	0.8	1.7
J1636+4808	21 April 2003	· · ·	· · ·	Y	16:36:15.70	+48:08:48.32	· · ·	· · ·	19.10±0.17	1.2	2.6
a	· · ·	16:36:16.04	+48:08:50.11	· · ·	· · ·	· · ·	87.46	97.73	· · ·	· · ·	· · ·
b	· · ·	16:36:15.16	+48:08:45.59	· · ·	· · ·	· · ·	147.42	165.66	· · ·	· · ·	· · ·
J1637+3223	03 June 2004	16:37:34.53	+32:23:05.84	N	16:37:34.53	+32:23:06.21	136.29	147.47	18.80±0.15	0.8	2.2
J1643+4518	03 June 2004	16:43:22.62	+45:18:06.68	N	16:43:22.79	+45:18:01.68	108.30	110.39	18.30±0.11	0.8	1.7
J1645+4152	03 June 2004	16:45:00.73	+41:52:14.20	N	16:45:00.80	+41:52:14.30	112.56	115.96	18.42±0.09	0.8	1.8
J1648+4233	23 April 2003	16:48:31.51	+42:33:22.42	Y	16:48:31.52	+42:33:21.82	167.44	169.30	19.00±0.17	2.1	2.5
J1649+3350	02 June 2004	16:49:24.21	+33:50:02.04	N	16:49:24.19	+33:50:02.17	162.25	163.91	16.86±0.03	0.9	0.8
J1654+4125	02 June 2004	16:54:43.87	+41:25:02.96	N	16:54:43.89	+41:25:03.00	225.60	228.56	18.15±0.10	0.9	1.6
J1655+2723	01 June 2004	· · ·	· · ·	Y	16:55:04.33	+27:23:28.91	· · ·	· · ·	18.52±0.09	0.8	1.9
a	· · ·	16:55:03.87	+27:23:32.00	· · ·	· · ·	· · ·	40.01	54.13	· · ·	· · ·	· · ·
b	· · ·	16:55:04.73	+23:23:26.47	· · ·	· · ·	· · ·	101.27	115.40	· · ·	· · ·	· · ·
J1656+2707	02 June 2004	16:56:16.29	+27:07:32.47	N	16:56:16.31	+27:07:33.05	160.33	164.76	18.88±0.15	0.9	2.3
J1707+2408	01 June 2004	17:07:44.58	+24:08:54.56	N	17:07:44.57	+24:08:54.41	144.83	169.15	17.96±0.09	0.8	1.5
J1715+3027	01 June 2004	17:15:48.29	+30:27:23.18	N	17:15:48.31	+30:27:23.18	378.27	385.34	18.54±0.09	0.8	2.0

Continued on Next Page. . .

Table 3.1 – Continued

Object Name[a]	date	radio RA	radio DEC	Extended?	K RA	K DEC	f_{peak}(mJy)	f_{int}(mJy)	K	seeing($''$)	z_{K-z}[b]
J2059−0603	02 June 2004	20:59:32.88	−06:03:00.34	N	20:59:32.87	−06:02:59.59	155.63	161.72	18.32±0.10	0.9	1.7
J2107−0701	02 June 2004	21:07:45.46	−07:01:07.83	N	21:07:45.47	−07:01:06.54	523.60	550.60	18.37±0.09	0.9	1.8
J2223−0757	01 June 2004	22:23:26.52	−07:57:08.07	N	22:23:26.51	−07:57:06.94	104.79	108.34	17.70±0.08	0.9	1.3
J2247−0910	01 June 2004	22:47:23.79	−09:10:49.74	Y	22:47:23.69	−09:10:49.26	77.10	103.37	17.99±0.09	0.9	1.5
J2309−0834	03 June 2004	23:09:04.29	−08:34:57.19	N	23:09:4.29	−08:34:56.83	103.19	111.67	18.23±0.12	0.9	1.7
J2316−0846	03 June 2004	23:16:35.08	−08:46:17.72	N	23:16:35.07	−08:46:17.16	101.85	105.40	18.59±0.14	0.9	2.0
J2336−0838	04 June 2004	⋯	⋯	Y	23:36:18.35	−08:38:48.87	⋯	⋯	18.50±0.15	0.9	1.9
a	⋯	23:36:18.11	−08:38:43.58	⋯	⋯	⋯	124.78	134.50	⋯	⋯	⋯
b	⋯	23:36:18.65	−08:38:48.27	⋯	⋯	⋯	104.16	110.32	⋯	⋯	⋯
J2337−0852	04 June 2004	23:37:32.44	−08:52:39.49	N	23:37:32.46	−08:52:38.83	118.04	120.14	18.20±0.13	0.9	1.6

[a] Objects named with a and b are double lobed sources with the radio properties listed corresponding to the object above them on the table

[b] Based on a fit to the $K - z$ Hubble diagram $K = 4.62 * \log(z) + 17.2$

[c] This object is an extended double lobe with a corresponding faint match in SDSS and should not have been included in our sample. The object has SDSS magnitudes g=23.25 r=22.29 i=21.26 z=19.90

[d] This object, *3C 257* was previously identified as a $z = 2.474$ radio galaxy (Hewitt and Burbidge, 1991).

The K-band contains Hα emission, leading to the underestimate of redshift from the K-z diagram (see van Breugel et al., 1998, for details).

[e] This object is a wide separation double lobe with several candidate objects along the radio axis. The probable match is faintly detected in SDSS with magnitudes of g=22.6 r=22.13 i=21.32 z=20.27

[f] Object J1411+0124 was observed on subsequent nights for a total integration time of 40 minutes

[g] This object has a match in SDSS g=22.86 r=22.45 i=22.11 z=21.12, was improperly targeted because it is a weak double lobe

TABLE 3.2

2003-2004 NON-DETECTIONS

Object Name	date	radio RA	radio DEC	Extended?	$f_{\rm peak}$(mJy)	$f_{\rm int}$(mJy)	K ($2\,\sigma$)	seeing($''$)	z_{K-z}
J1022+0357	23 April 2003	10:22:01.03	+03:57:37.56	N	194.31	200.86	>20.11	2.3	>3.2
J1028+0144	21 April 2003	10:28:02.79	+01:44:06.51	Y	56.82	114.81	>19.80	2.0	>2.7
J1044+0538	20 April 2003	10:44:19.88	+05:38:07.98	N	125.54	130.20	>20.32	1.2	>3.5
J1047+0216	23 April 2003	10:47:11.32	+02:16:28.21	N	122.32	125.81	>20.09	2.2	>3.1
J1144+0254	23 April 2003	11:44:34.26	+02:54:25.56	N	114.01	119.18	>20.13	2.1	>3.2
J1221+0248	23 April 2003	12:21:39.93	+02:48:28.01	N	139.93	142.87	>20.13	1.9	>3.2
J1234+0024	03 June 2004	12:34:30.79	+00:24:59.45	N	94.84	100.55	>20.35	1.2	>3.6
J1240−0017	21 April 2003	12:40:12.23	−00:17:30.34	N	137.73	150.90	>20.28	2.0	>3.4
J1303+0026	23 April 2003	13:03:57.48	+00:26:45.41	N	91.23	104.04	>20.15	2.0	>3.2
J1314+0330	21 April 2003	13:14:22.82	+03:30:22.14	Y	163.59	250.05	>20.31	1.6	>3.5
J1329+0133	01 June 2004	13:29:18.78	+01:33:40.80	N	87.80	102.64	>20.38	1.3	>3.6
J1350+0352[a]	2003-2004	13:50:24.37	+03:52:43.90	N	99.51	104.28	> 21.02	1.1	>5.0
J1421+0248	01 June 2004	···	···	Y	···	···	>20.33	1.0	>3.5
a	···	14:21:10.957	+02:48:35.76	···	152.15	165.01	···	···	···
b	···	14:21:11.20	+02:48:29.10	···	158.20	177.62	···	···	···
J1431+0511	04 June 2004	14:31:09.58	+05:11:17.85	Y	1.31	2.22	>20.19	0.9	>3.3
a	···	14:31:08.10	+05:11:21.18	···	216.42	226.17	···	···	···
b	···	14:31:10.86	+05:11:15.80	···	158.20	177.62	···	···	···
J1500+0031	23 April 2003	15:00:55.34	+00:31:58.52	N	141.31	145.90	>20.21	2.0	>3.3
J1507+6003	04 June 2004	15:07:44.31	+60:03:12.68	N	181.08	189.23	>20.18	0.9	>3.3
J1527+4352	02 June 2004	15:27:51.49	+43:52:4.79	N	138.95	140.11	>20.35	0.9	>3.6
J1554+3942	03 June 2004	···	···	Y	···	···	>20.23	0.9	>3.3
a	···	15:54:17.02	+39:42:27.44	···	35.95	55.94	···	···	···
b	···	15:54:17.81	+39:42:18.95	···	98.92	113.29	···	···	···
J1557+4657	04 June 2004	15:57:24.61	+46:57:54.29	N	198.10	204.20	>20.14	0.9	>3.2
J1618+5210	04 June 2004	16:18:55.60	+52:10:41.40	N	108.26	112.29	>20.21	0.9	>3.3
J1641+4209	22 April 2003	16:41:30.14	+42:09:25.99	N	260.20	263.68	>20.37	1.0	>3.6
J1648+3623	04 June 2004	···	···	Y	···	···	>20.12	0.9	>3.2
a	···	16:48:51.58	+36:23:39.10	···	121.33	128.45	···	···	···
b	···	16:48:53.02	+36:23:24.56	···	123.58	128.96	···	···	···
J1700+3830	20 April 2003	17:00:19.95	+38:30:33.93	N	428.65	430.20	>20.40	1.2	>3.6
J1711+3047	21 April 2003	17:11:26.65	+30:47:45.89	N	124.27	124.77	>20.41	1.2	>3.7
J2221−0901	02 June 2004	22:21:48.04	−09:01:58.95	N	224.64	234.50	>20.32	0.9	>3.5
J2242−0808[b]	01 & 04 June 2004	22:42:34.05	−08:08:21.86	N	125.64	129.97	>20.63	0.9	>4.1

[a] J1350+0352 was observed both 20 April 2003 and 02 June 2004, for a total integration time of 61 minutes with no detection

[b] J2242−0808 was observed on two nights in 2004 for a total integration time of 29 minutes

Table 3.3: 2005-2006 DRaGONS Galaxies

Name	date	radio RA	radio DEC	extended?	K_S RA	K_S DEC	f_{peak}	f_{int}	K_S	seeing($''$)	z_{Kz}
J2115-0743	2005 Sep 16	21:15:31.1	-07:43:49.1	No	21:15:31.1	-07:43:49.11	285.15	294.32	18.10±0.112	1.1	1.6
J2215-0900	2005 Sep 16	22:15:19.7	-09:00:05.8	Yes	22:15:19.65	-09:00:5.19	75.23	125.05	19.757±0.181	1.2	3.6
J0240-0022	2005 Sep 16	02:40:57.5	-00:22:52.7	No	02:40:57.51	-00:22:53.13	64.76	76.85	18.54±0.117	1.4	1.9
J2230+0013	2005 Sep 17	22:30:51.4	+00:13:47.1	No	22:30:51.4	+00:13:47.07	70.97	72.35	19.92±0.210	1.3	3.9
J2148-0836 [1]	2005 Sep 18	21:48:55.4	-08:36:40.1	No	21:48:55.40	-08:36:40.41	113.21	116.59	17.77±0.106	1.2	1.3
J2148-0836	2005 Sep 18	21:48:55.4	-08:36:40.1	No	21:48:55.49	-08:36:37.41	113.21	116.59	18.54±0.129	1.2	1.9
J2150-0055	2005 Sep 18	21:50:41.8	-00:55:20.1	No	21:50:41.78	-00:55:20.03	50.90	51.51	19.34±0.241	1.2	2.9
J0205-0819	2005 Sep 18	02:05:41.0	-08:19:42.1	Yes	02:05:40.98	-08:19:42.63	82.81	128.23	18.07±0.143	0.9	1.5
J0256-0659	2005 Sep 18	02:56:05.0	-06:59:21.3	Yes	02:56:5.02	-06:59:19.77	173.14	255.58	17.57±0.079	1.3	1.2
J2258-0958	2005 Sep 19	22:58:13.5	-09:58:16.6	No	22:58:13.48	-09:58:16.41	219.48	232.80	19.54±0.27	1.3	3.2
J2317+0029	2005 Sep 19	23:17:22.7	+00:29:44.3	Yes	23:17:22.79	+00:29:45.51	58.29	86.68	19.42±0.39	1.3	3.0
J2252+0003	2005 Sep 20	22:52:34.0	+00:03:31.0	Yes	22:52:34.06	+00:03:30.81	41.91	68.09	18.16±0.184	1.0	1.6
J2256+0038	2005 Sep 21	22:56:06.7	+00:38:02.6	No	22:56:6.71	+00:38:3.09	65.03	66.71	19.00±0.172	2.4	FIX
J0725+3826	2006 Mar 16	07:25:44.3	+38:26:39.6	No	07:25:44.350	+38:26:39.69	231.15	232.92	17.67±0.049	1.2	1.2
J0819+3504	2006 Mar 16	08:19:09.3	+35:04:29.2	No	08:19:09.325	+35:04:29.07	97.46	102.64	19.71±0.162	1.0	3.4
J1106+4722	2006 Mar 16	11:06:41.6	+47:22:04.7	No	11:06:41.636	+47:22:04.53	123.26	125.48	18.617±0.063	1.0	2.0
J1141+3857	2006 Mar 16	11:41:45.5	+38:57:09.7	No	11:41:45.465	+38:57:09.75	146.51	148.04	18.428±0.073	1.0	1.8
J1331+4108	2006 Mar 16	13:31:49.5	+41:08:57.4	DL	13:31:48.675	+41:08:55.17	101.51	111.75	19.595±0.195	1.0	3.3
...	...	13:31:48.0	+41:08:52.0	DL	...	...	11.75	14.37	...	...	...
J1530+2631	2006 Mar 16	15:30:50.4	+26:31:54.3	No	15:30:50.389	+26:31:54.87	107.74	108.98	18.949±0.110	1.0	2.4
J1619+1433	2006 Mar 16	16:19:11.4	+14:33:00.6	No	16:19:11.452	+14:32:59.85	647.52	692.11	17.920±0.061	0.9	1.4
J1636+3409	2006 Mar 16	16:36:40.6	+34:09:46.6	No	16:36:40.596	+34:09:46.53	123.04	124.91	19.840±0.198	1.0	3.7
J0732+4335	2006 Mar 17	07:32:43.7	+43:35:40.3	No	07:32:43.663	+43:35:39.62	371.27	383.45	18.859±0.143	1.3	2.3
J0940+4649	2006 Mar 17	09:40:52.6	+46:49:44.4	No	09:40:52.593	+46:49:43.89	122.41	124.78	19.578±0.164	1.2	3.3
J1052+3201	2006 Mar 17	10:52:12.2	+32:01:56.5	No	10:52:12.157	+32:01:56.97	127.70	127.92	19.293±0.097	1.4	2.8
J1221+4114	2006 Mar 17	12:21:14.1	+41:14:36.9	Yes	12:21:13.753	+41:14:31.83	76.92	100.78	18.055±0.065	1.5	1.5
J1438+2821	2006 Mar 17	14:38:10.0	+28:21:47.0	Yes	14:38:09.974	+28:21:46.71	671.87	831.68	17.090±0.088	1.5	0.9
J1600+3304	2006 Mar 17	16:00:45.5	+33:04:17.1	No	16:00:45.470	+33:04:15.86	166.47	169.74	16.801±0.087	1.5	0.8
J0845+2849	2006 Mar 18	08:45:36.8	+41:18:10.5	Yes	08:45:24.173	+28:49:23.97	78.46	102.39	18.540±0.087	1.2	1.9
J0948+6416	2006 Mar 18	09:48:24.2	+64:16:49.6	No	09:48:24.352	+64:16:49.57	212.80	214.55	20.309±0.112	1.2	4.7
J1123+6130	2006 Mar 18	11:23:10.2	+61:30:25.4	No	11:23:10.137	+61:30:25.59	105.90	108.38	18.071±0.065	1.1	1.5
J1356+0958	2006 Mar 18	13:56:47.4	+09:58:07.3	No	13:56:47.421	+09:58:07.71	132.74	136.79	18.689±0.091	1.2	2.1
J1546+1754	2006 Mar 18	15:46:02.1	+17:54:32.5	Yes	15:46:2.442	+17:54:36.81	77.12	109.26	17.286±0.044	1.2	1.0
J1643+2631	2006 Mar 18	16:43:49.4	+26:31:19.1	Yes	16:43:49.314	+26:31:19.89	72.73	136.46	18.575±0.102	1.3	2.0
J1047+0216	2006 May 11	10:47:11.3	+02:16:28.2	No	10:47:11.314	+02:16:28.59	122.32	125.81	18.740±0.195	1.0	2.1
J1429+3426	2006 May 11	14:29:05.1	+34:26:41.1	No	14:29:05.124	+34:26:41.07	256.22	260.41	19.615±0.232	1.0	3.3
J1514+4135	2006 May 11	15:14:04.5	+41:35:43.6	No	15:14:04.579	+41:35:43.53	144.69	149.02	19.121±0.184	1.0	2.6
J1554+3400	2006 May 11	15:54:29.5	+34:00:44.3	No	15:54:29.580	+34:00:44.37	106.78	107.22	17.770±0.076	1.0	1.3
J1056+0624	2006 May 12	10:56:05.3	+06:24:22.5	No	10:56:05.294	+06:24:22.41	175.15	181.31	18.780±0.151	1.2	2.2
J1326+4434	2006 May 12	13:26:36.9	+44:34:59.1	No	13:26:37.066	+44:34:57.21	161.71	179.33	18.515±0.166	1.3	1.9
J1442+3042	2006 May 12	14:42:41.6	+30:42:33.0	No	14:42:41.580	+30:42:32.67	534.88	540.18	18.190±0.086	1.4	1.6
J1558+3517	2006 May 12	15:58:10.4	+35:17:27.8	No	15:58:10.404	+35:17:27.93	371.93	384.32	18.069±0.097	1.4	1.5
J1630+2452	2006 May 12	16:30:14.7	+24:52:47.9	Yes	16:30:14.679	+24:52:47.37	89.25	102.07	16.750±0.050	1.0	0.8
J1255+3046	2006 May 13	12:55:46.2	+30:46:11.3	DL	12:55:46.351	+30:46:8.97	170.18	197.96	16.976±0.060	1.3	0.9
...	...	12:55:46.5	+30:46:05.2	DL	...	...	124.95	138.37	...	...	...
J1641+2005	2006 May 13	16:41:18.6	+20:05:47.8	Yes	16:41:18.589	+20:05:47.49	80.68	113.50	19.000±0.151	1.2	2.4
J1642+2414	2006 May 13	16:42:26.1	+24:14:43.7	Yes	16:42:26.121	+24:14:44.43	127.74	165.12	19.563±0.362	1.1	3.2
J1100+3324	2006 May 14	11:00:53.5	+33:24:50.5	DL	11:00:53.294	+33:24:48.87	82.08	101.10	19.021±0.118	1.2	2.5
...	...	11:00:52.9	+33:24:45.3	DL	...	...	79.75	91.49	...	...	...
J1245+3711	2006 May 14	12:45:42.9	+37:11:33.7	No	12:45:42.899	+37:11:33.45	112.66	121.11	18.9109±0.111	1.1	2.3
J1347+4113	2006 May 14	13:47:52.1	+41:13:45.5	No	13:47:52.117	+41:13:44.97	169.23	170.83	19.373±0.163	1.1	2.9
J1515+2458	2006 May 14	15:15:54.2	+24:58:40.1	No	15:15:54.181	+24:58:39.93	215.22	220.98	17.707±0.095	1.0	1.3
J1615+3216	2006 May 14	16:15:09.3	+32:16:59.5	Yes	16:15:09.253	+32:16:58.71	132.77	207.15	19.208±0.18	1.1	2.7

Continued on Next Page...

Table 3.3 – Continued

Name	date	radio RA	radio DEC	extended?	K_S RA	K_S DEC	f_{peak}	f_{int}	K_S	seeing($''$)	z_{Kz}
J1630+1308	2006 May 14	16:30:14.0	+13:08:31.0	Yes	16:30:14.105	+13:08:30.39	113.55	147.94	18.455±0.121	1.1	1.9
J1636+2347	2006 May 14	16:36:56.6	+23:47:50.2	Yes	16:36:56.625	+23:47:50.37	135.01	188.29	17.988±0.12	1.2	1.5
J1303+3509	2006 May 16	13:03:53.7	+35:09:51.1	No	13:03:53.758	+35:09:50.49	442.76	449.71	18.727±0.153	1.1	2.1
J1417+0710	2006 May 16	14:17:00.4	+07:10:37.3	DL	14:17:00.458	+07:10:47.49	483.38	505.73	18.218±0.122	1.0	1.7
...	...	14:17:00.5	+07:10:55.3	DL	...	...	979.64	1098.41	...	...	...
J1530+0644	2006 May 16	15:30:22.6	+06:44:08.0	Yes	15:30:22.658	+06:44:6.81	195.93	274.76	18.301±0.093	1.1	1.7
...	2006 May 16	EROinfield	...	...	15:30:27.149	+06:41:26.01	...	...	17.689±0.0647	1.1	1.3
J1601+0605	2006 May 16	16:01:55.1	+06:05:37.7	No	16:01:55.191	+06:05:37.83	211.64	218.05	17.791±0.063	1.2	1.3
J1615+1643	2006 May 16	16:15:52.5	+16:43:43.3	No	16:15:52.460	+16:43:42.81	330.64	356.23	19.822±0.265	1.3	3.7
J1629+2851	2006 May 16	16:29:12.3	+28:51:34.3	No	16:29:12.278	+28:51:34.29	517.11	525.55	18.074±0.156	1.1	1.5
J2137-0738	2006 Oct 07	21:37:08.3	-07:38:44.0	DL	21:37:08.350	-07:38:43.89	92.55	107.77	18.252±0.072	1.3	1.7
...	...	21:37:06.0	-07:39:07.4	...	...	...	1.39	1.18	...	...	...
J2200+0014	2006 Oct 07	22:00:18.5	+00:14:54.1	No	22:00:18.486	+00:14:53.79	82.86	85.70	19.779±0.243	1.2	3.6
J0150-0952	2006 Oct 07	01:50:02.8	-09:52:55.2	No	01:50:02.795	-09:52:54.99	197.76	203.47	19.082±0.176	1.2	2.5
J0230-0909	2006 Oct 07	02:30:54.8	-09:09:51.0	No	02:30:54.822	-09:09:50.67	195.15	200.80	19.187±0.190	1.3	2.7
J0252-0849	2006 Oct 07	02:52:38.6	-08:49:05.9	Yes	02:52:38.805	-08:49:05.91	83.72	102.92	18.142±0.112	1.3	1.6
J2145-0049	2006 Oct 08	21:45:12.0	-00:49:28.8	No	21:45:12.026	-00:49:28.77	89.57	93.64	19.101±0.185	0.9	2.6
J2150-0055	2006 Oct 08	21:50:41.8	-00:55:20.2	No	21:50:41.778	-00:55:20.07	50.90	51.51	19.878±0.189	1.0	3.8
J0230-0750	2006 Oct 08	02:30:17.7	-07:50:36.6	No	02:30:17.659	-07:50:36.63	113.50	115.36	19.546±0.209	1.1	3.2
J0230-0830	2006 Oct 08	02:30:25.7	-08:30:42.6	Yes	02:30:26.674	-08:30:42.87	145.81	245.20	19.513±0.247	1.2	3.2
J2202-0008	2006 Oct 10	22:02:01.2	-00:08:34.1	DL	22:02:01.362	-00:08:37.10	87.12	98.21	18.321±0.071	0.9	1.7
...	...	22:02:01.6	-00:08:40.4	DL	...	...	39.76	45.54	...	...	...
J2206-0054	2006 Oct 10	22:06:14.8	-00:54:34.6	No	22:06:14.85	8 -00:54:34.89	49.81	50.43	18.123±0.066	1.0	1.6
J2309-0029	2006 Oct 10	23:09:39.5	-00:29:36.9	DL	23:09:39.214	-00:29:43.23	87.71	89.32	19.810±0.188	1.2	3.7
...	...	23:09:38.6	-00:29:54.9	...	...	...	6.00	6.50	...	...	...
J2351-0027	2006 Oct 10	23:51:48.8	-00:27:16.3	No	23:51:48.822	-00:27:15.99	50.27	53.14	18.770±0.152	1.2	2.2
J0109-0853	2006 Oct 10	01:09:30.1	-08:53:01.4	DL	01:09:30.268	-08:53:05.01	251.61	267.39	19.204±0.151	1.2	2.7
...	...	01:09:30.5	-08:53:13.3	DL	...	...	31.60	35.33	...	...	...
J0135-0007	2006 Oct 10	01:35:12.9	-00:07:37.5	Yes	01:35:12.874	-00:07:37.53	115.43	146.45	19.217±0.100	1.0	2.7
J0148-0928	2006 Oct 10	01:48:06.5	-09:28:00.2	DL	01:48:06.068	-09:27:39.87	180.24	195.69	17.959±0.059	1.3	1.5
...	...	01:48:05.6	-09:27:13.9	DL	...	...	...	...	...	...	...
J0208+0023	2006 Oct 10	02:08:10.9	+00:23:09.6	DL	02:08:11.018	+00:23:06.15	187.67	200.06	18.640±0.180	1.2	2.0
...	...	02:08:11.2	+00:23:04.6	DL	...	...	212.92	216.06	...	...	...

[1] There are two sources associated with this object

Table 3.4: 2005-2006 Non-Detections

Object Name	date	radio RA	radio DEC	Extended?	f_{peak}(mJy)	f_{int}(mJy)	$1\sigma K_S limit$	$2\sigma K_S limit$	seeing($''$)	$2\sigma z_{Kz}$
J0051-0008	2005 Sep 17	00:51:03.2	-00:08:34.4	No	52.78	53.24	>20.64	>19.86	1.4	3.8
J2134+0110	2005 Sep 17	21:34:58.9	+01:10:15.5	No	52.70	55.69	>20.66	> 19.89	1.2	3.8
J0228+0031	2005 Sep 18	02:28:06.0	+00:31:18.7	Yes	187.94	268.19	>21.81	>20.99	1.1	6.6
J2119+0031	2005 Sep 19	21:19:25.5	+00:31:41.4	No	70.75	71.81	>20.84	>20.11	1.0	4.3
J2144+0019	2005 Sep 19	21:44:12.2	+00:19:21.8	No	134.94	138.40	>21.41	> 20.63	1.0	5.5
J2325-0021	2005 Sep 19	23:25:57.9	-00:21:23.5	DL	59.95	64.19	>20.93	>20.19	1.0	4.4
···	···	23:25:59.8	-00:21:32.0	···	9.26	14.19	···	···	···	···
J0905+3814	2006 Mar 16	09:05:13.1	+38:14:34.6	No	159.60	162.74	>22.09	>21.31	1.0	7.7
J1006+5621	2006 Mar 16	10:06:39.5	+56:21:18.3	No	154.92	164.60	>21.57	>20.86	1.0	6.2
J0856+4326	2006 Mar 17	08:56:18.1	+43:26:22.1	No	101.04	103.89	>21.77	>21.00	1.3	6.6
J0737+4128	2006 Mar 18	07:37:11.3	+41:28:33.6	No	118.14	122.24	>22.13	>21.33	1.1	7.8
J1249+4131	2006 Mar 18	12:49:56.6	+41:31:01.7	No	188.19	191.86	>21.90	>21.13	1.1	7.1
J1221+3543	2006 May 12	12:21:13.2	+35:43:00.9	No	195.52	200.14	>20.69	>19.97	1.2	4.0
J1629+2216	2006 May 12	16:29:40.2	+22:16:36.9	No	168.78	185.52	>21.29	>20.53	1.1	5.23
J1421+3835	2006 May 13	14:21:01.6	+38:35:45.3	No	135.06	146.76	>21.09	>20.35	1.1	4.8
J1547+3954	2006 May 13	15:47:40.2	+39:54:38.2	No	123.48	129.73	>21.03	>20.26	1.2	4.6
J1622+3313	2006 May 15	16:22:20.9	+33:13:19.9	Yes	87.13	109.49	>20.49	>19.76	1.0	3.6
J0231-0914	2006 Oct 07	02:31:59.3	-09:14:13.6	No	163.29	165.91	>20.93	>20.17	1.3	4.4
J0251-0114	2006 Oct 07	02:51:55.9	-01:14:11.3	No	69.31	70.75	>20.69	>19.98	1.2	4.0
J2242-0808	2006 Oct 08	22:42:34.1	-08:08:21.9	No	125.64	129.97	>21.43	>20.66	1.1	5.6
J0028-0027	2006 Oct 08	00:28:43.7	-00:27:29.3	No	54.55	59.17	>21.02	>20.29	1.1	4.6

In 2003-2004 we observed a total of 96 unique objects, detecting 70 of these at a $2\,\sigma$ level to a magnitude limit of $K \approx 19.5$ in most cases. During 2005-2006 we obtained imaging for 93 additional radio galaxies, 73 of which are detected in the deeper exposures, which reach $K_S \approx 20 - 21$, depending on seeing and conditions. Three objects, *J1102+0250*, *J1237+0135*, and *J1606+4751* show highly extended double radio lobes with complex morphologies. Subsequent visual inspection of the coadded *gri* SDSS images for these objects reveals a probable optical counterpart that was missed in an early visual inspection to eliminate optical identifications to extended objects. They thus do not meet our selection criteria, and we include them here merely for completeness. The total useable areal coverage of the infrared fields is 18096 square arcminutes (5.03 square degrees). This excludes two fields: *J0742+3256*, where a transient problem with the detector corrupted a portion of the field but did not affect the radio galaxy target, and *J0251-0114* where half of the observed field is not covered by SDSS imaging. This total area also excludes masked 20-45 arcsecond radius regions around saturated stars ($K \leq 8 - 9$ depending on individual frame exposure time) where the image corrupted by the high counts in adjacent FLAMINGOS frames. Of the 189 target objects, 38 are double lobed or multiple radio sources, having multiple components in the FIRST catalog. All but five of these multiple sources are detected in the NIR. In addition, 31 radio galaxies appear to be resolved in the radio postage stamp images, and 27 of these are identified with K-band or K_S-band counterparts.

Figure 3.9 shows images for a selection of our K-band detected objects. FIRST contours are overlaid with the outer contour at 5 mJy, and each subsequent contour indicating an increase by a factor of two. Postage stamp images for all galaxies can be found at `http://lahmu.phyast.pitt.edu/dragons/`.

Figure 3.10 shows the distribution of K-band magnitudes for our observed objects. The solid red histogram represents $2\,\sigma$ lower limits for our non-detections. The solid vertical line represents the magnitude of an object at our expected redshift cutoff of $z = 1.7$, given our fit to the $K - z$ relation. The hatched region represents the approximate spread of magnitudes for objects that follow the $K - z$ relation at this cutoff redshift, i. e. our selection criteria should cut out all objects below a K-band magnitude of $K \sim 17.6$. Figure 3.10 shows that there is a sizeable population of objects that are brighter than expected in the NIR. We

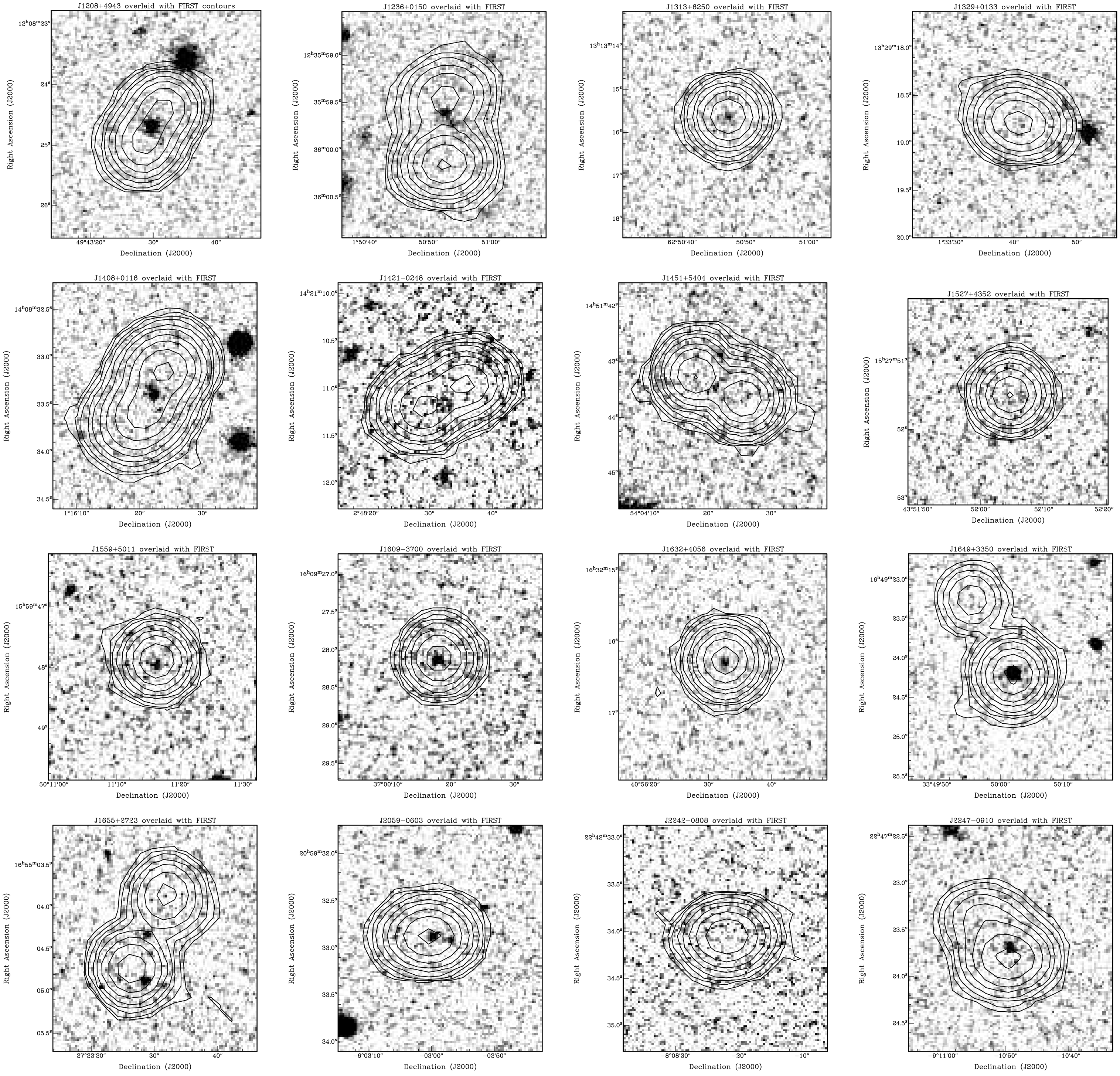

Figure 3.9 A selection of K-band images. North is to the right and East is down. FIRST radio contours are overlaid with an outer contour at 5mJy, and each subsequent contour indicating an increase by a factor of two.

have dubbed these objects "Red DRaGONS", and they will be discussed in detail in Section 3.8. Also shown in Figure 3.10 is the subset of radio galaxies selected within SDSS stripe 82, where deeper optical data allows us to select radio galaxies with fainter r-band limits (see Section 3.1.1 for details). The blue histogram shows detected galaxies, while the filled magenta represents those undetected. As can be seen, the deeper optical data does, indeed, select a fainter sample of radio galaxies.

Figure 3.11 shows the estimated redshift distribution based on converting K-band magnitudes into redshifts using our linear fit to the $K - z$ Hubble diagram. Caution is advised in interpreting this histogram, because of the large intrinsic scatter in the $K - z$ relation. The shaded portion of the histogram represents the lower limits on the estimated redshifts for the non-detected objects. The Monte-Carlo simulation of the Dunlop and Peacock dN/dz convolved with our selection criteria from Figure 3.3 is shown for comparison. If we assign redshifts to the radio galaxies based on the linear fit to the $K - z$ diagram, the mean redshift for this sample is $z = 2.7$ and the median redshift is $z = 2.2$. Comparison with the expected redshift distribution in Figure 3.11 shows that we have 54 objects with $K < 18.3$ that we expected to be excluded from our sample based on our model color tracks. While three of these objects are resolved in the radio images and subsequent closer examination revealed counterpart objects in SDSS, as indicated above, almost one third of our sample are brighter in K than expected. Much of this can be attributed to the large scatter in the $K - z$ relation if these galaxies are toward the upper end of the redshift range given their K magnitude. As an extreme example, the previously observed radio galaxy *3C 257* (J1123+0530) is known to be at $z = 2.474$, while its $K = 17.51$ magnitude corresponds to $z \sim 1.2$ on a linear fit to the $K - z$ diagram, indicative of the large intrinsic scatter in the $K - z$ relation. van Breugel et al. (1998) point out that $H\alpha$ falls into the K-band for *3C 257*, which may explain its relative brightness in K. Similar line contamination may be responsible for some of the brighter than expected objects in our sample, but even this does not fully explain the brightest and reddest of our objects, which are discussed in Section 3.8.

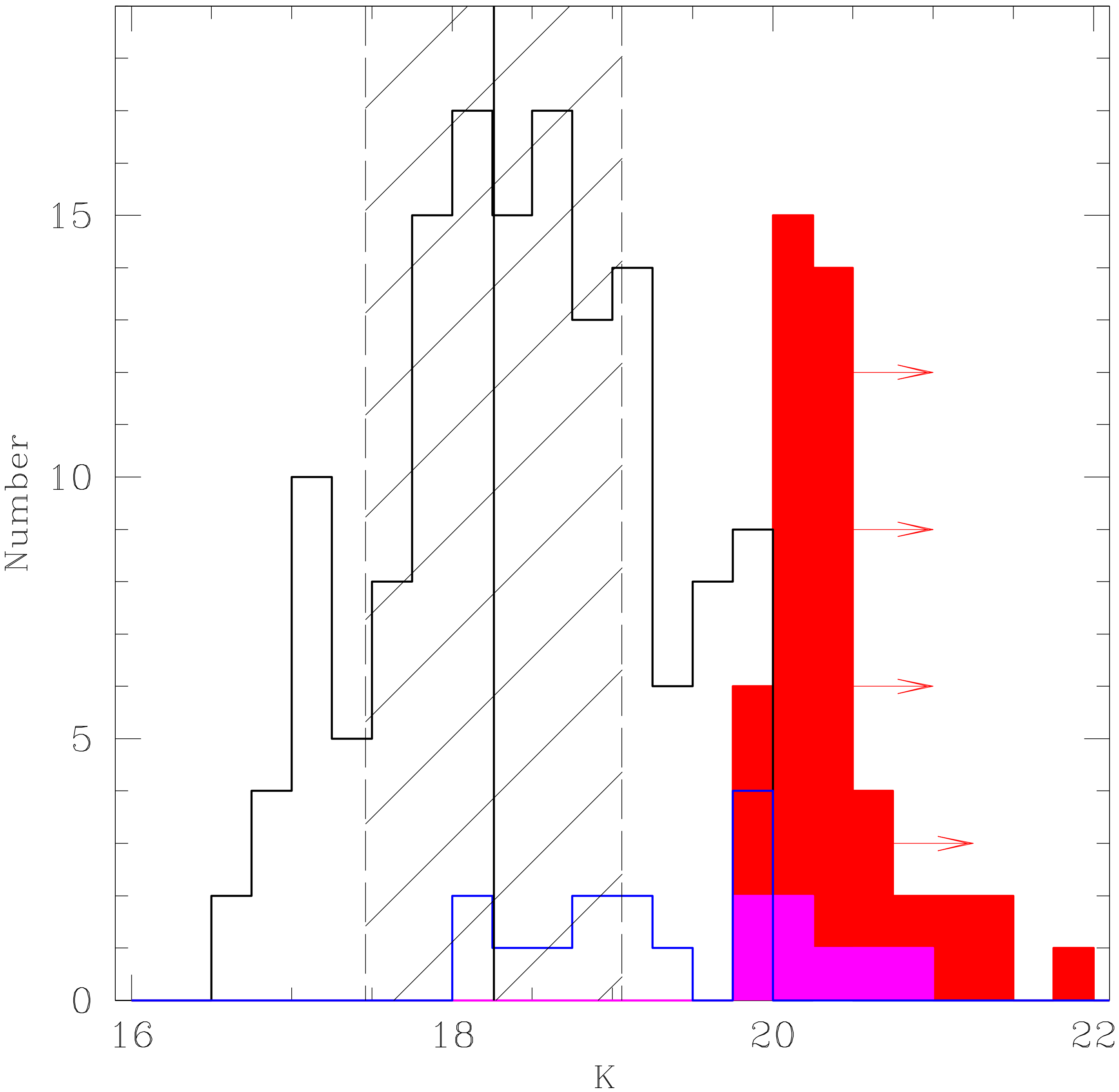

Figure 3.10 Distribution of K-band magnitudes for the observed objects. the black histogram represents detected objects, while the filled red histogram represents the $2\,\sigma$ limiting magnitudes of the non-detections. The solid vertical line represents the K-band magnitude for a galaxy at our expected lower redshift limit of $z = 1.7$ and the shaded area represents the approximate scatter given the $K - z$ diagram at this redshift. The blue and magenta histograms represent objects, detected and not detected respectively, selected from deep SDSS data.

3.6.1 Radio Spectral Index

Until now, the only widely used method for identifying high redshift radio galaxies, other than time consuming and expensive complete radio follow up surveys, was the Ultra Steep Spectrum (USS) radio galaxy selection method. The radio spectral index (α, given by $S_\nu \propto \nu^{-\alpha}$), assumes a power law form for the radio spectrum. The USS method was first adopted when it was noted that the fraction of USS sources identified with optical sources was much lower than for the overall population of radio sources (Blumenthal and Miley, 1979; Tielens et al., 1979). The USS sources also tend to have smaller angular size (Tielens et al., 1979) and are, therefore, more likely to be at higher redshift. It has also been noted that radio spectral index tends to steepen at shorter wavelengths, so selecting the steepest spectrum sources should preferentially select higher redshift sources, where the steeper rest frame portion of the radio spectrum has redshifted to longer wavelengths (analogous to a K-correction). Note, however, that the original motivation for the USS selection, namely fainter optical magnitudes, is related to the DRaGONS selection criteria.

Klamer et al. (2006) (and references therein) have compiled several theories as to why high redshift sources would have steeper radio spectra, and also posit a new one: In addition to noting the steepening with frequency, they note that the steepening could be due to enhanced inverse-Compton losses from scattering with cosmic microwave background photons, which have a higher energy density in the past. A third theory is that the correlation is actually between host galaxy luminosity and spectral slope, and the USS technique is selecting the brightest and most massive galaxies, in which case the USS selection is essentially due to a Malmquist bias. The novel explanation proposed by Klamer et al. (2006) notes that low redshift steep spectrum sources overwhelmingly reside in high density environments. If this correlation of density and α extends to higher redshifts, combined with evidence that high redshift radio galaxies preferentially occupy high density regions, this naturally explains the relation between redshift and spectral index, known as the $z - \alpha$ relation.

Many groups have employed this technique (e.g. Roettgering et al., 1994; van Breugel et al., 1998; De Breuck et al., 2000, 2001), which is responsible for finding the bulk of spectroscopically confirmed high redshift radio galaxies. The two obvious variables in USS searches

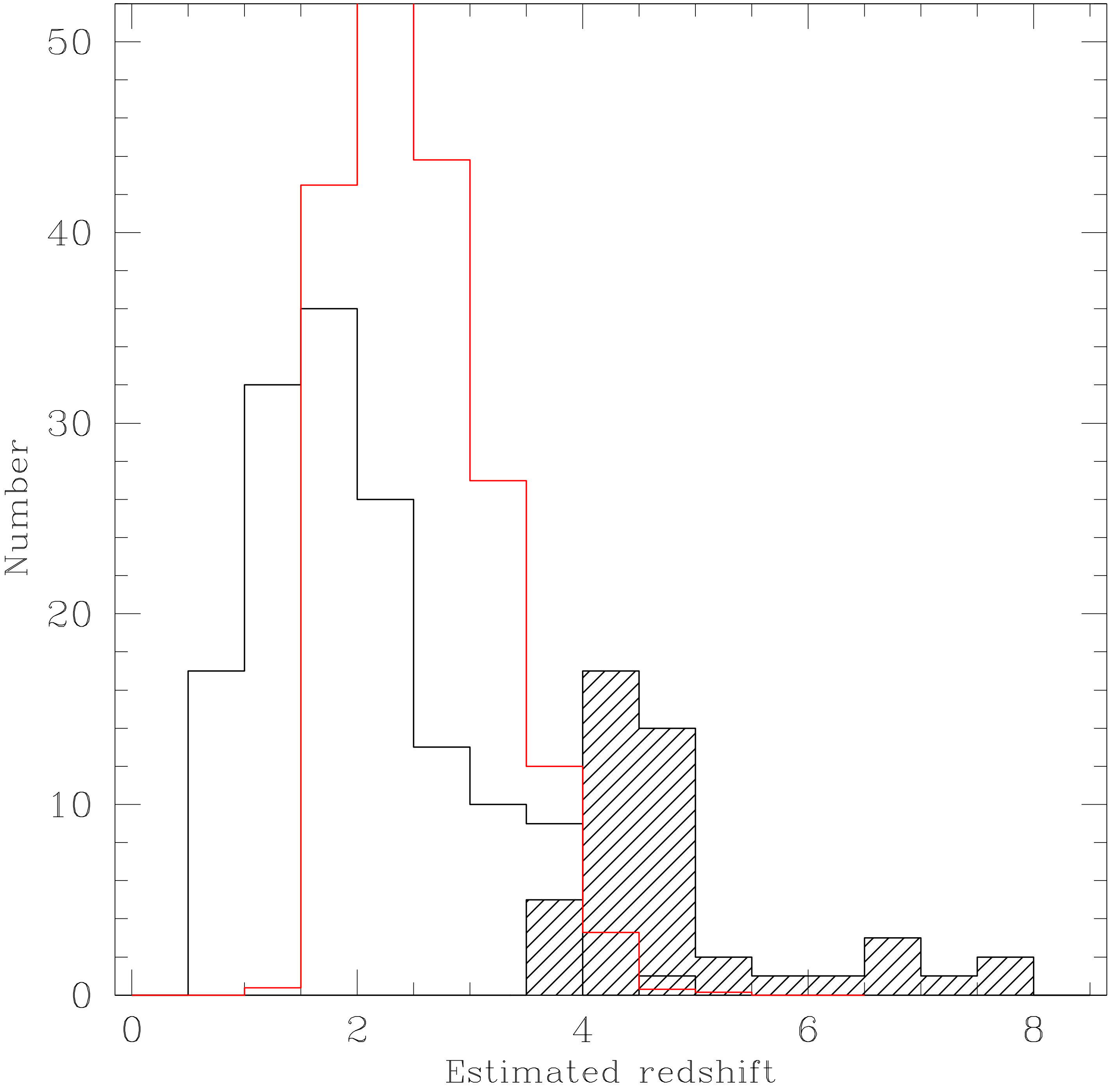

Figure 3.11 Estimated redshift distribution based on a linear fit to the $K - z$ Hubble diagram. The shaded histogram represents lower limit redshift estimates from the magnitude lower limits. The red histogram shows the distribution expected from convolving the Dunlop and Peacock (1990) dN/dz with our selection criteria.

are: what spectral slope is considered steep, and which frequencies to use in calculating α? USS cutoffs range from $\alpha > 0.8$ (van Breugel et al., 1998) to $\alpha > 1.3$ (De Breuck et al., 2000). Table 3.5 shows the radio spectral index computed from FIRST and the Texas 365 MHz survey (Douglas et al., 1996) for DRaGONS galaxies. van Breugel et al. (1998) used an ultra-steep spectrum (USS) cut of $\alpha_{365}^{1400} > 0.8$ to select a sample of high redshift radio galaxy candidates. Of our 189 targets, 141 have observations at 365 MHz, and of these 46 have $\alpha < 0.8$ and would not be selected by the van Breugel et al. (1998) criteria. Given the more stringent $\alpha > 1.3$ of De Breuck et al. (2001), only eight of our observed sources meet this criteria, with only half of those above $z_{K-z} = 2$.

Figure 3.12 shows the spectral index of our targets as a function of z_{K-z}. Figure 3.13 shows a histogram of the redshifts inferred from the $K - z$ diagram for two spectral index ranges, flatter and steeper than $\alpha = 0.8$. The median redshift of the $\alpha < 0.8$ sample is $z_{K-z} = 2.1$ and the mean is $z_{K-z} = 2.40$, compared to a median of $z_{K-z} = 2.2$ and mean $z_{K-z} = 2.50$ for the total sample, and median $z_{K-z} = 2.3$ and mean $z_{K-z} = 2.64$ for the $\alpha > 0.8$ sample. This suggests that flatter spectral slope systems may contribute a large fraction of the HzRG population. The insensitivity of our method to spectral slope allows us to select candidates that would be missed by USS selection techniques. Applying an USS criteria to our dataset would eliminate a full third of the targets. Also evident is that the USS technique has a similar number of probable low redshift ($z < 2$) sources. Thus, there is not a large discernible gain in efficiency with the USS method over our radio-optical selection. Figure 3.14 shows the 1.4 GHz luminosities of a subset of the galaxies given their α_{365}^{1400} and $K - z$ redshift. The three lines represent 100 mJy, 500 mJy, and 1 Jy 1.4 GHz flux limits, assuming $\alpha = 0.4$. Given the redshift distribution inferred from the $K - z$ diagram, it appears that we are at least as efficient as USS techniques at identifying $z > 2$ and $z > 3$ radio galaxies. In addition, we appear to select a large population of shallow spectrum radio sources missed by USS techniques.

Table 3.6 lists a subset of our candidates with additional radio observations at 4.85 GHz (From Gregory and Condon, 1991) and 151 MHz (From the 6C survey, Hales et al., 1988, 1990). This table shows the frequency dependence of the two point spectral slope. Several of the sources show significant deviations from a power law over the frequency range in question, showing that the USS sample selection will differ depending on frequencies used, while our selection method is unaffected by objects with concave radio spectra.

Figure 3.15, which is Figure 9 from De Breuck et al. (2001), shows the putative $z - \alpha$ relation for the 325 MHz WENSS or 365 MHz Texas and 1.4 GHz NVSS surveys plotted against redshift for 36 3CR (Spinrad et al., 1985), 152 MRC (McCarthy et al., 1996), and 35 WN/TN sources. The solid line shows a linear fit to the 3CR and MRC data while the dashed horizontal line indicates the spectral index cutoff we used in the WN/TN USS samples. Note that they define $S_\nu \propto \nu^\alpha$, so the spectral index has an additional minus sign. This Figure shows that there is a large amount of scatter in the $z - \alpha$ relation and is based on a small number of radio galaxies at high redshift. If even a fraction of DRaGONS galaxies with shallow spectral indexes are confirmed at $z > 3$, then they will have a large impact on the empirical fits to the $z - \alpha$ relation.

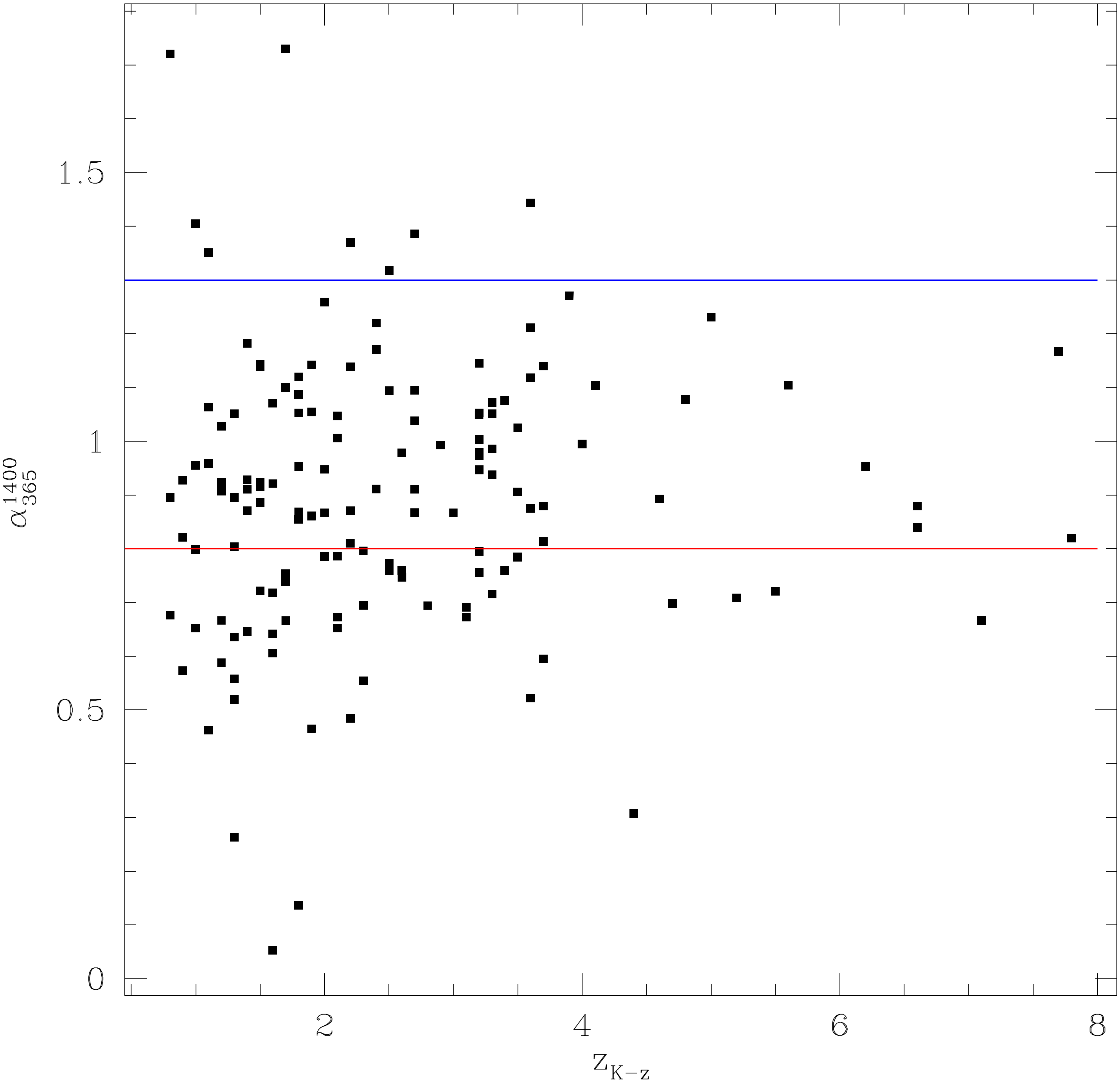

Figure 3.12 Spectral slope as a function of z_{K-z} for the 141 targets with $S_{365\,MHz}$ flux densities measured in the Texas survey. The red horizontal line represents the $\alpha > 0.8$ USS cut of van Breugel et al. (1998) and the blue line represents the $\alpha > 1.3$ cut of De Breuck et al. (2000)

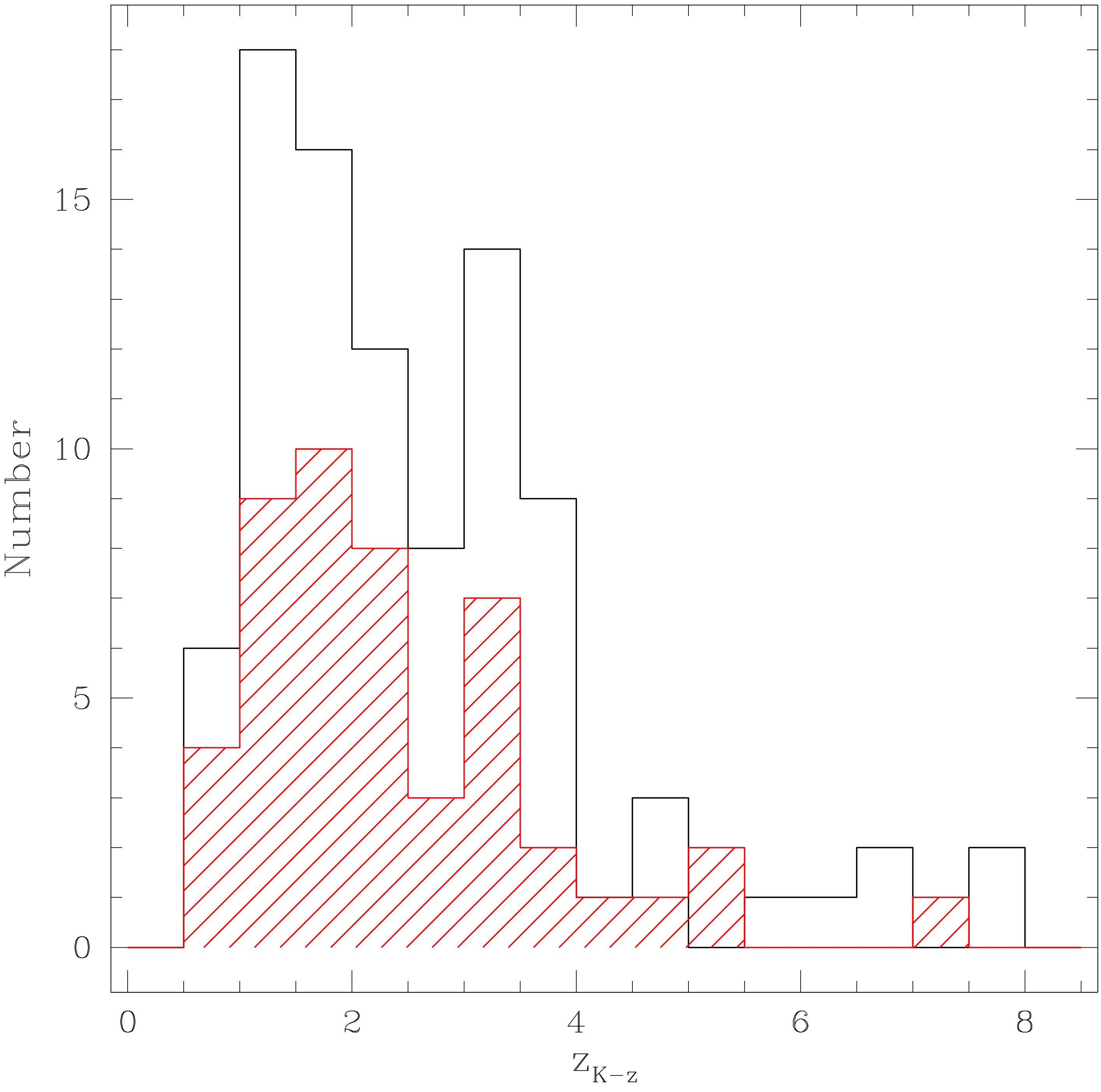

Figure 3.13 Histogram of redshifts inferred from the $K-z$ diagram divided into $\alpha < 0.8$(red shaded) and ultra-steep $\alpha > 0.8$ emphasizing the presence at high redshift ($z_{K-z} > 2$) of flatter spectrum sources.

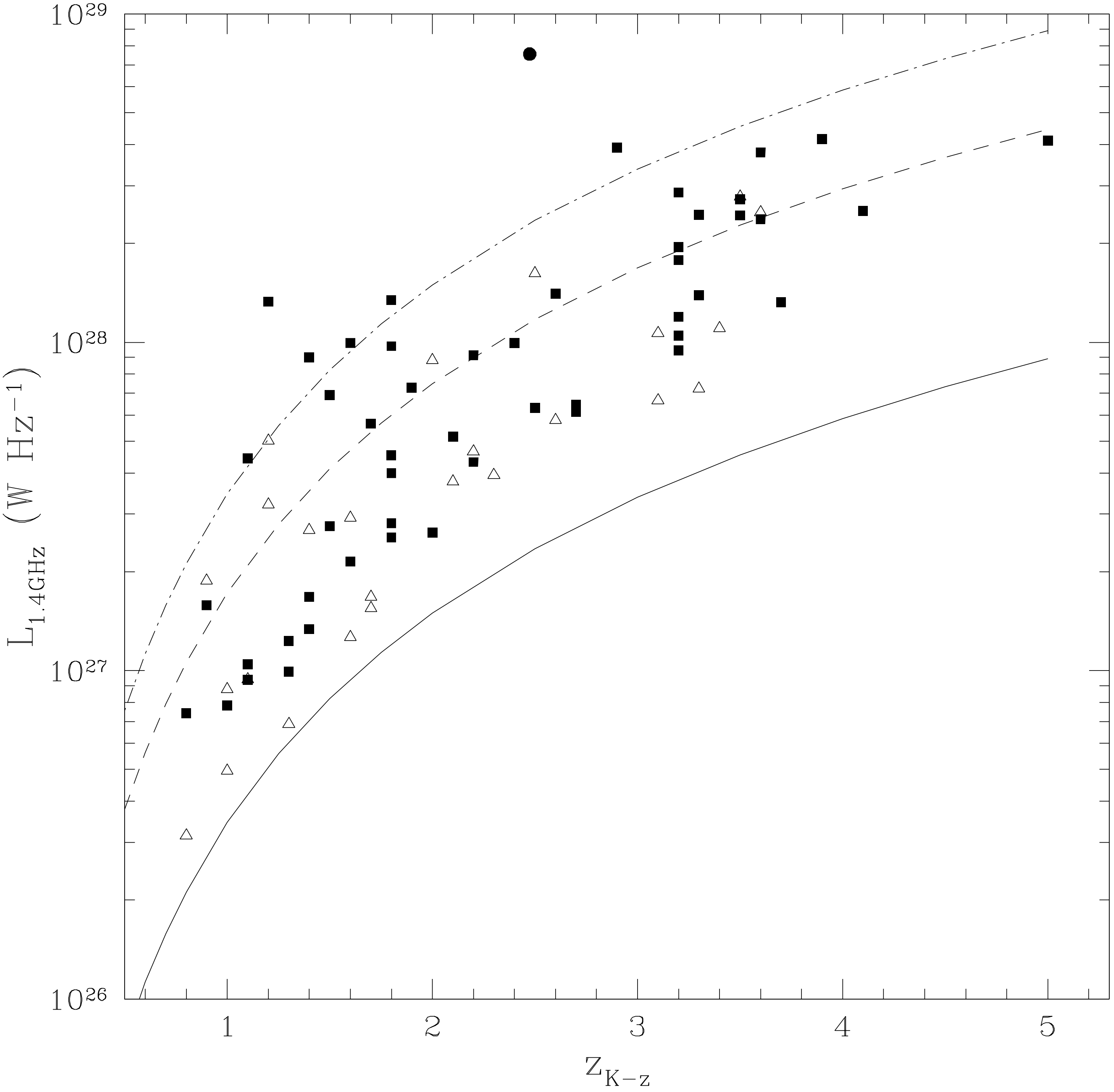

Figure 3.14 1.4 GHz radio luminosity as a function of $K - z$ redshift. The lines represent 100 mJy (solid), 500 mJy (dashed), and 1 Jy (dot-dashed) flux density limits assuming a spectral slope $\alpha = 0.4$. Squares mark objects with $\alpha_{365}^{1400} > 0.8$, triangles indicate $\alpha_{365}^{1400} \leq 0.8$. The solid black circle marks the radio luminosity of 3C 257 with spectroscopic redshift $z = 2.474$.

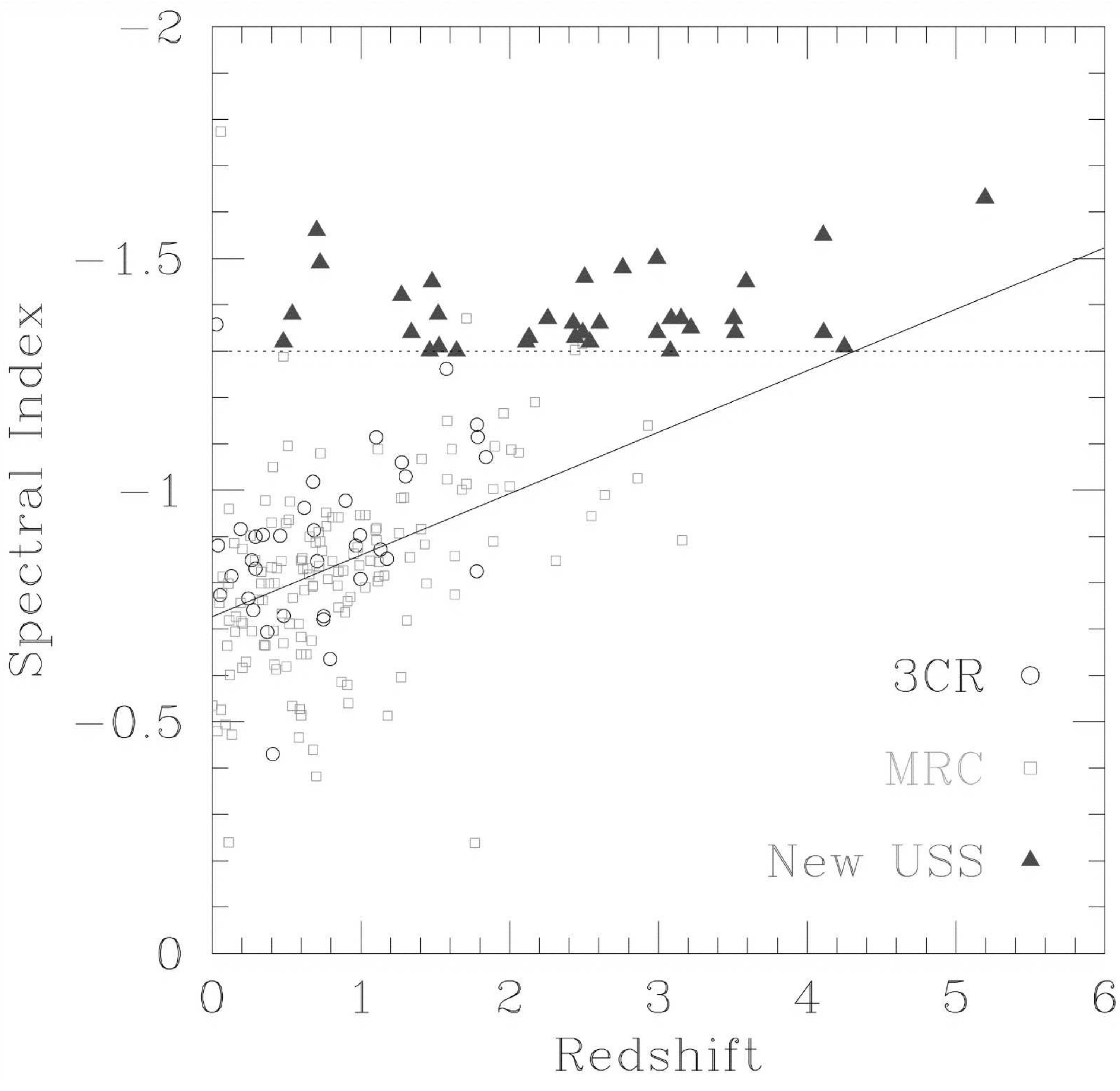

Figure 3.15 (Taken from De Breuck et al. (2001), their Figure 9):Spectral index from the 325 MHz WENSS or 365 MHz Texas and 1.4 GHz NVSS survey plotted against redshift for 36 3CR (Spinrad et al., 1985), 152 MRC (McCarthy et al., 1996), and 35 WN/TN sources. The solid line shows a linear fit to the 3CR and MRC data while the dashed horizontal line indicates the spectral index cutoff used in the WN/TN USS samples.

Table 3.5: Radio Spectral Index of DRaGONS Galaxies

Name	FIRST 1.4 GHz (mJy)	Texas 365 MHz (mJy)[1]	α_{365}^{1400}
J0742+3256	144.60	426.0	0.80
J0831+5210	246.00	837.0	0.91
J0941+0127	120.56	290.0	0.65
J0958+0324	638.00	2666.6	1.06
J1022+0357	200.86	823.0	1.05
J1028+0144	114.81	391.0	0.91
J1044+0538	130.20	...	...
J1047+0216	125.81	311.0	0.67
J1102+0250	161.00	1626.0	1.72
J1123+0530	1743.00	5903.0	0.91
J1135+0548	212.60	982.0	1.14
J1144+0254	119.18	445.0	0.98
J1155+0305	162.80	591.0	0.96
J1208+0414	641.00	2212.0	0.92
J1208+4943	198.98	678.0	0.92
J1221+0248	142.87	510.0	0.95
J1234+0024	100.55	700.0	1.44
J1236+0150	154.53	558.0	0.96
J1237+0135	426.00	1971.0	1.14
J1240-0017	150.90	419.0	0.76
J1250+6043	304.05	725.0	0.65
J1259+0559	178.90	806.0	1.12
J1303+0026	104.04	401.0	1.00
J1308-0022	241.17	...	...
J1312+0009	112.60	490.0	1.09
J1313+6250	132.18	476.0	0.95
J1314+0330	250.05	845.0	0.91
J1315+0533	146.96	423.0	0.79
J1329+0133	102.64	...	...
J1332+0101	411.00	1430.0	0.93
J1336+0207	127.76	410.0	0.87
J1350+0352	104.28	546.0	1.23
J1400+0053	130.80	...	...
J1402+0342	540.40	1192.0	0.59
J1403+6048	794.62	1946.0	0.67
J1408+0116	612.75	1325.0	0.57
J1411+0124	186.50	1029.0	1.27
J1421+0248	342.63	984.0	0.78
J1423+0139	211.65	394.0	0.46
J1431+0511	226.17	956.0	1.07
J1438+0150	118.50	413.0	0.93
J1438+6149	121.27	...	...
J1451+5404	554.63	2108.0	0.99

Continued on Next Page...

Table 3.5 – Continued

Name	FIRST 1.4 GHz (mJy)	Texas 365 MHz (mJy)[1]	α_{365}^{1400}
J1452+0032	639.00	3133.0	1.18
J1500+0031	145.90	549.0	0.99
J1507+6003	189.23	···	···
J1510+5244	505.76	1596.0	0.85
J1515+5744	144.16	400.0	0.76
J1523-0018	231.44	444.0	0.48
J1526+0408	156.40	504.0	0.87
J1527+4352	140.11	···	···
J1532+4432	249.65	···	···
J1541+5259	193.00	565.0	0.80
J1543+5711	103.39	279.0	0.74
J1547+4839	214.75	···	···
J1548+0036	126.00	313.0	0.68
J1548-0033	432.00	1221.0	0.77
J1549+4719	106.33	252.0	0.64
J1554+4729	149.73	612.0	1.05
J1554+3942	169.23	697.0	1.05
J1557+4657	204.20	756.0	0.97
J1559+5011	130.28	419.0	0.87
J1604+4746	366.10	···	···
J1604-0013	128.28	···	···
J1606+4751	109.02	670.0	1.35
J1609+3700	102.52	206.0	0.52
J1617+4848	244.32	···	···
J1618+5210	112.29	294.0	0.72
J1629+4937	197.05	499.0	0.69
J1632+4056	203.15	···	···
J1634+4155	263.47	1155.0	1.10
J1636+4808	263.30	981.0	0.98
J1637+3223	147.47	438.0	0.81
J1641+4209	263.68	1186.0	1.12
J1643+4518	110.39	304.0	0.75
J1645+4152	115.96	···	···
J1648+4233	169.30	···	···
J1648+3623	257.00	1197.0	1.14
J1649+3350	163.91	···	···
J1654+4125	228.56	600.0	0.72
J1655+2723	169.53	···	···
J1656+2707	164.76	347.0	0.55
J1700+3830	430.20	868.0	0.52
J1707+2408	169.15	787.0	1.14
J1711+3047	124.77	407.0	0.88
J1715+3027	385.34	1108.0	0.79
J2059-0603	161.72	···	···

Continued on Next Page…

Table 3.5 – Continued

Name	FIRST 1.4 GHz (mJy)	Texas 365 MHz (mJy)[1]	α_{365}^{1400}
J2107-0701	550.60	2373.0	1.09
J2221-0901	234.50	930.0	1.02
J2223-0757	108.34	361.0	0.90
J2242-0808	129.97	573.0	1.10
J2247-0910	103.37	...	...
J2309-0846	111.67	...	...
J2316-0846	105.40	338.0	0.87
J2336-0838	244.82	1137.0	1.14
J2337-0852	120.14	507.0	1.07
J2115-0743	294.32	665	0.61
J2215-0900	125.05	637	1.21
J0051-0008	53.24	...	...
J0240-0022	76.85	...	...
J2134+0110	55.69	...	...
J2230+0013	72.35	...	...
J2148-0836	116.59	274	0.64
J2150-0055	51.51	...	...
J0205-0819	128.23	422	0.89
J0228+0031	268.19	828	0.84
J0256-0659	255.58	1018	1.03
J2119+0031	71.81	...	...
J2144+0019	138.4	365	0.72
J2258-0958	232.8	643	0.76
J2317+0029	86.68	278	0.87
J2325-0021	64.19	320	1.19
J2252+0003	68.09	...	...
J2256+0038	66.71	185	0.76
J0725+3826	232.92	805	0.92
J0819+3504	102.64	436	1.08
J0905+3814	162.74	781	1.17
J1006+5621	164.6	593	0.95
J1106+4722	125.48	...	...
J1141+3857	148.04	178	0.14
J1331+4108	111.75	459	1.05
J1530+2631	108.98	562	1.22
J1619+1433	692.11	2356	0.91
J1636+3409	124.91	278	0.60
J0732+4335	383.45	976	0.69
J0856+4326	103.89	339	0.88
J0940+4649	124.78	...	...
J1052+3201	127.92	325	0.69
J1221+4114	100.78	...	...
J1438+2821	831.68	2508	0.82
J1600+3304	169.74	...	...

Continued on Next Page...

Table 3.5 – Continued

Name	FIRST 1.4 GHz (mJy)	Texas 365 MHz (mJy)[1]	α_{365}^{1400}
J0737+4128	122.24	368	0.82
J0845+2849	102.39	423	1.06
J0948+6416	214.55	549	0.70
J1123+6130	108.38	···	···
J1249+4131	191.86	470	0.67
J1356+0958	136.79	529	1.01
J1546+1754	109.26	722	1.40
J1643+2631	136.46	741	1.26
J1047+0216	125.81	311	0.67
J1429+3426	260.41	919	0.94
J1514+4135	149.02	407	0.75
J1554+3400	107.22	227	0.56
J1056+0624	181.31	585	0.87
J1221+3543	200.14	763	1.00
J1326+4434	179.33	335	0.46
J1442+3042	540.18	580	0.05
J1558+3517	384.32	1317	0.92
J1629+2216	185.52	481	0.71
J1630+2452	102.07	340	0.90
J1255+3046	197.96	···	···
J1421+3835	146.76	625	1.08
J1547+3954	129.73	431	0.89
J1641+2005	113.5	547	1.17
J1642+2414	165.12	481	0.80
J1100+3324	101.1	595	1.32
J1245+3711	121.11	353	0.80
J1347+4113	170.83	···	···
J1515+2458	220.98	315	0.26
J1615+3216	207.15	···	···
J1630+1308	147.94	471	0.86
J1636+2347	188.29	···	···
J1622+3313	109.49	···	···
J1303+3509	449.71	1082	0.65
J1417+0710	505.73	5173	1.73
J1530+0644	274.76	673	0.67
J1601+0605	218.05	896	1.05
J1615+1643	356.23	1064	0.81
J1629+2851	525.55	1388	0.72
J2137-0738	107.77	···	···
J2200+0014	85.7	278	0.88
J0150-0952	203.47	···	···
J0230-0909	200.8	875	1.09
J0231-0914	165.91	251	0.31
J0251-0114	70.75	···	···

Continued on Next Page...

Table 3.5 – Continued

Name	FIRST 1.4 GHz (mJy)	Texas 365 MHz (mJy)[1]	α_{365}^{1400}
J0252-0849	102.92	⋯	⋯
J2145-0049	93.64	⋯	⋯
J2150-0055	51.51	⋯	⋯
J2242-0808	129.97	573	1.10
J0028-0027	59.17	⋯	⋯
J0230-0750	115.36	475	1.05
J0230-0830	245.2	⋯	⋯
J2202-0008	143.75	⋯	⋯
J2206-0054	50.43	⋯	⋯
J2309-0029	95.02	440	1.14
J2351-0027	53.14	335	1.37
J0109-0853	302.72	1222	1.04
J0135-0007	146.45	944	1.39
J0148-0928	195.69	⋯	⋯
J0208+0023	416.12	1440	0.92

[1] From Douglas et al. (1996)

Table 3.6: Multifrequency Radio Spectral Indexes

Name	4.85 GHz (mJy)[1]	FIRST 1.4 GHz (mJy)	Texas 365 MHz (mJy)	151 MHz (mJy)[2]	α_{365}^{1400}	α_{1400}^{4850}	α_{151}^{1400}	α_{151}^{365}
J1123+0530	526 ± 73	1743.0 ± 69.7	5903 ± 140	…	0.9 ± 0.041	1.0 ± 0.12	…	…
J1208+4943	58 ± 8	199.0 ± 8.0	678 ± 34	990 ± 103	0.9 ± 0.053	1.0 ± 0.12	0.7 ± 0.052	0.4 ± 0.13
J1313+6250	29 ± 6	132.2 ± 5.3	476 ± 19	970 ± 48.5	1.0 ± 0.048	1.2 ± 0.17	0.9 ± 0.032	0.8 ± 0.072
J1403+6048	268 ± 26	794.6 ± 31.8	1946 ± 31	3070 ± 154	0.70 ± 0.039	0.9 ± 0.088	0.6 ± 0.032	0.5 ± 0.060
J1543+5711	25 ± 5	103.4 ± 4.1	279 ± 15	490 ± 24.5	0.70 ± 0.055	1.1 ± 0.17	0.7 ± 0.032	0.6 ± 0.083
J1554+472	34 ± 6	149.7 ± 6.0	612 ± 18	1260 ± 126	1.0 ± 0.043	1.2 ± 0.15	1.0 ± 0.050	0.8 ± 0.12
J1557+4657	39 ± 6	204.2 ± 8.2	756 ± 19	1580 ± 158	1.0 ± 0.042	1.3 ± 0.13	0.9 ± 0.050	0.8 ± 0.12
J1559+5011	37 ± 6	130.3 ± 5.2	419 ± 19	960 ± 103	0.90 ± 0.050	1.0 ± 0.14	0.9 ± 0.053	0.9 ± 0.13
J1606+4751	54 ± 8	109.0 ± 4.4	670 ± 44	1660 ± 166	1.4 ± 0.061	0.6 ± 0.13	1.2 ± 0.050	1.0 ± 0.14
J1618+5210	45 ± 7	112.3 ± 4.5	294.0 ± 20	590 ± 29.5	0.70 ± 0.063	0.7 ± 0.13	0.7 ± 0.032	0.8 ± 0.096
J1629+4937	87 ± 11	197.0 ± 7.9	499 ± 24	770 ± 103	0.70 ± 0.052	0.7 ± 0.11	0.6 ± 0.064	0.5 ± 0.16
J1637+3223	49 ± 8	147.5 ± 5.9	438 ± 24	660 ± 103	0.80 ± 0.055	0.9 ± 0.14	0.7 ± 0.074	0.5 ± 0.19
J1641+4209	67 ± 9	263.7 ± 10.5	1186 ± 25	1810 ± 181	1.1 ± 0.040	1.1 ± 0.12	0.9 ± 0.050	0.5 ± 0.12
J1643+4518	40 ± 7	110.4 ± 4.4	304 ± 20	480 ± 103	0.80 ± 0.061	0.8 ± 0.15	0.7 ± 0.099	0.5 ± 0.25
J1711+3047	41 ± 7	124.8 ± 5.0	407 ± 35	670 ± 103	0.90 ± 0.074	0.9 ± 0.14	0.8 ± 0.073	0.6 ± 0.20
J0725+3826	59 ± 9	232.92 ± 9.3	805 ±50	760 ± 75	0.92 ±0.046	1.11 ±0.123	0.53± 0.044	-0.07 ±0.132
J0819+3504	40 ± 7	102.64 ± 4.1	436 ±40	320 ± 75	1.08 ±0.068	0.76 ±0.141	0.51± 0.105	-0.35 ±0.285
J1006+5621	48 ± 7	164.6 ± 6.6	593 ±17	1130 ± 40	0.95 ±0.021	0.99 ±0.117	0.87± 0.016	0.73 ±0.052
J0732+4335	132 ± 16	383.45 ± 15.3	976 ±22	1510 ± 75	0.69 ±0.017	0.86 ±0.097	0.62± 0.022	0.49 ±0.062
J0856+4326	26 ± 6	103.89 ± 4.2	339 ±19	440 ± 50	0.88 ±0.042	1.11 ±0.186	0.65± 0.051	0.30 ±0.144
J1052+3201	42 ± 7	127.92 ± 5.1	325 ±19	250 ± 60	0.69 ±0.043	0.90 ±0.134	0.30± 0.108	-0.30 ±0.280
J1438+2821	232 ± 30	831.68 ± 33.3	2508 ±58	4060 ± 138	0.82 ±0.017	1.03 ±0.104	0.71± 0.015	0.55 ±0.047
J0737+4128	30 ± 6	122.24 ± 4.9	368 ±20	640 ± 75	0.82 ±0.040	1.13 ±0.161	0.74± 0.053	0.63 ±0.146
J0948+6416	86 ± 9	214.55 ± 8.6	549 ±48	440 ± 40	0.70 ±0.065	0.74 ±0.084	0.32± 0.041	-0.25 ±0.143
J1249+4131	81 ± 11	191.86 ± 7.7	470 ±19	750 ± 50	0.67 ±0.030	0.69 ±0.109	0.61± 0.030	0.53 ±0.088
J1429+3426	76 ± 11	260.41 ± 10.4	919 ±35	1330 ± 78	0.94 ±0.028	0.99 ±0.116	0.73± 0.026	0.42 ±0.079
J1221+3543	43 ± 8	200.14 ± 8.0	763 ±19	1260 ± 50	1.00 ±0.019	1.24 ±0.150	0.83± 0.018	0.57 ±0.053
J1326+4434	162 ± 19	179.33 ± 7.2	335 ±37	750 ± 50	0.46 ±0.082	0.08 ±0.094	0.64± 0.030	0.91 ±0.146
J1558+3517	125 ± 16	384.32 ± 15.4	1317 ±22	2130 ± 155	0.92 ±0.012	0.90 ±0.103	0.77± 0.033	0.54 ±0.085
J1100+3324	58 ± 9	101.1 ± 4.0	595 ±22	920 ± 62	1.32 ±0.028	0.45 ±0.125	0.99± 0.030	0.49 ±0.087
J1245+3711	41 ± 7	121.11 ± 4.8	353 ±20	470 ± 50	0.80 ±0.042	0.87 ±0.137	0.61± 0.048	0.32 ±0.137
J1303+3509	175 ± 15	449.71 ± 18.0	1082 ±21	1340 ± 50	0.65 ±0.014	0.76 ±0.069	0.49± 0.017	0.24 ±0.048

[1] From Gregory and Condon (1991)

[2] From Hales et al. (1988) and Hales et al. (1990)

3.7 ENVIRONMENT

If, as we assert, high redshift radio galaxies form in the most overdense regions of the early Universe, then hierarchical formation scenarios predict an enhanced number of (proto-)galaxies associated with this overdensity, as other small overdensities in the vicinity of the large overdensity will also be overdense enough to collapse very early (this is sometimes qualitatively described as “hilltops on top of hilltops”). Although the strong spatial clustering of EROs is often attributed to association with high redshift galaxy overdensities, it is only recently that direct evidence for this has been found (Georgakakis et al., 2005). We search for overdensities of both EROs and K-band selected galaxies in the vicinity of our radio galaxy candidates. As the radio galaxy is expected to be the most massive galaxy in the (proto)cluster, we expect to see an overdensity only in galaxies fainter than the radio galaxy.

We begin with a consideration of the source counts of both K-band objects, as well as EROs. Figure 3.16 shows the K-band differential number counts for the galaxies and stars in our 198 fields. No completeness corrections have been applied. Because more than half of our fields, those observed in 2003 and 2004, have total exposure times of under twenty minutes, the number counts begin to fall off at $K = 19$. Plotted for comparison are counts from Gardner et al. (1993), Szokoly et al. (1998) (K_s), Totani et al. (2001), and Cimatti et al. (2002) (from the $K20$ survey, also K_s). The raw counts are given in Table 3.7. As the Figure shows, we are in good agreement with previous infrared observations, and it appears that the radio galaxy target selection does not bias our K-band counts to the magnitude limits probed: because of the large field of view of FLAMINGOS, only a fraction of the infrared imaging ($\sim$ 10%) is within a conservatively large 2 arcminute radius around each radio galaxy, thus a modest overdensity will be diluted by the surrounding “field”.

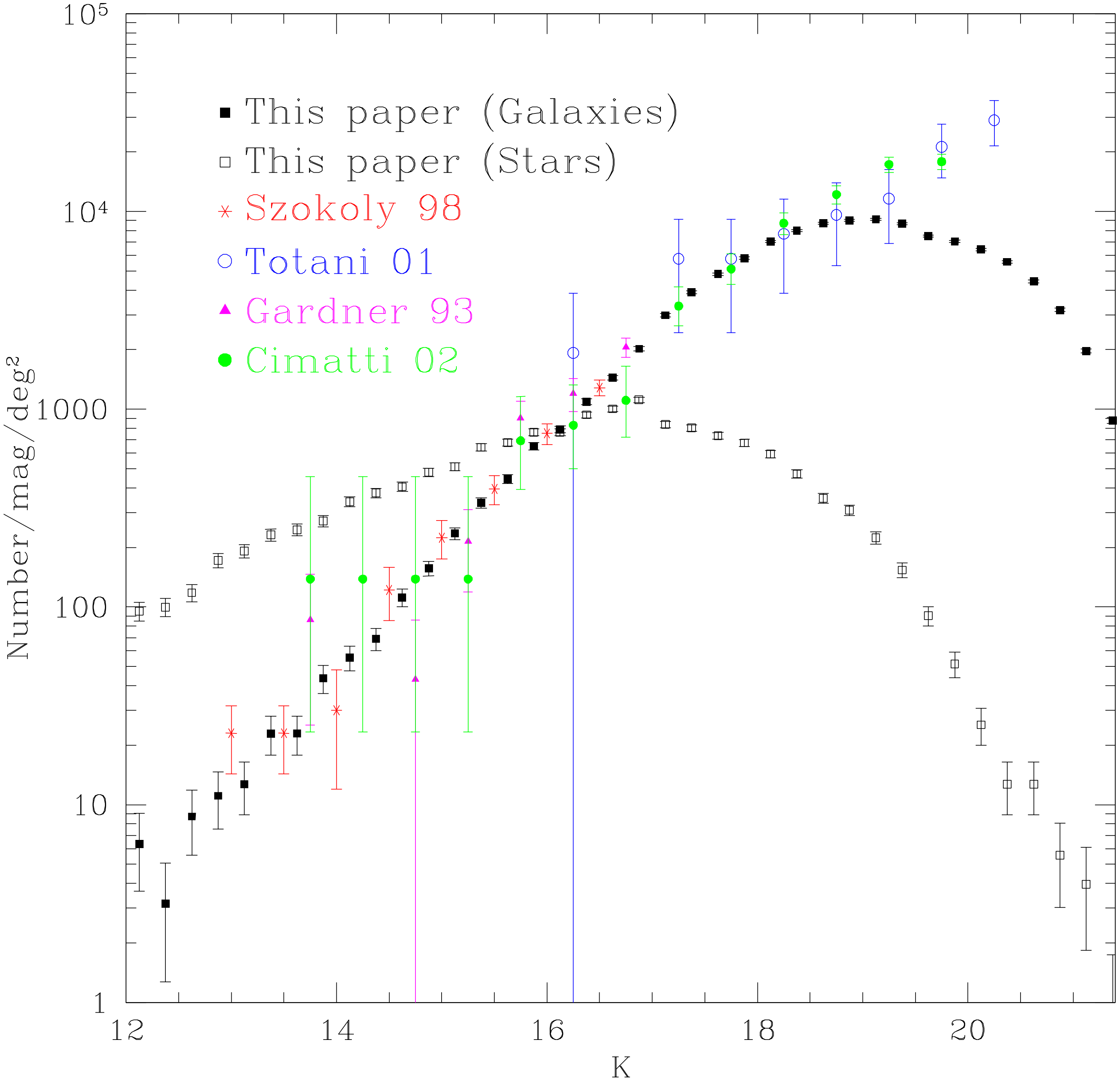

Figure 3.16 Differential K-band number counts for galaxies(filled squares) and stars (open squares) in the DRaGONS survey. Shown for comparison are the number counts from Gardner et al. (1993), Szokoly et al. (1998), Totani et al. (2001), and Cimatti et al. (2002).

Table 3.7

Differential *K*-band Number Counts

K	Galaxies	Stars
12.125	8	120
12.375	4	126
12.625	11	149
12.875	14	217
13.125	16	242
13.375	29	292
13.625	29	310
13.875	55	343
14.125	70	430
14.375	87	476
14.625	141	512
14.875	198	605
15.125	297	647
15.375	424	810
15.625	560	855
15.875	820	967
16.125	999	965
16.375	1378	1183
16.625	1821	1268
16.875	2553	1407
17.125	3773	1056
17.375	4918	1015
17.625	6079	926
17.875	7336	853
18.125	8890	749
18.375	10081	594
18.625	11008	448
18.875	11414	389
19.125	11497	283
19.375	10931	194
19.625	9467	114
19.875	8916	65
20.125	8109	32
20.375	7011	16
20.625	5593	16
20.875	4015	7
21.125	2490	5
21.375	1110	1
21.625	425	1
21.875	107	0

Figure 3.17 shows the $r - K$ as a function of K color-magnitude diagram after cross-matching our infrared catalog with the SDSS. We define an Extremely Red Object (ERO) as having $r - K \geq 5.50$ as indicated by the horizontal line on this Figure. Objects having no corresponding SDSS object within $3''$ are assigned a limiting magnitude of $r = 23.1$. This yields a total of 636 galaxy EROs with $K \leq 17.5$. Note that the K to K_S conversion mentioned in Section 3.4 has changed the number of EROs in the 2003-2004 dataset from the values from those given in Schmidt et al. (2006). This change reflects the many objects very close to the $r - K \geq 5.5$ definition of EROs evident in Figure 3.17. Figure 3.18 shows the cumulative ERO surface density for DRaGONS. Shown for comparison are the SDSS/FLAMEX ERO cumulative density for the ≈ 4.7 degrees^2 of the Boötes field (describe in Section 3.5. Error bars are estimated by varying the $r - K$ cut by the largest magnitude error in each bin. Wold et al. (2003) observe EROs surrounding $z \sim 2$ radio loud quasars, and the Figure shows a higher ERO surface density than the "field" surveys of Roche et al. (2002), Daddi et al. (2000), and Cimatti et al. (2002). It appears that we are consistent with the ERO counts of FLAMEX/SDSS, with only a slight overdensity in the $K = 17.5$ bin. This is, again, a different result than that shown in Schmidt et al. (2006), with the difference arising from the offset between K and K_S magnitudes. This lack of bright EROs is expected, as our radio targets should be the most massive and most luminous galaxies in a potential high redshift protocluster, and any associated red galaxies should be fainter by several magnitudes. It has been suggested that some of the high redshift radio galaxies are lensed by foreground clusters, which could help to account for their very large radio flux densities. The lack of observed bright EROs in the vicinity of our 189 targets shows no evidence for such lensing clusters. Because of the $r = 23.1$ limit from SDSS we are limited to studying $K \leq 17.50$ EROs for the bulk of our sample. Fainter ERO counts from deeper SDSS data and additional optical imaging from Apache Point Observatory will be discussed in Section 3.10.

Due to the small areas covered by previous ERO studies, surface densities at this bright K magnitude are uncertain. 12% (90 out of 726) of our EROs are classified as stars, similar to the $\approx 9 - 10\%$ of Mannucci et al. (2002) and Wold et al. (2003). At these bright K-band magnitudes, robust star galaxy separation is increasingly important. We note that our overall star and galaxy counts are in good agreement with Daddi et al. (2000) in the relevant magnitude range, leading us to believe that our star-galaxy separation is robust.

We now examine the clustering of EROs around our radio galaxies. We restrict our analysis to $K \leq 17.50$ EROs in order to remain complete given the $r_{\rm lim} = 23.1$ magnitude limit of our SDSS data. Because we expect the radio galaxy to be, by far, the most luminous galaxy in its local environment, we expect to see a possible overdensity around only the brightest of our targets. An overdensity of EROs with K-band magnitudes brighter than the radio galaxy would be a possible indication of a foreground structure. Field by field, the density of EROs is quite inhomogeneous, as expected. More than half of the fields have no bright EROs within $100''$ of the radio galaxy target, while twelve fields have three or more EROs within this radius; however, none of these twelve have more than one ERO within one arcminute. The densest fields have radio galaxy targets with magnitudes evenly spaced in the range $K = 17.4 - 20.6$, showing no trend of high ERO density with radio galaxy NIR brightness, contrary to our expectations. Figure 3.19 shows the average distribution of EROs with $K \leq 17.50$ as a function of radial distance from the radio galaxy for 187 of the target fields. We do not include the radio galaxy itself, although those with $K \leq 18.6$ are EROs. The horizontal line is a measure of the "local field" density of EROs, defined as the density of EROs between $60''$ and $240''$ from the radio source. There is no evidence of an overdensity around the radio galaxies, although the uncertainties are very large. Figure 3.20 shows the same as Figure 3.19 with the sample broken into four bins depending on the apparent magnitude of the radio galaxy target. Given the $K - z$ Hubble diagram, the radio galaxy apparent magnitude is a rough proxy for redshift. There is no statistically significant evidence for an excess of bright EROs in any of the four samples. This is consistent with Wold et al. (2003), who perform a similar analysis and see no evidence for clustering of EROs brighter than $K_s = 19.5$ around their $z \sim 2$ radio loud quasars. A deeper sample of EROs is necessary for a complete analysis of the radio galaxy environment. This will be discussed in Section 3.10

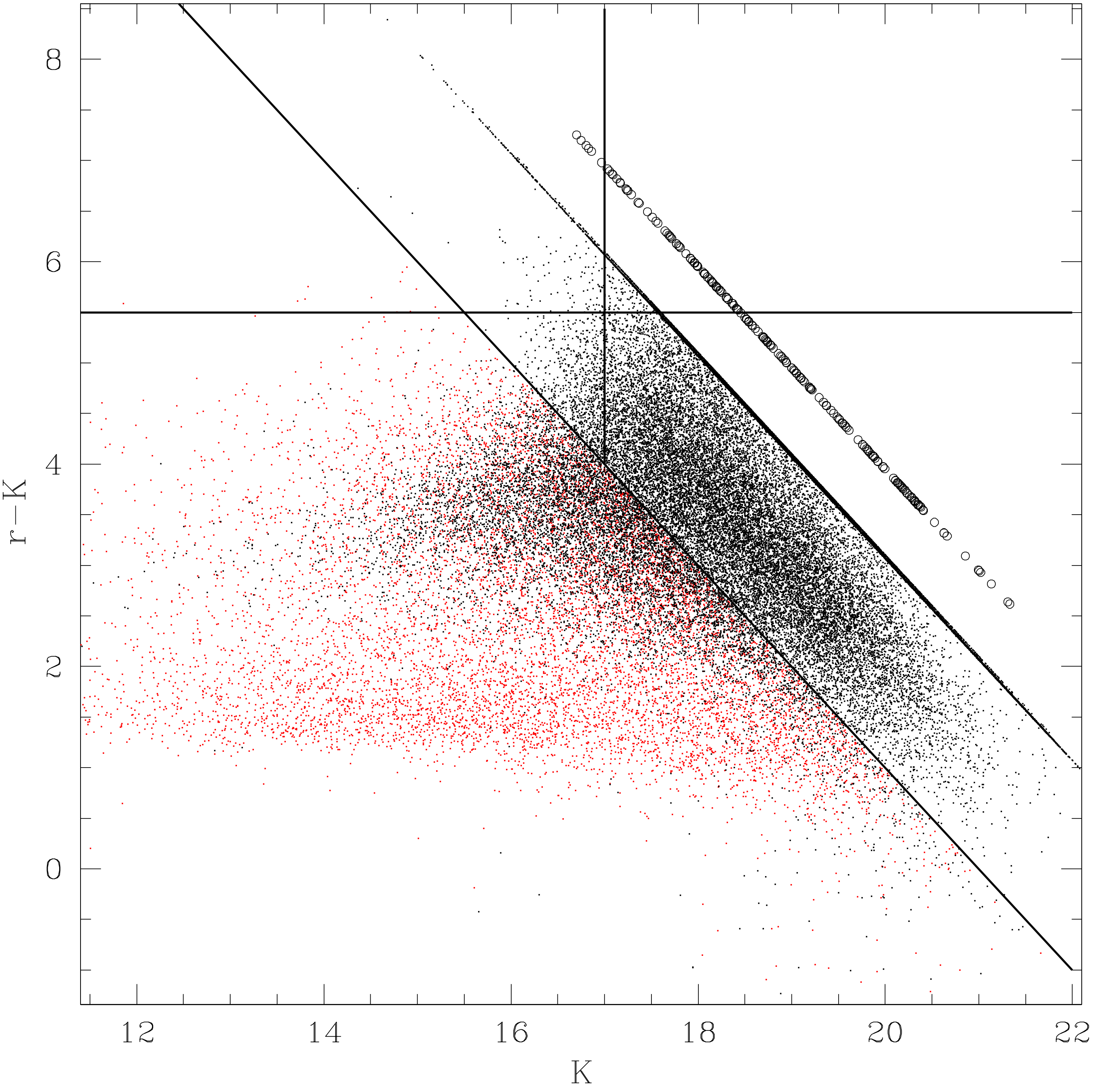

Figure 3.17 $r - K$ as a function of K, showing star-galaxy separation and ERO definition. The diagonal upper limit in the measurements is due to the $5\,\sigma$ r-band limit from the SDSS assigned to non-detections, while the horizontal line marks the $r - K = 5.50$ color used to define EROs. Red points are objects classified as stars, while black are galaxies. The diagonal line represents $r = 21.0$, below which the SDSS star-galaxy separation is used. No star-galaxy separation is done for objects above this diagonal line and to the right of the vertical line at $K = 17.0$. Open circles represent $2\,\sigma$ $r - K$ lower limits for the target radio galaxies in these fields.

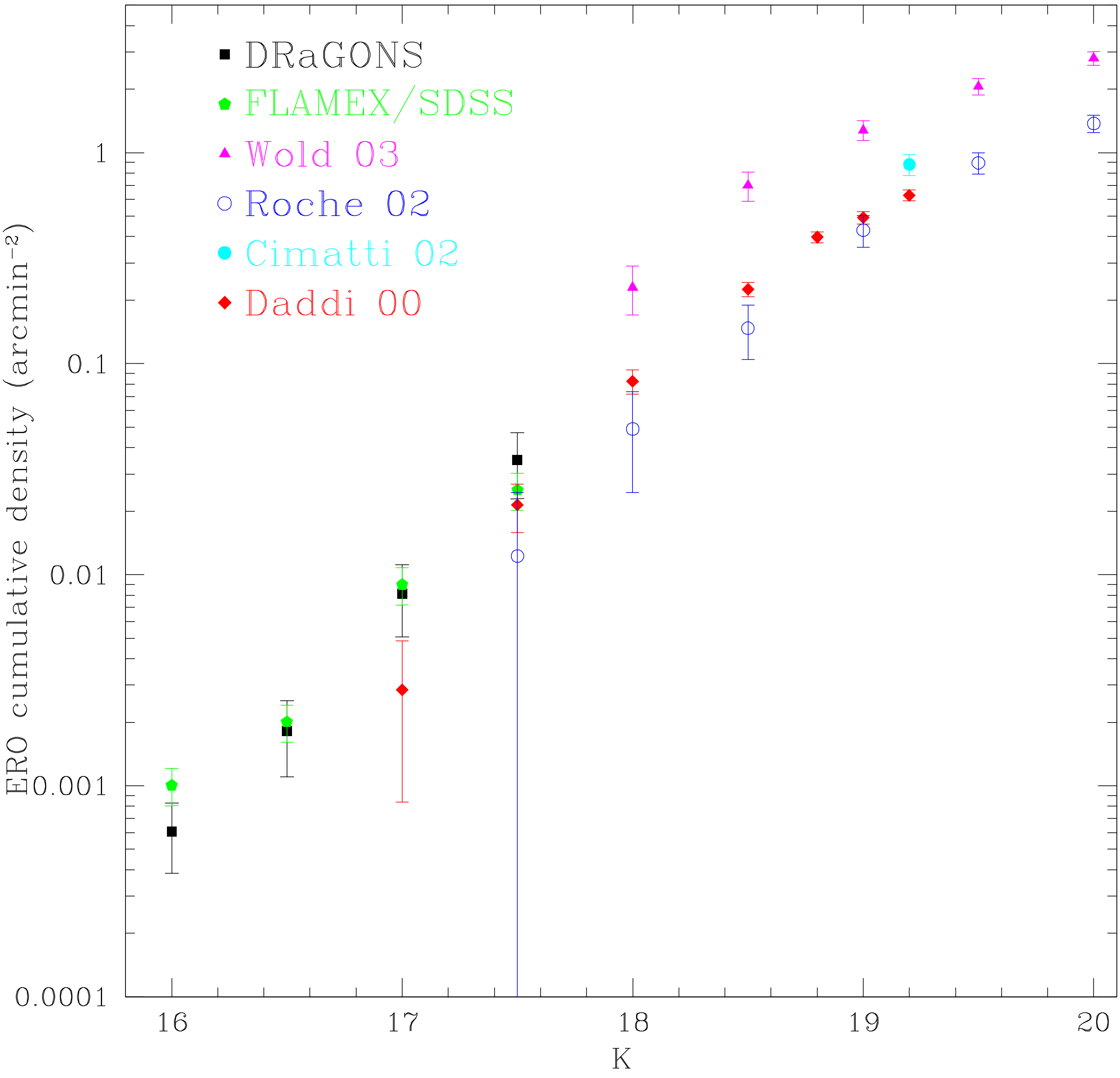

Figure 3.18 Cumulative ERO surface Density for DRaGONS. Shown for comparison are data from SDSS/FLAMEX (see Section 3.5), Daddi et al. (2000); Cimatti et al. (2002); Roche et al. (2002) and Wold et al. (2003).

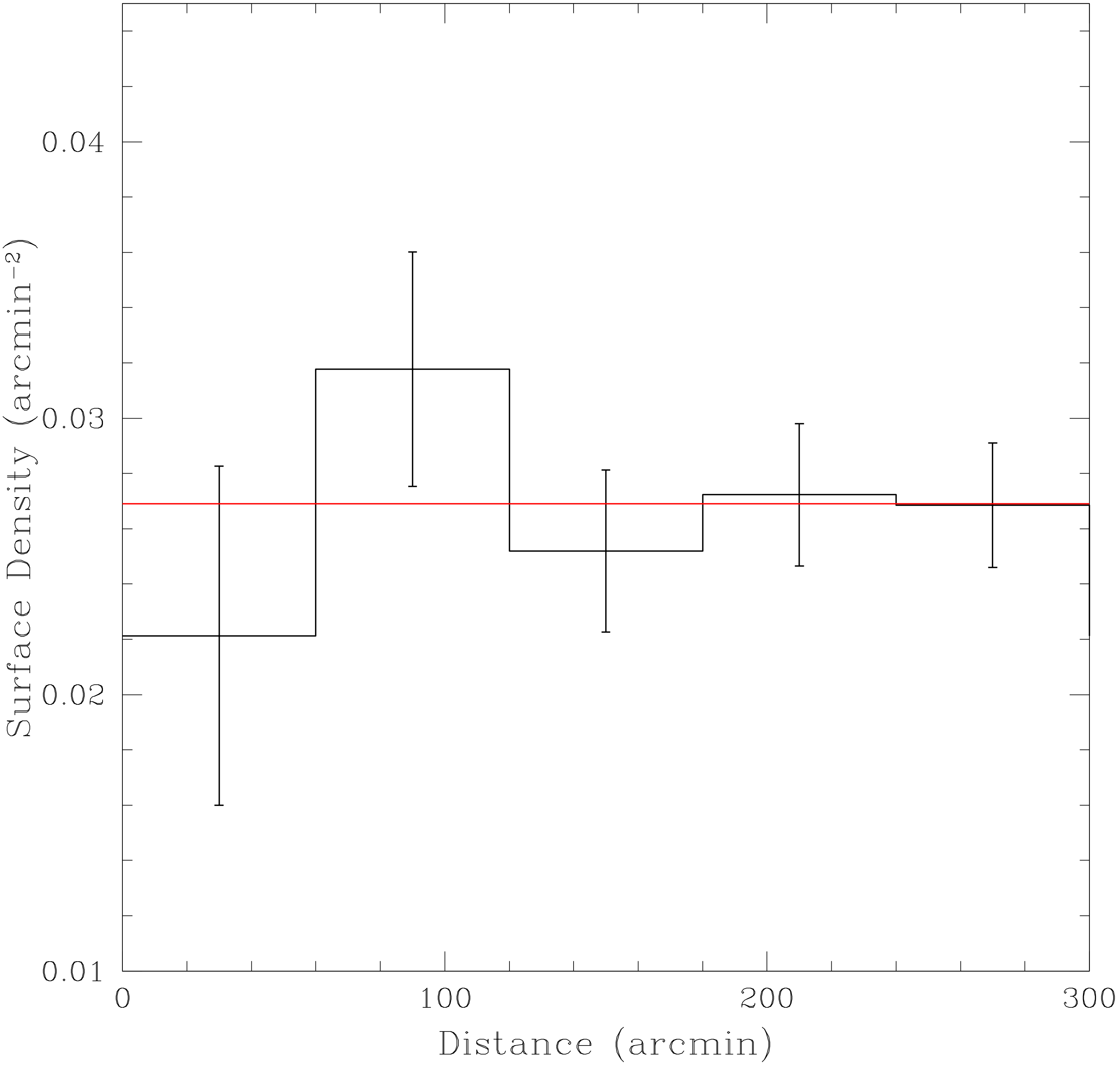

Figure 3.19 Average surface density of $K \leq 17.5$ EROs as a function of radial distance from the radio galaxy. The horizontal line represents the "local field density" of the sample, defined as the average density of EROs between 60″ and 240″ from the radio source position.

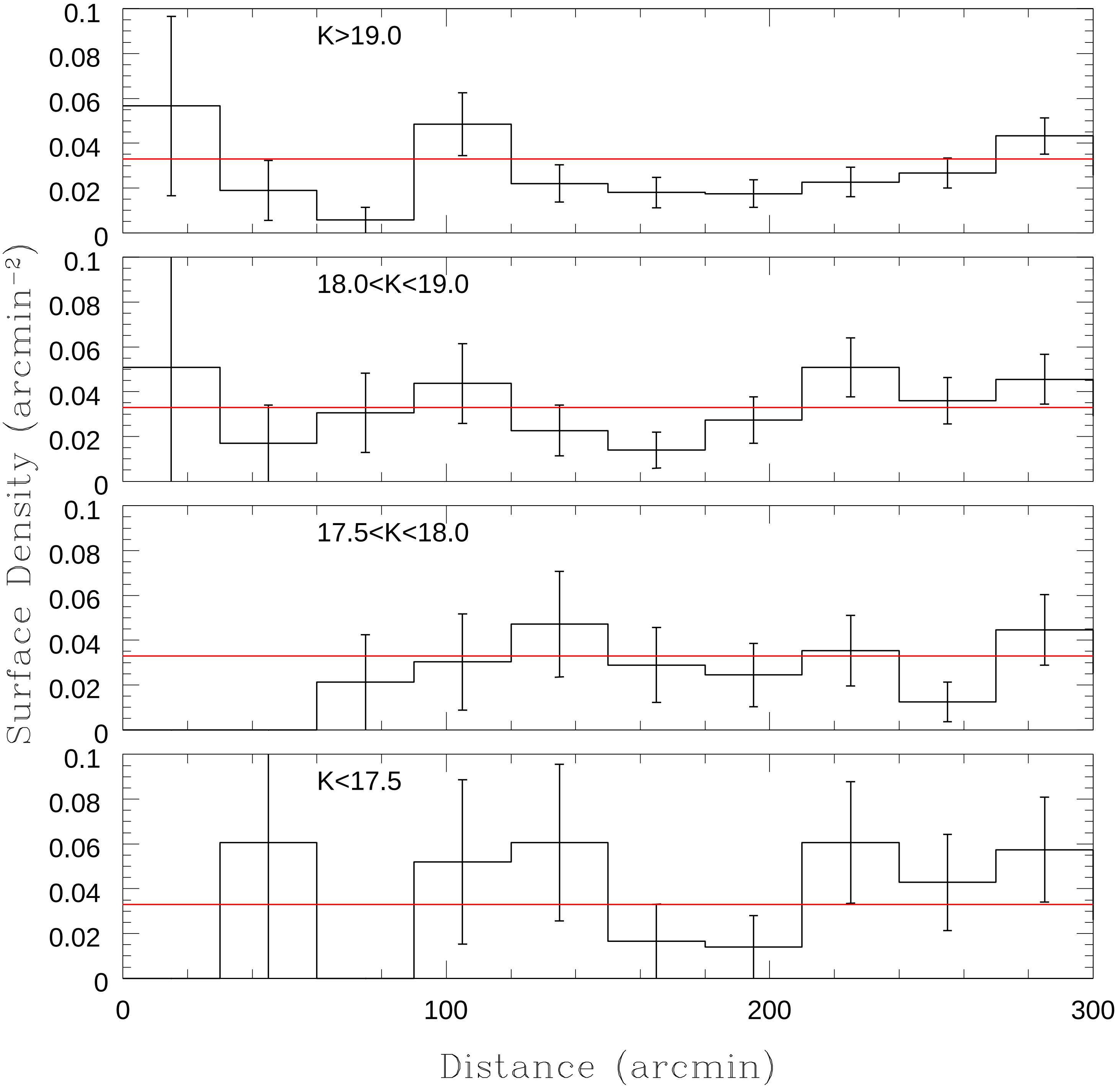

Figure 3.20 ERO average surface density as a function of distance (same as Figure 3.19) split into four bins by the target radio galaxy apparent magnitude. Error bars are Poisson.

To check for an excess of K-band detected galaxies around our radio galaxy targets we restrict ourselves to the deeper exposures that allow us to reach limiting magnitudes of $K \geq 20.0$. We take only fields observed for greater than forty minutes, eliminating all of the 2003-2004 fields, as well as six fields from 2005-2006 where technical or weather problems limited on target exposure time. A further cut is done based on seeing conditions (average seeing $< 1.4''$), eliminating another seven fields. Figures 3.21, 3.22, and 3.23 show the distribution of K-band galaxies around our targets for the remaining 80 fields. Figure 3.21 shows the average surface density of all galaxies as a function of distance from the target radio galaxies, in $30''$ bins. The horizontal line in each panel shows a measure of the "local field" density of galaxies (defined as the density of objects between $60''$ and $240''$ from the radio source). The Figure shows a small overdensity of galaxies in the inner $120''$. The four panels of Figures 3.22 and 3.23 represent the division of the sample by the apparent magnitude of the target radio galaxy, which is, again, a rough estimate of redshift. Figure 3.22 includes all $K \leq 19.0$ galaxies, and divides the 80 fields into $K \leq 17.5$ (4 fields), $17.5 < K \leq 18.0$ (9 fields), $18.0 < K \leq 19.0$ (22 fields), and $K > 19.0$ (45 fields). Figure 3.23 is the same, but includes all galaxies brighter than $K \leq 20.0$, and shows $K \leq 17.5$(4 fields), $17.5 < K \leq 18.0$ (9 fields), $18.0 < K \leq 18.5$ (10 fields), and $18.5 < K \leq 19.0$ (12 fields). The horizontal red lines indicate the local density of $K \leq 19$ and $K \leq 20$ galaxies. Figures 3.22 and 3.23 show significant overdensities within an arcminute in the two bins with $K \leq 18.0$, with the overdensity possibly extending to $120''$, though the errors are large in the $K \leq 17.5$ bin, as it contains only 4 radio galaxy fields. No clustering is seen in any of the $K > 18.0$ bins. This is not unexpected: as mentioned in the ERO overdensity discussion earlier in this section, we expect the radio galaxy to be several magnitudes brighter than other protocluster galaxies. Thus, the K-band images are deep enough to detect protocluster galaxies near our brightest (lower redshift) galaxies, but not the fainter targets. These results are similar to those of Hall and Green (1998) and Hall et al. (2001), which did not find an excess around $z \approx 1.5$ radio loud quasars below $K = 19$, but do see an excess of galaxies at $K = 19 - 20.5$. Even deeper imaging is necessary to search for galaxy overdensities near our fainter targets.

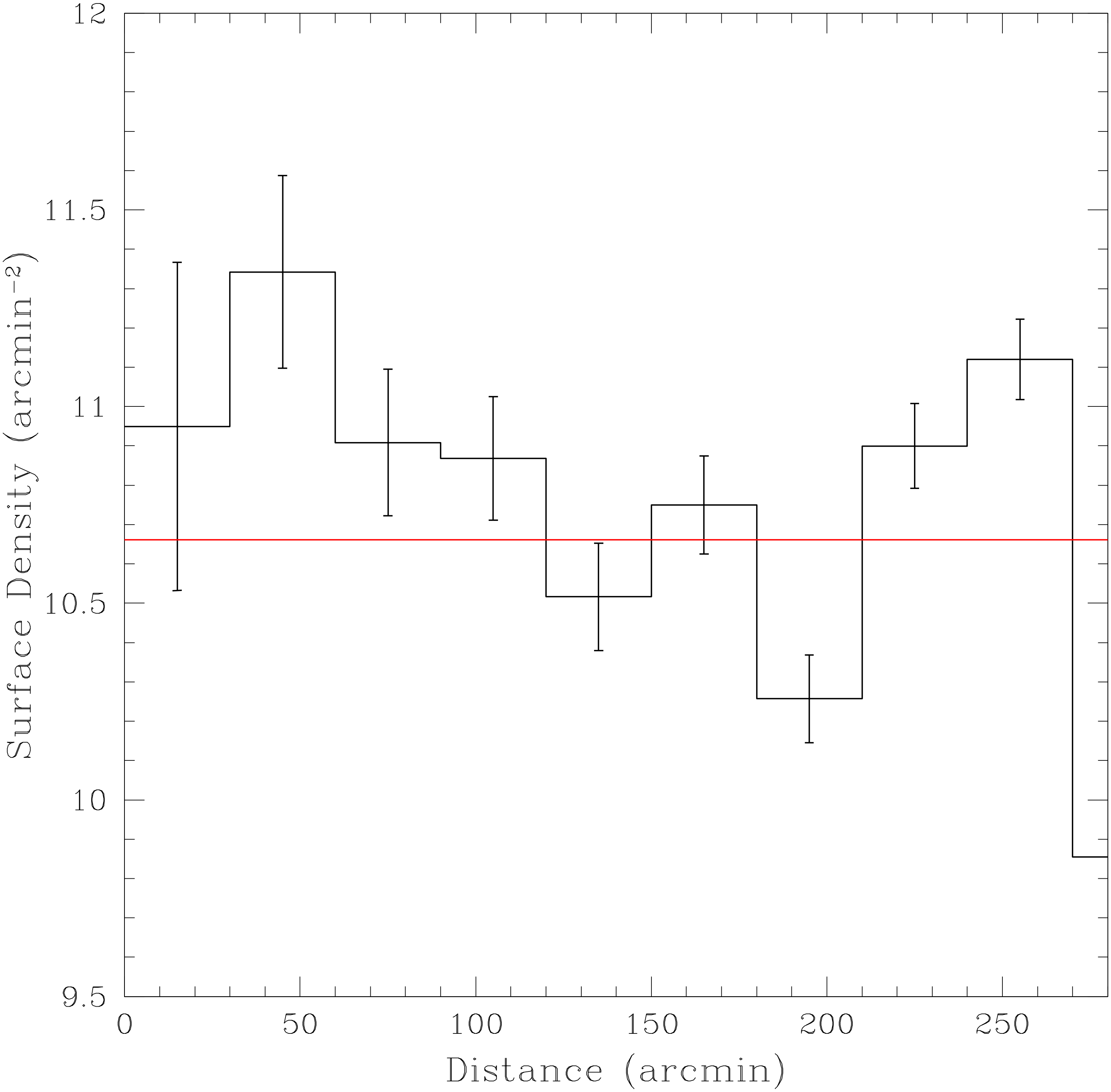

Figure 3.21 Average surface density of $K \leq 20.0$ galaxies as a function of radial distance from the radio galaxy. The horizontal line represents the "local field density" of the sample, defined as the average density of galaxies between 60″ and 240″ from the radio source position.

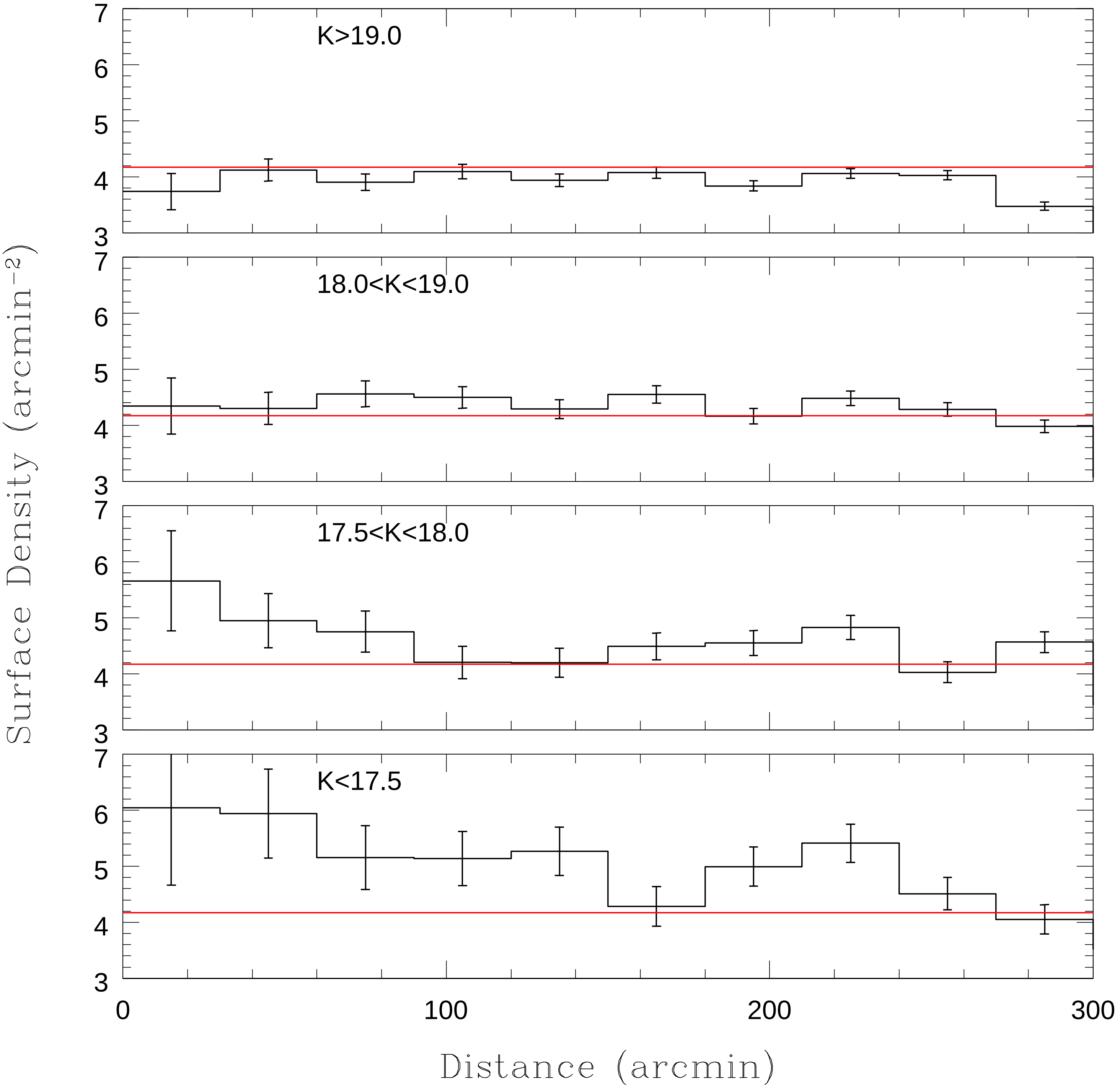

Figure 3.22 Average surface density of $K \leq 19.0$ galaxies as a function of distance (same as Figure 3.21) split into four bins by the target radio galaxy apparent magnitude.

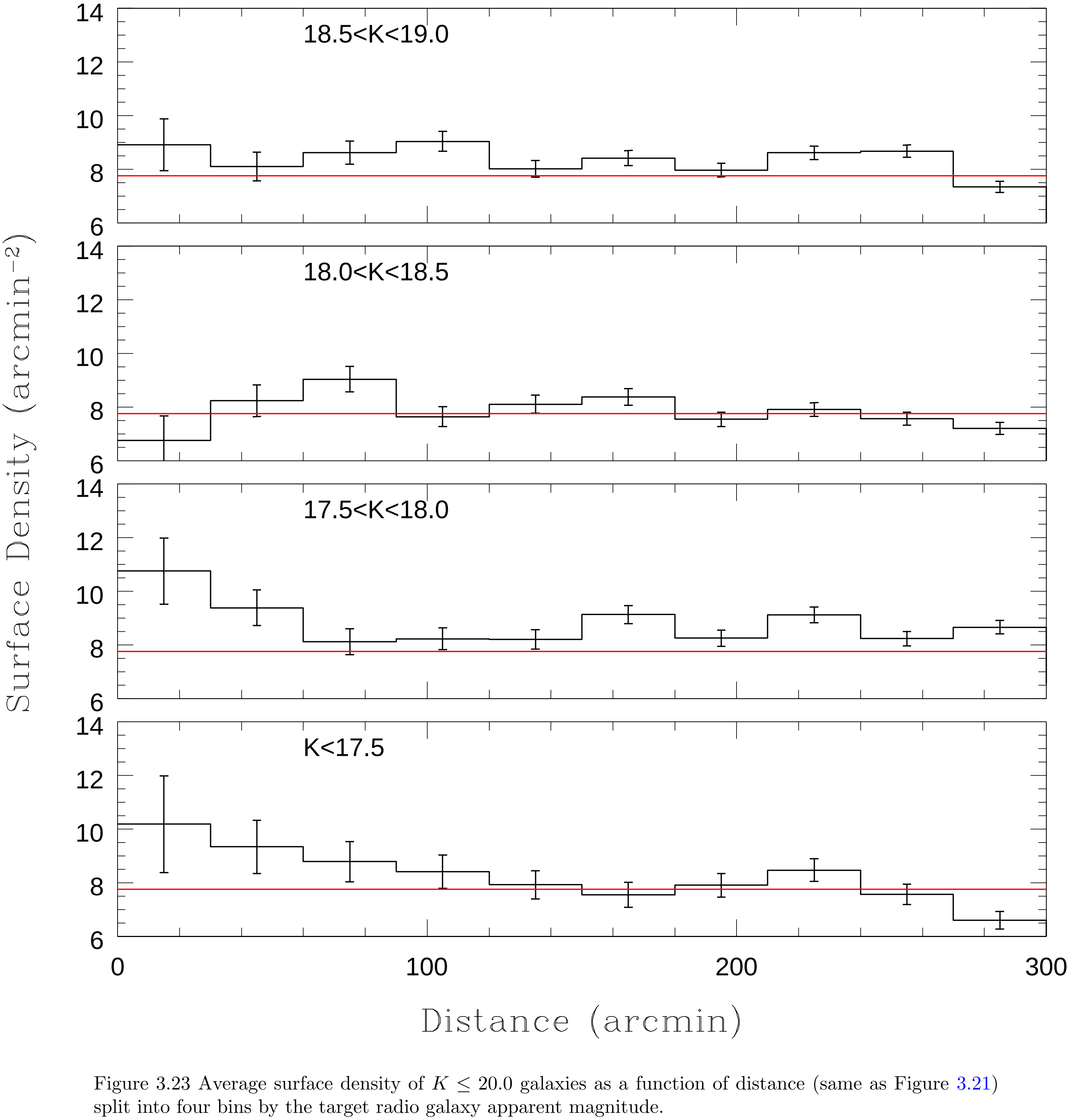

Figure 3.23 Average surface density of $K \leq 20.0$ galaxies as a function of distance (same as Figure 3.21) split into four bins by the target radio galaxy apparent magnitude.

3.8 RED DRAGONS

As mentioned in Section 3.6, about 10% of the radio galaxies observed are brighter than expected in the infrared given our selection criteria. There are several possible explanations for this: these galaxies could be low redshift $z \sim 1$ radio galaxies with faint optical properties, or they could be higher redshift objects with brighter than normal K-band flux, or a mix of the two cases. A high redshift galaxy where an emission line falls within the K-band is also a possibility. Twenty objects with $K < 17.6$, more than 10% of our sample, have anomalously red $g - K$, $r - K$, and $i - K$ colors that are not fit by even our extreme model templates. Galactic r-band extinction from the SDSS database for these objects are listed in Table 3.8, based on the dust maps of Schlegel et al. (1998). There is a modest amount of extinction for three objects: J0941+0127, J1548+0036, and J1604-0013, though not enough to fully explain their extreme color, so additional reddening is necessary if these galaxies are at low redshift. Applying the extinction model of Calzetti et al. (2000) to the non-evolving elliptical template of Coleman et al. (1980) and assuming a redshift of near unity given by the $K - z$ diagram, we require extinctions of $A_V > 0.5 - 1.5$ in order to reach the lower limit $r - K$ colors of these infrared bright sources. Such extinction is most likely associated with dust due to ongoing star formation. This is interesting, as there is still debate as to when and how massive galaxies assemble and form their stars (van Dokkum, 2005; De Lucia et al., 2006). Some models (Kauffmann et al., 1993; De Lucia et al., 2006) predict that massive galaxy progenitors form their stars in an intense burst, with SFRs of $> 1000 M_{sun}/yr$ at at $z > 4$, whereas a more extended and episodic star formation history is expected from hierarchical models. In the ΛCDM paradigm, these stars form early, but assemble hierarchically very late $z \sim 1$ through "dry" mergers of progenitor galaxies with little star formation. Major mergers are responsible for the build up of massive galaxies at high redshift (Conselice et al., 2003; Conselice, 2007), but the amount of star formation triggered by more recent mergers is still an open question, with traces of ongoing star formation found in some early type samples (e.g. Stanford et al., 2004; Teplitz et al., 2006). It is predicted that nearly all massive galaxies undergo a major merger at $z \leq 1.5$ (Conselice, 2007). It is possible that some of our Red DRaGONS are undergoing such a major merger, and if that is the case, then detailed study of the associated star formation will shed new light on the formation of massive elliptical galaxies; specifically, measuring the amount of star formation occurring during such a merger will help establish whether major mergers at low redshift are “dry”, or show the level of star formation induced by such mergers.

If the Red DRaGONS reside at higher redshift, it is possible that they consist of reddened radio loud quasars. The number of obscured quasars is of great interest in near infrared surveys. It is well know that optical selection is sensitive to a wide range of effects that bias samples against the detection of heavily obscured galaxy populations. Indeed, heavily obscured quasars may account for a significant fraction of the total population (Webster et al., 1995; White et al., 2003; Glikman et al., 2004). If Red DRaGONS galaxies fall into this category, then the DRaGONS selection criteria could be very useful in defining AGN samples complementary to those selected in the optical. The role of AGN feedback in explaining the “downsizing” scenario of galaxy formation has been explored by several groups (e.g. Scannapieco et al., 2005; De Lucia et al., 2006), where energy injected by the central black hole is responsible for quenching star formation, which gives rise to the observed old stellar populations. De Lucia et al. (2006) state that energy from supernovae is not high enough to suppress star formation, and significant AGN feedback (Croton et al., 2006) is necessary in order to do so. The interplay between star formation and AGN feedback has yet to be explored in detail. The extreme colors of Red DRaGONS galaxies, combined with their high radio luminosity, may mean that these galaxies are hosting simultaneous starburst and AGN activity. Therefore, they are excellent candidates for observing feedback processes in action.

Determining spectroscopic redshifts for these objects will be the best way to determine whether the anomalously red colors are due to obscuration at lower redshift, a more luminous galaxy at higher redshift, some combination of the two, or a class of objects not covered by our models. However, as spectroscopy of such faint sources is difficult and time consuming, we will discuss alternative studies of Red DRaGONS properties in the following sections, namely environment, as traced by Extremely Red Objects, and Spectral Energy Distribution fits for two Red DRaGONS galaxies.

TABLE 3.8

EXTINCTION FOR $K < 17.6$ GALAXIES

Name	K	Extinction
J0256-0659	17.57	0.15
J0941+0127	17.17	0.32
J0958+0324	17.46	0.08
J1155+0305	17.36	0.10
J1208+4943	17.03	0.06
J1255+3046	16.98	0.04
J1332+0101	17.05	0.08
J1400+0053	17.23	0.10
J1403+6048	17.55	0.05
J1408+0116	17.08	0.11
J1423+0139	17.37	0.09
J1438+2821	17.09	0.05
J1532+4432	17.16	0.05
J1541+5259	17.24	0.03
J1546+1754	17.29	0.08
J1548+0036	16.83	0.23
J1600+3304	16.80	0.09
J1604-0013	17.13	0.34
J1630+2452	16.75	0.10
J1649+3350	16.86	0.06

3.9 MULTIWAVELENGTH OBSERVATIONS

We obtained deep optical images for several Red DRaGONS at the Astrophysical Research Consortium (ARC) 3.5 meter telescope at Apache Point Observatory. Of seven half nights awarded, four were unusable due to weather (rain, snow, and lightning), and one additional night was lost due to slipping in the altitude motor control that resulted in blurred and unusable images. In the two useable half nights (15 Feb 2007 and 15 Mar 2007), we obtained 30 minute exposures in SDSS r and i bands for five Red DRaGONS galaxies with the SPIcam instrument (Seaver Prototype Imaging camera). SPIcam is a 2048 × 2048 pixel CCD camera with a pixel scale of $0.141''/pixel$, which gives a field of view of 4.78 × 4.78 arcminutes. Because seeing at Apache Point is typically near one arcsecond, we ran SPIcam in 2 × 2 binned pixel mode, resulting in 1024 × 1024 pixel images with a pixel size of $0.28''/pixel$. This is the same CCD and filter set used in the main SDSS camera (Gunn et al., 1998). We operated in point and stare mode (as opposed to the drift scan mode used by SDSS), taking 3-5 minute exposures at 4 dithered positions offset by $10''$ in a square pattern to facilitate bad pixel rejection. Flat fields were obtained from both twilight sky flats, as well as using dome lamps to illuminate the closed mirror covers. Images were reduced using standard IRAF routines: A bias frame was subtracted from individual frames, which were then divided by a flat field. These frames were aligned and registered to unsaturated SDSS stars and combined into the final image.

These images were calibrated with SDSS data using the same webservice interface to OpenSkyQuery described in 3.4, but using SDSS stars rather than 2MASS. The photometry from these fields are used to select the Extremely Red Objects discussed in Section 3.10 Table 3.9 shows the r and i-band magnitudes measured for the radio galaxies. Inspection of the r, i, and K images for object *J1630+2452* shows that this object is a superposition of the red radio galaxy and a foreground blue galaxy that contaminates the magnitude measurements in the r and i bands. Figure 3.24 shows the radio galaxy in r, i, and K bands, as well as a false color RGB K(red), i(green), r(blue) image of the target.

TABLE 3.9

APO DEEP OPTICAL IMAGING

Object Name	date	K	r RA	r DEC	r	i RA	i DEC	i	seeing($''$)
J0256-0659	2007 Feb 15	17.57 ± 0.079	02:56:05.002	-06:59:19.74	23.91 ± 0.121	02:56:05.002	-06:59:20.02	21.90 ± 0.061	1.6
J0725+3826	2007 Feb 15	17.67 ± 0.049	07:25:44.328	+38:26:40.02	23.79 ± 0.114	07:25:44.316	+38:26:39.98	22.59 ± 0.096	1.2
J1438+2821	2007 Mar 15	17.09 ± 0.088	14:38:09.910	+28:21:47.50	23.21 ± 0.107	14:38:09.952	+28:21:47.22	22.10 ± 0.050	1.4
J1546+1754	2007 Mar 15	17.29 ± 0.044	15:46:02.462	+17:54:36.58	22.66 ± 0.079	15:46:02.462	+17:54:36.02	21.24 ± 0.041	1.2
J1630+2452[1]	2007 Mar 15	16.75 ± 0.050	16:30:14.730	+24:52:47.59	22.46 ± 0.060	16:30:14.730	+24:52:47.59	22.75 ± 0.038	0.9

[1] Object J1630+2452 is a superposition of the target red radio galaxy and a faint blue galaxy

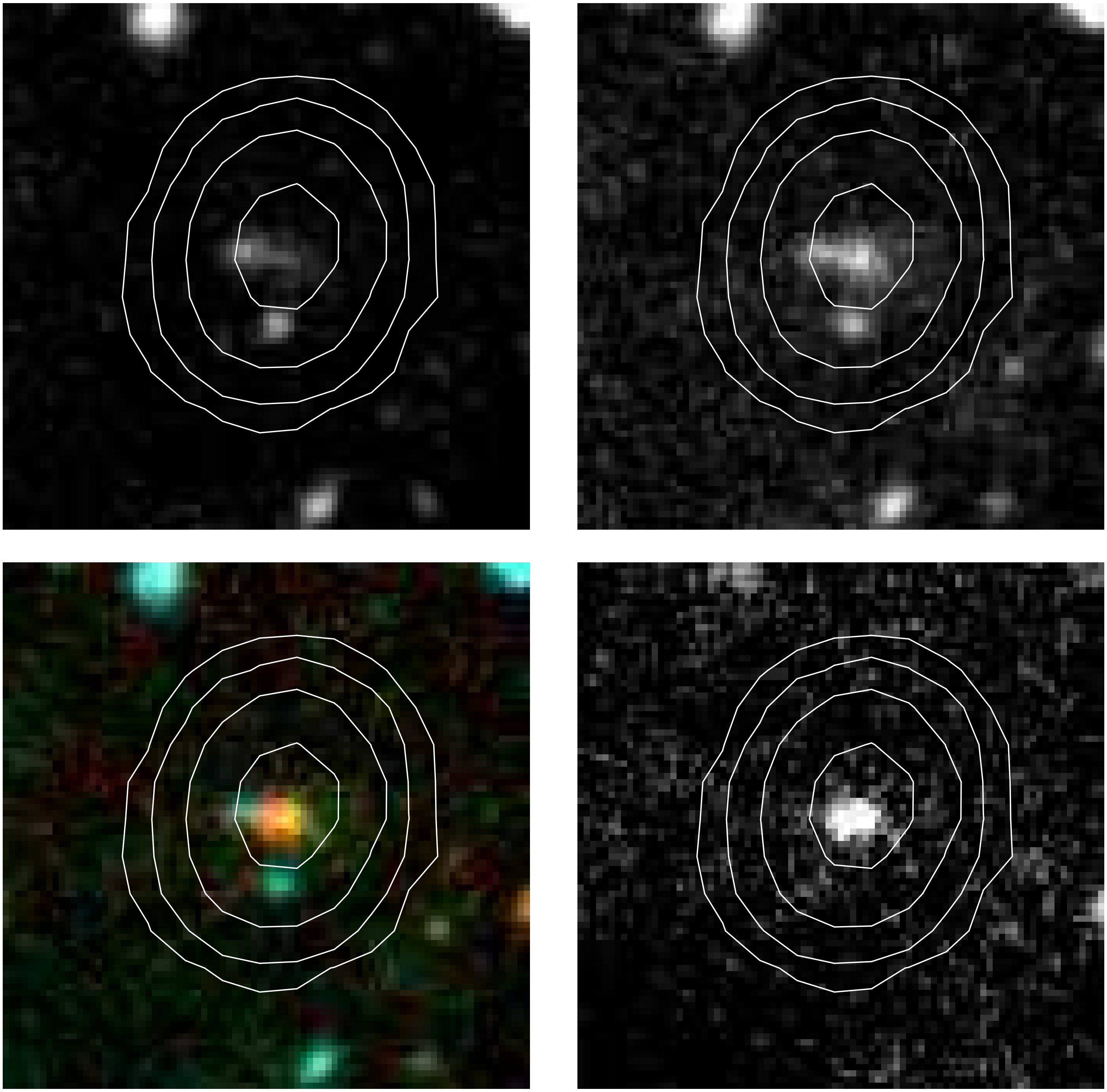

Figure 3.24 Clockwise from upper left: r,i,K, and RGB composite riK images of *J1630+2452* showing a blue foreground galaxy near the radio galaxy position.

TABLE 3.10

KPNO J AND H IMAGING

Object Name	date	K	J RA	J DEC	J	H RA	H DEC	H	seeing($''$)
J2223-0757	2006 Oct 07	17.70 ± 0.080	22:23:26.530	-07:57:07.77	19.45 ± 0.14	22:23:26.550	-07:57:08.07	18.68 ± 0.14	1.3
J0256-0659	2006 Oct 08	17.57 ± 0.079	02:56:05.005	-06:59:19.53	19.68 ± 0.15	02:56:05.045	-06:59:19.83	18.57 ± 0.13	1.2
J1546+1754	2007 May 28	17.29 ± 0.044	15:46:02.470	+17:54:36.32	20.09 ± 0.26[1]	15:46:02.500	+17:54:36.13	18.40 ± 0.14	1.2

[1] A passing cloud limited useable exposure in J band for J1546+1754 to 22 minutes. The radio galaxy also falls on a very noisy region of the chip, also contributing to the very large error in the magnitude measurement

In addition to the deep optical observations, further near-infrared imaging was taken for three Red DRaGONS fields. J and H-band images were taken with FLAMINGOS during the October 2006 and May 2007 FLAMINGOS runs at the Mayall 4m telescope. The same telescope and instrument set up used for the K-band data, and the photometry was, again, calibrated using 2MASS data (see Sections 3.2 and 3.3 for details). Longer individual frame exposure times of 45-60 seconds were possible, as the sky background is much lower in these shorter wavelength passbands. As the Red DRaGON targets are, by definition, very bright ($K \leq 17.6$) in the K-band (centered at 2.149 μm), they are expected to also have significant flux in the J (1.25 μm) and H (1.64 μm) passbands as well. Therefore, the total exposure time for each object was 1800 seconds (30 minutes) in each of the two bands, unless otherwise noted. Table 3.10 summarizes the supplemental near-infrared imaging. Note that two of the three objects also have data in r and i bands, and will be discussed further in Section 3.11.

3.10 DEEP ERO

While the main SDSS survey is deep enough to allow us to select the DRaGONS candidates, the $5\,\sigma$ limiting magnitude of $r = 23.1$ only allows us to identify EROs (using our $r - K > 5.5$ definition) brighter than $K \leq 17.6$, as luminous as only the brightest of our radio galaxy targets. In order to test for an excess of EROs in our fields, deeper optical data is needed. Fortunately, we have two sources of such data: the optical follow up of four Red DRaGONS fields discussed in Section 3.9, as well as the deeper SDSS "Stripe 82" data discussed in Section 2.2. The deep Apache Point data targeted four bright radio galaxies ($K < 17.7$), while the Stripe 82 imaging contains a relatively fainter sample of 21 targets, all of which were observed in either September 2005 or October 2006. 14 of these galaxies are detected with $18.2 < K\, 19.9$, and 7 undetected with $K > 20.0$.

The vast majority of Extremely Red Objects observed to date lie in the redshift range $1.5 \leq z \leq 3.0$. ERO galaxies consist mainly of two populations: dusty starburst galaxies and old passively evolving galaxies, where the starbursts owe their red color to dust obscuration, and the passive galaxies are red because of their old stellar populations. The lower redshift cutoff for EROs is due to redshift: at $z \sim 1.5$ enough stellar flux falls into the r-band that the $r-K$ color of even the oldest stellar populations and all but the most extreme obscured galaxies are not red enough to meet ERO criteria. This can clearly be seen by the $r - K$ color tracks shown in Figure 3.2, and is closely related to the reasoning behind our DRaGONS selection criteria; i.e. choosing red objects will effectively eliminate low redshift contaminants. The upper redshift limit could be due to either of, or a combination of, two effects: the fall in the number of ERO galaxies at high redshift, and the difficulty in observing such faint galaxies. Very deep optical imaging is necessary in order to detect such red objects at high redshift ($r \approx 26 - 27$ for $z \approx 3 - 4$). At such high redshifts we are beginning to probe the epoch of initial galaxy formation, and at some point, the galaxies simply are not there to observe, as they have not yet formed. It should be noted, though, that Zheng et al. (2006) see an overdensity of red galaxies around a radio loud quasar at $z = 5.8$, so it is likely that the redshift range extends beyond the commonly cited $z < 3$ limit. The lower redshift cutoff, however, may enable us to estimate the redshift of any radio galaxy with an associated ERO overdensity, as the presence of EROs implies a redshift $z > 1.5$. A recent study by Venemans et al (2006) finds typical protocluster sizes ∼2 Mpc for Ly α emitters. There are also indications that EROs are more compact tracers of protoclusters, with sizes ∼1 Mpc (Kurk et al. 2004). The SPIcam field of view covers $\sim 1.8 - 2.4$ Mpc over the redshift range of interest ($1.5 \leq z \leq 5$), allowing us to examine the scale of the overdensity.

3.10.1 Apache Point

The r-band data for four of the five fields in Table 3.9 were positionally cross matched with our DRaGONS catalogs (*J1630+2452* is not included, as it is a blended object, and the apparent magnitude of the unblended radio galaxy may be significantly fainter than other Red DRaGONS in this sample). The 4.78×4.78 arcminute FOV of SPIcam allows us to reliably identify EROs to a radius of $90''$ in these four fields. A recent study by Venemans (2006) finds typical protocluster sizes ∼2 Mpc for Ly α emitters. There are also indications that EROs are more compact tracers of protoclusters, with sizes ∼1 Mpc (Kurk et al., 2004). The SPIcam field of view covers $\sim 1.8 - 2.4$ Mpc over the redshift range of interest ($1.5 \leq z \leq 5$), allowing us to examine the scale of the overdensity. We conservatively assign non-detections $r = 24.5$. Figure 3.25 shows the cumulative ERO surface density within $60''$ and $90''$ for these four fields. There is an obvious overdensity of EROs at $K \geq 18.0$ that agrees very well with the overdensity seen by Wold et al. (2003). This is very interesting, as it indicates that the redshift distribution of the two samples may be very similar. The apparent K-band magnitudes of the four galaxies, (K=17.09,17.29,17.57, and 17.67), coupled with the $K - z$ relation, indicate that their redshifts are near $z \sim 1$, but the presence of the ERO overdensity suggests that they may be more luminous objects at higher redshift, e.g. obscured quasars. Two of these objects will be discussed in greater depth in Section 3.11.

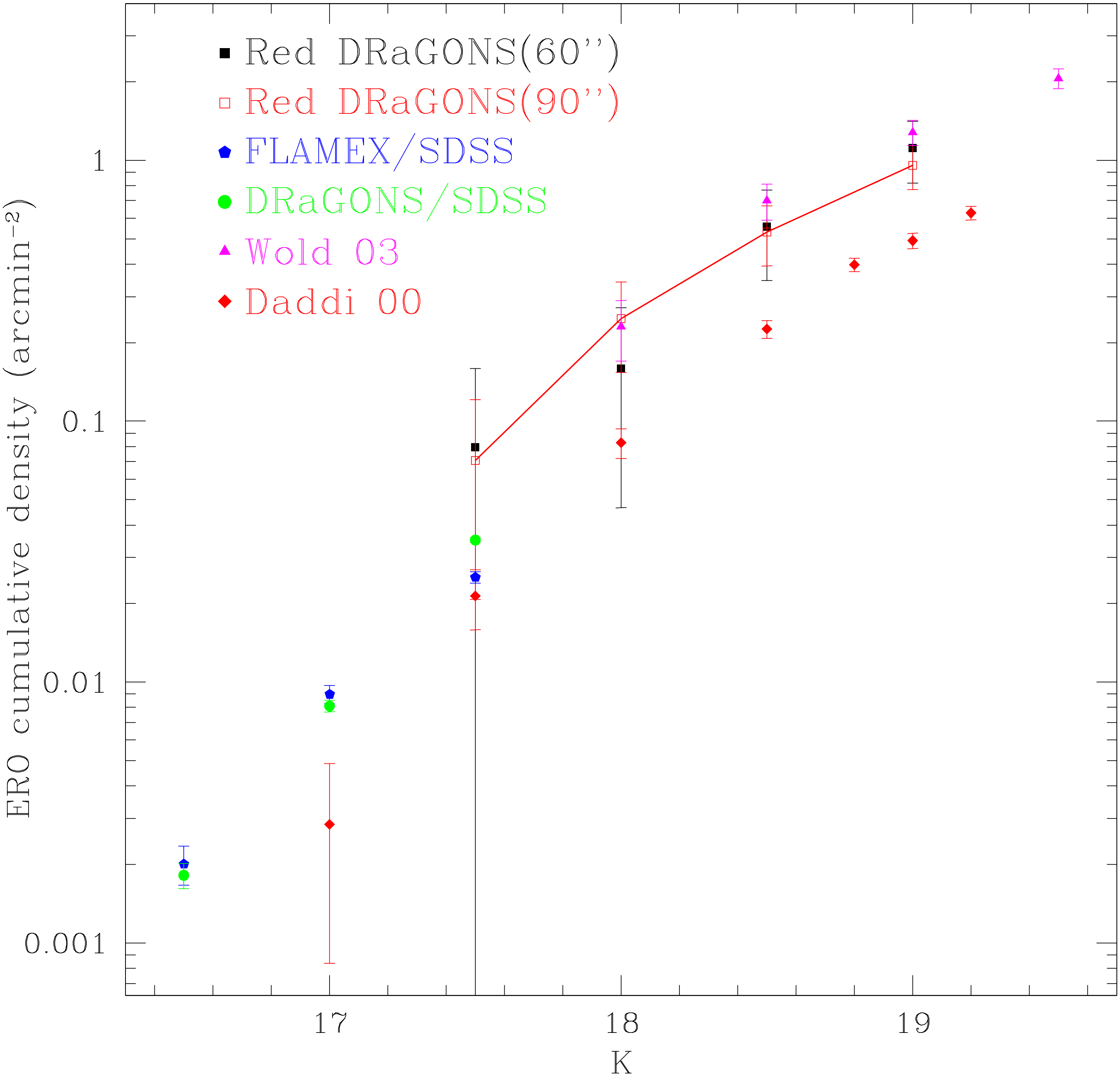

Figure 3.25 Cumulative ERO surface density for the four Red DRaGONS fields observed at Apache Point Observatory. Shown for comparison are the densities of Daddi et al. (2000) and Wold et al. (2003), as well as the DRaGONS and FLAMEX/SDSS counts from Figure 3.18. Black points represent the density within 60″ of the radio galaxy, while the red points and connecting line are the density within 90″.

3.10.2 SDSS Stripe 82

The SDSS Stripe 82 data is described in Section 2.2. The K-band catalogs were positionally cross matched with the Stripe 82 catalogs. Because the Stripe 82 catalog only contains objects detected at $> 5\,\sigma$ above the background, objects with no match within $3''$ were assigned a magnitude of $r = 23.5$, the approximate 5σ limit for the catalog. This allows us to examine ERO's down to $K \leq 18.0$, given the $r - K_{4''} > 5.50$ ERO criterion. The radio targets include sources with FIRST flux densities $S_{1.4\,\mathrm{GHz}} \geq 50.0$mJy. This is twice as faint as the 100 mJy limit in the Northern portion of the DRaGONS survey. None of the 21 radio galaxies are brighter than $K = 18.0$, thus our $K \leq 18.0$ ERO sample is not deep enough to detect red galaxies physically associated but less luminous than the radio source. Any evidence of an ERO overdensity would, therefore, indicate the presence of a foreground overdensity of EROs. The availability of deep r-band data over the entire $10' \times 10'$ area of each field, however, will allow us to test our ERO selection criteria: We will split the sample into EROs within $90''$ of the radio galaxy, and those between 90 and 240 arcseconds away. Any overdensity, either physically associated or foreground lensing structure, should be located very close to the radio galaxy. The 90 to $240''$ will define a "field" sample of EROs whose density we can, again, compare to those of Daddi et al. (2000), Roche et al. (2002), and Cimatti et al. (2002). Figure 3.26 shows the Stripe 82 cumulative ERO surface densities, for both the $distance < 90.0$ (Close) and $90.0 \leq distance < 240.0$ (Far) samples. No overdensity of EROs is seen in the sample, and none of the individual fields contain more than two EROs within $90''$ of the radio galaxy, consistent with the "field" distribution of EROs. Thus, we see no evidence of the presence of foreground clusters lensing the radio source for $K \leq 18.0$, though deeper optical data is needed to test for $K \leq 20 - 20.5$ EROs. The ERO surface density agrees very well with the "field" measurements of both our FLAMEX/SDSS measurement (Section 3.5) and Daddi et al. (2000), again confirming that our $r_{SDSS} - K_{4''} \geq 5.50$ agrees with the more common $R - K > 5.0$ ERO selection.

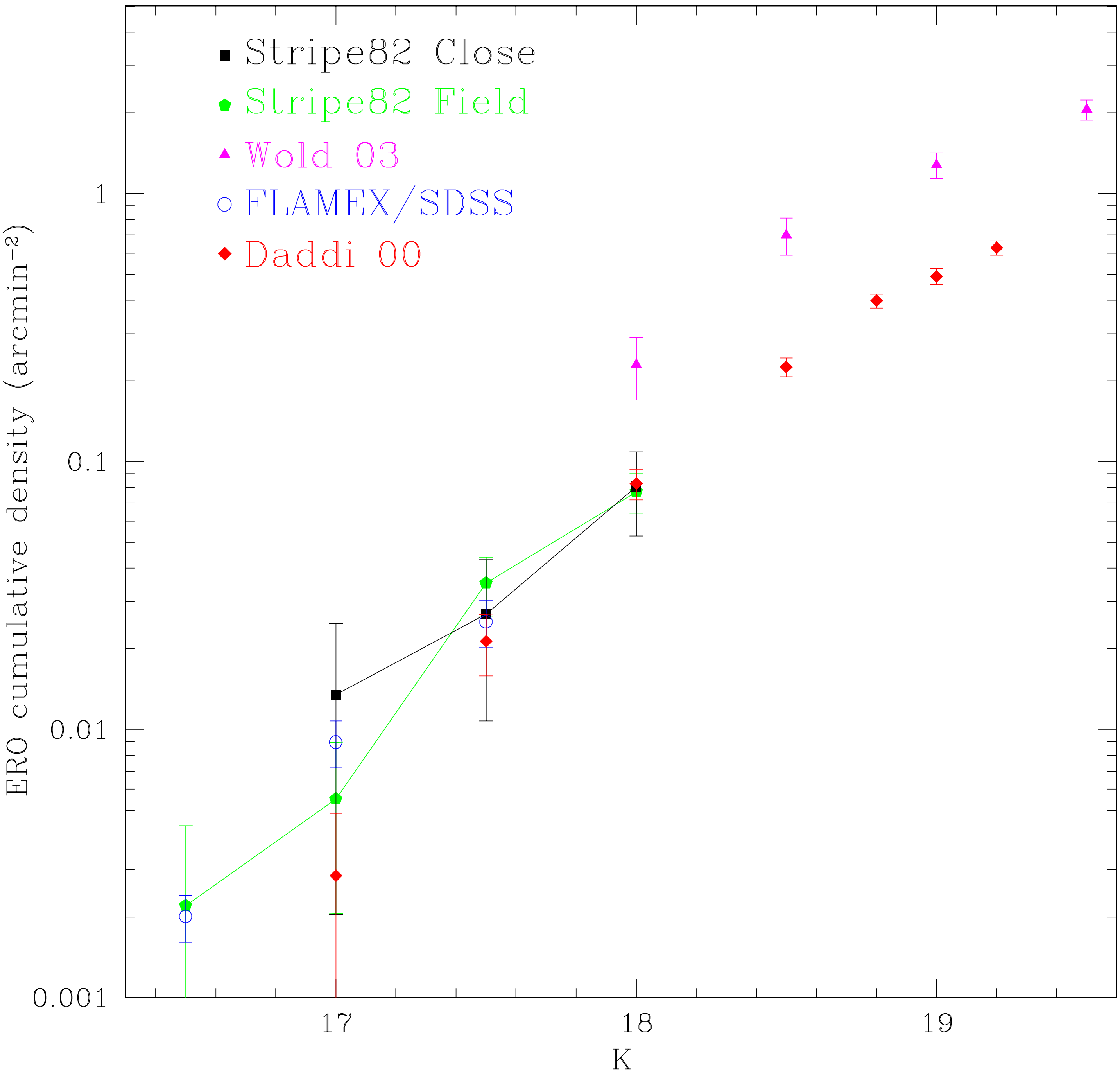

Figure 3.26 Cumulative ERO surface density for the 21 DRaGONS fields in SDSS Stripe 82. Shown for comparison are the densities of Daddi et al. (2000) and Wold et al. (2003), as well as the FLAMEX/SDSS counts from Figure 3.18. Black points represent the density within 90″ of the radio galaxy, while the green points and connecting line represent the "field surface density" from EROs at 90″ < *distance* < 240″.

3.11 SPECTRAL ENERGY DISTRIBUTIONS

Spectroscopic follow up of high redshift radio galaxies is very costly. By the nature of our selection criteria, we know that these galaxies emit very little flux at observed frame optical wavelengths. De Breuck et al. (2001) observed 62 USS selected high redshift radio galaxy candidates for 30 to 90 minutes on the 8-10 meter telescopes. In most cases, little to no stellar continuum was seen, and the galaxy redshift was determined by the position of one or several emission lines. Several sources show a small amount of continuum, but not discernible features that could be used to determine a redshift. While spectroscopy will, ultimately, be necessary to precisely determine redshifts and, in some cases, stellar populations and object types, an examination of the broad band photometric characteristics is also very useful. This is particularly true for the Red DRaGONS, as their unusual colors indicate that they may have distinct differences from previously observed radio galaxies. Before investing time on 8-10 meter class telescopes, we will estimate the spectral energy distributions (SEDs) of radio galaxies observed in multiple passbands.

SED fitting is intimately related to the calculation of template based photometric redshifts. Therefore, the discussion in Appendix B is particularly relevant. When using template based photoz methods, obtaining a type for the galaxy is part of the process of estimating the photoz, as the best fit template is the de facto galaxy type. For synthetic spectra, this can be used to estimate physical parameters for the galaxy in question. For example Conti et al. (2003) attempt to determine properties of galaxies in the Hubble Deep Field North (although they determine properties at the pixel level, and do so at a fixed redshift, which eliminates many degeneracies in the best fit template determination).

We will use the template based photometric redshift method described in Appendix B. In addition, in order to test the implication that Red DRaGONS may occupy the same $1.5 \leq z \leq 3.0$ redshift range of most EROs, we will run the photoz code with the redshift fixed at specific values between $0.5 \leq z \leq 3.5$ in order to determine the best fit template at each redshift.

To visualize our object colors compared to those of template spectra, we will convert the magnitudes to fluxes. First, we will convert our magnitudes to the AB system (Oke, 1974;

Oke and Gunn, 1983), which is defined by:

$$m_{AB} = 2.5\log(F_\nu) - 48.57 \tag{3.2}$$

where F_ν is the flux measured in $erg/s\,cm^2\,Hz$. Recalling that a Jansky (Jy) is defined as $10^{-23} erg/s\,cm^2\,Hz$, we can invert this to find that the flux given a AB magnitude m_{AB} is:

$$F_\nu(Jy) = 3630.0 \times 10^{-0.4(m_{AB})} \tag{3.3}$$

Converting to wavelength units (approximate, see Tokunaga and Vacca, 2005):

$$F_\lambda(erg/s\,cm^2\,\mu m) = F_\nu(Jy) \times 3.e^{-9}/(\lambda\,(\mu m))^2 \tag{3.4}$$

(Note that in practice, these conversions will be handled in code, and will be exact. The approximate conversion of Equation 3.4 will only be used for visualization purposes).

The template set includes spectral templates from a number of sources: Ten *GISSEL* (Galaxy Isochrone Synthesis Spectral Evolution Library Bruzual A. and Charlot, 1993) templates are included. This is the same set of SEDs used for calculating SDSS photozs (Budavári, private communication), and are designed to span early to late type galaxies at low redshift. To represent higher redshift, obscured, and active galaxies, templates from a variety of sources are included. Two templates from Coleman et al. (1980) are included: the elliptical and Scd galaxy templates where the reddening law of Calzetti et al. (2000) has been applied (with A_V =1.0, 1.5, and 2.0). Starburst galaxy templates from the Kinney-Calzetti Atlas of Galaxies(Kinney et al., 1996) both with and without additional reddening (A_V =0.0, 0.5, 1.0, 1.5, and 2.0 are included). The median composite SDSS quasar spectrum from Vanden Berk et al. (2001) is included with Calzetti reddening of A_V =0.0,0.5,1.5,2.5, and 5.0. Also included are the two PEGASE models discussed in Section 3.1, a solar metallicity instantaneous burst model with no obscuration and a zero initial metallicity exponentially declining star formation model with an e-folding SFR timescale $\tau = 0.5$ Gyr and "spheroid" type extinction assumed. Templates at six ages (1.2, 2.0, 3.0, 3.5, 4.5, and 5.0 Gyr) roughly corresponding to the ages of a galaxy at $z = 2$ and $z = 1$ for formation redshifts of z_{form} =10, 5, and 3.

The AB magnitude offsets used were obtained from the online documentation for *KCorrect* (`http://cosmo.nyu.edu/blanton/kcorrect/`), and are: $r_{\rm AB} = r_{\rm SDSS} + 0.010$, $i_{\rm AB} = i_{\rm SDSS} + 0.028$, $J_{\rm AB} = J_{\rm 2MASS} + 0.91$,$H_{\rm AB} = H_{\rm 2MASS} + 1.39$, and $K_{\rm S\,AB} = K_{\rm S\,2MASS} + 1.85$.

3.11.1 J0256-0659

The radio galaxy *J0256-0659* is a $K = 17.57$ radio galaxy that just meets our $K \leq 17.6$ Red DRaGON definition. As such, it may not be as anomalous as our more extreme Red DRaGONS candidates, which are up to a magnitude brighter in K-band. Measured and AB magnitudes for *J0256-0659* are given in Table 3.11 Magnitudes listed are SExtractor MAG_AUTO magnitudes. The radio galaxy appears to be fairly compact, regular, and isolated, so we will not use matched aperture magnitudes for the SED fit. Figure 3.27 shows r, i, J, H, and K_S band images for a $\sim$ 2.5 $\times$ 2.5 arcminute field around *J0256-0659*, along with an RGB composite of the r, i, and K images. EROs are circled in white in the riK composite image. FIRST radio contours are overlaid in green, with an outer contour indicating a flux density of 0.5mJy and each contour marking a 4× increase. Visual inspection of the riK composite image shows several very red objects that do not meet our ERO criteria, but whose color indicates that they may be associated with the radio galaxy. These moderately red objects could be the equivalent of EROs at lower redshift, which would be evidence in favor of a $z < 1.5$ position for the radio galaxy.

The photometry in Table 3.11 was input into the photometric redshift code with redshift unconstrained, as well as fixed redshifts spanning $0.5 \leq z \leq 3$ (i.e. fitting only the best template at a given redshift). The best fit redshift for *J0256-0659* is $z = 0.62$, where the best fit template is an elliptical galaxy with Calzetti extinction of A_V=1.0 magnitude. The fixed redshift analysis shows that the only other reasonable fit places the galaxy at $z = 0.90$, where the best fit template is an Scd galaxy with Calzetti reddenning of A_V=1.5 magnitudes. The redshift error reported for both fits is very large ($\sigma_z \approx 0.5$), as the minimum in the χ^2 distribution is broad and because the magnitude errors are fairly large. Figure 3.28 shows the two best fit templates at their respective redshifts. The $riJHK_S$ fluxes are shown at the central wavelength of their respective filters, and Figure 3.29 shows the χ^2 distribution

Table 3.11

J0256-0659 apparent and AB magnitudes

r SDSS	r AB	i SDSS	i AB	J 2MASS	J AB	H 2MASS	H AB	K_S 2MASS	K_S AB
23.91±0.12	23.92±0.12	21.90±0.061	21.928±0.061	19.68±0.15	20.59±0.15	18.57±0.13	19.96±0.13	17.57±0.079	19.42±0.079

as a function of redshift. Examination of the relative fluxes of the five bands indicates that the 4000 $\AA$ bread falls between the r (centered at 6156 $\AA$) and i (7470 $\AA$) bands, which puts the redshift between 0.5 and 0.9. The approximate redshift for a $K = 17.57$ galaxy from the $K - z$ relation is $z = 1.2 \pm \sim 0.5$. The preponderance of evidence suggests that *J0256-0659* is a lower redshift ($z \sim 1$) radio galaxy with moderate reddening, and that it is this reddening that caused it to meet our selection criteria. As mentioned previously, this galaxy barely meets our Red DRaGON criteria. It is possible that a number of our borderline Red DRaGONS are these moderately reddened radio galaxies.

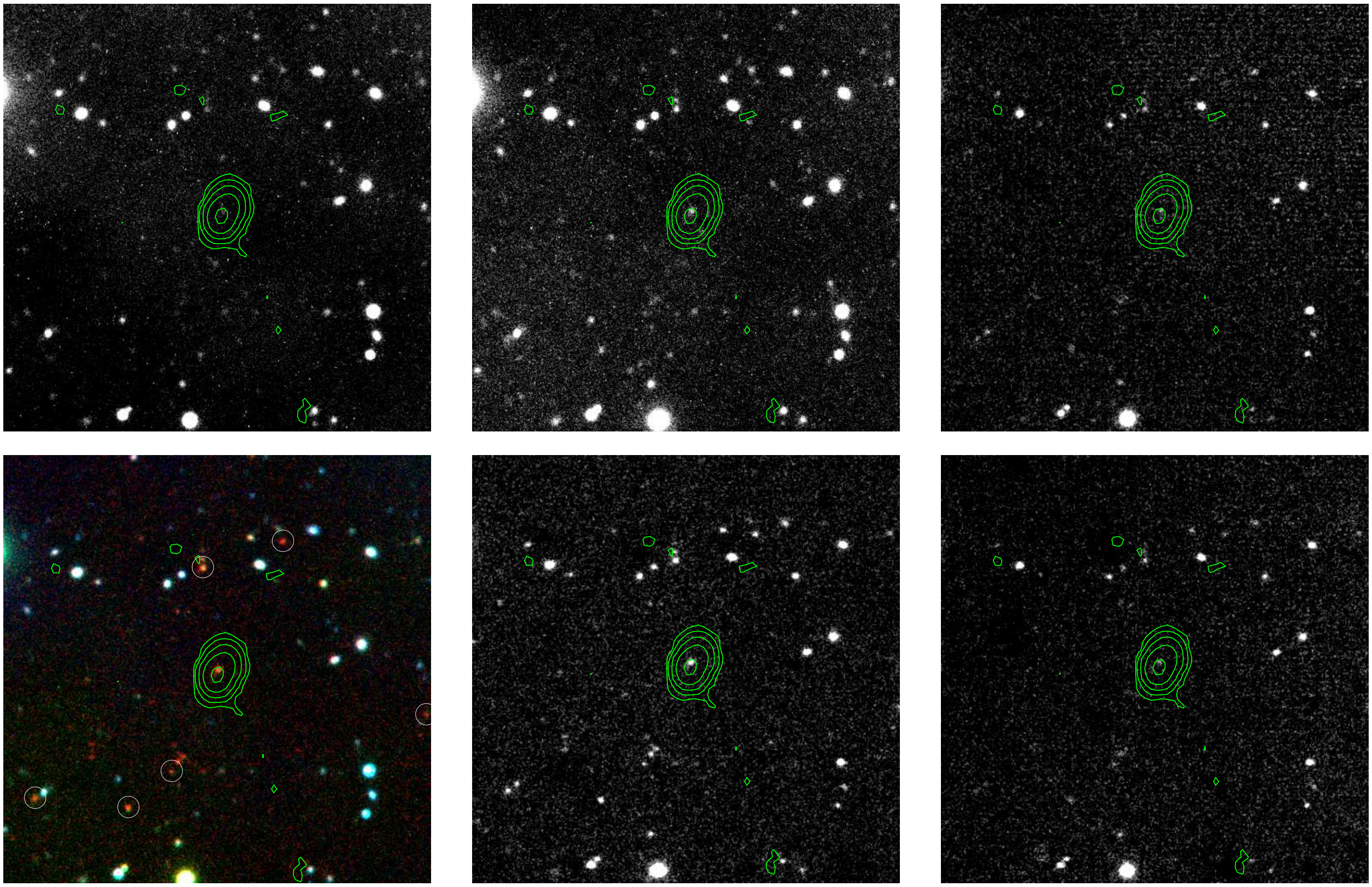

Figure 3.27 Clockwise from upper left: r, i, J, H, K_S, and RGB composite riK_S images of a $\sim 2.5 \times 2.5$ arcminute field around *J0256-0659*. EROs are marked with which circles on the RGB image. FIRST radio contours are overlaid in green.

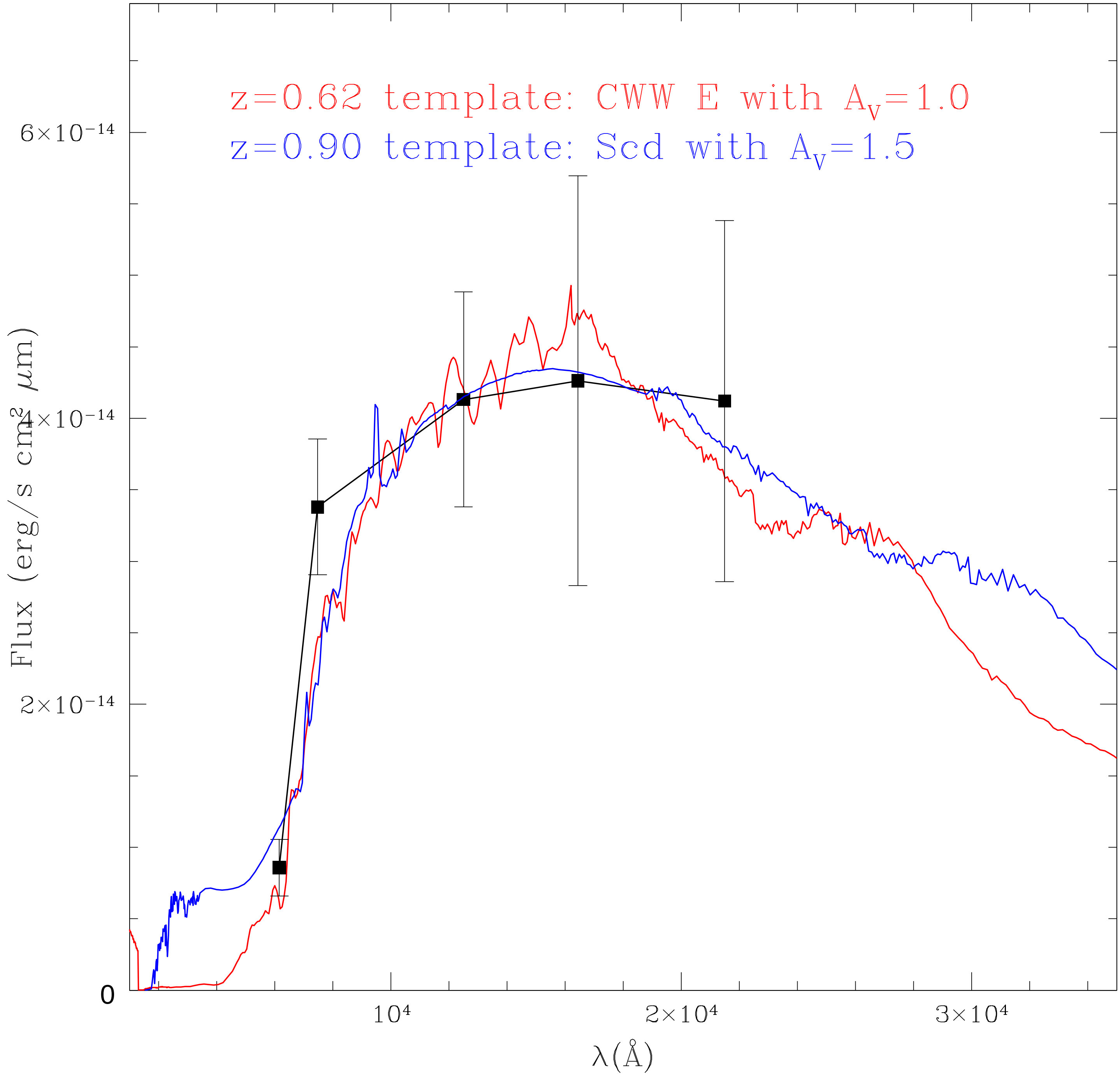

Figure 3.28 Best fit templates for *J0256-0659* with r, i, J, H, and K_S fluxes overlaid. Shown in blue is an elliptical galaxy template with Calzetti reddening of A_V=1.0 magnitudes at $z = 0.62$; in red is an Scd template at $z = 0.90$ with Calzetti reddening of A_V=1.5.

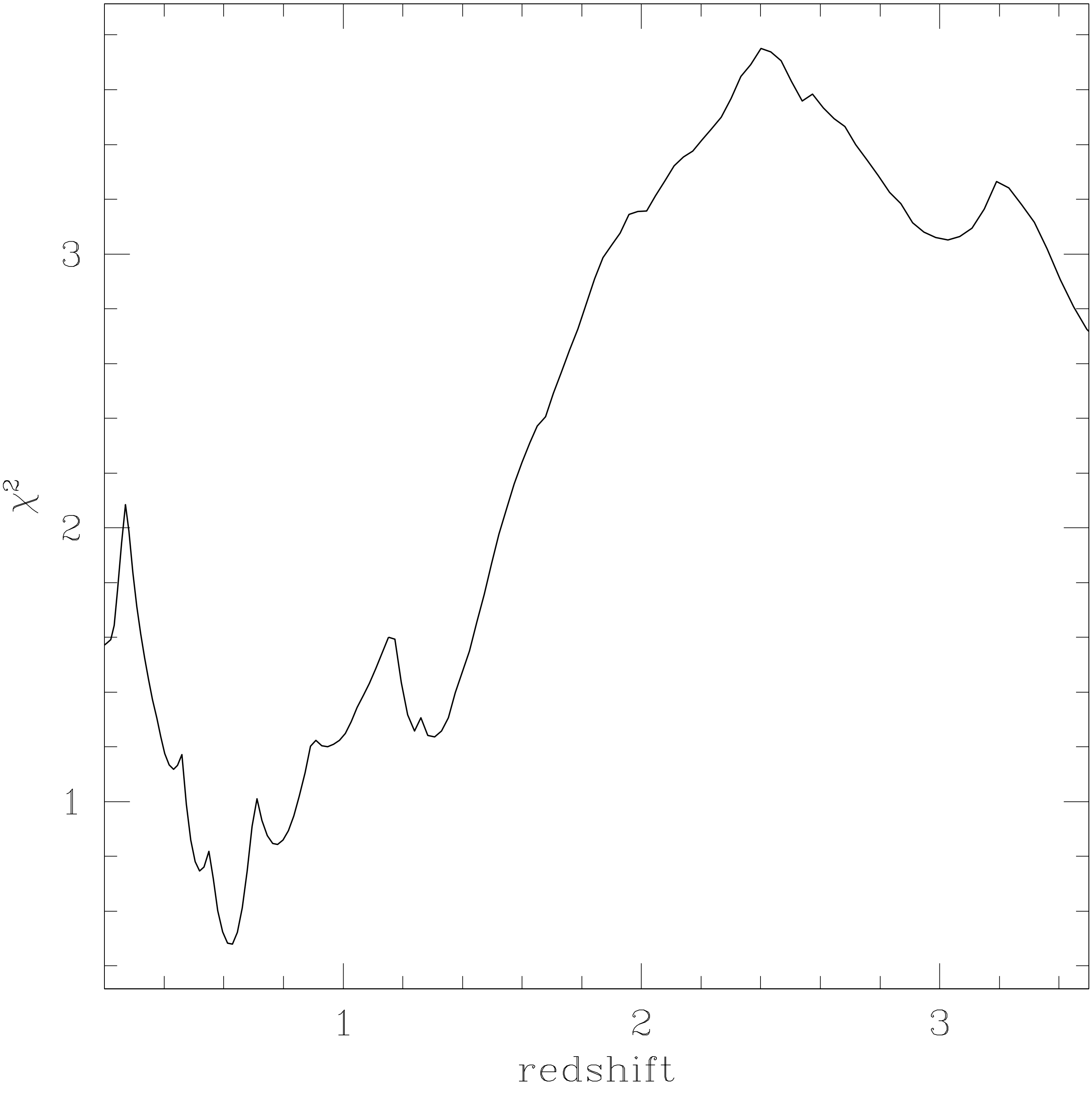

Figure 3.29 χ^2 as a function of redshift for the photometric redshift fit for *J0256-0659*.

3.11.2 J1546+1754

J1546+1754 is a $K = 17.29$ radio galaxy, which falls well within our Red DRaGON criteria. Figure 3.30 shows r, i, J, H, and K_S images of the radio galaxy, along with an riK_S RGB composite. The field of view is 2.5 × 2.5 arcminutes. Figure 3.31 shows a closer 20 × 20 arcsecond in r, i, K_S and RGB riK_S view, which shows that *J1546+1754* is extended, with multiple sources that have different morphologies and colors in the r, i, and K_S bands. This may indicate that the galaxy is undergoing a merger. However, because this galaxy consists of multiple components with different colors, it is a poor candidate for SED modeling (e.g. Figure 3.31 shows that the i band object consists of a blend of the main K_S detected object and a bluer object to the South. Because SExtractor does not deblend this into two objects, the colors computed from the total magnitudes will not reflect those of the two separate objects). We attempt to account for this by using $4''$ diameter aperture magnitudes in each band centered on the K_S-band object position. These magnitudes are given in Table 3.12. EROs are circled in white in the riK composite image. FIRST radio contours are overlaid in green, with an outer contour showing a flux density of 0.5mJy and each contour marking a factor of four increase. Visual inspection of the riK composite image shows several additional red objects that do not meet our ERO criteria, but whose color indicates that they may be associated with the radio galaxy.

Figure 3.32 shows the photoz residual χ^2 as a function of redshift for *J1546+1754*. The best fit redshift is $z = 0.52$; however, as the Figure shows, there are multiple chi^2 minima, and redshifts of $z = 0.76$, $z = 1.2$, and $z = 3.1$ are also very likely. Figure 3.33 shows the flux in the five bands as well as the best fit templates for the four most likely redshifts: black is an elliptical galaxy at with Calzetti reddening of $A_V = 1.0$ at $z = 0.52$, magenta shows an Scd galaxy reddened by $A_V = 1.5$ at $z = 0.76$, blue represents an Scd galaxy with $A_V = 1.0$ at $z = 1.2$, and red is the third starburst template of Kinney et al. (1996) with an additional $A_V = 0.5$ applied at a redshift of 3.1. The uncertainty in all four of these redshifts is $\sigma_z \sim 0.25$. As mentioned earlier, the J-band flux has a large error, due to a shorter total exposure time, as well as the radio galaxy position in the quadrant of the FLAMINGOS instrument with higher average noise. If our flux measurement is an underestimate, then the best fit redshifts are at lower redshift, where the 4000 $\AA$ break falls between the r and i bands, similar to *J0256-0659*, which is reflected in the three $z \leq 1.2$ SED fits. If the J-band flux is accurate, then this could be due to the 4000 $\AA$ break falling between the J and H bands, which characterizes the $z = 3.1$ starburst template fit. Obtaining a spectrum of the object is the only way to definitively discern the truth.

There is an ERO with similar colors only $14''$ from the radio galaxy position, visible to the South in Figure 3.30. If we assume that this galaxy is associated with *J1546+1754*, we can examine SED fits to the ERO in order to compare with those of the radio galaxy. The ERO is isolated and compact and, therefore, a much better candidate for SED fitting. The apparent and AB magnitudes for this ERO are listed in Table 3.12. The large errors in the J and H bands lead to large uncertainties on the estimated photozs. Figure 3.34 shows the photometric redshift χ^2 as a function of redshift for the ERO, with best fits at $z = 0.7$ and $z = 1.3$, and Figure 3.35 shows the two best fit SEDs. These redshifts are close to fits for *J1546+1754* at $z = 0.76$ and $z = 1.2$, but no SEDs fit the ERO at the $z = 0.5$ and $z = 3.1$ minima. If the ERO is physically associated with the radio galaxy, it is very likely that both objects are at $z \sim 0.6 - 0.7$ or $z \sim 1.2 - 1.3$. An apparent magnitude of $K = 17.29$ for *J1546+1754* translates into an approximate redshift of $z = 1.0$ on the $K - z$ Hubble diagram. Unless the $z \sim 3$ obscured starburst scenario is correct, it appears that, similar to *J0256-0659*, *J1546+1754* is a lower redshift ($z < 2$) radio galaxy that meets our selection criteria due to lower than average flux in the optical, most likely from internal reddening.

In any of these cases, the fact that *J1546+1754* appears to consist of multiple components is very intriguing. If the multiple components are physically associated, then the galaxy is undergoing a major merger. The fact that one of the components is blue indicates ongoing star formation, which would rule out a so called "dry merger" (van Dokkum, 2005, and references therein). If the blue object is in the foreground, then it is possible that the foreground object is strongly lensing the radio galaxy, which could account for its higher than expected K-band flux. It is also possible that the excess flux is due to a contribution from the foreground object, though in the case of *J1546+1754* it appears that the blue object contributes almost no flux in K_S band. Higher resolution imaging (e.g. Hubble Space Telescope) is necessary to examine the relationship between the components. Deeper J

and H-band photometry with smaller errors would also help better constrain the SED fits for both the radio galaxy and ERO, though spectroscopic redshifts are what is ultimately needed.

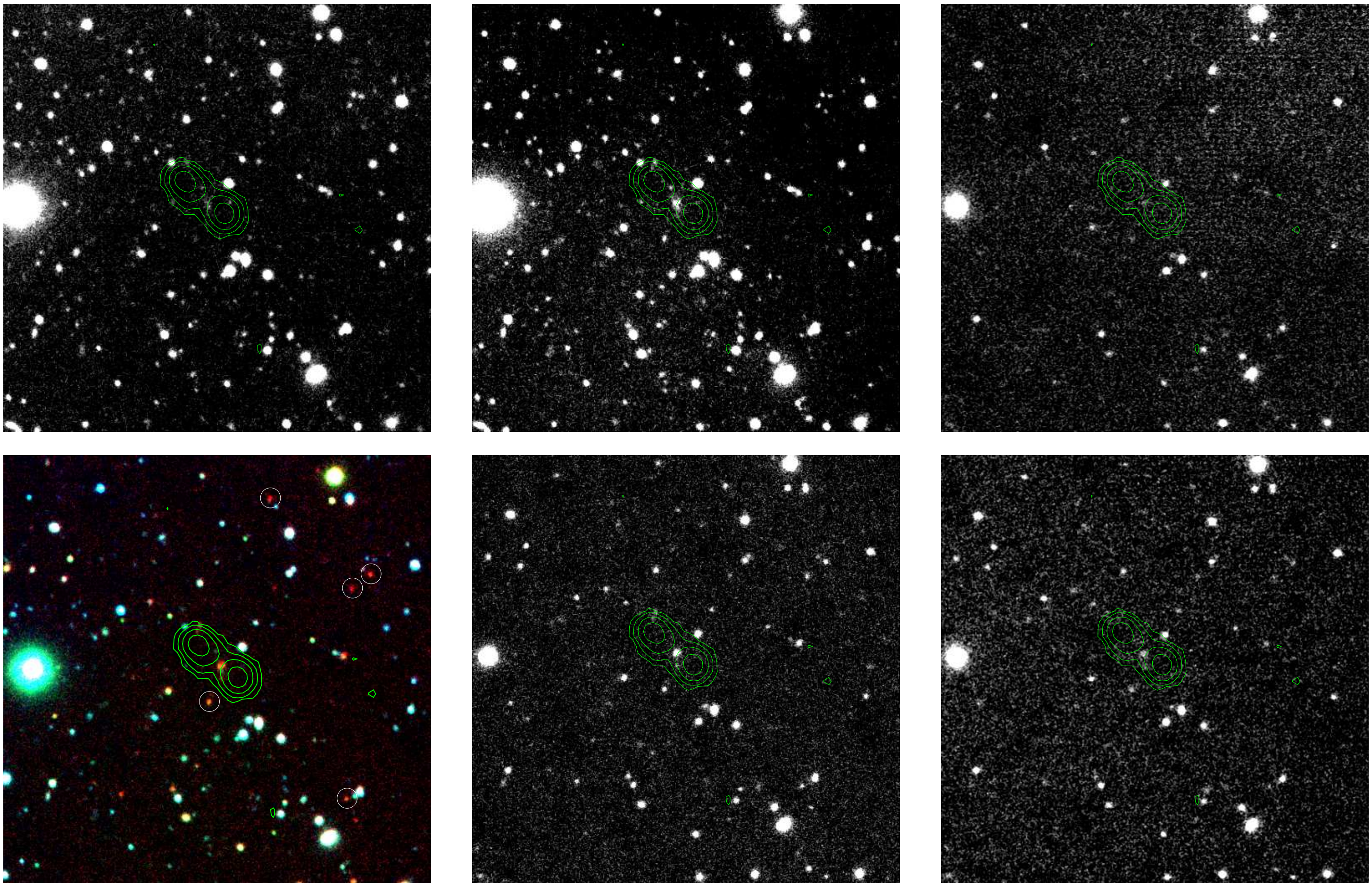

Figure 3.30 Clockwise from upper left: r, i, J, H, K_S, and RGB composite riK_S images of a $\sim 2.5 \times 2.5$ arcminute field around *J1546+1754*. EROs are marked with which circles on the RGB image. FIRST radio contours are overlaid in green.

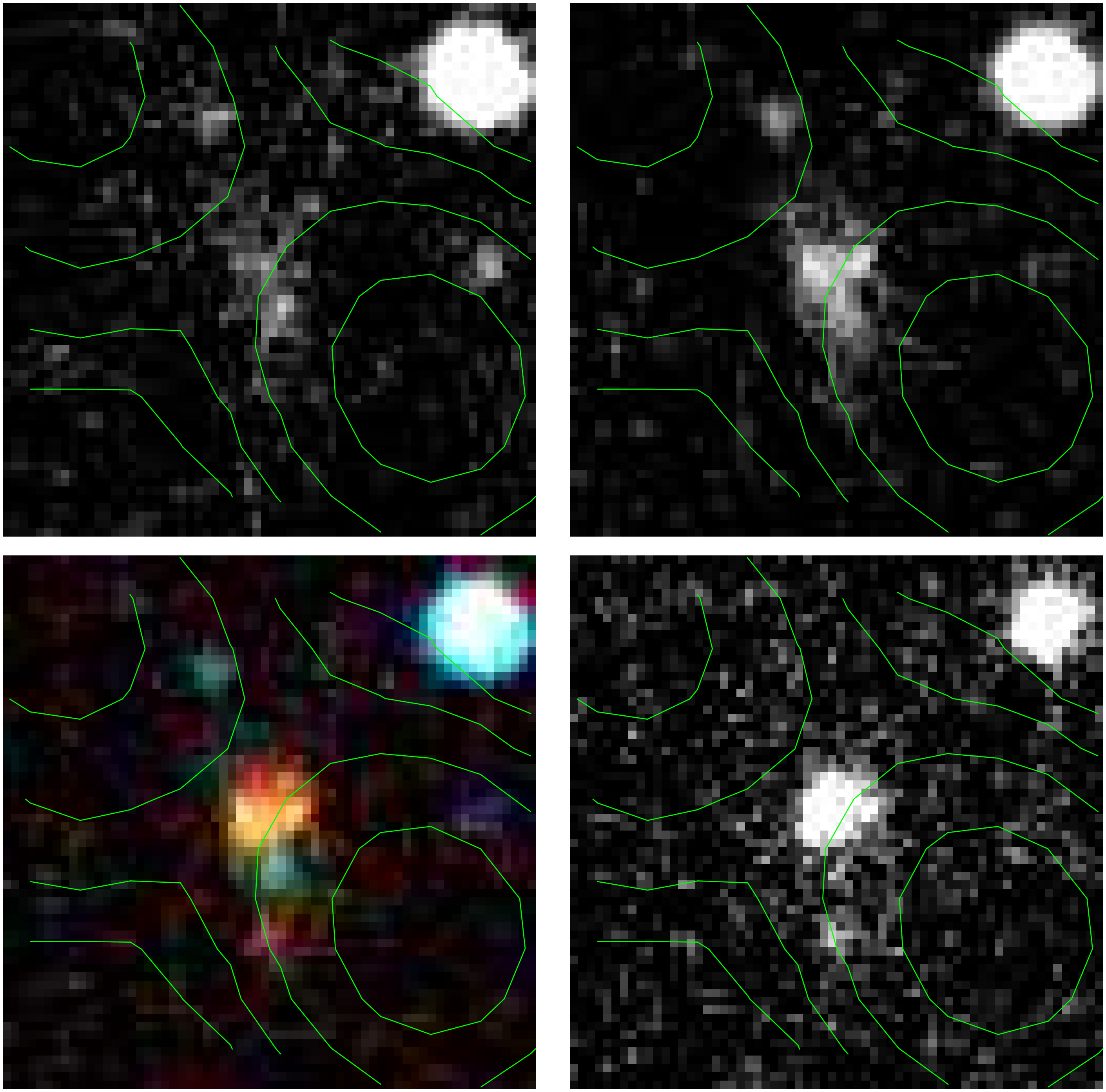

Figure 3.31 Clockwise from upper left: r, i, K_S, and RGB composite riK_S images of a 20 × 20 arcsecond field around *J1546+1754* showing multiple components. FIRST radio contours are overlaid in green.

Table 3.12: Apparent and AB magnitudes for total and 4" aperture magnitudes for J1546+1754

Type	r SDSS	r AB	i SDSS	i AB	J 2MASS[1]	J AB[1]	H 2MASS	H AB	K_S 2MASS	K_S AB
MAG_AUTO	22.66±0.10	22.67±0.10	21.24±0.061	21.27±0.061	20.09±0.24	21.00±0.24	18.40±0.14	19.79±0.14	17.29±0.05	19.14±0.05
$4''$	23.49±0.12	23.50±0.12	22.18±0.075	22.21±0.075	20.24±0.17	21.15±0.17	18.74±0.090	20.13±0.090	17.70±0.05	19.55±0.05
ERO	24.81±0.14	24.82±0.14	22.93±0.080	22.96±0.080	19.98±0.26	20.89±0.26	18.77±0.15	20.12±0.15	18.46±0.080	20.31±0.080

[1] The large error in J-band magnitude measurement is due to a limited exposure time of 22 minutes and the radio galaxy being positioned in the quadrant of the FLAMINGOS instrument with higher noise.

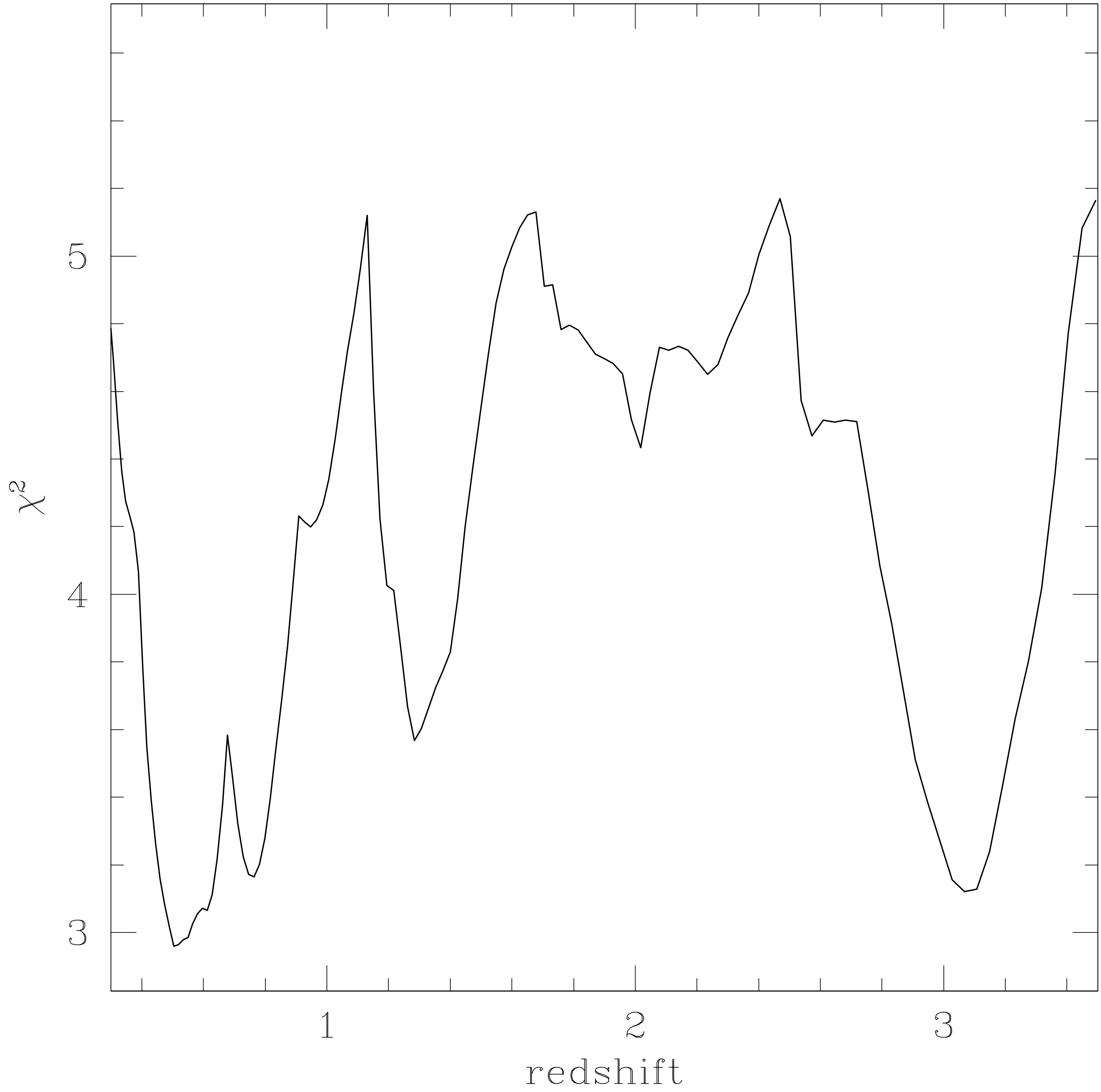

Figure 3.32 χ^2 as a function of redshift for the photometric redshift fit of *J1546+1754*.

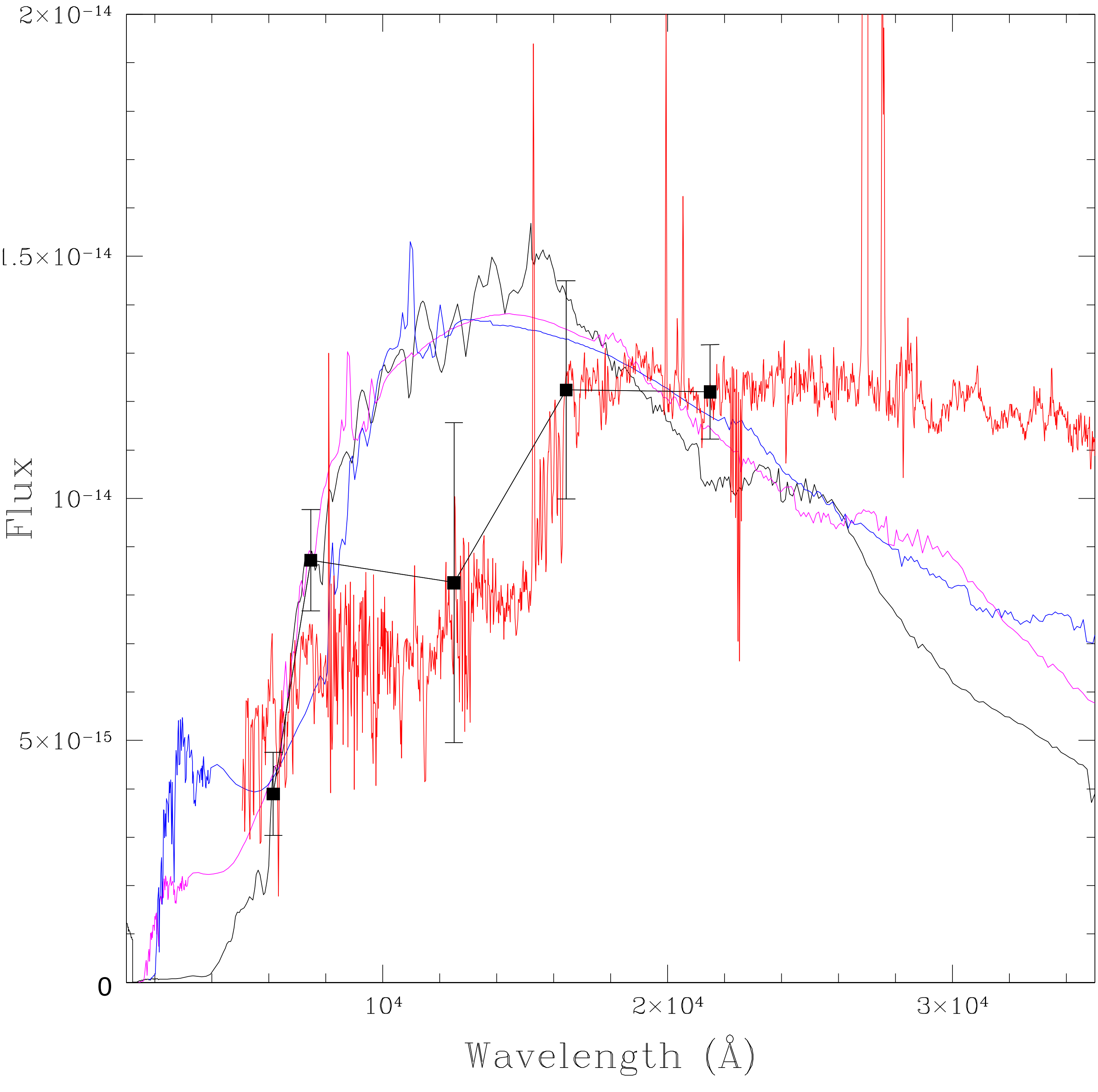

Figure 3.33 Best fit templates for *J1546+1754* with r, i, J, H, and K_S fluxes overlaid. Shown in black is an elliptical galaxy template with Calzetti reddening of A_V=1.0 magnitudes at z = 0.52; in magenta is an Scd template at z = 0.76 with Calzetti reddening of A_V=1.5; in blue is an Scd template at z = 1.2 with Calzetti reddening of A_V=1.0; in red is the third starburst template of Kinney et al. (1996) with an additional A_V=0.5 applied at a redshift of 3.1.

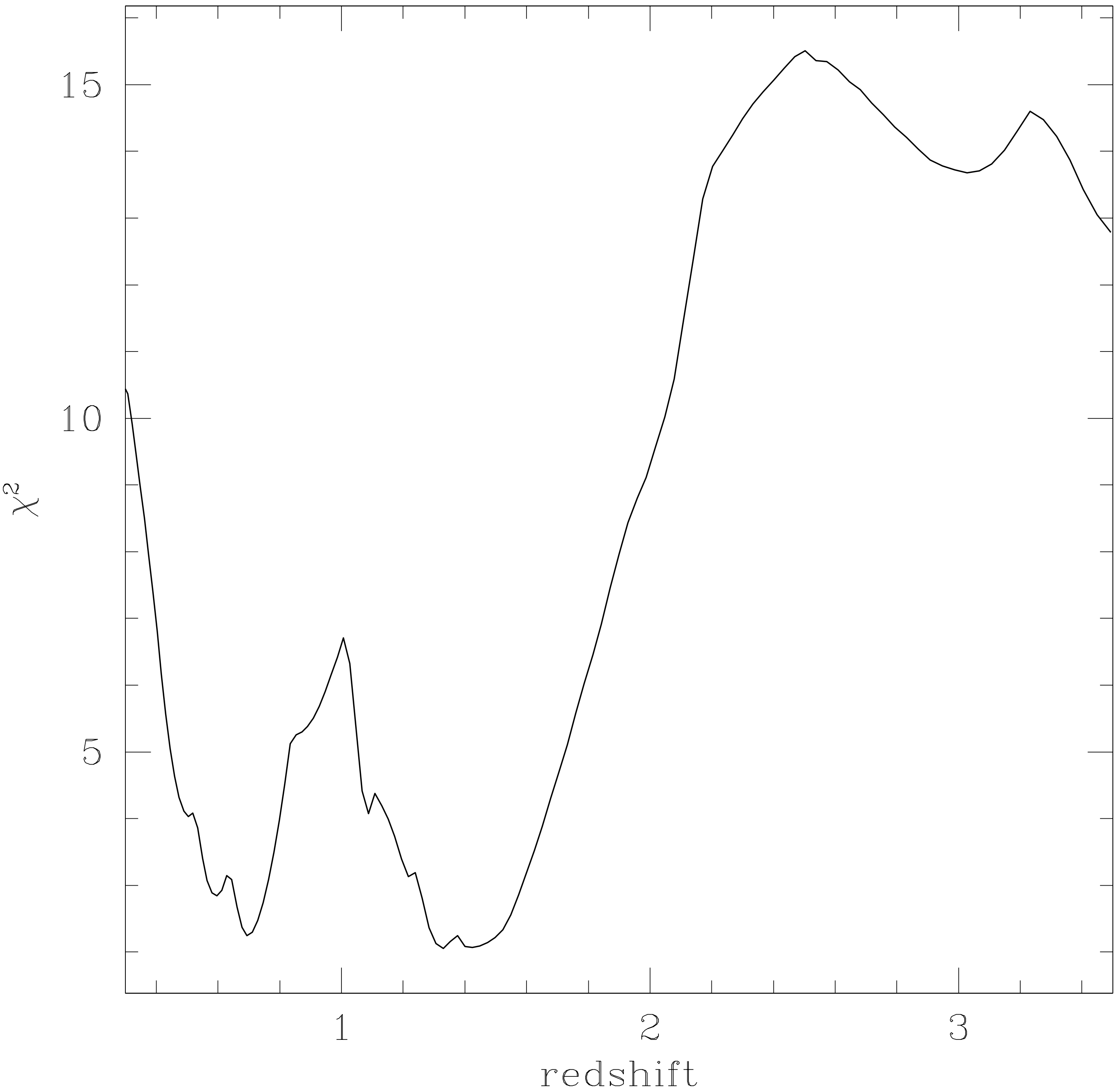

Figure 3.34 χ^2 as a function of redshift for the photometric redshift fit for the ERO 14″ from *J1546+1754*.

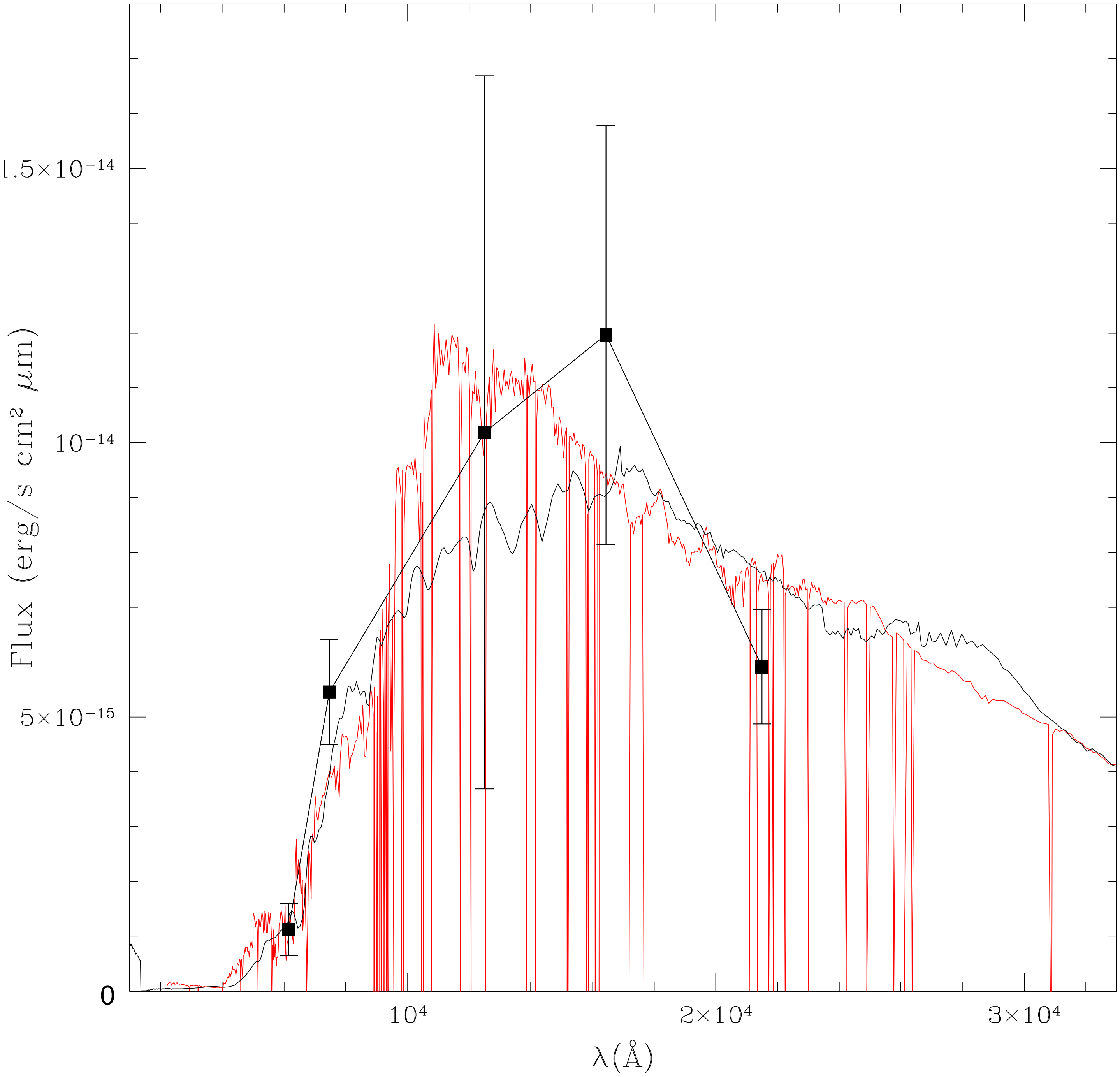

Figure 3.35 Best fit templates for the Extremely Red Object 14″ from *J1546+1754* with r, i, J, H, and K_S fluxes overlaid. Shown in black is an elliptical galaxy template with Calzetti reddening of A_V=1.0 magnitudes at $z = 0.7$, in red is an instantaneous burst PEGASE model with initial Solar metallicity and age of 1.2 Gyr at $z = 1.3$.

4.0 CONCLUSIONS

> “Yeah? Well y’know, that’s just, like, your opinion, man”
>
> -Jeffrey Lebowski, *The Big Lebowski*

4.1 GALAXY LUMINOSITY FUNCTION

In this thesis, we have implemented the new maximum likelihood estimator described in Sheth (2007). Using mock catalogs, we have demonstrated that realistic redshift uncertainties have a dramatic impact on the measured shape of the LF by using the 1/Vmax, STY, and SWML methods in the presence of the uncertainties. Our modified estimator, described in Section 2.1.5, is able to recover the true luminosity function, provided that the photometric redshift errors are smaller than $\sigma_z/z \approx 1$. The sensitivity of the estimator to even 10% of the sample having $\sigma_z/z > 1$ tells us that the error properties of the photometric redshift dataset must be well understood for the LF results to be trusted.

We have introduced a parameterization of the luminosity function in terms of cubic BSplines (Appendix A). This formulation, which reduces to the SWML if first order, rather than fourth order (cubic) polynomials are used, captures variations in the luminosity function seen in the SWML method, while providing a smooth parameterization that better reflects the continuous galaxy distribution, unlike the SWML and 1/Vmax methods. The number of BSplines used as basis functions can be changed to capture details of the distribution not possible with the two parameter Schecter function parameterization. BSplines also generalize well to two dimensions, and will be useful for calculation of bivariate luminosity functions in the future.

Using an existing template based photometric redshift code (photoz++) similar to that used in the SDSS, we have computed photozs for coadded data from SDSS Stripe 82. Comparison of the spectroscopic and photometric redshifts for galaxies in Stripe 82 with confirmed redshifts (Figure 2.33), as well as the photoz redshift distribution (Figure 2.35) show obvious systematic effects, with excess numbers of galaxies at some redshifts, and deficits at others. The photoz type distribution is also very different from the bimodal distribution expected (Figure 2.43). These results call into question the validity of the photometric redshifts output by the photoz code, particularly the galaxy types, and redshifts $z \geq 0.3$, for which we did not compute the luminosity function. For the remaining photozs, we find that the method used to estimate the redshift uncertainties output by the photoz++ code does not reflect the actual marginalized error distributions, which are often underestimated. Use of these uncertainties with our modified likelihood estimator undercorrect the luminosity function, supporting the conclusion of underestimated errors. As a solution, we output the marginalized probabilities, based on the χ^2 difference between template and observed fluxes, and perform a two Gaussian fit to estimate the probability distribution for each galaxy. This parameterization accurately reflects the uncertainties for nearly all of the galaxies, and was used in the final computation of the Luminosity function. In order to minimize the number of galaxies with large redshift uncertainties, we find that galaxies with $r > 20.5$ should be excluded for this dataset.

We have computed the luminosity function for galaxies in two redshift ranges: $0.1 \leq z \leq 0.2$ and $0.2 \leq z \leq 0.3$. For the $0.1 \leq z \leq 0.2$ data, we find that the bright end of the luminosity function given by our modified estimator was consistent with both a small spectroscopic galaxy sample and the results of Blanton et al. (2001). For the $0.2 \leq z \leq 0.3$ data, we see that the modified estimator Schechter function is very similar to the COMBO-17 LF, which uses data from the redshift range $0.2 \leq z \leq 0.4$. We further confirm the bright end of the luminosity function by computing the SWML LF for the SDSS DR6 main galaxy sample, which agrees very well with our Schechter function estimate. The BSplines LF fits to both datasets show deviations from the expected form, particularly an sharp area of underprediction at the faint end. This is consistent with the effect seen for galaxies with large errors at the faint end of the LF seen in the mock datasets, and is most likely due to galaxies with bimodal redshift uncertainties and large non-Gaussian tails in their probability distributions. The extra degrees of freedom of the BSplines fit allows for a more generalized shape than the two parameter Schechter function form; however, this freedom also makes this parameterization much more sensitive to the effects of redshift errors, as well as systematic effects in the data, which may also play a role in the poor fits (e.g. a bias in the photozs, where the distribution is skewed away from an mean photoz equal to the average spectroscopic redshift). We have deferred much of the BSplines analysis until a better photometric dataset becomes available (see Future Work in the next Section).

In order to examine the type dependence of the luminosity function, we divided the galaxy sample in the $0.1 \leq z \leq 0.2$ range into quartiles according to the continuous type parameter output by photoz++. Qualitatively, the distribution is as expected, with red/early galaxies comprised the bright end, then falling in number at lower luminosities, while blue/late galaxies make up the faint tail of the distribution, with a population still increasing at the limits of the absolute magnitude range probed. When the $0.2 \leq z \leq 0.3$ dataset is split using these same type bins, several problems are evident: The sum of the four Schechter functions at the bright end is fainter than the single Schechter function fit to the same dataset, indicative of a systematic failing of this particular dataset. The bluest quartile of the data was best fit by a nearly one parameter, steep ($\alpha = -2.96$) power law, which forced the value of $M*$ and $\phi*$ to unrealistic values of $M* = -34.204$ and $\phi* = 8.7 \times 10^{-14}$, and the shape of this distribution is far from that expected. It appears that an excess of misclassified galaxies at both the faint and bright end of the blue quartile cause this behavior. The type histograms shown in Figures 2.43 and 2.45 did not show the characteristic bimodal distribution expected. This, once again, called into question the quality of the photoz dataset. We hold off on a complete analysis of the type dependent LF, and the BSplines parameterization of the LF until an improved version of the photometric redshift code is available. However, we emphasize that the success of our modified estimator in recovering the true luminosity function in the mock data samples lead us to conclude that the method is sound, provided that the redshift errors are not large, and the error distribution used is reflective of the actual redshift errors.

4.2 THE DRAGONS SURVEY

Based on the approximate redshifts given by the $K-z$ Hubble diagram for radio galaxies, it appears that our novel radio-optical selection criteria are very efficient at identifying $z > 2$ radio galaxies. We have obtained near-infrared imaging for 189 radio galaxy candidates, and more than 70% should lie at $z > 2$, and 35% at $z > 3$. With less than 150 $z > 3$ radio galaxies spectroscopically confirmed, it is likely that we have increased the known population of such objects by $\sim$ 50%. Due to the large scatter in $K-z$ redshift estimates, spectroscopic confirmation is needed to verify these conclusions.

This selection technique is not sensitive to radio spectral slope, and avoids the frequency dependence of USS techniques for galaxies with non-power law radio spectra. Of the 141 target galaxies present in the Texas 365 MHz survey 46 have $\alpha^{1.4\mathrm{GHz}}_{365\mathrm{MHz}} < 0.8$. These would be excluded by the USS criteria of van Breugel et al. (1998), and all but 8 of these 141 have $\alpha^{1.4\mathrm{GHz}}_{365\mathrm{MHz}} < 1.3$, which would be excluded from more recent USS selections (e.g. De Breuck et al., 2001; Jarvis et al., 2001). Spectroscopic confirmation that even a small number of these galaxies reside at high redshift will have a dramatic effect on fits of the $z-\alpha$ relation.

Comparison with the previous surveys of Best et al. (1999) and De Breuck et al. (2001) shows that our technique selects nearly all of their high redshift targets, while also eliminating the low redshift sources. The K-band number counts are consistent with previous work, and the large non-contiguous area (5.05 square degrees) covered by the *DRaGONS* survey to date makes it an excellent resource for exploring galaxy properties through the combination of NIR and optical data. A reanalysis of data from Schmidt et al. (2006), combined with new DRaGONS data, shows no excess of $K \leq 17.5$ Extremely Red Objects around the radio galaxies. We do, however, see evidence for an excess number of faint K-band selected galaxies within 1-2 arcminutes of our $K \leq 18.0$ DRaGONS galaxies. This is consistent with the radio galaxy being the brightest member of a protocluster.

We have uncovered a previously unseen class of radio sources with anomalously red colors ($r-K > 6.5-7$) which we have dubbed "Red DRaGONS". Their extreme color may be evidence of significant obscuration at moderate redshifts, though it appears that at least some Red DRaGONS are $z \sim 1$ galaxies with excess reddening that causes them to meet our $r - K$ selection criteria. These galaxies represent almost ten percent of our observed sample, indicating that they may be a substantial percentage of the radio galaxy population. Being non-detections in SDSS (with $r > 24.1$), current optical AGN selection techniques are insensitive to these sources. Radio loud QSOs comprise only $\sim 5-10\%$ of overall QSOs; therefore, these objects could represent a significant contribution to radio loud AGNs that are not counted in current samples.

Deep optical imaging of four Red DRaGONS fields shows an excess number of EROs with $18 \leq K \leq 19.0$. The ERO surface density is consistent with that seen by Wold et al. (2003) around $z \sim 2$ quasars. The presence of this excess argues against these objects being at $z < 1.5$, as the number of ERO galaxies decreases dramatically at lower redshifts. Photometric redshift and SED fits to two Red DRagons with r, i, J, H, K_S photometry, however, do indicate probable $z < 1.5$ redshifts for at least some of these K-band bright galaxies, where their extreme colors would then be due to excess reddening. Two of the five Red DRaGONS with deep optical imaging show multiple objects with distinct colors. This could either be evidence for a merger or a chance superposition of two objects projected on the sky. If the objects are physically associated, these galaxies are undergoing a major merger, and star formation triggered by the merger could explain their brighter than expected K-band flux and reddened colors. If the proximity is due to projection, it could indicate that the foreground object is lensing the radio galaxy, or the interloper object could simply contaminate the K-band measurement with added flux. High resolution imaging and spectroscopy of the multiple components is needed to discover the true nature of these systems.

4.3 FUTURE WORK

4.3.1 Luminosity Functions

The most pressing need for further development of the luminosity function work is improvement of the photometric redshift estimation. The systematic offsets and gaps seen in the photometric vs. spectroscopic redshift plot shown in Figure 2.33, and dN/dz distribution of Figure 2.35 should be greatly reduced with a fairly simple modifications of the photometric redshift code: Better star-galaxy separation would help eliminate contamination of the galaxy sample with stars, and improve the completeness of compact high redshift galaxies. With the proper use of Bayesian priors, such as a magnitude and/or dN/dz prior, the redshift distribution output by photoz should be much closer to the expected redshift distribution. The unusual type distributions shown in Figures 2.43 and 2.45 are a major concern. The choice of templates will be reexamined in future runs of the improved photoz code. The templates used will have to reproduce the bimodal type distribution known to exist out to redshifts $z \approx 1$. Many of these changes are already implemented in the newest version of photoz++ used on the official SDSS data releases. The main shortcoming of the current photoz++ version is the improper estimation of photoz errors, as discussed in Section 2.2.3 and illustrated in Figure 2.32. As discussed in this thesis, proper error estimation is essential to our modified likelihood estimator. The two gaussian estimation of the redshift error shown if Figure 2.32 added only a fraction of the run time compared to the photoz code. Such an error estimate, or even a more precise method, could easily be implemented in future photoz++ versions, which would greatly aid in the proper treatment of photometric redshift uncertainties in many applications, not limited to the luminosity function. However, even this is not ideal. The marginalized error distribution output by photoz++ is calculated based on χ^2 values of the five SDSS magnitudes compared to a set of templates. This difference may or may not reflect the *actual* distribution of errors, in the sense of $\Delta z = z_{spec} - z_{phot}$. Ideally, what is needed is a very large set of spectroscopic redshifts that completely span the redshift, type, and luminosity range of the galaxies in the overall photometric sample. We can then empirically determine the photometric redshift uncertainty as a function of redshift, type, and luminosity. This will be a time consuming and expensive undertaking, but it is essential to most applications of photometric redshifts, as unknown biases in the redshift distribution or the characterization of errors can severely bias results. Thankfully, due to the prominent role that photozs play in many future surveys (e. g. DES and LSST) there is an intense effort to characterize these effects, and the necessary hard work is already underway.

Once an improved photometric redshift dataset is available, many of the applications discussed above will be greatly enhanced. The universal LF can be computed using our modified maximum likelihood method to as high a redshift as the σ_z/z limits allow. This applies, not only to the stripe 82 data, but also to SDSS in general. If the photoz uncertainties are properly calculated, the entire SDSS survey can be used to compute the luminosity function, though datasets of this size, with tens or hundreds of millions of galaxies, will require code optimization or parallelization in order to run in finite timescales. With proper redshift and type distributions and large datasets, details of the bivariate luminosity function, versus type, environment, color, etc..., can be explored. The very large dataset available through SDSS and future surveys will allow not just binning, as preliminarily explored here, but use of the entire continuous distribution of such parameters. One of the major motivations for the introduction of the BSpline parameterization is that in generalizes well to two dimension, as a knot sequence on a line segment is simply replaced by a grid of knot positions on a plane. We are still working out the implications and implementation of type/color/density uncertainties on the form of our modified estimator. Again, code optimization or parallelization will be necessary to carry out this two dimensional analysis, as the parameterization will have more degrees of freedom, as well as a more complex maximum likelihood estimator to account for the additional error in the second bivariate parameter.

4.3.2 The DRaGONS Survey

Two imaging runs were completed this year, covering 2007 March 30 to April 4, and 2007 May 27 to June 1. Another 76 new radio galaxy targets were observed, and four Red DRaGONS were imaged in J and H-bands. These data will be reduced and included in an upcoming paper. These additional 76 radio galaxies bring the total number observed to 265, which is half of the total number of candidates that meet our selection criteria. The original survey plan called for imaging of $\sim$ 400 targets, but more time was lost than expected to bad weather and technical problems. We will apply for further time at the Mayall 4m telescope to image more targets.

Spectroscopic confirmation of DRaGONS' galaxy redshifts is of the utmost importance in order to verify unequivocally that our $K - z$ relation redshift distribution is accurate. Redshifts are particularly needed for Red DRaGONS and galaxies with shallow spectral slopes; spectroscopy will reveal whether the Red DRaGONS are lower redshift radio galaxies with sufficient reddening to meet our $r - K$ selection criteria, or higher redshift galaxies with unusually bright K-band flux. Spatially resolved spectra of the multi component Red DRaGONS will also distinguish between mergers and chance superpositions. Confirmation of even a small number of high redshift radio galaxies with shallow spectral slopes will be very interesting, especially in light of the new justification of Klamer et al. (2006), which posits that USS nature of high redshift radio galaxy spectra could be due to their location in dense environments. Examining properties of USS vs shallow spectrum sources could shed light on the validity of this claim.

Further deep optical imaging of Red DRaGONS is necessary to increase the ERO sample size, as ERO surface density is highly inhomogeneous. A larger sample of EROs will also allow for a more quantitative examination of clustering (i.e. calculation of the ERO 2 point correlation function). High resolution imaging of the Red DRaGONS with multiple components, in conjunction with spectroscopy, is needed to uncover the nature of the different components.

Deeper optical imaging will also soon be available for candidates in SDSS Stripe 82. Further imaging runs have been completed, and the SDSS team is currently working on a new reduction of this even deeper coaddition of the data in all five SDSS bands. This very deep data will allow us to establish colors and SED fits for our higher redshift DRaGONS candidates, as well as detect associated EROs to faint magnitudes for those at intermediate redshifts.

APPENDIX A

B(ASIC) SPLINES

This appendix is a quick summary based on a paper by Carl DeBoor, the CAGD handbook DeBoor (2001), which can be found at (`http://wisc.edu/Approx/cagdhand.ps.gz`). Many of the equations are nearly identical to those in this paper, as I have copied his notation for clarity. BSplines, or Basic Splines, are a set of piecewise polynomial basis functions. They are defined recursively on an interval divided into a series of segments defined by points known as the **knot sequence t** that partitions the interval:

$$\mathbf{t} \ = t_1 \leq t_2 \leq \ldots \leq t_j \leq t_{j+1} \ldots$$

The jth first order BSpline for the knot sequence t is defined as:

$$B_{j,1}(x) \equiv \begin{cases} 1 & t_j \leq x < t_{j+1} \\ 0 & otherwise \end{cases}$$

where the first subscript indicates the BSpline index, and the second indicates the order. In other words, the first order BSplines are simply a set of step functions. Higher order BSplines are defined recursively with the following relation:

$$B_{j,k} \equiv \omega_{j,k} B_{j,k-1} + (1 - \omega_{j+1,k}) B_{j+1,k-1}$$

where

$$\omega_{j,k}(x) = \frac{x - t_j}{t_{j+k-1} - t_j}$$

Note that $B_{j,k}$ is a k-th order piecewise polynomial that is non-zero and positive in the interval $t_j \leq x < t_{j+k}$ and is zero otherwise. In other words, $B_{j,k}$ has support over k knots; For example, first order BSplines consist of two linear components defined over two adjacent two knot intervals, third order BSplines consist of three quadratic polynomials defined over three knot intervals, etc…

One of the great advantages of BSplines is in their flexibility. The smoothness of the BSpline basis can be adjusted based on the specific choice of knot sequence. For a k-th order BSpline defined by k unique knots, The BSpline and all of its derivatives are smooth. However, if n of the k knots are at the same position (e. g. $t_j = t_{j+1}$), then only the first k-n-1 derivatives of the BSpline are continuous at that point, which allows for jump discontinuities in the BSpline and its derivatives at the knot points. More concisely, the number of smoothness conditions is equal to the order minus the knot multiplicity. An example of this effect is shown if figure A1, which shows three sets of BSplines. The bottom panel is second order (linear), middle is third order (quadratic), and the top is fourth order (cubic) BSplines. The squares show the knot points, and the individual BSplines are shown in color. Note that the jump discontinuity at $x = 0$ is allowed by the multiple knot at this position in each case. The double knot at $x = 6$ gives jump discontinuities in the second derivative inflection point in the cubic splines, first derivative cusp in the quadratic splines, and jump discontinuity for linear splines. Note also that the cubic splines have support over four knot intervals, quadratic over three, and linear over two.

The BSplines form a basis set from which we will fit our luminosity function. The actual spline curve is a linear combination of BSplines given by:

$$s(x) = \sum_i a_i B_{i,k}(x)$$

where the a_i coefficients are found that best fit the data. It should be noted that for first order (constant) BSplines, this formulation is identical to the stepwise maximum likelihood (SWML) method of Efstathiou et al. (1988), i.e. a set of tophat step functions. The BSplines functional form can be inserted into the standard STY estimator (Equation 2.7) just as EEP 88 and Lin 96 do for the SWML method in order to determine the ai coefficients that maximize the likelihood. Figure A2 shows an example spline fit using fourth order (cubic)

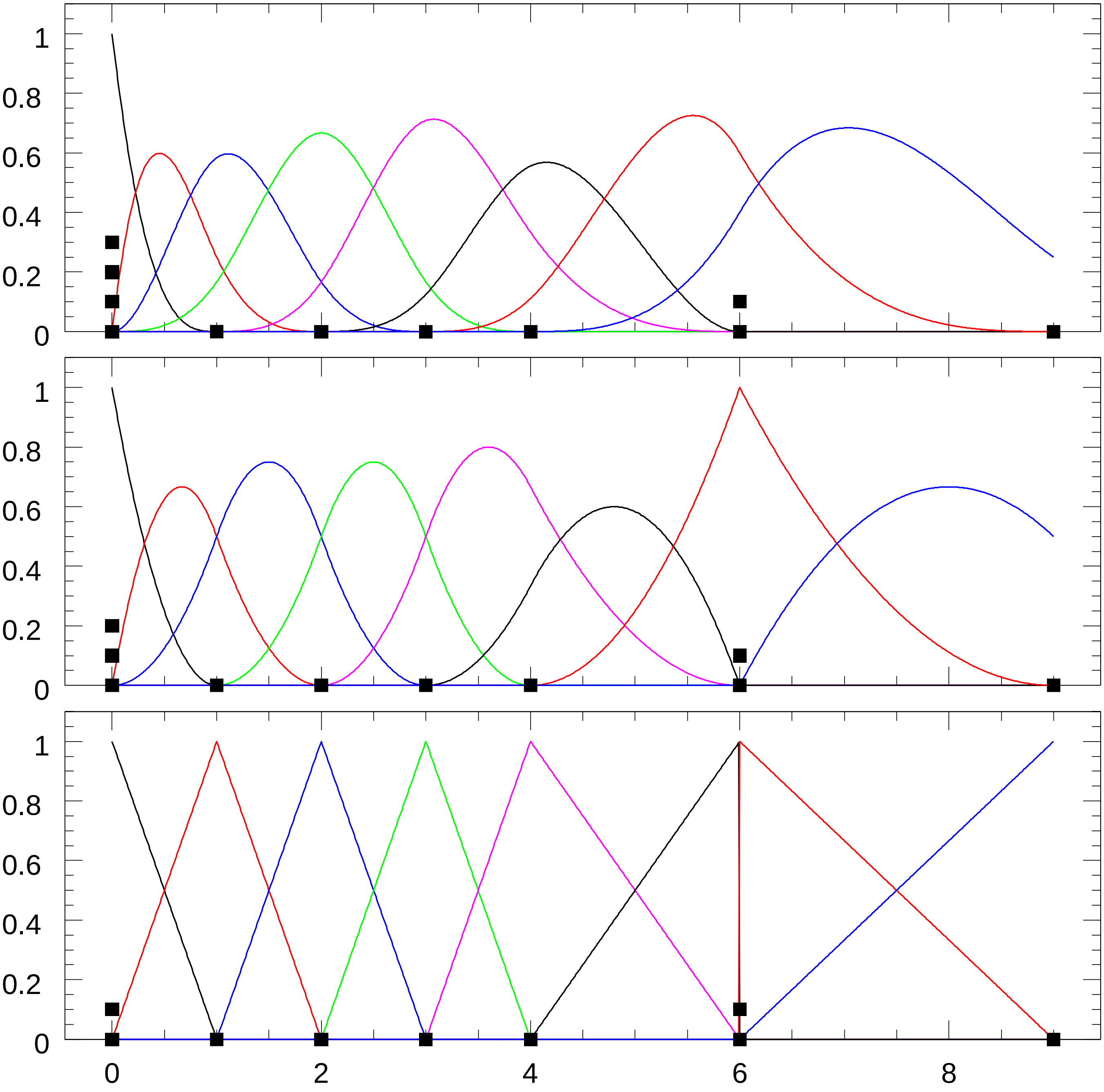

Figure A1 Three sets of BSplines for the knot sequence Lower panel is second order linear, middle panel is third order quadratic, and upper panel is fourth order cubic BSplines

BSplines to fit a Schechter function, showing both the individual weighted BSplines, as well as the total spline function.

The choice of knot positions is somewhat arbitrary, as a set of BSpline basis functions can be defined on any knot sequence that spans the magnitude range covered by the LF data. To make the choice of knot positions somewhat less arbitrary I will choose the knot sequence that best reproduces the best fit Schechter function determined from the MLE. This results in an unevenly spaced knot sequence, with more knots near the exponential break in the LF. This is understandable, as we are fitting an exponential fall off with polynomial basis functions, and more knots are required to approximate the rapid change in the function in the range.

A.1 SMOOTHING

BSplines are often referred to as "nonparametric" forms for estimating a function. This is not technically true, as pointed out by Eilers and Marx (1996). The fit is parameterized by the weights given to a set of piecewise polynomial functions. Unlike, for instance, the Schechter function parameterization, there is no physical interpretation behind the individual parameters that best fit the data (whereas in the Schecther function case, M_{star} is the "turnover" of the distribution and α is the power law slope of the faint end tail). Eilers and Marx, therefore, recommend using the term "overparametric" rather than "nonparametric". This applies equally to the stepwise maximum likelihood method in section 2.1.4. While the values in each step function do have an easy interpretation as a galaxy density, it is still a parametric form.

The total number of knots/BSplines is a free parameter. This is chosen arbitrarily, and we use fifteen to twenty, as a compromise between an accurate representation of the LF and an observed tendency of the estimator to overfit when more knots are used. Even with this number of BSplines, overfitting is a concern. To combat this, the smoothing criterion of

Eilers and Marx (1996) is added to the maximum likelihood estimator, which has the form:

$$\ln \mathcal{L}' = \ln \mathcal{L} - \lambda \sum_{\mathrm{i+2}} (\mathrm{a_i} - 2\mathrm{a_{i-1}} + \mathrm{a_{i-2}})^2$$

where the a_i's are the BSpline coefficients and λ is an arbitrary weight factor that controls the level of smoothing. The choice of Δa_is in the sum is motivated as an approximation of the second derivative of the spline function, so this penalty is similar to forcing continuous second derivatives. Viewed another way, this form simply penalizes rapid variation in adjacent spline coefficients, in effect reducing the likelihood of rapid changes in the function seen in overfitting. The amount of smoothing needed is very small for most datasets, and we will use values of $\lambda = 100 - 500$. With tens to hundreds of thousands of galaxies in the datasets, this is a rather modest penalty.

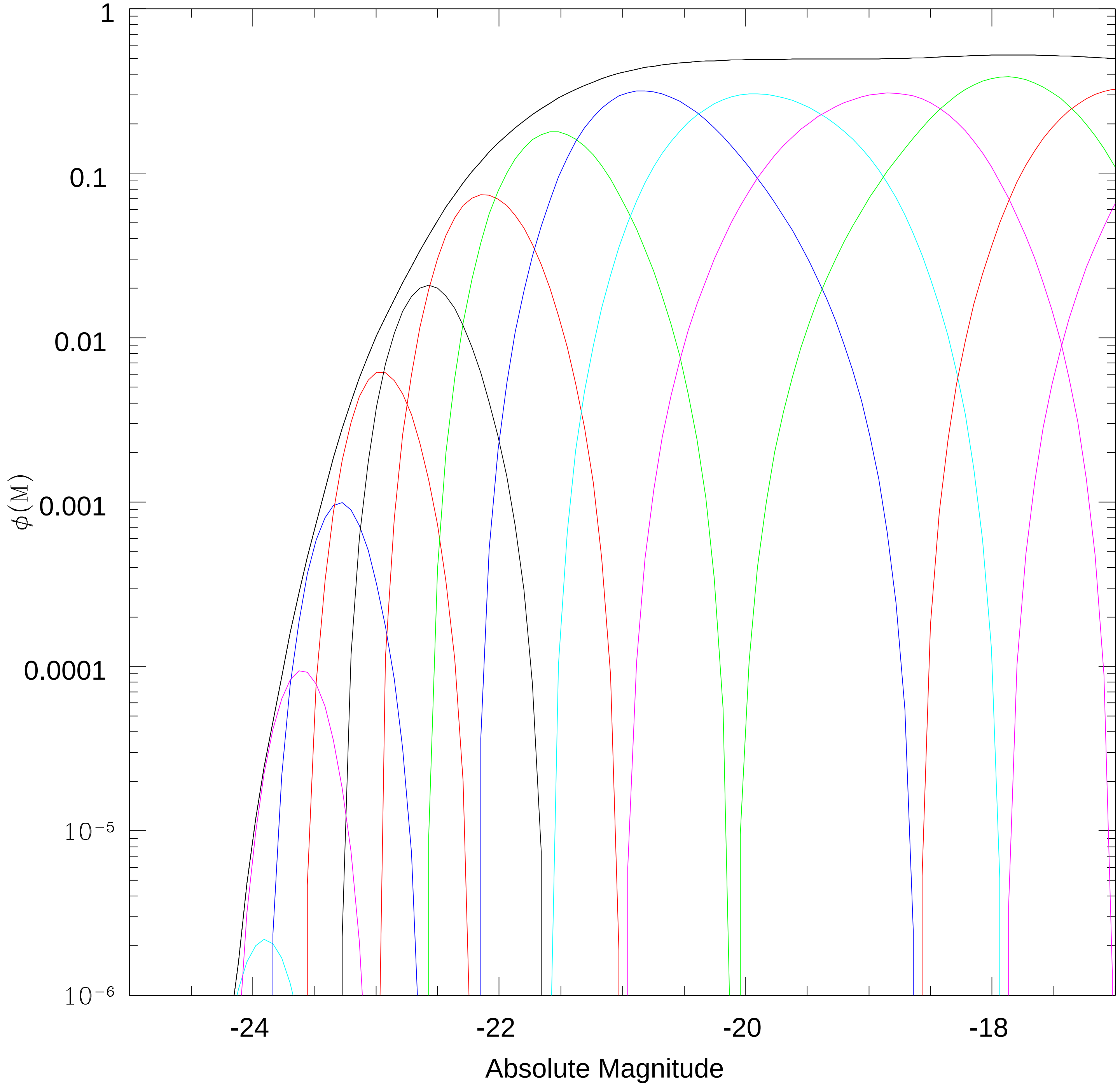

Figure A2 An example spline fit to a Schechter function (black) showing the contribution from the individual BSpline functions.

APPENDIX B

PHOTOMETRIC REDSHIFTS

Finding the redshift of objects is extremely important in astronomy. To calculate the galaxy luminosity function, we require the absolute brightness, or luminosity, of each galaxy. However, what we actually observe is the apparent brightness, or flux. Measuring the amount of flux from a galaxy or other object (usually through a specific bandpass filter), be it with a ccd, a photographic plate, or your eye, requires no additional information about the object. However, to translate this flux into an absolute luminosity, a distance to the object is needed. Luckily, the expansion of the Universe provides us with an excellent distance measure: redshift. As the Universe expands, light travelling through space is stretched, making the wavelength longer, or redder. The longer light travels, the more it is stretched, thus, measuring this shift (and assuming that we know the expansion history of the Universe) tells us just how far the light has travelled.

For a galaxy, redshift is measured by identifying narrow features of the spectrum, usually emission or absorption lines, so that the redshift can be determined very precisely, for example the O[III] forbidden line at $\lambda = 5007\mathring{A}$. Redshift is defined as if the light was doppler shifted, rather than stretched:

$$\frac{\lambda_{obs}}{\lambda_{emit}} = 1 + z \tag{B.1}$$

So if an O[III] line is observed at $\lambda = 7510.5$, then the galaxy is at a redshift of $z = 0.5$. Once the redshift is known, we can use Equation 2.4 to determine the distance. The luminosity is then simply

$$L = 4\pi \, dL^2 \, S \tag{B.2}$$

where L is the luminosity and S is the observed flux. Or, if absolute magnitudes are desired, we can use Equation 2.3.

The main drawback to spectroscopic redshifts is the expense of obtaining them, especially for the faintest and/or most distant objects. Rather than all of the flux falling on to just a few pixels, as would happen with a broad band filter, a spectrograph passes the light from the distant object through a grism, spreading it out over hundreds of pixels that make up the wavelength range of light, so there is much less flux in each individual pixel. In order to reach the same signal to noise, you must therefore increase the integration time and/or the size of the telescope collecting area, both of which are expensive, in terms of telescope time and money.

An alternative to this very precise method of determining redshifts through spectroscopy is to instead look at the broad band characteristics of galaxies in order to get a less exact idea of the redshift. Rather than targeting a narrow emission line to measure the shift of the line to within a few angstroms, the target of broad band techniques are ”breaks” in the galaxy spectrum: rapid changes over a small wavelength range. The most common breaks are the 4000 angstrom break and the Lyman break. The position of these breaks within the filters used will dramatically affect the observed ”colors” (which is just the magnitude difference between two filters). These are known as photometric redshifts, or photozs. Photozs can be thought of as a very low resolution spectrum of the galaxy, where instead of hundreds of pixels with widths of a few angstroms, we instead have (in the case of SDSS) five pixels with widths on the order of a thousand angstroms. This idea was first proposed in Baum (1962), who undertook a program to observe cluster elliptical galaxies. After averaging the measurements from several galaxies in each cluster, he compared the rough spectrum to measurements of local elliptical galaxies in order to estimate a wavelength shift in the spectrum (redshift) as well as any overall flux offsets (luminosity evolution, after taking account of cosmological dimming). The technique works best when the filters do not have gaps between their response curves, but do not significantly overlap. That is, as close to adjacent pixels in a traditional spectrum as possible.

An example is shown in Figure B1, which shows the five SDSS filter transmission curves with two elliptical galaxy spectra overlaid. The solid black line is in the rest frame at $z = 0$. The 4000$\mathring{A}$ break is the obvious feature of the spectrum, which contains no sharp emission or absorption features. The 4000$\mathring{A}$ break in the dashed spectrum falls near $\lambda = 6000\mathring{A}$, putting this galaxy near $z = 0.5$. Figure B2 shows an elliptical galaxy spectrum at $z = 1.2$ as well as the fluxes obtained by convolving this spectrum with six filter transmission curves: SDSS r, i, and z, as well as the J, H, and K_S filters from the KPNO 4 meter telescope. The fluxes are shown at the center position of the six filter curves. This example illustrates how photozs work: a broad galaxy feature, in this case the 4000$\mathring{A}$ break falls within the z-band. Redward of this band (the J, H, and K_S bands) we have higher flux, and blueward (r, and i) we have less, akin to a very low resolution spectrum. This is also the basic idea behind ”dropout” techniques to find high redshift objects, only instead of lower flux in the bands blueward of the break, you are looking for non-detections. For example, many of the highest redshift SDSS quasars were found through the i-band dropout technique, where the quasar is only detected in the z band. This corresponds to the Lyman α emission line falling in the z-band, putting a rough lower redshift limit of $z \sim 5.5$, thus selecting mainly a high redshift sample.

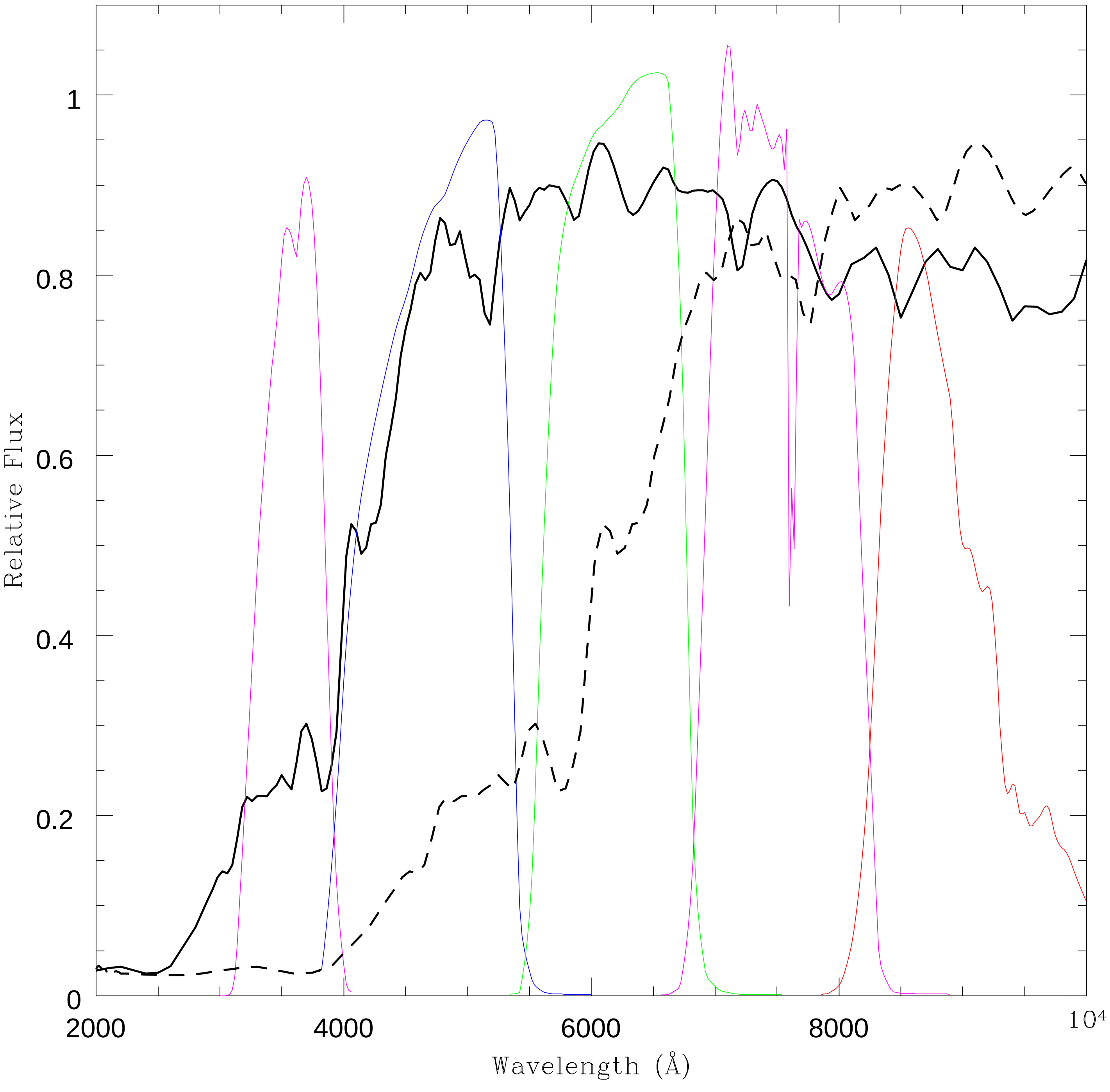

Figure B1 SDSS u,g,r,i,z filter transmission curves (magenta, blue, green, magenta, and red) with an elliptical galaxy spectrum at $z = 0$ (solid) and $z = 0.5$ (dashed) overlaid.

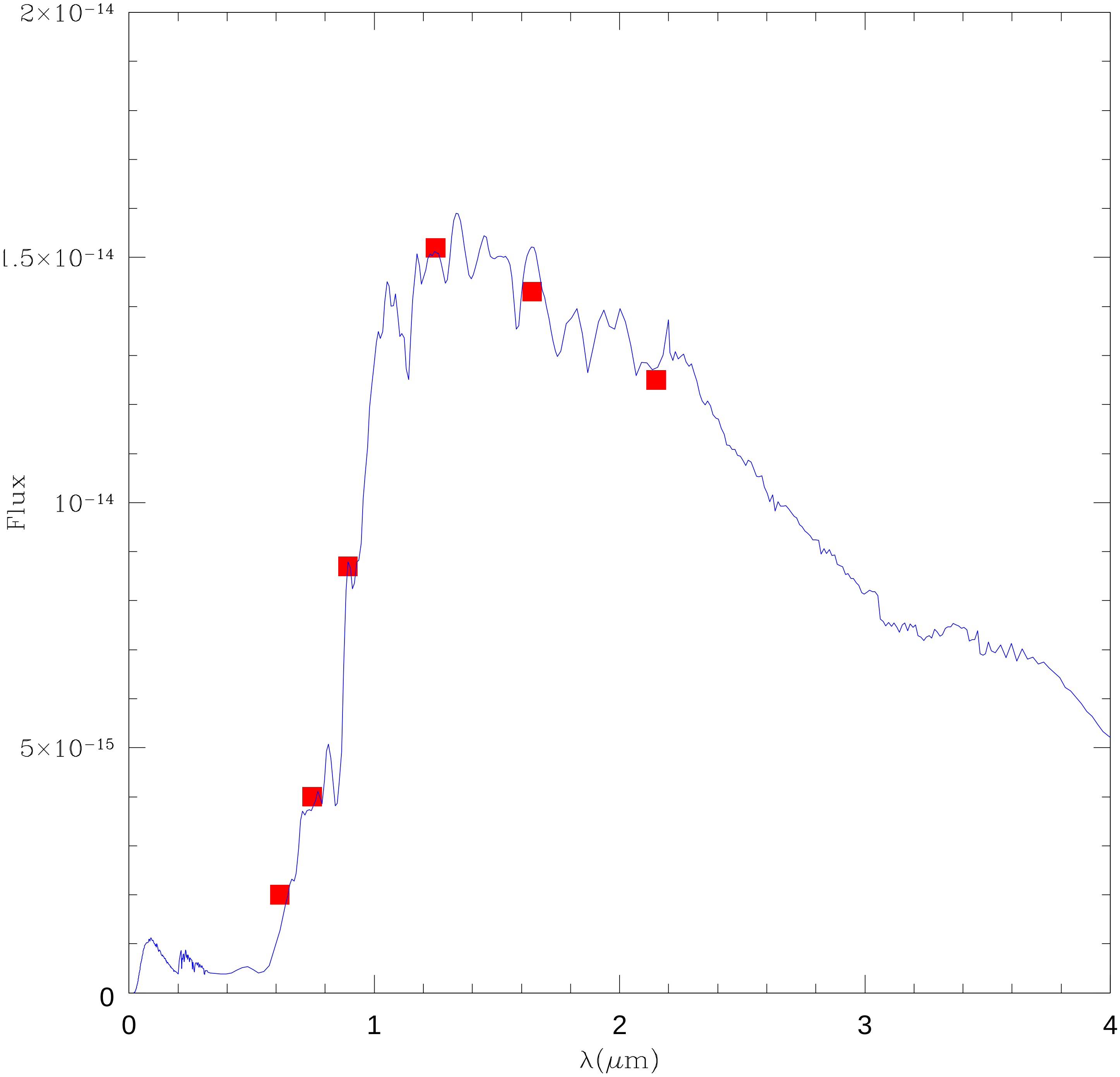

Figure B2 An elliptical galaxy template at $z = 1.2$ (black line) and fluxes obtained by convolving the spectrum with the SDSS r,i,z and KPNO J,H, and K_S filter transmission curves (red squares).

There are currently two broad types of photoz estimation: empirical and template based methods. Empirical photozs are determined from galaxy colors or magnitudes themselves, finding an empirical relation between these colors and a subset of the sample with spectroscopic redshifts (usually called the "training" set). The empirical relation is then assumed to hold for the remainder of the photometric sample. Connolly et al. (1995) fit polynomial functions to magnitudes measured in four band (U, B, R, I) to a set of galaxies with spectroscopic redshifts. Another technique is to define a nearest neighbor criterion, and simply assign the nearest spectroscopic redshift to each photometric galaxy, or an average of the *k* nearest redshifts. Another empirical technique that is gaining popularity is that of Artificial Neural Network photozs (ANNz's) Collister and Lahav (2004); Oyaizu et al. (2007), where the galaxy colors (and additional properties, such as surface brightness, if desired) are input into a neural net, which optimizes weights on one or more "hidden" levels, and finally outputs a photometric redshift for each galaxy. Once again, a training set is necessary to determine the neural network, which is then used on the rest of the dataset. In all empirical methods, the training set is a major concern. The training set should span a representative sample of the galaxies in the photometric data. If a category of galaxies is missing from the training set, any such galaxies will be misclassified as one of the types that are represented, possibly at a different redshift. The training set should also cover the full range of magnitude and redshift as the photometric data, otherwise we will be extrapolating beyond the range covered, which will lead to larger errors. A major advantage of empirical methods is that evolution effects are not a concern; because the training set includes real high redshift galaxies, any changes in the galaxy types will be reflected in a change in the training galaxies as a function of redshift (if the training sample is a truly representative set). In practice, obtaining such a representative set is difficult, as spectra of the faintest galaxies are expensive, and some objects simply do not have enough sharp spectral features to assign a spectroscopic redshift. Each of the individual methods has its own benefits and drawbacks: The polynomial method sometimes returns unrealistic (outside of local galaxies with proper motion toward us) negative redshifts. Nearest neighbor methods can have problems with redshift distribution, as galaxies are assigned redshifts based on the finite set of training galaxies, rather than a smooth distribution. The "hidden" layers of neural network photozs do not tell us what information is producing the photoz distribution.

Template based methods, on the other hand, derive their photometric redshifts by taking a set of spectra, either observed or synthetic, shifting each spectrum through a set of redshifts, and convolving them with the filter response functions to determine a grid of model galaxy colors (Bolzonella et al., 2000; Csabai et al., 2003). These colors are then compared to those observed for each galaxy to determine which SED at which redshift is the closest fit. Minimizing the difference between the observed and model colors is, essentially, a χ^2 fit. This is closely related to Spectral Energy Distribution (SED) modeling, as in Section 3.11. One advantage of this technique is that you get an estimate of the galaxy properties for ”free” as the best fit template gives you the probable galaxy type.

The specific choice of templates is a major concern in this method. For the most accurate photometric redshifts, your templates must fully span the array of galaxy types; if an observed galaxy is of a type not included in your templates, it will be misclassified as the galaxy with the nearest colors, albeit with a high value of χ^2. However, adding many templates leads to problems with degeneracies. The method works with any number of templates, however, if you compare a galaxy with four colors to one thousand templates, there are almost assuredly going to be multiple templates with very similar colors in the given five bands. Conti et al. (2003) and Welikala et al. (in prep) use the Pixelz method to estimate physical parameters for individual galaxy pixels by comparing to 2160 different templates. However, this is done for galaxies of known redshift, eliminating the major source of degeneracy. Also, they show that, even with redshift fixed, there is noticeable degeneracy in the templates, and estimate errors on the derived parameters based on the χ^2 fits. In practice a small number of templates is normally used, from four to ten. Current template methods use the same templates at all redshifts, ignoring galaxy evolution. We know that galaxies do evolve, and so this is a major concern for higher redshift galaxies, which could be addressed by changing the template set as a function of redshift.

One problem intrinsic to both empirical and template based methods is degeneracies. With only a handful of galaxy colors available, comparison to the full range of observed galaxies over a large redshift range is certain to lead to degenerate solutions. For instance, if a broad band feature is found, where all magnitudes short of one of the filters have very small fluxes, this could be either the $4000\mathring{A}$ break, or it could be the Lyman break. Unless the filter set covers a wavelength range in which several features (i.e. both the Lyman and $4000\mathring{A}$ breaks) can be seen, these two scenarios often cannot be differentiated. Figure B3 shows an example χ^2 distribution output by the photoz++ code with such a degeneracy. While the "best fit" redshift reported as the photoz is at $z = 0.76$, the χ^2 plot shows that a nearly equally likely solution exists at $z \approx 1.4$ (for a different template, the plot is χ^2 marginalized over the templates). Bayesian priors are a powerful tool that can be used to break such degeneracies. As an example, if an SDSS galaxy with $r = 17$ has a degenerate solution with $z = 0.3$ or $z = 3.0$, using the fact that a $z = 3$ galaxy with apparent magnitude $r = 17$ would make this galaxy incredibly bright to discount the high redshift solution. A luminosity function prior will help to distinguish these degenerate cases, as will surface brightness, concentration, etc... However, one must now worry over the accuracy of these priors. As this thesis shows, the luminosity function of galaxies evolves, and using an incorrect parameterization of the LF and its evolution as prior information can skew the results of the output photometric redshifts. Caution must be used when applying such priors.

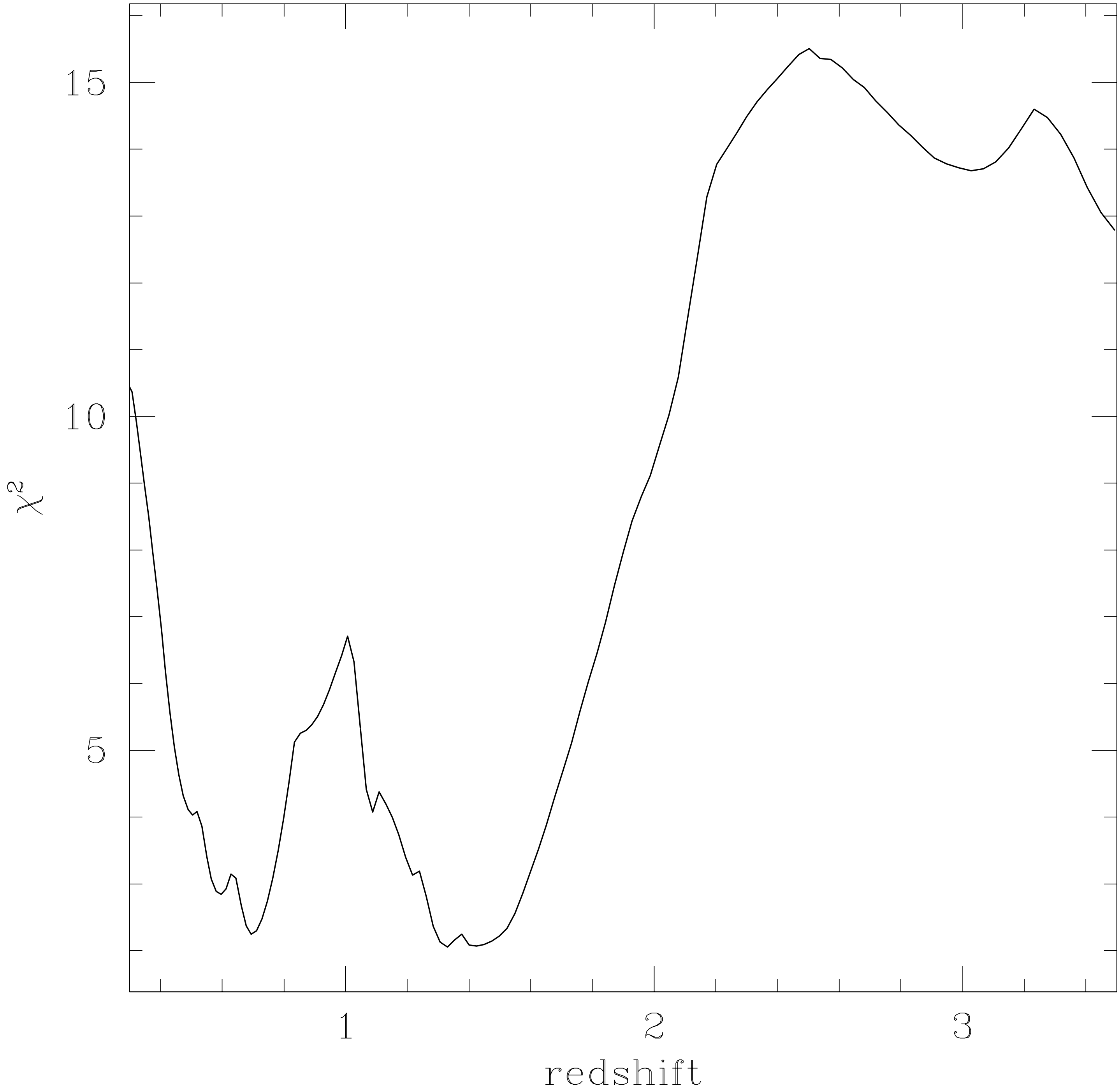

Figure B3 χ^2 as a function of redshift a sample galaxy with indeterminate redshift.

Figure B4 shows a plot of the spectroscopic vs. photometric redshifts for those galaxies with confirmed redshifts for the dataset described in Section 2.2.3. There is, as expected, a scatter in the photozs due to the coarseness of the photoz estimation. But, there are several other noticeable features as well. First are the ”catastrophic outliers”, galaxies with vastly misestimated redshifts. Some are misclassified stars that contaminate the sample (with spectroscopic redshifts of zero, but photozs greater than zero along the bottom of the plot), or galaxies which the photometric redshift code misidentifies as stars or local galaxies (with photoz equal to zero but specz greater than zero, along the left edge of the plot), and some in between that are simply wrong, possibly because they are not represented in the template set (e.g. strong emission line galaxies), or galaxies with a bimodal chi^2 probability distribution. Also visible are systematic trends in the data. Near photoz values of $z \approx 0.15$ there are many more galaxies $photoz > specz$ than galaxies with $specz > photoz$, that is, there is a systematic offset between the mean photoz and the mean specz. Such an offset will affect the results differently than a simple scatter about the mean for photozs versus spectroscopic redshifts. However, as long as these catastrophic outliers and systematic effects are well known and samples are large enough that they can be statistically accounted for, their effects can be greatly reduced or eliminated.

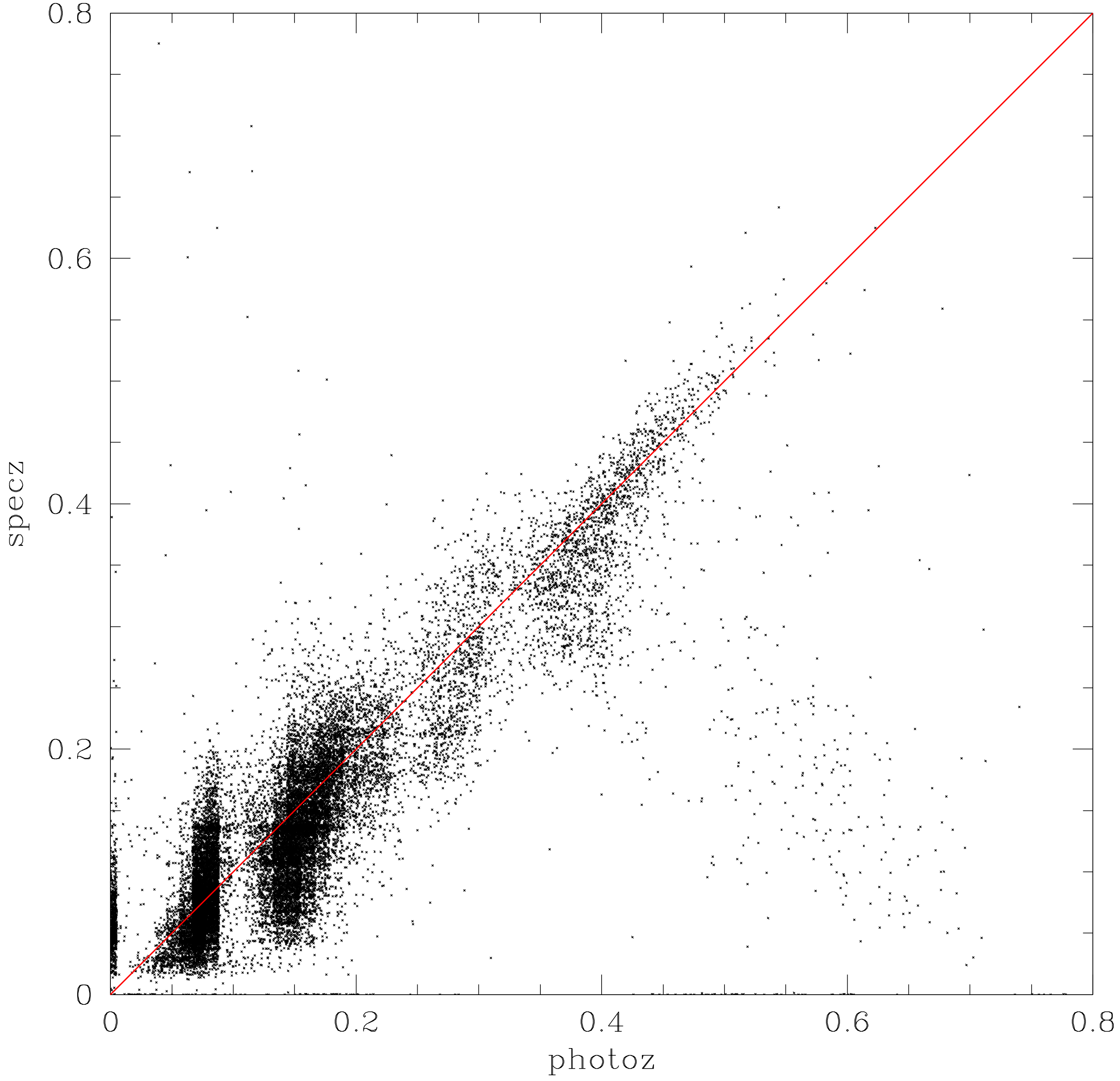

Figure B4 A plot of spectroscopic versus photometric redshifts for galaxies in Stripe 82 withe measurements of both.

BIBLIOGRAPHY

R. Barkana and A. Loeb. Detecting reionization in the star formation histories of high-redshift galaxies. MNRAS, 371:395–400, September 2006.

W. A. Baum. Photoelectric Magnitudes and Red-Shifts. In G. C. McVittie, editor, *Problems of Extra-Galactic Research*, volume 15 of *IAU Symposium*, pages 390–+, 1962.

E. Bertin and S. Arnouts. SExtractor: Software for source extraction. A&AS, 117:393–404, June 1996.

P. N. Best, H. J. A. Röttgering, and M. D. Lehnert. A 98 per cent spectroscopically complete sample of the most powerful equatorial radio sources at 408MHz. MNRAS, 310:223–254, November 1999.

B. Binggeli, A. Sandage, and G. A. Tammann. The luminosity function of galaxies. ARA&A, 26:509–560, 1988.

M. R. Blanton, J. Dalcanton, D. Eisenstein, J. Loveday, M. A. Strauss, M. SubbaRao, D. H. Weinberg, J. E. Anderson, Jr., J. Annis, N. A. Bahcall, M. Bernardi, J. Brinkmann, R. J. Brunner, S. Burles, L. Carey, F. J. Castander, A. J. Connolly, I. Csabai, M. Doi, D. Finkbeiner, S. Friedman, J. A. Frieman, M. Fukugita, J. E. Gunn, G. S. Hennessy, R. B. Hindsley, D. W. Hogg, T. Ichikawa, Ž. Ivezić, S. Kent, G. R. Knapp, D. Q. Lamb, R. F. Leger, D. C. Long, R. H. Lupton, T. A. McKay, A. Meiksin, A. Merelli, J. A. Munn, V. Narayanan, M. Newcomb, R. C. Nichol, S. Okamura, R. Owen, J. R. Pier, A. Pope, M. Postman, T. Quinn, C. M. Rockosi, D. J. Schlegel, D. P. Schneider, K. Shimasaku, W. A. Siegmund, S. Smee, Y. Snir, C. Stoughton, C. Stubbs, A. S. Szalay, G. P. Szokoly, A. R. Thakar, C. Tremonti, D. L. Tucker, A. Uomoto, D. Vanden Berk, M. S. Vogeley, P. Waddell, B. Yanny, N. Yasuda, and D. G. York. The Luminosity Function of Galaxies in SDSS Commissioning Data. AJ, 121:2358–2380, May 2001.

M. R. Blanton, D. W. Hogg, N. A. Bahcall, J. Brinkmann, M. Britton, A. J. Connolly, I. Csabai, M. Fukugita, J. Loveday, A. Meiksin, J. A. Munn, R. C. Nichol, S. Okamura, T. Quinn, D. P. Schneider, K. Shimasaku, M. A. Strauss, M. Tegmark, M. S. Vogeley, and D. H. Weinberg. The Galaxy Luminosity Function and Luminosity Density at Redshift z = 0.1. ApJ, 592:819–838, August 2003.

G. Blumenthal and G. Miley. Spectral index dependent properties of steep spectrum radio sources. A&A, 80:13–21, November 1979.

K. M. Blundell, S. Rawlings, S. A. Eales, G. B. Taylor, and A. D. Bradley. A sample of 6C radio sources designed to find objects at redshift z > 4 - I. The radio data. MNRAS, 295: 265–279, April 1998.

M. Bolzonella, J.-M. Miralles, and R. Pelló. Photometric redshifts based on standard SED fitting procedures. A&A, 363:476–492, November 2000.

K. Brand, S. Rawlings, G. J. Hill, and J. R. Tufts. The three-dimensional clustering of radio galaxies in the Texas-Oxford NVSS structure survey. MNRAS, 357:1231–1254, March 2005.

G. Bruzual A. and S. Charlot. Spectral evolution of stellar populations using isochrone synthesis. ApJ, 405:538–553, March 1993.

T. Budavári, A. J. Connolly, A. S. Szalay, I. Szapudi, I. Csabai, R. Scranton, N. A. Bahcall, J. Brinkmann, D. J. Eisenstein, J. A. Frieman, M. Fukugita, J. E. Gunn, D. Johnston, S. Kent, J. N. Loveday, R. H. Lupton, M. Tegmark, A. R. Thakar, B. Yanny, D. G. York, and I. Zehavi. Angular Clustering with Photometric Redshifts in the Sloan Digital Sky Survey: Bimodality in the Clustering Properties of Galaxies. ApJ, 595:59–70, September 2003.

T. Budavári, A. S. Szalay, S. Charlot, M. Seibert, T. K. Wyder, S. Arnouts, T. A. Barlow, L. Bianchi, Y.-I. Byun, J. Donas, K. Forster, P. G. Friedman, T. M. Heckman, P. N. Jelinsky, Y.-W. Lee, B. F. Madore, R. F. Malina, D. C. Martin, B. Milliard, P. Morrissey, S. G. Neff, R. M. Rich, D. Schiminovich, O. H. W. Siegmund, T. Small, M. A. Treyer, and B. Welsh. The Ultraviolet Luminosity Function of GALEX Galaxies at Photometric Redshifts between 0.07 and 0.25. ApJ, 619:L31–L34, January 2005.

D. Calzetti, L. Armus, R. C. Bohlin, A. L. Kinney, J. Koornneef, and T. Storchi-Bergmann. The Dust Content and Opacity of Actively Star-forming Galaxies. ApJ, 533:682–695, April 2000.

J. M. Carpenter. Color Transformations for the 2MASS Second Incremental Data Release. AJ, 121:2851–2871, May 2001.

R.-R. Chary, D. Stern, and P. Eisenhardt. Spitzer Constraints on the z = 6.56 Galaxy Lensed by Abell 370. ApJ, 635:L5–L8, December 2005.

H.-W. Chen, R. O. Marzke, P. J. McCarthy, P. Martini, R. G. Carlberg, S. E. Persson, A. Bunker, C. R. Bridge, and R. G. Abraham. The Las Campanas Infrared Survey. IV. The Photometric Redshift Survey and the Rest-Frame R-Band Galaxy Luminosity Function at 0.5=z=1.5. ApJ, 586:745–764, April 2003.

A. Cimatti, E. Daddi, M. Mignoli, L. Pozzetti, A. Renzini, G. Zamorani, T. Broadhurst, A. Fontana, P. Saracco, F. Poli, S. Cristiani, S. D'Odorico, E. Giallongo, R. Gilmozzi, and N. Menci. The K20 survey. I. Disentangling old and dusty star-forming galaxies in the ERO population. A&A, 381:L68–L72, January 2002.

A. Cimatti, D. Villani, L. Pozzetti, and S. di Serego Alighieri. The density of extremely red objects around high-z radio-loud active galactic nuclei. MNRAS, 318:453–461, October 2000.

G. D. Coleman, C.-C. Wu, and D. W. Weedman. Colors and magnitudes predicted for high redshift galaxies. ApJS, 43:393–416, July 1980.

A. A. Collister and O. Lahav. ANNz: Estimating Photometric Redshifts Using Artificial Neural Networks. PASP, 116:345–351, April 2004.

J. J. Condon. The 1.4 gigahertz luminosity function and its evolution. ApJ, 338:13–23, March 1989.

A. J. Connolly, I. Csabai, A. S. Szalay, D. C. Koo, R. G. Kron, and J. A. Munn. Slicing Through Multicolor Space: Galaxy Redshifts from Broadband Photometry. AJ, 110:2655–+, December 1995.

C. J. Conselice. The Assembly History of Massive Galaxies: What Do We Know? *ArXiv e-prints*, 706, June 2007.

C. J. Conselice, M. A. Bershady, M. Dickinson, and C. Papovich. A Direct Measurement of Major Galaxy Mergers at z lt 3. AJ, 126:1183–1207, September 2003.

A. Conti, A. J. Connolly, A. M. Hopkins, T. Budavári, A. S. Szalay, I. Csabai, S. J. Schmidt, C. Adams, and N. Petrovic. The Star Formation History of Galaxies Measured from Individual Pixels. I. The Hubble Deep Field North. AJ, 126:2330–2345, November 2003.

L. L. Cowie, A. Songaila, E. M. Hu, and J. G. Cohen. New Insight on Galaxy Formation and Evolution From Keck Spectroscopy of the Hawaii Deep Fields. AJ, 112:839–+, September 1996.

D. J. Croton, G. R. Farrar, P. Norberg, M. Colless, J. A. Peacock, I. K. Baldry, C. M. Baugh, J. Bland-Hawthorn, T. Bridges, R. Cannon, S. Cole, C. Collins, W. Couch, G. Dalton, R. De Propris, S. P. Driver, G. Efstathiou, R. S. Ellis, C. S. Frenk, K. Glazebrook, C. Jackson, O. Lahav, I. Lewis, S. Lumsden, S. Maddox, D. Madgwick, B. A. Peterson, W. Sutherland, and K. Taylor. The 2dF Galaxy Redshift Survey: luminosity functions by density environment and galaxy type. MNRAS, 356:1155–1167, January 2005.

D. J. Croton, V. Springel, S. D. M. White, G. De Lucia, C. S. Frenk, L. Gao, A. Jenkins, G. Kauffmann, J. F. Navarro, and N. Yoshida. The many lives of active galactic nuclei: cooling flows, black holes and the luminosities and colours of galaxies. MNRAS, 365:11–28, January 2006.

I. Csabai, T. Budavári, A. J. Connolly, A. S. Szalay, Z. Győry, N. Benítez, J. Annis, J. Brinkmann, D. Eisenstein, M. Fukugita, J. Gunn, S. Kent, R. Lupton, R. C. Nichol, and C. Stoughton. The Application of Photometric Redshifts to the SDSS Early Data Release. AJ, 125:580–592, February 2003.

E. Daddi, A. Cimatti, L. Pozzetti, H. Hoekstra, H. J. A. Röttgering, A. Renzini, G. Zamorani, and F. Mannucci. Detection of strong clustering of extremely red objects: implications for the density of z 1 ellipticals. A&A, 361:535–549, September 2000.

E. Daddi, A. Cimatti, A. Renzini, A. Fontana, M. Mignoli, L. Pozzetti, P. Tozzi, and G. Zamorani. A New Photometric Technique for the Joint Selection of Star-forming and Passive Galaxies at 1.4 lessim z lessim 2.5. ApJ, 617:746–764, December 2004.

M. Davis and J. Huchra. A survey of galaxy redshifts. III - The density field and the induced gravity field. ApJ, 254:437–450, March 1982.

C. De Breuck, W. van Breugel, H. Röttgering, D. Stern, G. Miley, W. de Vries, S. A. Stanford, J. Kurk, and R. Overzier. Spectroscopy of Ultra-steep-Spectrum Radio Sources. AJ, 121:1241–1265, March 2001.

C. De Breuck, W. van Breugel, H. J. A. Röttgering, and G. Miley. A sample of 669 ultra steep spectrum radio sources to find high redshift radio galaxies. A&AS, 143:303–333, April 2000.

R. S. de Jong and C. Lacey. The Local Space Density of SB-SDM Galaxies as Function of Their Scale Size, Surface Brightness, and Luminosity. ApJ, 545:781–797, December 2000.

G. De Lucia, V. Springel, S. D. M. White, D. Croton, and G. Kauffmann. The formation history of elliptical galaxies. MNRAS, 366:499–509, February 2006.

C. DeBoor. The CAGD Handbook, 2001. URL `citeseer.ist.psu.edu/607036.html`.

A. Dey, H. Spinrad, and M. Dickinson. Discovery of a Z = 2.76 Dusty Radio Galaxy? ApJ, 440:515–+, February 1995.

J. N. Douglas, F. N. Bash, F. A. Bozyan, G. W. Torrence, and C. Wolfe. The Texas Survey of Radio Sources Covering -35.5 degrees lt declination lt 71.5 degrees at 365 MHz. AJ, 111:1945–+, May 1996.

A. Dressler. A catalog of morphological types in 55 rich clusters of galaxies. ApJS, 42: 565–609, April 1980.

J. S. Dunlop and J. A. Peacock. The Redshift Cut-Off in the Luminosity Function of Radio Galaxies and Quasars. MNRAS, 247:19–+, November 1990.

W. T. Eadie, D. Drijard, F. E. James, M. Roos, and B. Sandoulet. Statistical Methods in Experimenting Physics. *North Holland, Amsterdam*, 1971.

G. Efstathiou, R. S. Ellis, and B. A. Peterson. Analysis of a complete galaxy redshift survey. II - The field-galaxy luminosity function. MNRAS, 232:431–461, May 1988.

H. C. Eilers and B. D. Marx. Flexible Smoothing with B-splines and Penalties. *Statistical Science*, 11:89–121, February 1996.

R. J. Elston, A. H. Gonzalez, E. McKenzie, M. Brodwin, M. J. I. Brown, G. Cardona, A. Dey, M. Dickinson, P. R. Eisenhardt, B. T. Jannuzi, Y.-T. Lin, J. J. Mohr, S. N. Raines, S. A. Stanford, and D. Stern. The FLAMINGOS Extragalactic Survey. ApJ, 639: 816–826, March 2006.

M. Fioc and B. Rocca-Volmerange. PEGASE: a UV to NIR spectral evolution model of galaxies. Application to the calibration of bright galaxy counts. A&A, 326:950–962, October 1997.

S. Folkes, S. Ronen, I. Price, O. Lahav, M. Colless, S. Maddox, K. Deeley, K. Glazebrook, J. Bland-Hawthorn, R. Cannon, S. Cole, C. Collins, W. Couch, S. P. Driver, G. Dalton, G. Efstathiou, R. S. Ellis, C. S. Frenk, N. Kaiser, I. Lewis, S. Lumsden, J. Peacock, B. A. Peterson, W. Sutherland, and K. Taylor. The 2dF Galaxy Redshift Survey: spectral types and luminosity functions. MNRAS, 308:459–472, September 1999.

J. P. Gardner, L. L. Cowie, and R. J. Wainscoat. Galaxy number counts from K = 10 to K = 23. ApJ, 415:L9–L12, September 1993.

A. Georgakakis, J. Afonso, A. M. Hopkins, M. Sullivan, B. Mobasher, and L. E. Cram. The Phoenix Deep Survey: The Clustering and Environment of Extremely Red Objects. ApJ, 620:584–594, February 2005.

E. Glikman, M. D. Gregg, M. Lacy, D. J. Helfand, R. H. Becker, and R. L. White. FIRST-2Mass Sources below the APM Detection Threshold: A Population of Highly Reddened Quasars. ApJ, 607:60–75, May 2004.

T. Goto, C. Yamauchi, Y. Fujita, S. Okamura, M. Sekiguchi, I. Smail, M. Bernardi, and P. L. Gomez. The morphology-density relation in the Sloan Digital Sky Survey. MNRAS, 346:601–614, December 2003.

J. R. Graham and A. Dey. The Redshift of an Extremely Red Object and the Nature of the Very Red Galaxy Population. ApJ, 471:720, November 1996.

J. R. Graham, K. Matthews, B. T. Soifer, J. E. Nelson, W. Harrison, J. G. Jernigan, S. Lin, G. Neugebauer, G. Smith, and C. Ziomkowski. Infrared observations of the Z = 3.8 radio galaxy, 4C 41.17, with the W. M. Keck telescope. ApJ, 420:L5–L8, January 1994.

P. C. Gregory and J. J. Condon. The 87GB catalog of radio sources covering delta between O and + 75 deg at 4.85 GHz. ApJS, 75:1011–1291, April 1991.

J. E. Gunn, M. Carr, C. Rockosi, M. Sekiguchi, K. Berry, B. Elms, E. de Haas, Ž. Ivezić, G. Knapp, R. Lupton, G. Pauls, R. Simcoe, R. Hirsch, D. Sanford, S. Wang, D. York,

F. Harris, J. Annis, L. Bartozek, W. Boroski, J. Bakken, M. Haldeman, S. Kent, S. Holm, D. Holmgren, D. Petravick, A. Prosapio, R. Rechenmacher, M. Doi, M. Fukugita, K. Shimasaku, N. Okada, C. Hull, W. Siegmund, E. Mannery, M. Blouke, D. Heidtman, D. Schneider, R. Lucinio, and J. Brinkman. The Sloan Digital Sky Survey Photometric Camera. AJ, 116:3040–3081, December 1998.

S. E. G. Hales, J. E. Baldwin, and P. J. Warner. The 6C survey of radio sources. II - The zone delta = 30-51 deg, alpha = 08h30m-17h30m. MNRAS, 234:919–936, October 1988.

S. E. G. Hales, C. R. Masson, P. J. Warner, and J. E. Baldwin. The 6c Survey of Radio Sources - Part Three - the Zone Dec: 48DEG lt 68DEG Ra: 05H25M lt 18H17M. MNRAS, 246:256–+, September 1990.

P. B. Hall and R. F. Green. An Optical/Near-Infrared Study of Radio-loud Quasar Environments. II. Imaging Results. ApJ, 507:558–584, November 1998.

P. B. Hall, M. Sawicki, P. Martini, R. A. Finn, C. J. Pritchet, P. S. Osmer, D. W. McCarthy, A. S. Evans, H. Lin, and F. D. A. Hartwick. Galaxies in the Fields of Z˜1.5 Radio-Loud Quasars. AJ, 121:1840–1862, April 2001.

A. Hewitt and G. Burbidge. An optical catalog of extragalactic emission-line objects similar to quasi-stellar objects. ApJS, 75:297–356, February 1991.

D Hogg. Distance Measures in Cosmology. *astroph*, pages 1–16, December 2000.

E. Hubble. The Luminosity Function of Nebulae. I. The Luminosity Function of Resolved Nebulae as Indicated by Their Brightest Stars. ApJ, 84:158–+, September 1936a.

E. Hubble. The Luminosity Function of Nebulae. II. The Luminosity Function as Indicated by Residuals in Velocity-Magnitude Relations. ApJ, 84:270–+, October 1936b.

E. P. Hubble. Extragalactic nebulae. ApJ, 64:321–369, December 1926.

Ž. Ivezić, J. Goldston, K. Finlator, G. R. Knapp, B. Yanny, T. A. McKay, S. Amrose, K. Krisciunas, B. Willman, S. Anderson, C. Schaber, D. Erb, C. Logan, C. Stubbs, B. Chen, E. Neilsen, A. Uomoto, J. R. Pier, X. Fan, J. E. Gunn, R. H. Lupton, C. M. Rockosi, D. Schlegel, M. A. Strauss, J. Annis, J. Brinkmann, I. Csabai, M. Doi, M. Fukugita, G. S. Hennessy, R. B. Hindsley, B. Margon, J. A. Munn, H. J. Newberg, D. P. Schneider, J. A. Smith, G. P. Szokoly, A. R. Thakar, M. S. Vogeley, P. Waddell, N. Yasuda, and D. G. York. Candidate RR Lyrae Stars Found in Sloan Digital Sky Survey Commissioning Data. AJ, 120:963–977, August 2000.

B. T. Jannuzi and A. Dey. The NOAO Deep Wide-Field Survey. In R. Weymann, L. Storrie-Lombardi, M. Sawicki, and R. Brunner, editors, *Photometric Redshifts and the Detection of High Redshift Galaxies*, volume 191 of *Astronomical Society of the Pacific Conference Series*, pages 111–+, 1999.

M. J. Jarvis, S. Rawlings, S. Eales, K. M. Blundell, A. J. Bunker, S. Croft, R. J. McLure, and C. J. Willott. A sample of 6C radio sources designed to find objects at redshift z gtr 4 - III. Imaging and the radio galaxy K-z relation. MNRAS, 326:1585–1600, October 2001.

G. Kauffmann, S. D. M. White, and B. Guiderdoni. The Formation and Evolution of Galaxies Within Merging Dark Matter Haloes. MNRAS, 264:201–+, September 1993.

A. L. Kinney, D. Calzetti, R. C. Bohlin, K. McQuade, T. Storchi-Bergmann, and H. R. Schmitt. Template Ultraviolet to Near-Infrared Spectra of Star-forming Galaxies and Their Application to K-Corrections. ApJ, 467:38–+, August 1996.

I. J. Klamer, R. D. Ekers, J. J. Bryant, R. W. Hunstead, E. M. Sadler, and C. De Breuck. A search for distant radio galaxies from SUMSS and NVSS - III. Radio spectral energy distributions and the z-α correlation. MNRAS, 371:852–866, September 2006.

J. D. Kurk, L. Pentericci, H. J. A. Röttgering, and G. K. Miley. A search for clusters at high redshift. III. Candidate H alpha emitters and EROs in the PKS 1138-262 proto-cluster at z = 2.16. A&A, 428:793–815, December 2004.

S. J. Lilly. Discovery of a radio galaxy at a redshift of 3.395. ApJ, 333:161–167, October 1988.

S. J. Lilly and M. S. Longair. Stellar populations in distant radio galaxies. MNRAS, 211: 833–855, December 1984.

H. Lin, R. P. Kirshner, S. A. Shectman, S. D. Landy, A. Oemler, D. L. Tucker, and P. L. Schechter. The Luminosity Function of Galaxies in the Las Campanas Redshift Survey. ApJ, 464:60, June 1996.

H. Lin, H. K. C. Yee, R. G. Carlberg, S. L. Morris, M. Sawicki, D. R. Patton, G. Wirth, and C. W. Shepherd. The CNOC2 Field Galaxy Luminosity Function. I. A Description of Luminosity Function Evolution. ApJ, 518:533–561, June 1999.

J. Loveday. Evolution of the galaxy luminosity function at z lt 0.3. MNRAS, 347:601–606, January 2004.

D. Lynden-Bell. A method of allowing for known observational selection in small samples applied to 3CR quasars. MNRAS, 155:95–+, 1971.

M. Magliocchetti, S. J. Maddox, E. Hawkins, J. A. Peacock, J. Bland-Hawthorn, T. Bridges, R. Cannon, S. Cole, M. Colless, C. Collins, W. Couch, G. Dalton, R. de Propris, S. P. Driver, G. Efstathiou, R. S. Ellis, C. S. Frenk, K. Glazebrook, C. A. Jackson, B. Jones, O. Lahav, I. Lewis, S. Lumsden, P. Norberg, B. A. Peterson, W. Sutherland, and K. Taylor. The 2dF galaxy redshift survey: clustering properties of radio galaxies. MNRAS, 350: 1485–1494, June 2004.

F. Mannucci, L. Pozzetti, D. Thompson, E. Oliva, C. Baffa, G. Comoretto, S. Gennari, and F. Lisi. The relative abundances of ellipticals and starbursts among the extremely red galaxies. MNRAS, 329:L57–L61, February 2002.

P. J. McCarthy, V. K. Kapahi, W. van Breugel, S. E. Persson, R. Athreya, and C. R. Subrahmanya. The Molonglo Reference Catalog/1 Jansky Radio Source Survey. I. Radio Galaxy Identifications. ApJS, 107:19–+, November 1996.

P. J. McCarthy, S. E. Persson, and S. C. West. Infrared imaging of Z greater than 2 radio galaxies. ApJ, 386:52–58, February 1992.

D. G. Monet. The 526,280,881 Objects In The USNO-A2.0 Catalog. In *Bulletin of the American Astronomical Society*, volume 30 of *Bulletin of the American Astronomical Society*, page 1427, December 1998.

J. B. Oke. Absolute Spectral Energy Distributions for White Dwarfs. ApJS, 27:21–+, February 1974.

J. B. Oke and J. E. Gunn. Secondary standard stars for absolute spectrophotometry. ApJ, 266:713–717, March 1983.

M. Ouchi, K. Shimasaku, S. Okamura, H. Furusawa, N. Kashikawa, K. Ota, M. Doi, M. Hamabe, M. Kimura, Y. Komiyama, M. Miyazaki, S. Miyazaki, F. Nakata, M. Sekiguchi, M. Yagi, and N. Yasuda. Subaru Deep Survey. V. A Census of Lyman Break Galaxies at z˜=4 and 5 in the Subaru Deep Fields: Photometric Properties. ApJ, 611:660–684, August 2004.

H. Oyaizu, M. Lima, C. E. Cunha, H. Lin, J. Frieman, and E. S. Sheldon. A Galaxy Photometric Redshift Catalog for the Sloan Digital Sky Survey Data Release 6. *ArXiv e-prints*, 708, July 2007.

B. Rocca-Volmerange, D. Le Borgne, C. De Breuck, M. Fioc, and E. Moy. The radio galaxy K-z relation: The $10^{12} M_{sun}$ mass limit. Masses of galaxies from the L_K luminosity, up to z > 4. A&A, 415:931–940, March 2004.

N. D. Roche, O. Almaini, J. Dunlop, R. J. Ivison, and C. J. Willott. The clustering, number counts and morphology of extremely red (R-K gt 5) galaxies to K lt = 21. MNRAS, 337: 1282–1298, December 2002.

H. J. A. Roettgering, M. Lacy, G. K. Miley, K. C. Chambers, and R. Saunders. Samples of ultra-steep spectrum radio sources. A&AS, 108:79–141, November 1994.

H. J. A. Roettgering, R. van Ojik, G. K. Miley, K. C. Chambers, W. J. M. van Breugel, and S. de Koff. Spectroscopy of ultra-steep spectrum radio sources: a sample of z gt 2 radio galaxies. A&A, 326:505–527, October 1997.

M. Rowan-Robinson, C. R. Benn, A. Lawrence, R. G. McMahon, and T. J. Broadhurst. The evolution of faint radio sources. MNRAS, 263:123–130, July 1993.

A. Sandage, G. A. Tammann, and A. Yahil. The velocity field of bright nearby galaxies. I - The variation of mean absolute magnitude with redshift for galaxies in a magnitude-limited sample. ApJ, 232:352–364, September 1979.

E. Scannapieco, J. Silk, and R. Bouwens. AGN Feedback Causes Downsizing. ApJ, 635: L13–L16, December 2005.

P. Schechter. An analytic expression for the luminosity function for galaxies. ApJ, 203: 297–306, January 1976.

D. J. Schlegel, D. P. Finkbeiner, and M. Davis. Maps of Dust Infrared Emission for Use in Estimation of Reddening and Cosmic Microwave Background Radiation Foregrounds. ApJ, 500:525–+, June 1998.

M. Schmidt. Space Distribution and Luminosity Functions of Quasi-Stellar Radio Sources. ApJ, 151:393, February 1968.

S. J. Schmidt, A. J. Connolly, and A. M. Hopkins. The DRaGONS Survey: A Search for High-Redshift Radio Galaxies and Heavily Obscured Active Galactic Nuclei. ApJ, 649: 63–78, September 2006.

R. Scranton, D. Johnston, S. Dodelson, J. A. Frieman, A. Connolly, D. J. Eisenstein, J. E. Gunn, L. Hui, B. Jain, S. Kent, J. Loveday, V. Narayanan, R. C. Nichol, L. O'Connell, R. Scoccimarro, R. K. Sheth, A. Stebbins, M. A. Strauss, A. S. Szalay, I. Szapudi, M. Tegmark, M. Vogeley, I. Zehavi, J. Annis, N. A. Bahcall, J. Brinkman, I. Csabai, R. Hindsley, Z. Ivezic, R. S. J. Kim, G. R. Knapp, D. Q. Lamb, B. C. Lee, R. H. Lupton, T. McKay, J. Munn, J. Peoples, J. Pier, G. T. Richards, C. Rockosi, D. Schlegel, D. P. Schneider, C. Stoughton, D. L. Tucker, B. Yanny, and D. G. York. Analysis of Systematic Effects and Statistical Uncertainties in Angular Clustering of Galaxies from Early Sloan Digital Sky Survey Data. ApJ, 579:48–75, November 2002.

R. K. Sheth. On estimating redshift and luminosity distributions in photometric redshift surveys. MNRAS, 378:709–715, June 2007.

R. K. Sheth, M. Bernardi, P. L. Schechter, S. Burles, D. J. Eisenstein, D. P. Finkbeiner, J. Frieman, R. H. Lupton, D. J. Schlegel, M. Subbarao, K. Shimasaku, N. A. Bahcall, J. Brinkmann, and Ž. Ivezić. The Velocity Dispersion Function of Early-Type Galaxies. ApJ, 594:225–231, September 2003.

K. Shimasaku, M. Fukugita, M. Doi, M. Hamabe, T. Ichikawa, S. Okamura, M. Sekiguchi, N. Yasuda, J. Brinkmann, I. Csabai, S.-I. Ichikawa, Z. Ivezić, P. Z. Kunszt, D. P. Schneider, G. P. Szokoly, M. Watanabe, and D. G. York. Statistical Properties of Bright Galaxies in the Sloan Digital Sky Survey Photometric System. AJ, 122:1238–1250, September 2001.

D. N. Spergel, L. Verde, H. V. Peiris, E. Komatsu, M. R. Nolta, C. L. Bennett, M. Halpern, G. Hinshaw, N. Jarosik, A. Kogut, M. Limon, S. S. Meyer, L. Page, G. S. Tucker, J. L. Weiland, E. Wollack, and E. L. Wright. First-Year Wilkinson Microwave Anisotropy Probe

(WMAP) Observations: Determination of Cosmological Parameters. ApJS, 148:175–194, September 2003.

H. Spinrad, J. Marr, L. Aguilar, and S. Djorgovski. A third update of the status of the 3CR sources - Further new redshifts and new identifications of distant galaxies. PASP, 97: 932–961, October 1985.

S. A. Stanford, M. Dickinson, M. Postman, H. C. Ferguson, R. A. Lucas, C. J. Conselice, T. Budavári, and R. Somerville. The Evolution of Early-Type Field Galaxies Selected from a NICMOS Map of the Hubble Deep Field North. AJ, 127:131–155, January 2004.

C. C. Steidel, K. L. Adelberger, A. E. Shapley, M. Pettini, M. Dickinson, and M. Giavalisco. Lyman Break Galaxies at Redshift z ˜ 3: Survey Description and Full Data Set. ApJ, 592: 728–754, August 2003.

C. C. Steidel, M. Giavalisco, M. Pettini, M. Dickinson, and K. L. Adelberger. Spectroscopic Confirmation of a Population of Normal Star-forming Galaxies at Redshifts Z geq 3. ApJ, 462:L17+, May 1996.

D. Stern, A. Dey, H. Spinrad, L. Maxfield, M. Dickinson, D. Schlegel, and R. A. González. New High-Redshift Radio Galaxies from the MIT-Green Bank Catalog. AJ, 117:1122–1138, March 1999.

M. U. Subbarao, A. J. Connolly, A. S. Szalay, and D. C. Koo. Luminosity Functions From Photometric Redshifts. I. Techniques. AJ, 112:929–+, September 1996.

A. S. Szalay, A. J. Connolly, and G. P. Szokoly. Simultaneous Multicolor Detection of Faint Galaxies in the Hubble Deep Field. AJ, 117:68–74, January 1999.

G. P. Szokoly, M. U. Subbarao, A. J. Connolly, and B. Mobasher. The Near-Infrared Number Counts and Luminosity Functions of Local Galaxies. ApJ, 492:452–+, January 1998.

H. I. Teplitz, B. Siana, T. M. Brown, R. Chary, J. W. Colbert, C. J. Conselice, D. F. de Mello, M. Dickinson, H. C. Ferguson, J. P. Gardner, and F. Menanteau. Far-Ultraviolet Imaging of the Hubble Deep Field-North: Star Formation in Normal Galaxies at z lt 1. AJ, 132:853–865, August 2006.

D. Thompson, S. Djorgovski, M. Vigotti, and G. Grueff. Identifications and spectroscopy of faint radio galaxies from the B3 VLA survey. AJ, 108:828–836, September 1994.

A. G. G. M. Tielens, G. K. Miley, and A. G. Willis. Westerbork Observations of 4C Sources with Steep Radio Spectra. A&AS, 35:153–+, February 1979.

A. T. Tokunaga and W. D. Vacca. The Mauna Kea Observatories Near-Infrared Filter Set. III. Isophotal Wavelengths and Absolute Calibration. PASP, 117:421–426, April 2005.

T. Totani, Y. Yoshii, T. Maihara, F. Iwamuro, and K. Motohara. Near-Infrared Faint Galaxies in the Subaru Deep Field: Comparing the Theory with Observations for Galaxy Counts, Colors, and Size Distributions to K ~ 24.5. ApJ, 559:592–605, October 2001.

W. J. M. van Breugel, S. A. Stanford, H. Spinrad, D. Stern, and J. R. Graham. Morphological Evolution in High-Redshift Radio Galaxies and the Formation of Giant Elliptical Galaxies. ApJ, 502:614–+, August 1998.

P. G. van Dokkum. The Recent and Continuing Assembly of Field Elliptical Galaxies by Red Mergers. AJ, 130:2647–2665, December 2005.

D. E. Vanden Berk, G. T. Richards, A. Bauer, M. A. Strauss, D. P. Schneider, T. M. Heckman, D. G. York, P. B. Hall, X. Fan, G. R. Knapp, S. F. Anderson, J. Annis, N. A. Bahcall, M. Bernardi, J. W. Briggs, J. Brinkmann, R. Brunner, S. Burles, L. Carey, F. J. Castander, A. J. Connolly, J. H. Crocker, I. Csabai, M. Doi, D. Finkbeiner, S. Friedman, J. A. Frieman, M. Fukugita, J. E. Gunn, G. S. Hennessy, Ž. Ivezić, S. Kent, P. Z. Kunszt, D. Q. Lamb, R. F. Leger, D. C. Long, J. Loveday, R. H. Lupton, A. Meiksin, A. Merelli, J. A. Munn, H. J. Newberg, M. Newcomb, R. C. Nichol, R. Owen, J. R. Pier, A. Pope, C. M. Rockosi, D. J. Schlegel, W. A. Siegmund, S. Smee, Y. Snir, C. Stoughton, C. Stubbs, M. SubbaRao, A. S. Szalay, G. P. Szokoly, C. Tremonti, A. Uomoto, P. Waddell, B. Yanny, and W. Zheng. Composite Quasar Spectra from the Sloan Digital Sky Survey. AJ, 122: 549–564, August 2001.

E. Vardoulaki, S. Rawlings, G. J. Hill, S. Croft, K. Brand, J. Riley, and C. Willott. The TOOT00 redshift survey of radio sources. *Astronomische Nachrichten*, 327:282–285, March 2006.

B. P. Venemans. Protoclusters associated with distant radio galaxies. *Astronomische Nachrichten*, 327:196–203, March 2006.

M. Villar-Martín, S. F. Sánchez, C. De Breuck, R. Peletier, J. Vernet, A. Rettura, N. Seymour, A. Humphrey, D. Stern, S. di Serego Alighieri, and R. Fosbury. VIMOS-VLT and Spitzer observations of a radio galaxy at z= 2.5. MNRAS, 366:L1–L5, February 2006.

R. L. Webster, P. J. Francis, B. A. Peterson, M. J. Drinkwater, and F. J. Masci. Evidence for a Large Undetected Population of Dust-Reddened Quasars. Nature, 375:469–+, June 1995.

R. L. White, D. J. Helfand, R. H. Becker, M. D. Gregg, M. Postman, T. R. Lauer, and W. Oegerle. An I-Band-selected Sample of Radio-emitting Quasars: Evidence for a Large Population of Red Quasars. AJ, 126:706–722, August 2003.

C. J. Willott, S. Rawlings, and K. M. Blundell. Extremely red galaxy counterparts to 7C radio sources. MNRAS, 324:1–17, June 2001.

M. Wold, L. Armus, G. Neugebauer, T. H. Jarrett, and M. D. Lehnert. Overdensities of Extremely Red Objects in the Fields of High-Redshift Radio-Loud Quasars. AJ, 126: 1776–1786, October 2003.

C. Wolf, K. Meisenheimer, H.-W. Rix, A. Borch, S. Dye, and M. Kleinheinrich. The COMBO-17 survey: Evolution of the galaxy luminosity function from 25 000 galaxies with 0.2 lt z lt 1.2. A&A, 401:73–98, April 2003.

C.-W. Yip. *Understanding the properties and diversity of galaxies and quasars through spectral decomposition.* PhD thesis, University of Pittsburgh, United States – Pennsylvania, November 2005.

D. G. York, J. Adelman, J. E. Anderson, Jr., S. F. Anderson, J. Annis, N. A. Bahcall, J. A. Bakken, R. Barkhouser, S. Bastian, E. Berman, W. N. Boroski, S. Bracker, C. Briegel, J. W. Briggs, J. Brinkmann, R. Brunner, S. Burles, L. Carey, M. A. Carr, F. J. Castander, B. Chen, P. L. Colestock, A. J. Connolly, J. H. Crocker, I. Csabai, P. C. Czarapata, J. E. Davis, M. Doi, T. Dombeck, D. Eisenstein, N. Ellman, B. R. Elms, M. L. Evans, X. Fan, G. R. Federwitz, L. Fiscelli, S. Friedman, J. A. Frieman, M. Fukugita, B. Gillespie, J. E. Gunn, V. K. Gurbani, E. de Haas, M. Haldeman, F. H. Harris, J. Hayes, T. M. Heckman, G. S. Hennessy, R. B. Hindsley, S. Holm, D. J. Holmgren, C.-h. Huang, C. Hull, D. Husby, S.-I. Ichikawa, T. Ichikawa, Ž. Ivezić, S. Kent, R. S. J. Kim, E. Kinney, M. Klaene, A. N. Kleinman, S. Kleinman, G. R. Knapp, J. Korienek, R. G. Kron, P. Z. Kunszt, D. Q. Lamb, B. Lee, R. F. Leger, S. Limmongkol, C. Lindenmeyer, D. C. Long, C. Loomis, J. Loveday, R. Lucinio, R. H. Lupton, B. MacKinnon, E. J. Mannery, P. M. Mantsch, B. Margon, P. McGehee, T. A. McKay, A. Meiksin, A. Merelli, D. G. Monet, J. A. Munn, V. K. Narayanan, T. Nash, E. Neilsen, R. Neswold, H. J. Newberg, R. C. Nichol, T. Nicinski, M. Nonino, N. Okada, S. Okamura, J. P. Ostriker, R. Owen, A. G. Pauls, J. Peoples, R. L. Peterson, D. Petravick, J. R. Pier, A. Pope, R. Pordes, A. Prosapio, R. Rechenmacher, T. R. Quinn, G. T. Richards, M. W. Richmond, C. H. Rivetta, C. M. Rockosi, K. Ruthmansdorfer, D. Sandford, D. J. Schlegel, D. P. Schneider, M. Sekiguchi, G. Sergey, K. Shimasaku, W. A. Siegmund, S. Smee, J. A. Smith, S. Snedden, R. Stone, C. Stoughton, M. A. Strauss, C. Stubbs, M. SubbaRao, A. S. Szalay, I. Szapudi, G. P. Szokoly, A. R. Thakar, C. Tremonti, D. L. Tucker, A. Uomoto, D. Vanden Berk, M. S. Vogeley, P. Waddell, S.-i. Wang, M. Watanabe, D. H. Weinberg, B. Yanny, and N. Yasuda. The Sloan Digital Sky Survey: Technical Summary. AJ, 120:1579–1587, September 2000.

W. Zheng, R. A. Overzier, R. J. Bouwens, R. L. White, H. C. Ford, N. Benítez, J. P. Blakeslee, L. D. Bradley, M. J. Jee, A. R. Martel, S. Mei, A. W. Zirm, G. D. Illingworth, M. Clampin, G. F. Hartig, D. R. Ardila, F. Bartko, T. J. Broadhurst, R. A. Brown, C. J. Burrows, E. S. Cheng, N. J. G. Cross, R. Demarco, P. D. Feldman, M. Franx, D. A. Golimowski, T. Goto, C. Gronwall, B. Holden, N. Homeier, L. Infante, R. A. Kimble, J. E. Krist, M. P. Lesser, F. Menanteau, G. R. Meurer, G. K. Miley, V. Motta, M. Postman, P. Rosati, M. Sirianni, W. B. Sparks, H. D. Tran, and Z. I. Tsvetanov. An Overdensity of Galaxies near the Most Distant Radio-loud Quasar. ApJ, 640:574–578, April 2006.